UNIVERSITÀ DEGLI STUDI DI NAPOLI FEDERICO II

SCUOLA POLITECNICA E DELLE SCIENZE DI BASE

Dipartimento di Ingegneria Chimica, dei Materiali
e della Produzione Industriale

Dottorato di Ricerca in Ingegneria Chimica
XXVII Ciclo

PHYSICAL MODELLING OF NEAR-WALL PHENOMENA IN ENTRAINED-FLOW COAL GASIFIERS

Ph.D. Thesis

Scientific Committee

Prof. Piero Salatino

Prof. Pier Luca Maffettone

Prof. Fabio Montagnaro

Dr. Roberto Solimene

Prof. Kevin J Whitty

Candidate

Maurizio Troiano

Abstract

Combustion and gasification under slagging conditions are key aspects of the design of modern entrained-flow reactors for thermal conversion of solid fuels, aimed at increasing the overall energy efficiency. In these systems, solid particles migrate toward the reactor walls, due to swirled/tangential flow induced in the reaction chamber and to turbophoresis, generating, thanks to the very high operating temperatures, a slag layer that flows along the reactor internal walls and is drained to the bottom of the reactor. The recent literature on entrained-flow gasification has addressed the fate of char particles as they impinge on the wall slag layer. Different micromechanical char–slag interaction patterns may establish, depending on the stickiness of the wall layer and of the impinging char particle (namely *sticky wall–sticky particle*, *non sticky wall–non sticky particle*, *non sticky wall–sticky particle* and *sticky wall–non sticky particle* regimes).

This study aims to contribute to the development of a phenomenological model of the fate of coal/ash particles which considers the establishment of particle segregated phases in the near-wall region of the gasifier. In particular, near-wall phenomena were investigated and mechanistic understanding of particle–wall interaction patterns in entrained-flow gasifiers was pursued using the tool of physical modeling. Montan wax was used to mimic, at atmospheric conditions, particle-wall interactions relevant in entrained-flow gasifiers. As a matter of fact, this wax had rheological/mechanical properties resembling under molten state, those of a typical coal slag and, under solid state, those of char particles. Experiments have been carried out in a lab-scale cold entrained-flow reactor, optically accessible, and equipped with a nozzle whence molten wax atomized into a mainstream of air to simulate the near-wall fate of char/ash particles in a real hot environment. Reactor lengths in the range 0.1–0.6 m were investigated, while the wax was atomized at a temperature of 100–110 °C. The four particle-wall interaction regimes were investigated. Assessment of the flow and segregation patterns was based on direct visual observation by means of a progressive scan CCD video camera, while the partitioning of the wax droplets/particles into the different phases was characterized by their selective collection at the reactor exhaust. Results showed that the particle-wall interaction mechanisms and segregation patterns are deeply affected by the stickiness of both the wall layer and the impinging particle. In particular, the partitioning results of the wax into the lean-dispersed phase and the wall layer indicated that sticky particles mainly adhere on the wall surface, regardless the stickiness of the wall, whereas non sticky particles may rebound, deposit and be resuspended into the main flow upon the impact on a dry wall, depending also from the local hydrodynamic conditions. As regards the interaction of non sticky particles with a sticky wall, the partitioning results lie between those obtained for the other regimes. Moreover, from a phenomenological point of view, particles follow

the gaseous streamlines at the center of the duct, as expected in dilute particle-laden flows. On the other hand, the particle flow pattern in the near-wall region is barely influenced by the gas flow, whereas it is strongly affected by particle–wall micromechanics, which induces particle segregation and accumulation phenomena. It is possible to conclude that micromechanical interaction of a particle with a sticky wall enhances particle transport to the wall and the tendency to reach a segregation-coverage regime with the formation of a dense-dispersed phase in the near-wall of the reactor.

Another kind of experiments was also accomplished, in order to study the micromechanical particle-wall interaction. To achieve this objective, a proper lab-scale apparatus was designed and built up, in which high speed imaging and tracking of wax particles impacted onto a flat surface at near-ambient conditions were carried out. Particle–wall collision was described in terms of normal and lateral restitution coefficients and capture efficiency. The influence of the particle stickiness, impact velocity and angle, and surface properties and structure of the target on the rebound patterns was studied. Results indicated that the elastic–plastic adhesive model provides an adequate representation of the non sticky particle–wall collisions. Moreover, the presence of a powder layer on the target favours energy dissipation and accumulation of particles close to the surface. This pattern promotes the establishment of a dense-dispersed phase in the near-wall zone of entrained-flow slagging gasifiers. Increasing the temperature, particles shift from the solid/plastic to the fluid state and the coefficient of restitution drops to vanishingly small values, confirming that deposition is the prevailing phenomenon during the collision of sticky particles on a wall.

Contents

List of Figures

List of Tables

Chapter 1. Literature review on the main topics of this Ph.D. Thesis: gasification, coal gasification modelling and near-wall particle segregation in entrained-flow slagging gasifiers

1.1 Global Energy Map: outlook and issues

The global energy map is in continuous redrawing and evolution, in order to meet the growing energy needs, led by rising incomes and populations in emerging economies, to provide energy access to the poorest Countries and to reach the climate change objectives. The IEA (International Energy Agency) released the 2014 edition of the World Energy Outlook (*www.iea.org*). Its executive summary certifies a resurgence in oil and gas production, a retreat from nuclear power in some Countries, as well as a rapid growth in the use of wind and solar technologies and the global spread of unconventional gas production. Renewable energy technologies, a critical element of the low-carbon pillar of global energy supply, are rapidly gaining ground, helped by global subsidies amounting to $120 billion in 2013. The consumption of biomass (for power generation) and biofuels grows four-fold, with increasing volumes being traded internationally. Worldwide, roughly 39% of the global electrical energy is attributed to coal conversion technologies, as coal is cheap, plentiful and it represents the 24% of the global energy sources *(Greb et al., 2006; Song et al., 2011)*. However, its long-term dominating role will depend on the strength of the policy measures promoting *clean coal technologies*, such as lower-emissions energy technologies, the deployment of more efficient coal-burning technologies and, especially important in the long term, CCS (*Carbon Capture and Storage*) systems.

In order to restrain the global warming and maintain the objective of a long-term temperature increase of no more than 2°C, the major energy-consuming Countries have announced and adopted new measures: China aims at a 16% reduction in the energy intensity by 2015; in the United States a switch from coal to gas in the power generation helped to reduce the emissions by 200 million tonnes (Mt), bringing them back to the level of the mid-1990s; the European Union has engaged in a cut of 20% in its 2020 energy demand, and Japan aims to cut 10% from the electricity consumption by 2030. In this scenario, syngas can assume a leading role as a source of electricity, chemicals and for the clean transportation fuel production.

Syngas is a gas mixture which contains primarily carbon monoxide and hydrogen, plus amounts of carbon dioxide, methane and water vapor. These “basic building blocks” can be used in many different processes in order to obtain chemical products such as ammonia, methanol, hydrogen, or synthetic petroleum to use as fuel or lubricant via the *Fischer-Tropsch process*. In addition, the syngas has 50% the energy density of the natural gas, allowing it to be burnt and used as a fuel source in the fuel-cells or in gas/steam turbines to produce electricity.

Gasification offers one of the cleanest and most flexible ways of converting coal, biomass, petroleum coke, refinery residues or other low-grade fuels (such as waste) into syngas and, thus, into electricity, chemicals or clean transportation fuels. Moreover, Integrated Gasification Combined Cycle (IGCC) power plants result in a highly efficient and environmentally friendly technology for coal-based power generation. As a matter of fact, gasification-based plants can easily include readily available technologies for the CO_2 capture and sequestration.

1.2 Gasification basics and technologies

Gasification is the conversion of a carbonaceous material (liquid or solid) into a gaseous product with a useable heating value for the production of energy products and by-products in an oxygen starved environment *(Higman and van der Burgt, 2008)*. Typically, steam and oxygen are used as oxidants. The carbonaceous or "organic" material is processed in an oxygen-deficient environment, externally heated, to produce a syngas comprising mainly carbon monoxide (CO) and hydrogen (H_2). The Chemical bonds of the carbonaceous materials (complex chemical compounds) break down with heat to produce the more simple and thermodynamically stable gaseous molecules of CO and H_2, while the inorganic or "mineral" fractions are converted to a solid rocklike material called slag or vitrified slag or ash. There are four main steps for the conversion of the particles during gasification *(Basu, 2006)*. The first step is drying, at about 150°C, during which the moisture in the solid evaporates. Pyrolysis is the second step, occurring in the range of temperature between 350°C and 700°C; it can take as little as milliseconds to attain completion. During this sub-process, water vapor, organic liquids and non-condensable volatile gases are released and separated from the remaining skeleton, called char. The third step of fuel conversion is the char oxidation. Although there is not enough O_2 to fully oxidize the char, any O_2 remaining after the volatiles oxidation will react with the char since O_2 is the most effective agent for gasification *(Niksa et al., 2003)*. The last step is the char gasification by reactions with CO_2, H_2O, CO and H_2.
Char oxidation/partial oxidation and the volatiles oxidation by O_2 mostly follow these strongly exothermic reactions:

$$C + O_2 \rightarrow CO_2$$

$$C + {}^{1}/_{2}\, O_2 \rightarrow CO$$

$$H_2 + {}^{1}/_{2}\, O_2 \rightarrow H_2O$$

$$CO + {}^{1}/_{2}\, O_2 \rightarrow CO_2$$

These reactions provide heat which will dry the coal, break the chemical bonds in the coal, raise the temperature of the compounds and drive the following main endothermic char gasification reactions:

$$C + H_2O \leftrightarrow CO + H_2$$

$$C + CO_2 \leftrightarrow 2CO$$

where the first is commonly called *Steam gasification* and the second is the *Boudouard reaction*.
The carbon monoxide produced can be oxidized by steam to produce carbon dioxide and hydrogen by the *Shift* (exothermic) reaction:

$$CO + H_2O \leftrightarrow CO_2 + H_2$$

which results in an increase in the ratio hydrogen to carbon monoxide in the syngas produced.

Another important reaction is the *Methanation* (exothermic):

$$C + 2H_2 \leftrightarrow CH_4$$

which is preferred in IGCC applications due to the high methane heating value.

The overall gasification process depends on parameters such as the particles mean residence time, temperature and pressure, steam to fuel ratio and *Equivalence Ratio*. In particular, an increase in the temperature leads to a syngas rich in CO and H_2; an increase in the operative pressure promotes the reactions with a reduction in moles number, resulting in a syngas rich in CO_2, CH_4 and H_2O, while a larger steam to fuel ratio determines a greater content of CO_2, H_2O and H_2 in the product gas.
Gasification requires the presence of an oxidant as air or pure oxygen, evaluable from the *Equivalence Ratio* (ER):

$$ER = \frac{m_{air}/m_{fuel}}{\left(m_{air}/m_{fuel}\right)_{st}} \quad (1)$$

which represents the ratio between actual and stoichiometric conditions in terms of air to fuel mass flow rates ratio. In a gasification process this ratio is minor than 1 and, usually, a value ranging between 0.2-0.3 is chosen in industrial plants *(Basu, 2006)*.

In the practical realization of gasification processes there are many reactor solutions which differ in the mechanical design and operating conditions. They can be grouped into three categories: moving-bed gasifiers, fluid-bed gasifiers and entrained-flow gasifiers (EFG). Some of their characteristics are summarized in Table 1, referring to coal as the carbonaceous feed *(Higman and van der Burgt, 2008)*.

Table 1. Characteristics of different gasification technologies (Adapted from *Higman and van der Burgt, 2008*).

Category	**Moving-bed**		**Fluid-bed**		**Entrained-flow**
Installed capacity (%)	42		2		56
Ash conditions	Dry bottom	Slagging	Dry ash	Agglomerating	Slagging
Typical processes	Lurgi	BGL	Winkler, HTW, KBR, CFB, HRL	KRW, U-Gas	KT, Shell, GEE, E-Gas, Siemens, MHI, PWR
Feed characteristics					
Size (mm)	6-50	6-50	6-10	6-10	<0.1
Acceptability of fines	Limited	Injection through tuyères	Good	Better	Unlimited
Acceptability of caking coal	Yes	Yes	Possibly	Yes	Yes
Preferred coal rank	Any	High	Low	Any	Any
Operating characteristics					
Outlet gas temperature	Low (425-650°C)	Low (425-650°C)	Moderate (900-1050°C)	Moderate (900-1050°C)	High (1200-1600°C)
Oxidant demand	Low	Low	Moderate	Moderate	High
Steam demand	High	Low	Moderate	Moderate	Low
Other characteristics	Hydrocarbons in gas	Hydrocarbons in gas	Lower carbon conversion	Lower carbon conversion	Pure gas, high carbon conversion

Moving-bed gasifiers (also called *fixed-bed gasifiers*) account for nearly 42% of the worldwide total installed gasification capacity *(Young, 2010)*. They are characterized by a bed in which the coal moves slowly downward under the action exerted by gravity, while reacting with the gases usually moving in a counter-current blast to the coal. In such a counter-current arrangement, hot synthesis gas from the gasification zone is used to preheat and volatilize the downward flowing coal. This technology permits the oxygen consumption to be very low, although the pyrolysis products are present in the synthesis gas. The outlet temperature of the synthesis gas is generally low, even if high, slagging temperatures (>1300-1500°C) are reached in the heart of the bed. The moving-bed processes operate on lump coal because an excessive amount of fines, particularly if the coal has strong caking properties, can block the passage of the up-flowing syngas.

Fluid-bed gasifiers account for about 2% of the installed capacity and appear to have potential for low-ranked coals. They offer an extremely good mixing between feed and oxidant, which promotes both the heat and mass transfer. This ensures a uniform distribution of the material in the bed, but a certain amount of only partially reacted fuel is inevitably removed with the ash, resulting in a limitation in the carbon conversion. The sizing of the particles in the feed is a crucial point; material that is too fine will tend to be entrained in the syngas and leave the bed overhead. This is partially captured in a cyclone and recycled into the bed. The operation of fluid-bed gasifiers is generally restricted to temperatures below the softening point of the ash, since ash slagging would

disturb the fluidization of the bed. Coal particles enter the reactor sideways while steam and oxygen or air enter the bottom and the ash is removed from the bottom. The restriction in the operating temperature limits the fluid-bed processes to using reactive feedstock, such as low-rank coals and biomass.

Entrained-flow gasifiers represent about 56% of the installed capacity. They are widely used because of the following reasons: reliable and proven design (widely used in the chemical industry), no internal moving parts, compact size, minimal byproducts and ability to supply syngas at higher pressures. Entrained-flow gasifiers operate with solid feed and gas in co-current flow. The residence time in these processes is short (a few seconds), hence, high temperatures are required to ensure a good conversion; for this reason, almost all the entrained-flow gasifiers operate in slagging mode. These operating temperatures ensure the destruction of tars and oils and, if the gasifier is appropriately designed and operated, a high carbon conversion of over 99% is reached. Some coal-water slurry-fed plants do not achieve this carbon conversion in a single pass, thus, a carbon recycle is used. The feed is ground to a size of 100 μm or less to promote mass transfer and allow its transport in the gas. Differently from the moving-bed reactors, a high oxygen demand is required for this type of process, in order to ensure and maintain high temperatures. Entrained-flow gasifiers do not have any specific technical limitations on the type of coal used, although coals with a high moisture (>15% wt) or ash content (>20% in slurry-feed gasifiers and 40% in dry feed gasifiers) will drive the oxygen consumption to levels where alternative processes may have an economic advantage. One important point to note throughout all the above is the significance of the slagging behavior of the ash. At temperatures above the ash-softening point, the ash becomes sticky and will agglomerate, causing blockage of the beds or fouling of the heat exchange equipment. Once above the slagging temperature (about 1300-1500°C), ash has a fully liquid behavior with a relatively low viscosity, hence, it is possible again to reliably remove it from the system.

The majority of the most successful coal gasification processes developed after 1950 are the entrained-flow slagging gasifiers operating at pressures of 20–70 bar and at high temperatures of at least 1400°C. Figure 1 shows a schematic of a typical entrained-flow coal gasifier.

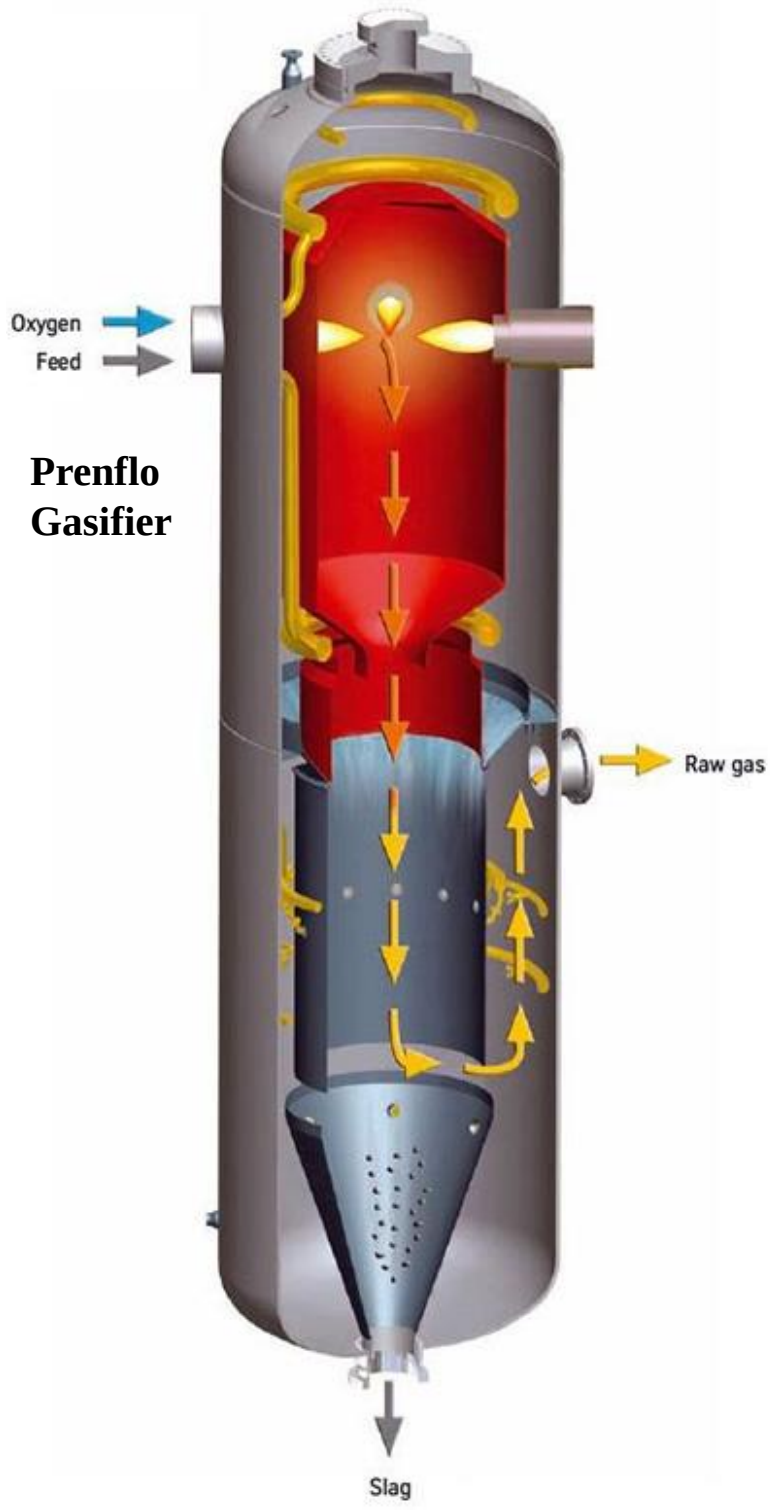

Figure 1. Schematic of a Prenflo entrained-flow coal gasifier.

Entrained-flow gasifiers have become the preferred technology for hard coals, and have been selected for the majority of commercial-sized IGCC applications. The current development in next generation coal-fired power stations uses IGCC technologies in order to address a number of problems related to the increase of the emissions of NOx, SOx, and particulates from conventional

pulverized coal-fired power stations. The IGCC technology uses a combined cycle layout with a gas turbine driven by the syngas coming from the gasifier, whereas the exhaust gases are heat exchanged with water/steam to generate superheated steam to drive a steam turbine. This technology offers a basis for the development of low and ultimately zero emissions power generation technologies. O_2/steam-blown entrained-flow gasifiers have been successfully demonstrated in IGCC in Europe (Shell and Prenflo gasifier) and in the United States (GE gasifier). The various designs of entrained-flow gasifiers differ in their feed systems (dry coal fed in a high-density fluidized state or coal-water slurries), vessel containment for the hot conditions (refractory or membrane wall), configurations for introducing the reactants and ways in which the sensible heat is recovered from the raw gas. Table 2 outlines the characteristics of some important entrained-flow processes *(Higman and van der Burgt, 2008)*.

Table 2. Characteristics of gasification entrained-flow reactors (Adapted from *Higman and van der Burgt, 2008*).

Process	Stages	Feed	Flow	Reactor wall	Syngas cooling	Oxidant
Koppers-Totzek	1	Dry	Up	Jacket	Syngas cooler	Oxygen
Shell	1	Dry	Up	Membrane	Gas quench and syngas cooler	Oxygen
Prenflo	1	Dry	Up	Membrane	Gas quench and syngas cooler	Oxygen
Siemens	1	Dry	Down	Membrane	Water quench and/or syngas cooler	Oxygen
GE	1	Slurry	Down	Refractory	Water quench or syngas cooler	Oxygen
E-Gas	2	Slurry	Up	Refractory	Two-stage gasification	Oxygen
MHI	2	Dry	Up	Membrane	Two-stage gasification	Air
Eagle	2	Dry	Up	Membrane	Two-stage gasification	Oxygen

One advantage of a slagging reactor over a non-slagging combustor is the fact that the collected slag has in general a higher economic value compared to the bottom ash, because of its longer durability and resistance to surface wear. In addition, the slag layer results in a molten protective coating and reduces the heat loss to the wall, generally increasing the cold gas efficiency of the gasifier *(Yong and Ghoniem, 2012)*. However, the increasing slag layer can bring about gasifier

plugging, and the slag deposition on the wall membrane reduces the overall heat-transfer coefficient. The molten ash flows through the bottom of the gasifier and is quenched in a water bath, where it can be typically divided into coarse slag and fine slag *(Li and Whitty, 2009)*. Both the coarse and fine slag have a relatively large content of unburned carbon. Coarse slag is derived from the slag which accumulates on and flows down the reactor wall before entering the slag quench chamber (which may also serve as gas quench depending on the gasifier design). Finer particles of mineral matter also enter the slag quench and are designated as fine slag. A third stream is the fly slag, which leaves the gasifier with the syngas. This third stream may be collected separately in a dry filter or washed out in a scrubber. In the latter case the rundown water is usually mixed with the quench water blowdown, so the fine slag is a mixture from two sources *(Higman and Tam, 2014)*. The presence of unburned carbon within the slag is a result of the incomplete gasification of the coal, which is the major determinant of the gasification efficiency in entrained-flow processes. The carbon content in fine and coarse slags can reach 60% and 30–35% respectively *(Xu et al., 2009; Zhao et al., 2010; Montagnaro et al., 2011)*, and this is a crucial key also in the coal gasification modeling.

1.3 Modeling coal gasification in entrained-flow slagging gasifiers

Modeling of coal gasification in slagging conditions still has large areas of uncertainty. The first one-dimensional models were developed in the Seventies/Eighties *(Wen and Chaung, 1979; Govind and Shah, 1984)*. They assumed a plug flow regime for both the gaseous and solid phases. Other models have been proposed to take into account the complex reactive multiphase fluid dynamics on the performance of the gasifiers *(Abani and Ghoniem, 2013; Chen et al., 2000; Chen et al., 2001; Silaen and Wang, 2010; Tominaga et al., 2000; Vascellari et al., 2013-2014; Watanabe and Otaka, 2006)*. Typically two approaches have been used: Lagrangian– Particle Eulerian–Fluid models (LPEF) and Eulerian–Particle Eulerian–Fluid models (EPEF). In the LPEF method, the solid phase particles are tracked using a Lagrangian approach, while the surrounding gas phase is modeled using an Eulerian approach. The two phases are coupled by means of source terms in the conservation equations of mass, momentum and energy. When the EPEF method is used, both the solid and gas phases are solved using an Eulerian approach and an additional equation is solved, the ‘‘volume fraction’’, which represents the fractional volume of the solid-phase locally. Typically the EPEF is used when the solid phase occupies high volume and the velocities of the flow are relatively small *(Zimmermann and Taghipour, 2005)*. As a matter of fact, the EPEF method is preferred for calculating the group effect of the solid phase in regions where the volume fraction of the solid phase is large. On the other hand, the LPEF method is used when the solid particles are widely dispersed within the flow and the flow velocities are much larger, as

typically found in EFG *(Wu et al., 2010)*. The influence of various models for turbulence and particle dispersion in different gasifier geometries has been rigorously investigated, as well *(Kumar and Ghoniem, 2012)*. In particular, the shear stress transport (SST) k−ω model performs best among the tested Reynolds-Averaged Navier Stokes (RANS) models and it is able to reasonably predict complex flow structures. Finally, *Abani and Ghoniem (2013)* and *Pedel et al. (2012)* investigated the BYU gasifier using a Large Eddy Simulation (LES) approach for modeling turbulence, the former authors using a standard Lagrangian approach for the solid phase, the latter authors employing the direct quadrature method of moments. The slag flow and slagging combustion/gasification have been also widely investigated. *Seggiani (1998)* developed a one-dimensional time-dependent model for the slag accumulation and flow for the Prenflo coal gasifier being used at the IGCC plant in Puertollano (Spain), and integrated it into a three-dimensional gasifier code. The averaged analytical solutions derived from the conservation equations were calculated to get the slag velocity, molten and solid slag thickness, and the temperature profiles, with the particle mass deposition rate, gas temperature, concentration and heat flux from the three-dimensional code used as input variables. *Wang et al. (2007)* simulated the slagging combustion by dividing the reactive process into two parts: the particle suspension combustion and the particle wall burning. In particular, the particle deposition process, wall burning process, slag flow process, and suspension combustion process of the true physical phenomenon were considered in the hypothesis of two-dimensional axisymmetric structures. *Bockelie et al. (2002)* simulated the slag flow in a one-stage and two-stage gasifier using a slagging wall model (two-dimensional model). *Li et al. (2009)* also used this model to analyze the slag flow in a black liquor recovery boiler and a coal gasifier. This two-dimensional approach is able to capture the spatial distribution of ash deposition due to the gas phase flow field, improving the accuracy of the slag modeling in three-dimensional CFD simulation. However, this approach cannot fully resolve the three-dimensional flow behavior in the case of horizontally-oriented reactors, or reactors with complicated geometry *(Chen and Ghoniem, 2013)*. *Losurdo et al. (2012)* proposed a visco-elastic approach to model ash particle deposition and stickiness behavior. Aiming at this goal, a mechanical adhesion approach was used which takes into account the surface energy, the particle size and the hardness of both the particle and the impacted surface. Also the thermal/rheological behavior of the slag has been studied, as the viscosity of coal ash slag plays a crucial role in determining the operating conditions of entrained-flow gasifiers *(Goldman, 1981; Richards et al., 1993; Erickson et al., 1995; Coda et al., 2007; Song et al., 2009; Song et al., 2010; Song et al., 2011)*. As a matter of fact, the liquid coal ash slag tapped from the gasifier can be homogenous liquid slag or heterogeneous liquid slag containing crystallized particles. It is, therefore, important to describe not only the viscosity of the fully liquid phase but also the viscosity of the liquid phase containing the partly crystallized solid particles in the coal ash.

1.4 Near-wall segregation regimes

The recent literature on entrained-flow gasification has addressed the fate of char particles as they impinge on the wall slag layer. Coal particles are fed to the gasification chamber through nozzles as a lean-dispersed particle-laden gas flow. Particle transport to the wall can be the result of different mechanisms such as Brownian motion, turbulent diffusion, turbophoresis, lift forces, electrostatic forces, virtual mass effect and wall surface roughness *(Guha, 2008; Eskin et al., 2011)*. In the gasification process, the inertial and turbophoretic mechanisms seem to be predominant, the first being enhanced by swirled or tangential flow, and the latter being active near the reactor walls. Moreover, inertia is relevant to coarser particles, turbophoresis to finer ones. Turbophoresis (in which the particle transport is caused by gradients in fluctuating velocities) cannot be properly reproduced by any tuning of the theoretical model for the diffusion (which is driven by the gradients in concentration) *(Caporaloni et al.; 1975* and *Reeks, 1983)*. Turbophoresis results in a particles drift from regions of high turbulence intensity to regions with lower turbulence intensity near the wall *(Marchioli and Soldati, 2002)*, and it is now known to be the main mechanism for transporting particles with substantial inertia in turbulent wall layers *(Slater et al., 2003)*. Both the inertial and turbophoretic mechanisms play a significant role in the transport of particles from the dispersed phase to the walls and in the build-up of a slag layer *(Montagnaro and Salatino, 2010)*. In particular, *Shannon et al. (2008)* analyzed the char-slag interactions taking into account the drag-, capillary-, and added mass-forces acting on spherical particles of different sizes. *Ghoniem* and co-workers *(Yong and Ghoniem, 2012; Yong et al., 2012; Chen et al., 2013)* have developed a steady-state model to describe the flow and heat transfer characteristics of the slag, taking into account the contribution of the momentum of captured particles and the possibility of slag re-solidification along the walls. They also introduced a criterion for particle capture or rebound after impingement on the slag layer, based on the comparison of the kinetic energy and the interfacial surface tension energy between the particle and the slag surface. A simple model was proposed for the char capture by a molten slag surface under high-temperature gasification conditions *(Shimizu and Tominaga, 2006)*. In this model, char particles were pneumatically conveyed onto the molten slag surface. The char particles were assumed to be captured if they reached the molten slag surface, whereas they were repelled if they reached the part that was covered by the unreacted char particles. *Montagnaro and Salatino (2010)* analyzed the relevance of the segregation of carbon particles in a near-wall region of the gasifier to the coal conversion, by considering the effects of turbulence- and swirl-promoted particle migration toward the wall, the interaction of the impinging particles with the wall ash layer, the coverage of the slag layer by refractory carbon particles, the accumulation of carbon particles in a dense-dispersed phase near the wall of the gasifier. In particular, they highlighted that char particles impinging on the wall slag layer can: *i)* be entrapped inside the melt,

and this prevents further progress of the combustion/gasification (*entrapment* regime, Fig. 2); *ii)* adhere onto the slag layer's surface without being fully engulfed, and this permits further progress of the combustion/gasification (*segregation* regime, Fig. 2). In the latter case and if the coverage of the slag layer with carbon particles is extensive, a dense-dispersed annular phase may establish in the close proximity of the wall ash layer, where the excess impinging char particles that cannot be accommodated on the slag surface accumulate (*segregation-coverage* regime, Fig. 2). This annular phase is likely to be characterized by a velocity that is intermediate between that of the fast lean-dispersed particle phase and that of the slowly moving molten ash wall layer (Fig. 2). This feature is beneficial to the carbon conversion, as it gives rise to a longer mean residence time of the carbon particles belonging to this dense phase (with respect to the particle mean residence time in the lean phase). This phenomenological model has received qualitative validation from the analysis of the properties of ash streams generated in a full-scale entrained-flow gasification plant (*Montagnaro et al., 2011*). Moreover, the complex phenomenology associated with the interaction of a particle-laden turbulent flow with the inelastic slag-covered wall of the gasifier has been the subject of numerical simulation *(Ambrosino et al., 2012; Ambrosino et el., 2013)*, which confirmed both that the near-wall accumulation of particles may be extensive and the relevance of such phenomena to the performance of entrained-flow gasifiers.

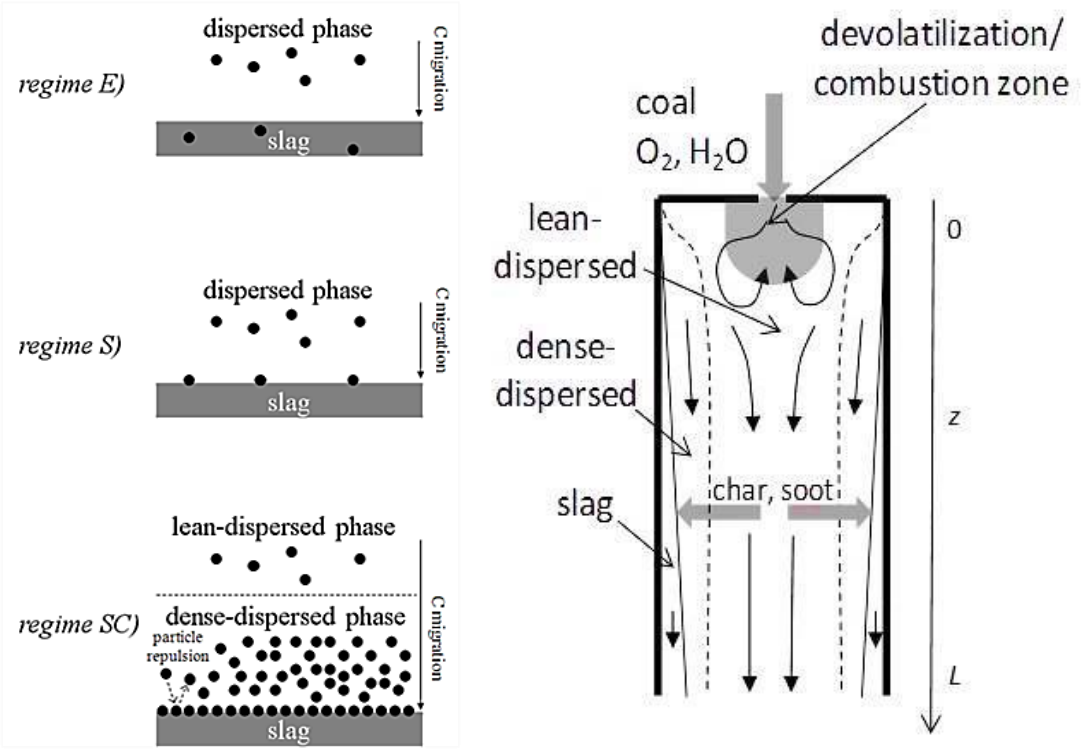

Figure 2. Left: near-wall segregation regimes (E=entrapment; S=segregation; SC=segregation-coverage). Right: schematic diagram of the entrained-flow gasifier.

A further key to the establishment of the regimes outlined in Fig. 2 is represented by the stickiness of the particle and of the wall layer. As a matter of fact, according to *Baxter (1993)* and *Baxter and Desollar (1993)*, the collection efficiency (a measure of the ash deposition rate) of ash particles caused by inertial impact is proportional to the particle capture efficiency, which depends on the ash stickiness and the impacting surface properties. *Isaak et al. (1986)* found that for synthetic ash the stickiness criterion is 10-20% weight fraction of the liquid phase in the particle and *Tran et al. (2002)* confirmed that the stickiness criterion for alkali-rich ash is 15% weight fraction of the molten phase. Other authors also considered the carbon content in the ash as a parameter affecting the stickiness. As examples, *Bool and Johnson (1995)* studied the ash deposition behavior during the coal combustion using an entrained-flow reactor at high temperature. They observed that the collection efficiency of the ash deposit on the deposition probe increased dramatically to a maximum value at a critical char burnout, and then slightly decreased throughout the burnout process. This result, from a macroscopic view, suggests that the effective ash stickiness is dependent upon the residual carbon content. Furthermore, the sharp rise in the stickiness indicates a substantial change in the structure of the ash particles around the critical burnout, possibly the transition from porous, non sticky char to molten, sticky slag. On the other hand, at a later stage of gasification (above a 90% conversion), the transition from porous char to nonporous slag affects the overall carbon conversion because the decrease in porosity enhances the resistance of the reacting gas diffusing into the particle. *Li and Whitty (2009)* also studied the transition of coal char to molten slag at high conversion for a bituminous coal using a laminar entrained-flow reactor under oxidizing conditions. In the initial stage of coal oxidation (the initial stage of the char-slag transition), included minerals are encapsulated by the residual carbon in the char particle. However, the char particle is not sticky because carbon does not melt at the typical combustion temperatures. At intermediate to intermediate-high conversion (the middle stage of the char-slag transition), the included minerals begin to appear on the external surface of the char and they melt, increasing the effective stickiness of the char particle. At high conversion (the final stage of the char-slag transition), fragmentation occurs and a large amount of included minerals are released, forming molten slag. This char-slag transition occurs at a carbon burn-off $X_C \approx 90\%$ *(Li and Whitty, 2009; Li et al., 2010; Li and Whitty, 2012)* and as the temperature is beyond the ash melting point.

1.5 Micromechanics of particle-wall interactions

Yong et al. (2012) described different particle-wall interaction patterns on the basis of the stickiness of the impinging particles and of the wall layer. These patterns are outlined in Fig. 3:

i) Sticky Wall – Sticky Particle (*SW–SP*): char particles with low carbon content (large X_C) impinge on the slag layer;

ii) Sticky Wall – Non Sticky Particle (*SW–NSP*): particles characterized by large carbon content impinge on the slag layer;

iii) Non Sticky Wall – Sticky Particle (*NSW–SP*): char particles characterized by low carbon content impinge on either a dry wall or on a carbon-covered slag layer;

iv) Non Sticky Wall – Non Sticky Particle (*NSW–NSP*): char particles with large carbon content impinge on either a dry wall or on a carbon-covered ash layer.

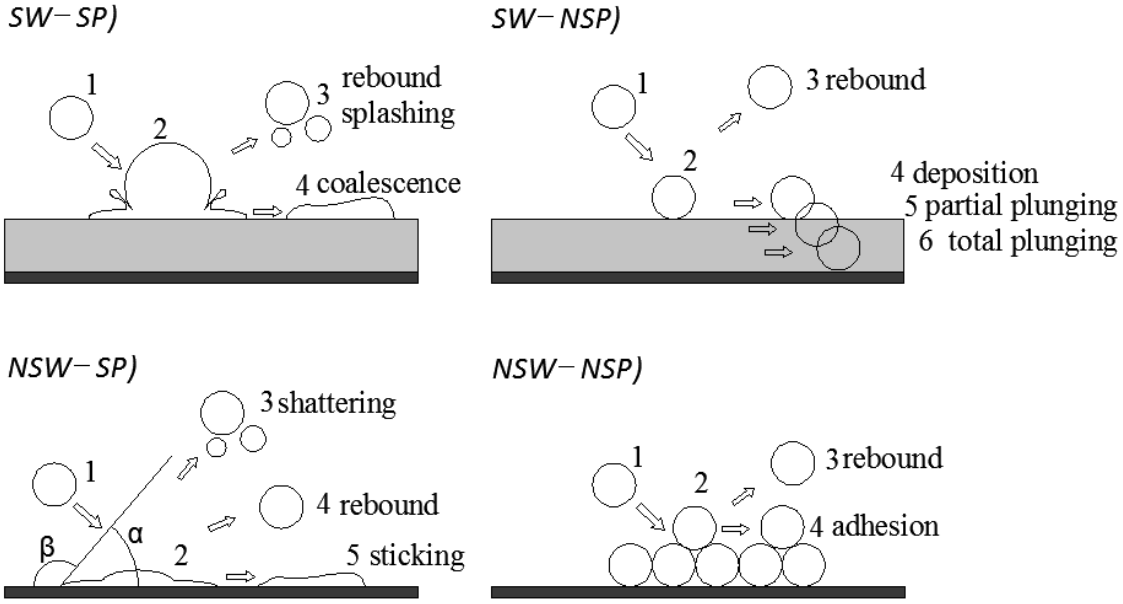

Figure 3. Micromechanical interaction patterns (*SW* stands for "sticky wall", *SP* for "sticky particle", *NSW* for "non sticky wall" and *NSP* for "non sticky particle"). (1) pre-impact, (2) impact, (3-6) post-impact.

Figure 4 shows how the different near-wall carbon-slag segregation regimes (entrapment, segregation, segregation-coverage) can occur as a function of the reactor axial coordinate and of the progress of X_C. The fate of the char particles depends on the complex mechanics of the liquid-solid, liquid-liquid and solid-solid interphase interactions.

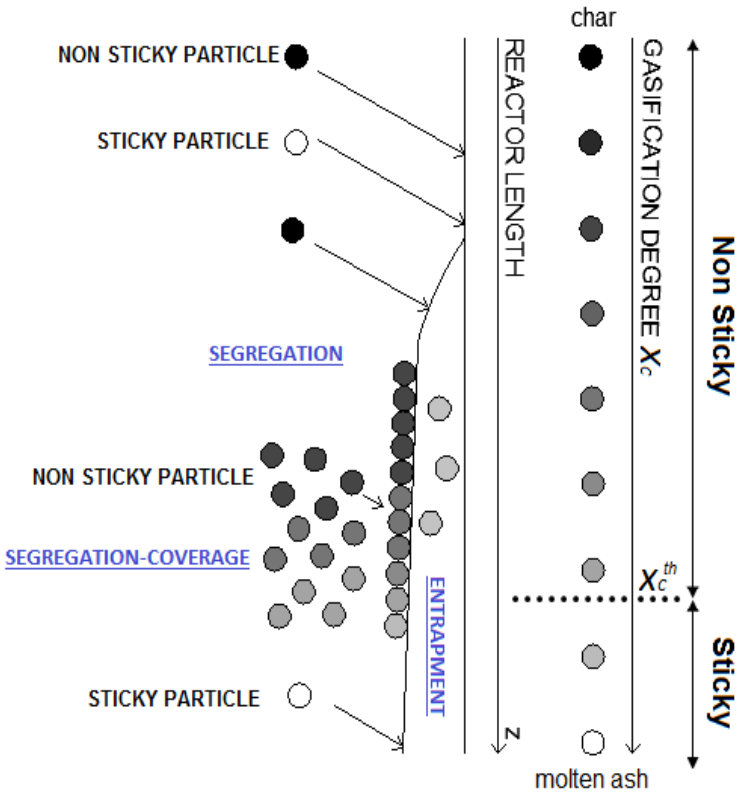

Figure 4. Particle-wall micromechanical interactions and near-wall segregation regimes along the reactor axial coordinate ($\boldsymbol{X_C^{th}}$ is the threshold X_C-value).

For the first regime (*SW–SP*), the sticky particles impinging on the slag layer can either rebound/splash or be entrapped by the liquid surface, contributing, in the latter case, to the wall layer build-up. *Worthington (1908)* was one of the first to investigate drop impacts on deep liquid pools. *Jayaratne and Mason (1964)*, *Ching et al. (1984)*, *Yarin (2006)* and *Pan and Law (2007)* studied the impact of droplets upon liquid surfaces and showed that the droplet diameter, velocity, impact angle and liquid layer thickness all affect rebound and coalescence. *Cossali et al. (1997)* experimentally established the condition of drop splashing on pre-existing liquid films and the data of *Wang and Chen (2000)* and *Rioboo et al. (2003)* are in reasonable agreement. Moreover, *Rein (1993)* described and reviewed the fluid dynamic phenomena of liquid drop impact. In particular, he examined the Weber number effect for bouncing or coalescence to occur, while *Zhbankova and Kolpakov (1990)* studied the effect of the impact angle, emphasizing that there are no sharp boundaries between bouncing and coalescence, but rather regions where one outcome is more likely than the other.

SW–NSP interactions were also studied to establish entrapment, coverage and rebound criteria. *Montagnaro and Salatino (2010)* developed theoretical criteria for particles plunging into the slag layer and for full carbon-coverage of the wall ash layer. In particular, about plunging criterion, an order-of-magnitude analysis based on typical operating conditions of the gasifier and properties of

the molten slag suggests that particle plunging is not likely to occur, unless a combination of large particle sizes (>200 μm) and extremely small ash viscosities (<1 kg m^{-1} s^{-1}) applies. This conclusion is in agreement with the results of detailed computation of the dynamics of particle-slag interaction reported by *Shannon et al. (2008)*. The possibility that a particle deposited on the slag layer surface can subsequently suffer partial/total plunging as the particle gasification degree increases (thus letting the particle itself transform from non sticky to sticky) was postulated and experimentally verified by *Montagnaro et al. (2011)*. About the carbon coverage of the slag layer, the establishment of a segregated carbon regime at the surface of a steadily flowing slag layer was also analyzed by *Shimizu and Tominaga (2006)*. As result, the slag coverage by carbon particles affects the micromechanical interaction with newly impinging char, making the repulsion of an impinging char particle more probable.

From a micromechanical point of view, *Antonyuk et al. (2009)* investigated the normal impact of spherical granules on a flat wall covered by a liquid layer. In particular, the influence of the thickness of the liquid layer and its viscosity as well as the impact velocity on the rebound characteristics was studied. Experimental measurements of the particle restitution coefficient - i.e. the ratio of rebound and impact velocity - upon the impact onto the liquid layer were compared with experiments performed in absence of the liquid layer, showing that in the former case the restitution coefficient decreased, due to a larger energy dissipation during the impact. Furthermore, increasing the liquid viscosity, the restitution coefficient and the minimum thickness of the liquid layer for particle capture decreased. Force and energy balances were solved for a particle impacting on a liquid layer in order to compare modeling and experimental results and also numerical simulations were performed in order to simulate wet particle collisions for application in fluidized bed granulators *(Jain et al., 2012; Fries et al., 2013)*.

NSW–SP interactions have also been the subject of investigation in different contexts. *Ni et al. (2011)* proposed a sub-model for predicting the slag droplets interaction with the wall, hence the slag layer formation. They specifically investigated the effects of slag viscosity, impact velocity, impact angle, molten slag surface tension and particle size on the maximum spread diameter and on the rebound criterion, as developed by *Pasandideh-Fard et al. (1996)* and *Mao et al. (1997)*. *Yoon et al. (2006)* developed a criterion to discriminate whether shattering, rebound and sticking occur, based on results obtained by *Mundo et al. (1995)*. *Rioboo et al. (2002)* and *Šikalo et al. (2005)* studied, experimentally, the time evolution of the normal impact of drops on dry surfaces and the impact of drops on inclined dry surfaces, respectively. Their experimental results were used to validate the VOF model and predictions in the work of *Lunkad et al. (2007)*.

Shimizu and Tominaga (2006) developed a model for the char capture based on a slag layer covered, at least partially, by other char particles valid for the *NSW–NSP* case. In their model, a

char particle impinging the slag surface will rest, whereas it will be repelled if it reaches the part of the slag layer which is covered by unreacted or partly reacted carbon-rich char particles.

Several empirical models were proposed in the literature to determine particle sticking criteria. Slagging is defined as the formation of molten, partially fused or resolidified deposits on the furnace walls and other surfaces exposed to radiant heat. Slagging can also extend into convective surface if the gas temperatures are not sufficiently reduced. Traditional models apply slagging indices based on the ash composition, fusion temperatures and viscosity to predict the slagging potential of coal ash. These engineering indices were developed for specific coal types as an industrial standard and they are summarized in Table 3 *(Kitto and Stultz, 2005)*.

Table 3. Indices of slagging potential.

Slagging Index	Required analysis	Coal ash	Slagging Potential			
			Low	**Medium**	**High**	**Severe**
$R = \frac{base}{acid}$ $a)$	Ash chemistry	Bituminous	<0.6	0.6–2	2–2.6	>2.6
$R = \frac{HT + 4IT}{5}$ $b)$	Ash fusibility	Lignitic	>1616	1505–1606	1422–1505	<1422
$R = \frac{T_{250}^{oxid} - T_{10000}^{red}}{97.5\ fs}$ $c)$	Viscosity	Bituminous and lignitic	<0.5	0.5–1	1–2	>2

$a)$ $\frac{base}{acid} = \frac{CaO+MgO+Fe_2O_3+Na_2O+K_2O}{SiO_2+Al_2O_3+TiO_2} \cdot S$, S = weight % sulfur, on a dry coal basis.
$b)$ HT, hemispherical temperature, IT, initial deformation temperature.
$c)$ T_{250}^{oxid} is the temperature corresponding to a viscosity of 250 poise in an oxidizing atmosphere and T_{10000}^{red} the temperature corresponding to a viscosity of 10000 poise in a reducing atmosphere. fs is a correlation factor based on the average of the oxidizing and reducing temperatures corresponding to a viscosity of 2000 poise.

The modified "Urbain Model" is widely used to model the viscosity of coal ash on the basis of the acid-to-base ratio *(van Dyk et al., 2009)*. The temperature at which the amorphous slag transforms into a crystalline phase is used to calculate the critical viscosity. Therefore, for particle viscosity lower than the critical value (namely, at higher temperatures), the particle sticks. The drawback of these viscosity models to predict particle sticking is that they do not take into account the effect of residual carbon on particle stickiness, and the stickiness of the target wall. Other models use thermodynamic equilibrium calculations to evaluate the properties, transformation and reaction of ash, which is considered as multicomponent and multiphase during combustion and gasification. These models are based on the principle of minimization of the free Gibbs energy and on thermodynamic data of ash components, with an assumption that equilibrium is reached in the system. Some commercial software packages were developed, such as FactSage and Mingtsys. The

thermodynamic equilibrium is combined with fuels analysis to calculate the temperatures at which the ash particle reaches the stickiness criterion. v*an Dyk et al. (2009)* studied the mineral matter transformation during Sasol–Lurgi fixed bed dry bottom gasification using viscosity predictions together with FactSage modelling. The FactSage modeling results confirmed the high temperature XRD observation, and provided insight into the specific mineral matter transformation and reactions including organic and inorganic matter. However, the complexity of the combustion system, great variation of coal composition and uncertainty of some thermodynamic properties are a source of error in the thermodynamic calculations.

The fate of char/ash particles in the near-wall region of EFG is better predicted by detailed mathematical and physical modelling. Particle–wall interactions can be investigated and described in terms of a coefficient of restitution (the ratio between the rebound and the impact velocities). *Dong et al. (2013)* investigated the normal restitution coefficient of fly ash particles impacting a planar surface at room temperature. *Pisupati* and co-workers *(Gibson et al., 2013)* carried out EF and drop experiments at ambient conditions to simulate the different particle–surface collision patterns relevant in EFG. The restitution coefficient is an important parameter when modelling multiphase flow in the gasification chamber, e.g. by the tools of CFD-DPM, as it critically affects the boundary condition for particle−wall collisions.

Particle–wall collisions are generally characterized in terms of a restitution coefficient ε, defined as the ratio between the rebound and the impact velocity. The coefficient takes the value ε=1 when the impact is perfectly elastic, whereas $\varepsilon \rightarrow 0$ when the particles dissipate all their kinetic energy at the impact, and adhere on the surface. The restitution coefficient embodies phenomena like elastic and plastic deformation of solid materials, surface contact forces and particle–wall friction *(Hertz, 1896; Johnson et al., 1971; Rogers and Reed, 1984)*. *Thornton and Ning (1998)* developed a model for the normal impact of elastic–perfectly plastic spheres, which also takes into account adhesion effects. In their model, the normal restitution coefficient is zero at impact velocities smaller than a threshold value: the particles adhere on the surface as the impact energy is lower than the adhesion energy *(Rogers and Reed, 1984)*. This critical velocity, also called "capture" or "sticking" velocity, v_s, is a function of particle size and density, particle surface energy and elastic properties of both the particle and surface (Young's moduli and Poisson's ratios), as follows:

$$v_s = 1.84 \left[\frac{4\left(\frac{2\Gamma}{d_p}\right)^5}{3\rho_p^3 K^2} \right]^{\frac{1}{6}} \tag{2}$$

where Γ is the surface energy at the interface, d_P and ρ_P are the particle diameter and density, respectively, and K is the composite Young's modulus. Γ and K can be expressed as:

$$\Gamma = 2(\Gamma_1 \Gamma_2)^{0.5} \tag{3}$$

$$K = \frac{4}{3}\left(\frac{1-\nu_1^2}{E_1} + \frac{1-\nu_2^2}{E_2}\right)^{-1} \quad (4)$$

where Γ_1 and Γ_2 are the surface energies, E_1 and E_2 are the Young's moduli, and ν_1 and ν_2 are the Poisson's ratios, for the particle and the surface, respectively.

For impact velocity larger than the sticking velocity, particles rebound. For elastic materials, the normal restitution coefficient approaches 1, whereas for elastic–plastic materials the restitution coefficient increases with the impact velocity, as far as the material displays elastic behaviour. When the impact velocity is further increased, plastic deformation begins, inducing additional energy losses during the impact, and a decrease in the value of the normal restitution coefficient. The limiting velocity above which plastic deformation occurs is called "yielding velocity" v_y, and it is determined by the bulk properties of the particles and the wall, while it is independent of the particle size *(Rogers and Reed, 1984; Thornton and Ning, 1998; Wall et al., 1990)*:

$$v_y = \left(\frac{2\pi}{3K}\right)^2 \left(\frac{2}{5\rho_p}\right)^{\frac{1}{2}} p_y^{\frac{5}{2}} \quad (5)$$

where p_y is the limiting contact pressure at which the first irreversible deformation occurs (also called "cut-off pressure"). It depends on both the impact parameters (velocity) and the particle mechanical properties (yield strength).

Thornton and Ning (1998) derived an analytical solution for the coefficient of restitution for normal impacts of adhesive, elastic–perfectly plastic spheres, expressed in terms of the impact, capture and yielding velocities (v_i, v_s and v_y, respectively), by assuming that the work dissipated due to plastic deformation and the work dissipated due to adhesive rupture are additive. The restitution coefficient is, thus, expressed as:

$$\varepsilon_n = 0 \qquad \text{for } v_i \le v_s \quad (6)$$

$$\varepsilon_n = \left[1 - \left(\frac{v_s}{v_i}\right)^2\right]^{\frac{1}{2}} \qquad \text{for } v_s \le v_i \le v_y \quad (7)$$

$$\varepsilon_n^2 = \frac{6\sqrt{3}}{5}\left[1 - \frac{1}{6}\left(\frac{v_y}{v_i}\right)^2\right]\left[\frac{\frac{v_y}{v_i}}{\frac{v_y}{v_i} + 2\sqrt{\frac{6}{5} - \frac{1}{5}\left(\frac{v_y}{v_i}\right)^2}}\right]^{\frac{1}{2}} - \left(\frac{v_s}{v_i}\right)^2 \qquad \text{for } v_i \ge v_y \quad (8)$$

When an oblique impact is considered, the particle–wall friction expressed by the tangential restitution coefficient has to be taken into account *(Brach and Dunn, 1998; Gorham and Kharaz, 2000; Wu et al., 2003; Wu et al., 2009)*. Moreover, particle rolling and sliding may occur on the

verge of the impact. Figure 5 shows a particle impacting and bouncing off a flat surface with its velocity components and angles.

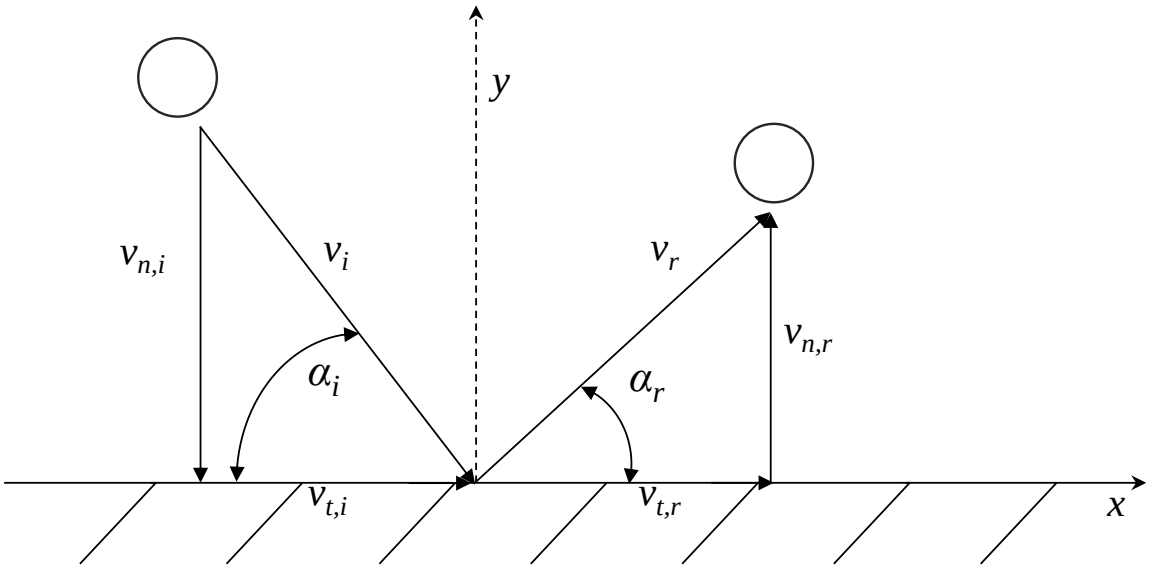

Figure 5. Outline of particle impact with a planar surface.

It is useful to define a normal and a tangential coefficient of restitution, ε_n and ε_t, respectively, as:

$$\varepsilon_n = \frac{-v_{n,r}}{v_{n,i}} \tag{9}$$

$$\varepsilon_t = \frac{v_{t,r}}{v_{t,i}} \tag{10}$$

where $v_{n,i}$ and $v_{n,r}$ are the normal components of the impact and rebound velocity, respectively, and $v_{t,i}$ and $v_{t,r}$ are the corresponding tangential components. It is also possible to define a global coefficient of restitution ε_g as:

$$\varepsilon_g = \frac{v_r}{v_i} = \sqrt{\frac{v_{n,r}^2}{\frac{v_{n,i}^2}{sin^2\,\alpha_i}} + \frac{v_{t,r}^2}{\frac{v_{t,i}^2}{cos^2\,\alpha_i}}} = \sqrt{\varepsilon_n^2\,sin^2\,\alpha_i + \varepsilon_t^2\,cos^2\,\alpha_i} \tag{11}$$

where ε_g tends to ε_n for large impact angles ($\alpha_i \rightarrow 90°$) and to ε_t for small impact angles ($\alpha_i \rightarrow 0°$). The particle rebound behaviour is deeply influenced by the impact angle. According to the rigid body theory, a sphere, upon the impact, slides at small impact angles and rolls at near-normal angles. When sliding occurs throughout the impact, the tangential coefficient of restitution can be expressed as a function of ε_n, α_i and of the tangential-to-normal impulse ratio f *(Gorham and Kharaz, 2000; Wu et al., 2003; Wu et al., 2009)*, as:

$$\varepsilon_t = 1 - f(1 + \varepsilon_n)\tan\alpha_i \tag{12}$$

The critical impact angle at which the transition from sliding to rolling occurs can be expressed as *(Wu et al., 2009)*:

$$\alpha_i^{cr} = \cot^{-1}\left[\frac{7k-1}{k}\frac{f}{2}(1+\varepsilon_n)\right] \tag{13}$$

where k is the ratio of the tangential to the normal composite stiffness:

$$k = \frac{\frac{1-\nu_1}{G_1}+\frac{1-\nu_2}{G_2}}{\frac{1-\frac{\nu_1}{2}}{G_1}+\frac{1-\frac{\nu_2}{2}}{G_2}} \tag{14}$$

G_1 and G_2 being the shear modulus for the particle and the surface, respectively.

Furthermore, particle rebound characteristics depend on the structure and roughness of the substrate. *van Steenhoven* and co-workers *(Abd-Elhady et al., 2006; van Beek et al., 2006)* experimentally investigated the rebound characteristics of micron-size particles colliding on a powdery layer. The results were compared with those obtained by solving forces and moment balances, confirming the validity of physical modelling in describing particle–particle and particle–wall interactions. Furthermore, a numerical code was developed, which was based on the discrete element method. The numerical results were validated by experimental results and were found to be in good agreement with them.

Another phenomenon which can be relevant during the gasification of solid particles in an EFG is the resuspension of adhered particles from the wall layer into the lean-dispersed phase, under the action of a gaseous flow field in the near-wall region. Several authors have modeled resuspension from a micromechanical point of view, considering the sliding and rolling motion as a first step of this mechanism for the particle removal, and taking into account the effect of physical parameters such as particle size, fluctuations of turbulent flow velocity and surface roughness. *Guingo and Minier (2008)* developed a model for the simulation of particle resuspension from horizontal surfaces, based on a stochastic description of wall roughness and adhesion forces. When the hydrodynamic forces overcome the adhesion ones, the particle detaches from the wall surface and, then, it can be easily dragged into the bulk gas flow. Three different mechanisms of particle detachment from a wall surface, namely lift-off, sliding and rolling can be considered, as depicted in Fig. 6, basing on a quasi-static approach (force and moment balances) *(Goldasteh et al., 2013; Ibrahim et al., 2003; Ibrahim et al., 2008; Ziskind et al., 1997)*.

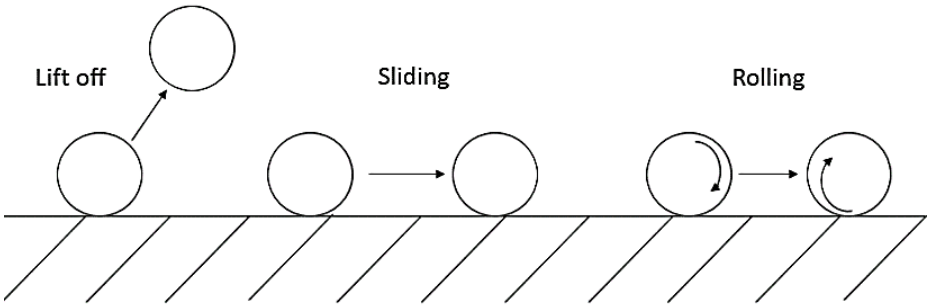

Figure 6. Micromechanical mechanisms of particle detachment from a flat surface.

The threshold gas velocity for the detachment of a microparticle embedded in a viscous sublayer from a vertical flat surface can be calculated, for all the three detachment mechanisms, by:

- normal force balance (lift-off mechanism)

$$F_L = F_{PO} \tag{15}$$

- tangential force balance (sliding mechanism)

$$F_D + F_G = k_S(F_{PO} - F_L) \tag{16}$$

- moment balance (rolling mechanism)

$$1.4\frac{d_p}{2}F_D + \frac{d_p}{2}F_G = a(F_{PO} - F_L) \tag{17}$$

where F_L is the lift force, F_G the force due to the gravity, F_{PO} the adhesion force and F_D the drag force. k_s is the static coefficient of friction, d_p is the particle diameter and a the contact radius between the particle and the surface, as reported in Fig. 7. In the moment balance Eq. (17), the factor 1.4 accounts for the non-uniformity of the flow field *(O'Neill, 1968)*. The mean aerodynamic lift force is estimated in dimensionless form and for a particle fully embedded in the viscous sublayer *(Leighton and Acrivos, 1985; Ziskind et al., 1995)* as:

$$F_L^+ = 0.58\left(d_p^+\right)^4 \tag{18}$$

where $F_L^+ = F_L\rho/\mu^2$, ρ is the density of the fluid and μ its viscosity, while $d_p^+ = d_p u_{fr}\rho/\mu$ and u_{fr} is the friction velocity (a function of the flow velocity u). The adhesion force F_{PO}, also called pull-off force, may be defined as the opposite of the force required to separate two bodies. According to the JKR model *(Johnson et al., 1971)*, the pull-off force for a smooth surface, assuming elastic contact, is:

$$F_{PO,S} = 1.5\pi\Gamma\frac{d_p}{2} \tag{19}$$

where Γ is the surface energy of adhesion per unit area of contact. The contact radius at separation, *a*, according to the JKR model, is given as:

$$a = \left(\frac{F_{PO} d_p}{2K}\right)^{\frac{1}{3}} \tag{20}$$

where *K* is the particle–wall composite Young's modulus (Eq. 4). Surface roughness makes the real contact area between the particle and the surface drastically decrease *(Cheng et al., 2002)*. The rough-surface pull-off force can be estimated as *(Ibrahim et al., 2008)*:

$$F_{PO} = C F_{PO,s} \tag{21}$$

where *C* represents a ratio of rough-to-smooth pull-off forces. The drag force applied to the particle is taken as the Stokes drag, as the particle is completely embedded in the viscous sublayer, and it is given by:

$$F_D = 3\pi\mu u d_p f_w \tag{22}$$

where the factor f_w (f_w=1.7009) accounts for the wall effect *(O'Neill, 1968)*.

By solving the balance Equations (15), (16) and (17) it is possible to estimate the free-stream velocity required for particle detachment from the surface according to the lift-off, sliding and rolling modes, respectively.

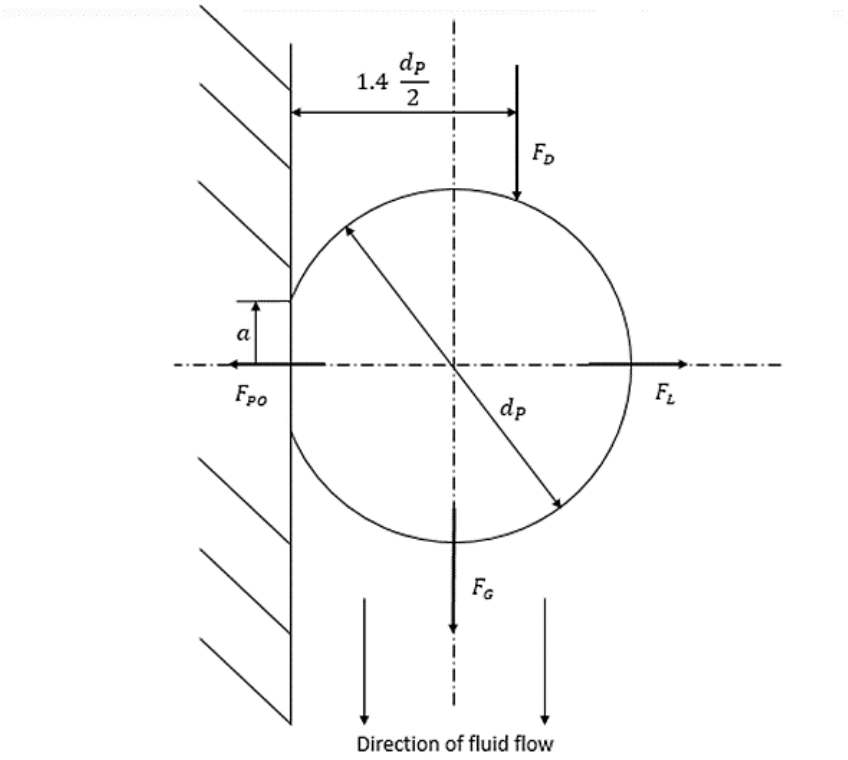

Figure 7. A schematic of a microparticle attached to a surface and the forces acting on it at the moment of detachment.

Previous studies have highlighted that in the viscous sublayer burst-sweep events occur, associated with the turbulent flow character in the wall-adjacent region, thus causing an instantaneous increase in the flow velocities *(Marchioli and Soldati, 2002; Soltani and Ahmadi, 1994; Soltani and Ahmadi, 1995; Ziskind et al., 1995)*. This phenomenon can facilitate the detachment process and, hence, particles resuspension, as depicted in Fig. 8. *Soltani and Ahmadi (1994, 1995)* proposed an expression for the maximum axial velocity in the viscous sublayer during turbulent burst events:

$$u^+ = \Psi x^+ \tag{23}$$

where $u^+ = u/u_{fr}$ and $x^+ = x u_{fr}\,\rho/\mu$ (x is the distance from the wall), while Ψ is a factor which takes into account the velocity increase during a burst event. Ψ=1 means a linear profile in the viscous sublayer, while during a burst event Ψ=1.84 is generally used *(Ibrahim et al., 2003; Ibrahim et al., 2008; Goldasteh et al., 2013)*.

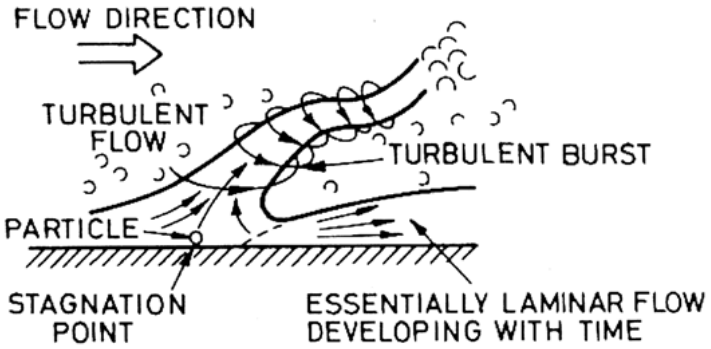

Figure 8. A schematic of a burst event.

As regards the *NSW–SP* interactions, *Ni et al. (2011)* modeled the formation of the slag layer and the interaction of sticky particles with a flat surface by using energy balances. In particular, they used the maximum spread diameter of the droplet, D_{max}, as the key parameter to predict sticking and rebound phenomena. The collision event can be divided into different steps, as depicted in Fig. 9 *(Mao et al., 1997)*.

- Stage (a), *pre-impact*: the *SP* impact energy consists of surface energy, kinetic energy, and potential energy, while the energy level of the solid surface is defined equal to zero as a reference for the system;
- Stage (b), *maximum spread*: this is the point at which the molten liquid flow changes direction from spreading outwards to recoiling inwards. The flattened droplet is assumed to be a thin circular disk with a top surface area of $\frac{\pi}{4}D_{max}^2$ and a height (h) of $\frac{2}{3}\left(\frac{D_0^3}{D_{max}^2}\right)$. The surface energy

of the droplet is at a maximum, while the kinetic energy is zero. The potential energy in both stages (a) and (b) is negligible compared with other forms of energy;

- Stage (c), *maximum recoil*: the droplet changes its direction of motion from up to down under the influence of the gravity. This stage signifies the maximum extent to which a droplet recoils upwards. The droplet possesses potential and surface energy but no kinetic energy;
- Stage (d), *sticking*: the droplet possesses a minimum energy that is equal to the static surface energy. It adheres on the surface and contributes to the formation of the slag layer;
- Stage (r), *rebound*: the droplet, with its original spherical shape, is in a position just above the substrate and momentarily at rest. At this stage the droplet upward acceleration is counterbalanced by gravity. However, if the energy possessed by the droplet in the stage (c) is larger than in the stage (r), the droplet will further pop up and be entrained by the syngas flow. Therefore, a rebound criterion is formulated: the droplet bounces off the surface if the energy possessed in the stage (c) is greater than that in the stage (r). Conversely, the droplet remains on the surface if the energy is smaller in the stage (c) than in the stage (r).

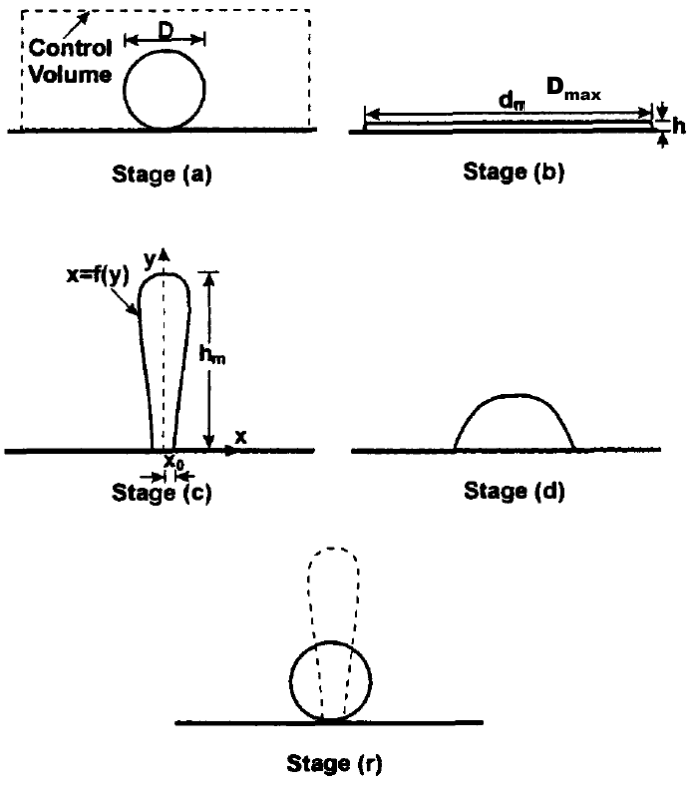

Figure 9. A schematic of a droplet impact on a flat surface.

On such considerations, it is possible to calculate the energy before and after each stage, and model the maximum spread and the rebound phenomena *(Mao et al., 1997; Pasandideh-Fard et al., 1996)*.

The energy conservation equation between the stages (a) and (b) can be expressed as:

$$E_{KA} + E_{SA} = E_{KB} + E_{SB} + E_{diss,A-B} + \Delta E_k \tag{24}$$

where:

$$E_{KA} = \frac{1}{2} m v_i^2 = \left(\frac{1}{2}\rho_D v_i^2\right)\left(\frac{1}{6}\pi D_o^3\right)$$ kinetic energy in the pre-impact stage (25)

$$E_{SA} = A\gamma_{LV} = \pi D_0^2 \gamma_{LV}$$ surface energy in the pre-impact stage (26)

$$E_{KB} = 0$$ kinetic energy at maximum spread (27)

$$E_{SB} = \left(\frac{\pi}{4} D_{max}^2 + \frac{2}{3}\pi \frac{D_0^3}{D_{max}}\right)\gamma_{LV} + \frac{\pi}{4} D_{max}^2(\gamma_{SL} - \gamma_{SV}) =$$

$$= (\frac{\pi}{4} D_{max}^2(1 - \cos\theta_c) + \frac{2}{3}\pi \frac{D_0^3}{D_{max}})\gamma_{LV}$$ surface energy at maximum spread (28)

$$E_{diss,A-B} = 0.2 \frac{We^{0.83}}{Re^{0.33}} \left(\frac{D_{max}}{D_0}\right)^2 \pi D_0^2 \gamma_{LV}$$ viscous dissipation energy between (a) and (b) (29)

$$\Delta E_K = \left(\frac{\pi}{4}\bar{d}^2\bar{s}\right)\left(\frac{1}{2}\rho_D v_i^2\right)$$ loss of kinetic energy due to droplet solidification (30)

where m, ρ_D, v_i, D_0 e D_{max} are the mass, the density, the impact velocity, the initial diameter and the maximum diameter of the droplet, respectively; γ_{SL}, γ_{LV} and γ_{SV} are the solid-liquid, liquid-vapor and solid-vapor surface tensions, respectively, which are related by the Young's equation:

$$\gamma_{SV} - \gamma_{SL} - \gamma_{LV}\cos\theta_c = 0 \tag{31}$$

where θ_c represents the static liquid–solid contact angle. The expression for the viscous dissipation energy between the stages (a) and (b) was taken by *Mao et al. (1997)*.

$\bar{d}$ e $\bar{s}$ in Eq. (30) are the mean diameter and the mean thickness of the solidified droplet at the impact *(Aziz and Chandra, 2000)*. $\bar{d}$ ranges from 0 to D_{max} and can be approximated to $\frac{D_{max}}{2}$. The growth in thickness of the solidified layer was calculated using an approximate analytical solution developed by *Poirier and Poirier (1994)*. The dimensionless solidification thickness s^+ was expressed as a function of the *Stefan* number (*Ste*), *Péclet* number (*Pe*), and φ:

$$s^+ = \frac{\bar{s}}{D_0} = \frac{2}{\sqrt{\pi}} Ste \sqrt{\frac{t^+ \varphi_w}{Pe \varphi_D}} \tag{32}$$

where the dimensionless time $t^+ = t\frac{v_i}{D_0}$ and $\varphi = k_t \rho C_s$ for the droplet (φ_D) and the wall (φ_w), k_t being the thermal conductivity and C_s the heat capacity. The Stefan number represents the ratio between the heat capacity and the heat related to the fusion of the droplet, $Ste = \frac{C_s(T_m - T_w)}{H_m}$, where T_m and T_w are the fusion temperature of the droplet and the wall temperature, respectively. The Péclet number is the ratio of the convective to diffusive thermal flux, $Pe = \frac{v_i D_o}{\omega}$, where ω is the thermal slag diffusivity. Substituting Eqs. (25)-(32) into (24) gives the maximum spread factor of the slag droplet during the impact $\xi = \frac{D_{max}}{D_0}$:

$$\left[\frac{1}{4}(1 - \cos\theta_c) + 0.2\frac{We^{0.83}}{Re^{0.33}} + \frac{1}{16} We \cdot s^+\right]\xi^3 - \left(\frac{We}{12} + 1\right)\xi + \frac{2}{3} = 0 \tag{33}$$

where Re is the droplet Reynolds number, $Re = \left(\rho_D v_i D_0 / \mu_D\right)$, μ_D is the droplet viscosity, and We is the Weber number, $We = \left(\rho_D v_i^2 D_0 / \gamma\right)$.

When the solidification is negligible, Eq. (33) becomes:

$$\left[\frac{1}{4}(1 - \cos\theta_c) + 0.2\frac{We^{0.83}}{Re^{0.33}}\right]\xi^3 - \left(\frac{We}{12} + 1\right)\xi + \frac{2}{3} = 0 \tag{34}$$

The solution of Eqs. (33-34) has the general expression:

$$\xi = \sqrt[3]{-\frac{q}{2} + \sqrt{\left(\frac{q}{2}\right)^2 + \left(\frac{p}{3}\right)^3}} + \sqrt[3]{-\frac{q}{2} - \sqrt{\left(\frac{q}{2}\right)^2 + \left(\frac{p}{3}\right)^3}} \tag{35}$$

Furthermore, it is possible to use this spread factor ξ to formulate a rebound criterion. In particular, *Mao et al. (1998)* proposed the following rebound criterion :

$$ERE = \frac{E_C - E_R}{E_R} = \frac{E_B - E_{diss,B-C} - E_R}{E_R} > 0 \tag{36}$$

where ERE is defined as the excess rebound energy (stage (c)) normalized with respect to the energy possessed in the stage (r). The total energy in the stage (r) is the surface energy which can be expressed as:

$$E_R = \pi D_0^2 \gamma_{LV} \tag{37}$$

whereas the energy in the stage (c) E_C may be expressed as $E_B - E_{diss,B-C}$, where $E_B = E_{SB}$ was defined in Eq. (28) and an empirical correlation of the energy dissipated between the stages (b) and (c) as a function of ξ and θ was developed:

$$\frac{E_{diss,B-C}}{E_R} = 0.12(\xi)^{2.3}(1-\cos\theta_c)^{0.63} \quad (38)$$

Substituting Eqs. (28), (37) and (38) into Eq. (36), one gets the rebound model equation:

$$ERE = 0.25(\xi)^2(1-cos\,\theta_c) - 0.12(\xi)^{2.3}(1-cos\,\theta_c)^{0.63} + \frac{2}{3\xi} - 1 \quad (39)$$

ERE describes the tendency of a droplet to rebound upon the impact. The limit condition is represented by $ERE = 0$, for which the energy at maximum recoil is equal to that at rest ($E_C = E_R$); when $ERE > 0$ it means that the energy at stage (c) is larger than in the stage (r), thus, the droplet will rebound; when $ERE \leq 0$ the droplet will stick on the surface *(Mao et al., 1998; Ni et al., 2011)*.

Oblique droplet impacts have also been investigated *(Sommerfeld and Tropea, 1994; Šikalo and Ganić, 2006)*. In particular, *Sommerfeld and Tropea (1994)* proposed a rebound criterion on the basis of the parameter K_D, as a function of the physical properties of the droplet and its impact velocity:

$$K_D = Oh \cdot Re^{1.25} \quad (40)$$

where $Oh = {\mu_D}/{\sqrt{\rho_D \gamma D_0}} = {\sqrt{We}}/{Re}$ is the *Ohnesorge* number, which relates viscous, inertial and surface forces. The transition from rebound to deposition was found for K_D= 3 *(Šikalo and Ganić, 2006)* for the normal impact of a droplet on a dry wall. For $K_D < 3$ rebound occurs, as the initial kinetic energy of the droplet and the surface tension overwhelms the viscous dissipation energy occurring during the spreading phase. For $K_D > 3$, on the other hand, the viscous energy is larger than the others, thus, the droplet adheres on the surface.

1.6 Aim of the Ph.D. Thesis

This doctoral research program (Ph. D. in Chemical Engineering) engages an investigation of the main near-wall phenomena which characterize coal gasification in entrained-flow slagging gasifiers, in collaboration with: Istituto di Ricerche sulla Combustione (Consiglio Nazionale delle Ricerche), Dipartimento di Ingegneria Chimica, dei Materiali e della Produzione Industriale (Università degli Studi di Napoli Federico II) and Dipartimento di Scienze Chimiche (Università

degli Studi di Napoli Federico II) in Naples (Italy). This research group has recently analyzed the relevance of the segregation of carbon particles in the near-wall region of the gasifier to the coal conversion *(Montagnaro and Salatino, 2010)*, validated by the analysis of the properties of ash streams generated in a full scale entrained-flow gasification plant *(Montagnaro et al., 2011)*. Furthermore, particle accumulation in the near-wall region has been confirmed by numerical simulations performed by this research group *(Ambrosino et al., 2012; Ambrosino et al., 2013)* and a recent thesis work *(Carbone, 2012)* has permitted to design an experimental apparatus able to reproduce, at atmospheric conditions, the fluid dynamic conditions of entrained-flow slagging gasifiers.

This doctoral research program aims at giving a contribution to the development of a phenomenological model of the fate of coal/ash particles which considers the establishment of particle segregated phases in the near-wall region of the gasifier. Three scales of investigation are under scrutiny, on the basis of a hierarchical scheme, using the tool of physical modelling:

- *Compartments scale*. This scale is relevant to study the fluid dynamic conditions which lead to near-wall particle segregation, the forces governing particle-to-wall segregation phenomena and their effect on the particles trajectories;
- *Near-wall segregation scale*. At this scale it is possible to study the different particle segregation regimes in the near-wall region and their relative importance at different operating and fluid dynamic conditions. Furthermore, at this level, it is important to study the different segregation regimes on the basis of the complex mechanism of liquid-solid, liquid-liquid and solid-solid interphase interactions;
- *Micromechanical interactions scale*. This length scale takes into account the micromechanical particle-wall interaction patterns on the basis of the stickiness of the impinging particles and of the wall layer (*SW–SP*, *SW–NSP*, *NSW–SP*, *NSW–NSP*). At this level, it is important to study the mechanisms governing particle impact on the wall and the consequent post-impact phenomena.

To achieve these objectives, a physical downscaled lab-scale cold flow model reactor has been set up in order both to avoid the difficulties related to the 'hard' operating conditions of entrained-flow slagging gasifiers in terms of pressure and temperature, and to ensure the optical accessibility of the reactor walls. The design regarded the choice of a suitable material to simulate, at atmospheric conditions and at low temperature, the slag phase behavior in an actual entrained-flow gasifier. In this respect, wax has been chosen as the best material. Molten wax is atomized into a mainstream of air to simulate the fate of char/ash particles in a real hot environment. The physical downscaled lab-scale cold flow reactor ensures the formation of two phases, a dispersed phase and a near-wall layer, in order to study the complex near-wall segregation phenomena. Furthermore, the

micromechanical particle-wall interaction is going to be studied by means of another lab-scale experimental apparatus in which single impacts of droplets/particles on a target are recorded. Analysis of frames can allow to determine the effect of particle size, particle temperature, impact velocity and impact angle on the rebound characteristics of particles/droplets upon collision on a surface.

The results could be used as the starting point for the development of criteria and constitutive equations useful for the set up of computational fluid dynamic models, in order to embed particle–wall interactions in the simulation of gasification processes in pilot and large scale entrained-flow reactors. Furthermore, such models would allow to take into account the segregation patterns in the phenomenological description of the fate of char/ash particles during entrained-flow gasification.

At the end of this dissertation, in the Appendix, the papers published by the author referring to this Ph. D. research program are reported.

Chapter 2. Experimental apparatuses, materials, operating conditions and techniques

The experimental campaign has been carried out by means of two lab-scale apparatuses. The first one (*Section 2.2*) consists in a lab-scale cold flow physical model of an entrained-flow gasifier. The downscaling did not conform to rigorous scaling rules, but rather aimed at reproducing the basic general features of the interaction between a lean-dispersed particle/droplet phase and a confining wall, with special emphasis on the conditions which promote the formation of a liquid layer on the reactor wall. On the other hand, the second apparatus (*Section 2.3*) was designed and set up in order to investigate the particle–wall micromechanical interaction patterns on the basis of the stickiness of the impinging particles and of the wall layer, from a physical point of view.

2.1 Choice of the material to simulate the slag phase behavior

In order to simulate the slag layer behavior, some of its properties should be recalled. The slag layer consists in molten ash, which can be defined as silicate melts. Its major components are aluminum, calcium, iron and silicon oxides, but small amounts of potassium, sodium, magnesium, phosphorus and titanium oxides are also present. One of the major requirements for the normal operation of a slagging gasifier is the continuous and even removal of the slag. Therefore, coal slag viscosity is one of the most important factors determining the suitability of a particular coal for the slagging gasification process. In particular, the coal slag viscosity should not exceed 25 kg m^{-1} s^{-1} at the slag tap hole region of the gasifier, where typical tapping temperatures range between 1300−1500°C *(Patterson and Hurst, 2000)*. Another important physical property is the surface tension; as a matter of fact, sintering and agglomeration phenomena are proportional to the surface tension of the liquid slag and inversely proportional to its viscosity *(Raask, 1985)*. Several models were developed to determine the slag viscosity, and that proposed by *Song et al. (2011)* seems to be the most suitable for slagging gasification processes *(Ni et al., 2010*; *Ni et al., 2011)*. In the published literature, surface tension data of coal ash slag are limited. *Melchior et al. (2009)* measured the slag surface tension under reducing conditions, and they found that the surface tension ranges between 0.4 kg s^{-2} and 0.7 kg s^{-2} for different coal ash samples. However, *Gupta et al. (2002)* proposed an empirical formula to evaluate the slag surface tension, by knowing the surface tension corresponding to each oxide and their molar percentage. In order to study the fluid dynamic behavior of the slag layer flowing down the reactor walls, another physical property of the slag should be taken into account, the kinematic viscosity, i.e. the slag dynamic viscosity divided by its density. Typical values for the slag layer density are 2500-3000 kg m^{-3} *(Ni et al., 2010)*.

On the basis of these considerations, the plastic/fluid behavior of softened or molten ash and of the wall slag layer will be simulated, at nearly ambient conditions, by using molten wax as a surrogate of fuel ash. In this respect, the use of melted wax (1-hexadecanol) has been reported by *Shimizu et al. (2010)*, even if for a different application, while *Wang et al. (2013)* used a syrup as material to simulate the slag deposition and accumulation at the tap hole region of a Shell gasifier. After a screening of different candidates, Waradur E^{TM} (Völpker Spezialprodukte GmbH, Germany) was selected as the best material, since its rheological/mechanical properties resembled those of a typical coal slag. Waradur E^{TM} is a montan wax, obtained from various lignites, but unlike the other mineral waxes it is composed by mixtures of long-chain esters accompanied by high molecular weight alcohols, acids, and resins. As a result, this montan wax is hard and brittle. Its properties are those of the wax named Luwax E (BASF). Figure 10 shows the Luwax E (BASF) wax viscosity as a function of the temperature. The wax melting range is 75–85°C, as the viscosity sharply decreased, while the wax viscosity varies in the range 0.02–0.1 kg m^{-1} s^{-1} as the temperature ranges between 130°C and 90°C *(Li et al., 2008)*, and wax density is around 1000 kg m^{-3}. Accordingly, the kinematic viscosity is in the order of 10^{-5}–10^{-4} m^2 s^{-1}, consistent with the values commonly reported in the literature for coal slag (viscosity and density on the order of 0.01–1 kg m^{-1} s^{-1} and 2500–3000 kg m^{-3}, respectively, in the temperature range 1200–1500°C) *(Shannon et al., 2008*; *Ni et al., 2011*; *Song et al., 2011*; *Yang et al., 2011*; *Duchesne et al., 2012)*. The kinematic viscosities of the wax are consistent with the establishment of a laminar flow of the molten phase along the reactor walls. Besides, taking into account its surface tension (0.03 kg s^{-2} at 100°C), the wax properties are such that the entrapment and over-layering criteria are not satisfied, whereas the segregation or segregation–coverage regimes are likely to be established, as expected for realistic particle–slag interaction in entrained-flow gasifiers *(Montagnaro and Salatino, 2010*; *Montagnaro et al., 2011)*.

Furthermore, the mechanical characteristics of the montan wax permit to study the behaviours of both particles and droplets in a near-ambient temperature range. This feature is useful to investigate the four interaction scenarios relevant in entrained-flow slagging gasifiers (*NSW–NSP*, *SW–NSP*, *NSW–SP*, *SW–SP*).

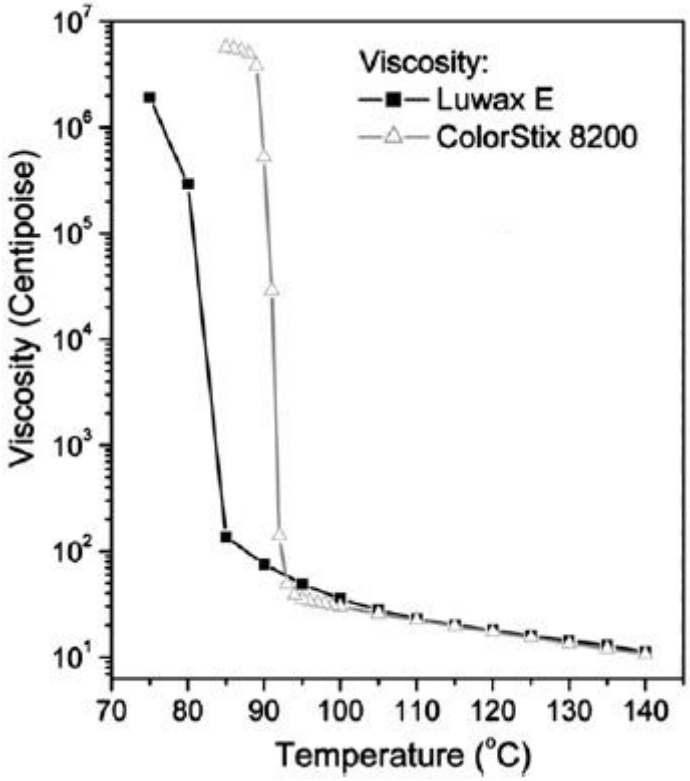

Figure 10. Wax viscosity versus temperature (adapted from *Li et al., 2008*).

2.2 *The lab-scale cold entrained-flow reactor for the investigation of near-wall particle segregation phenomena*

2.2.1 *Design*

In order to simulate the slag layer behavior, the molten wax needs to be atomized into droplets with a mean diameter ranging between 10–100 μm. Furthermore, the fluid dynamics must promote wax deposition on the wall, and hence, the formation of a falling molten wax layer. On the basis of these objectives, the experimental apparatus was set up as depicted in Fig. 11.

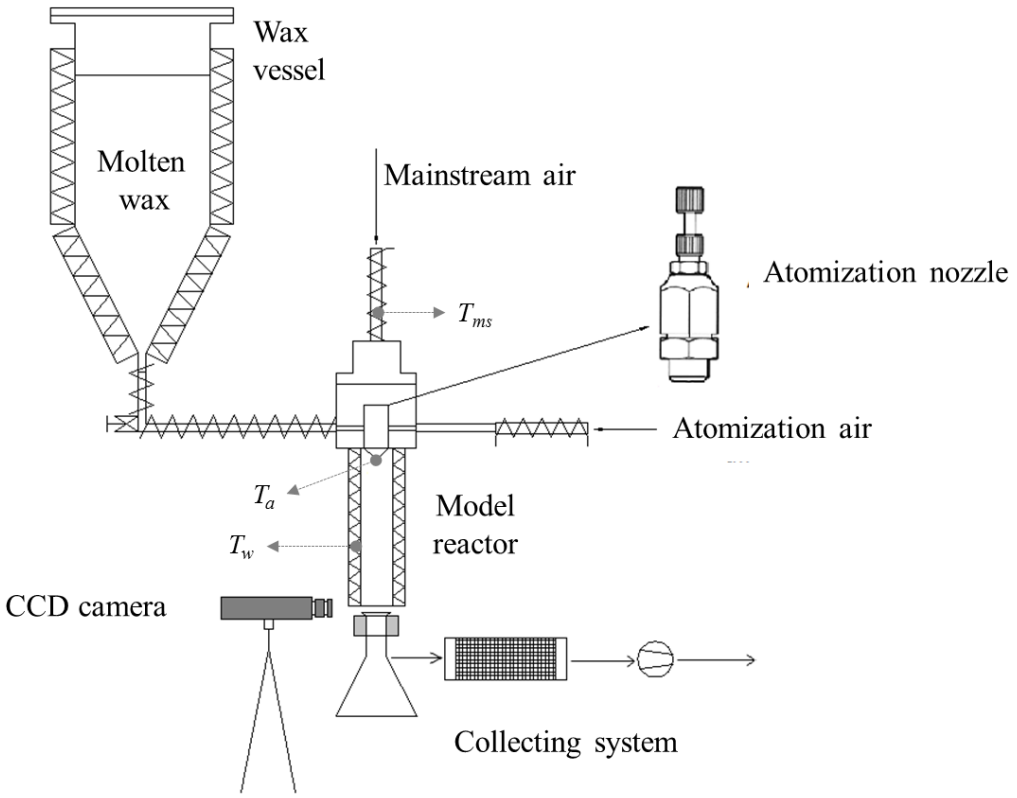

Figure 11. Scheme of the lab-scale cold flow model reactor with a detailed view of the atomization nozzle.

The wax was liquefied and stored in a 9 L heated vessel. A three-way valve could be opened to convey the wax to the atomization vessel through a heated horizontal tube. The atomization vessel consisted of a plenum chamber, a distributor plate, an atomizer positioning section and a nozzle. The wax storage vessel, the horizontal tube connecting the storage vessel with the atomization vessel and the atomization vessel itself were all made of stainless steel. The atomization system generated a spray of molten wax in the model reactor which eventually gave rise, upon deposition onto the wall, to a layer of molten wax. The nozzle was a commercial Delavan^{TM} atomizer (AL model), designed so as to generate a spray of conical shape with an aperture angle of θ_{max}=22–25° and a uniform cross-sectional distribution of the atomized dispersed phase (Fig. 12). Air-assisted atomization of wax resulted into droplets of 10–100 μm size. The atomization air was fed directly to the nozzle.

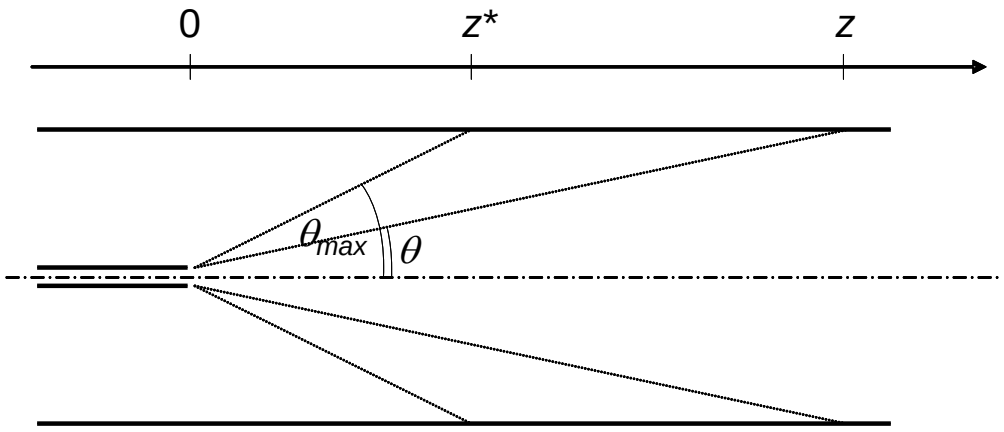

Figure 12. Geometrical parameters of the jet in the model reactor.

The reactor consisted of a Pyrex™ tube (D=0.04 m-ID) on which the atomizing system is fitted. A mainstream of air was fed at the top of the plenum chamber, flowing through a distributor plate in order to equalize the distribution of the air mainstream across the reactor.

A different configuration of the atomizing section has also been set up, as depicted in Figure 13. In this configuration the atomization zone consisted of a plenum chamber, including a distributor plate, an atomizer positioning section and the nozzle. In this layout the plenum chamber, including the distributor plate and the atomizer positioning section, was made of polytetrafluoroethylene (Teflon™), whereas the nozzle was again the commercial Delavan™ atomizer. As in the other configuration, the atomization air was fed directly to the nozzle, while the mainstream of air was fed sideways the atomization zone, flowing through a plenum chamber and a distributor plate in order to equalize the distribution of the mainstream air across the reactor. The reactor consisted of a Pyrex™ tube (D=0.10 m-ID) on which the atomizing system was fitted. The internal diameter of the reactor was chosen in order to permit, under specific operating conditions, the droplets to solidify during their flight toward the walls and, thus, to simulate particles impact on both a dry wall and other particles.

The experimental configuration with the 0.04 m-ID reactor was used as test protocol for the *SW–SP* regime, while the layout providing the larger 0.10 m-ID reactor was designed in order to study the effect of the reactor size on the phenomenology of particle–wall interactions when testing *SW–SP*, and to investigate the interactions in the other regimes (*SW–NSP*, *NSW–SP*, *NSW–NSP*).

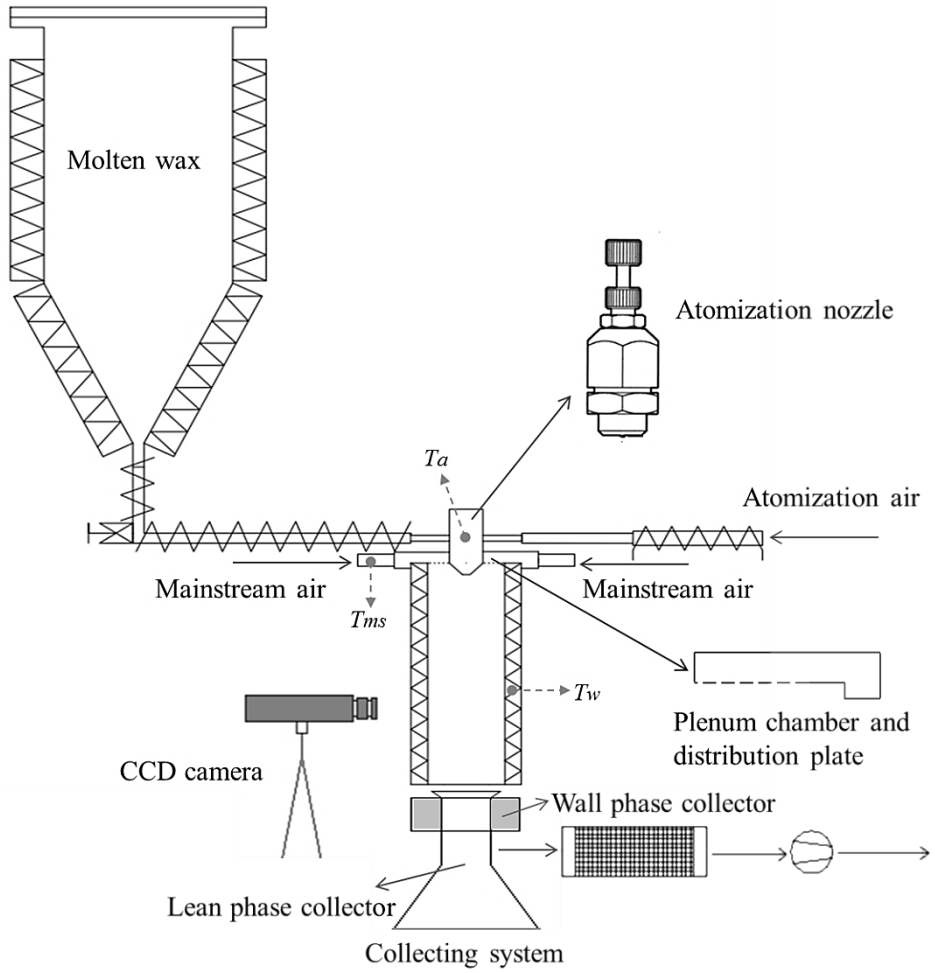

Figure 13. Scheme of the lab-scale cold flow model reactor with a different atomization section.

2.2.2 Operating conditions

The experimental apparatus, regardless of the atomization section layout, was designed in such a way to control the actual status of both the lean-dispersed phase and the wall layer. This goal was reached by adjusting the values of three temperatures:

- Atomization temperature (T_a), i.e. the nozzle temperature. This temperature must be set at values large enough to ensure good flowability and effective atomization of the wax;
- Mainstream temperature (T_{ms}). This gas temperature determines the status of the wax immediately after its atomization. As a matter of fact, an energy balance around a single droplet in the dispersed phase, based on the assumption that Bi«1, indicates that the temperature of the droplet closely approaches the temperature of the mainstream gas over about 10^{-4} s, far shorter than the typical residence times of the droplets in the reactor. Accordingly, it can be assumed that the droplets instantaneously reach the thermal equilibrium with the mainstream air. Adjusting T_{ms} with respect to the wax critical temperature at which

the liquid–solid transition occurs (around 85°C for the wax used in the present study) enables an accurate control of the physical status (liquid vs. solid) of the wax, as well as its viscosity. In particular, an energy balance on a single droplet can be written in order to evaluate the solidification time, as:

$$\frac{d}{dt}\left(\rho_{wax}\pi\frac{d_{D,wax}^3}{6}\,x_s H_m\right) = U\,A\,\Delta T \tag{41}$$

$$\frac{dx_s}{dt} = \frac{U\,A\,\Delta T}{\rho_{wax}\pi\frac{d_{D,wax}^3}{6}H_m} \tag{42}$$

where $\rho_{wax}\pi\frac{d_{D,wax}^3}{6}$ is the mass of the droplet of wax, A is the heat transfer area, ($A = \pi d_{p,wax}^2$), $\Delta T = T_m - T_{ms}$ is the difference between the melting temperature and the mainstream temperature (which is equal to the wax temperature under the assumption of *Bi*«1), U is the overall heat transfer coefficient, H_m the fusion heat (for wax, H_m=220 kJ kg^{-1}) and x_s the solidified fraction of wax. Solving the Eq. (42), the solidification time is obtained as:

$$t(x_s = 1) = \frac{\rho_{wax}\pi\frac{d_{D,wax}^3}{6}H_m}{UA\,\Delta T} \tag{43}$$

For a particle of 100 µm-sized and $T_{ms} = 30°C$, it is $t(x_s = 1) = 0.109$ s, which is the time required for a droplet to completely solidify;

- Wall temperature (T_w). This temperature can be varied to control the physical status and the viscosity of the wax accumulated on the wall. It is accomplished by heating the reactor with flexible heaters.

The operating conditions were selected so as to reproduce the four possible regimes (*SW–SP*, *NSW–NSP*, *NSW–SP*, *SW–NSP*), and are listed in Table 4. The wax feeding rate was $W_{wax}^{lean}(z{=}0)$=0.2–1 g s^{-1}. The flow rate of mainstream air, Q_{ms}, and the flow rate of atomization air, Q_a, were treated as parameters for the purposes of exploring, evaluating and testing their effect on the phenomenology of interaction between the lean-dispersed phase and the wall layer. The experiments in the *SW–SP* regime were carried out in the two reactor configurations, to study the effect of the reactor size on the phenomenology of particle–wall interactions. The gas flow rates (Q_a and Q_{ms}) and the three temperatures (T_a, T_{ms} and T_w) were fixed in such a way to keep similar flow conditions. For the *NSW–NSP* regime, T_{ms} and T_w were fixed at room temperature in order to ensure the droplet solidification. Q_{ms} ranged between 1 m^3 h^{-1} and 20 m^3 h^{-1} at 273 K (corresponding to a velocity range of about 0.04–0.8 m s^{-1}), while Q_a ranged between 0.275 m^3 h^{-1} and 0.8 m^3 h^{-1} at 273 K (corresponding to a normal-to-wall velocity component in proximity of the nozzle of about 8.5–25 m s^{-1}), with a reference case of 1 m^3 h^{-1} and 0.5 m^3 h^{-1}, respectively. For the

NSW–SP regime, Q_{ms} ranged between 1 $m^3 h^{-1}$ and 10 $m^3 h^{-1}$ at 273 K, while Q_a was fixed at 0.275 $m^3 h^{-1}$ at 273 K and the operating pressure was 1.2 bar in order to keep the molten status of the droplet. As a consequence, the wax feeding rate was $W_{wax}^{lean}(z=0)$=1 g s^{-1}. Also in this case T_w was fixed at room temperature, while T_{ms} was 90°C, to keep the wax in a molten status after the injection. Two kinds of tests were performed; the first using polished and dry ducts, the second using ducts covered by a powdery layer. This second type was carried out by performing first a typical test in *NSW–NSP* conditions (Q_a=0.275 $m^3 h^{-1}$ and Q_{ms} =1 $m^3 h^{-1}$) and then by switching the operating conditions to those of the *NSW–SP* regime. The experiments in the *SW–NSP* regime were carried out by setting T_{ms} at room temperature, while T_w was 110–190°C, in order to ensure the molten status of the wax at the wall. For this regime Q_a was 0.5 $m^3 h^{-1}$ at 273 K, while Q_{ms} ranged between 2 $m^3 h^{-1}$ and 10 $m^3 h^{-1}$ at 273 K. The values of Q_a complied with the nozzle constraints and assured good wax atomization in terms of size and dispersion of droplets for both the investigated regimes. The reactor length *L* was varied to study the influence of the distance from the injection nozzle on the fractional mass of wax transferred form the lean-dispersed phase to the wall layer. Reactor ducts of different lengths were used for this purpose: *L* was varied in the 0.1–0.6 m range for the *SW–SP* and *NSW–SP* cases, in the 0.1–0.45 m range for the *NSW–NSP* and 0.15–0.6 m range for the *SW–NSP* case.

Table 4. Main reactors design and operating parameters.

	SW–SP		***NSW–NSP***	***NSW–SP***	***SW–NSP***
Reactor internal diameter *D* [m]	0.04	0.1	0.1	0.1	0.1
Reactor length *L* [m]	0.03–0.27	0.1–0.6	0.1–0.45	0.1–0.6	0.15–0.6
Atomization temperature T_a [°C]	120–155	110	100	120	100
Mainstream temperature T_{ms} [°C]	120	160	30	90	30
Wall temperature T_w [°C]	135	140	30	30	110–190
Wax feeding rate W_{wax}^{lean} (*z*=0) [g s^{-1}]	0.2	0.6	0.2–0.3	1	0.2–0.3
Flow rate of mainstream air Q_{ms} [$m^3 h^{-1}$ at 273 K]	0.6–0.7	5	1–20	1–10	2–10
Flow rate of atomization air Q_a [$m^3 h^{-1}$ at 273 K]	0.23–0.32	0.275	0.275–0.8	0.275	0.5

2.2.3 Analysis of the experimental results

The experimental tests aimed at characterizing the general phenomenology of the interaction between the dispersed phase generated by the spray and the reactor walls. The partitioning of the atomized wax between the dispersed and the wall phases was quantitatively assessed as a function of the distance from the nozzle. To accomplish this task, the reactor was equipped with a system for the collection of wax issuing from the reactor in either phase (Figs. 12–13). This consisted, for testing in *SW–SP* and *SW–NSP* regimes, of a vacuum flask with a 0.03 m-OD and 0.09 m-OD inlet tube, collecting the wax issuing in the lean phase for the 0.04 m-ID and the 0.10 m-ID reactor, respectively. The flask was fitted with an outer annular section where wax flowing in the wall layer was collected. The collection system was equipped with a filter and a suction pump. The mass flow rates in the dispersed phase and in the wall layer phase were obtained by dividing the amounts of wax cumulatively collected by the duration of the test. On the other hand, with regard to the partitioning measurements for the *NSW–NSP* and *NSW–SP* regimes, the apparatus was equipped with a vacuum flask (0.12 m-OD) collecting the wax in the lean phase, while the amount of wax on the walls was obtained by weighing the reactor before and after each experimental test.

Regardless of the testing operating conditions and regime, the mass flow rate of wax conveyed in the dispersed phase, $W_{wax}^{lean}(z=L)$, was worked out to calculate the fractional mass of wax in the dispersed phase at $z=L$, defined as:

$$y^{lean}(z=L) = \frac{W_{wax}^{lean}(z=L)}{W_{wax}^{lean}(z=0)} \tag{44}$$

where L is the reactor length. The reactor length L was varied to investigate the influence of the distance from the injection nozzle on the fractional mass of wax transferred form the lean-dispersed phase to the wall layer $y^{lean}(z=L)$. On the other hand, the flow rate of mainstream air, Q_{ms}, and the flow rate of atomization air, Q_a, were treated as parameters for the purposes of evaluating the effect of different fluid dynamic conditions on the phenomenology of interaction between the lean-dispersed phase and the wall layer.

A preliminary characterization of the jet shape and its aperture angle was carried out. Images of the jet were taken and transformed into binary images. This was accomplished by an algorithm written in LABVIEW® language. Digitalized images underwent subtraction of the background and filtering. The result is an image where the background is depicted in black and the jet is in red. An example of recognition of the jet shape and aperture angle is shown in Fig. 14. It is possible to compare the original image and its corresponding binary image. The spray has a conical shape

(triangular in a planar image) with an aperture angle θ_{max}=22–25°, in agreement with the technical data of the nozzle. Moreover, a good axial symmetry of the spray is also visible in Fig. 14.

Furthermore, the particles surface topology and the mean particles size was evaluated with a scanning electron microscope (SEM) Philips EL30 LaB6. Particles were affixed to the sample holder using gold as conductive base. The accelerating voltage was 7.5–15 kV. Samples of particles (*NSP)* from the dispersed phase were collected to assess, from a qualitative point of view, the good atomization and dispersion of the droplets after their injection.

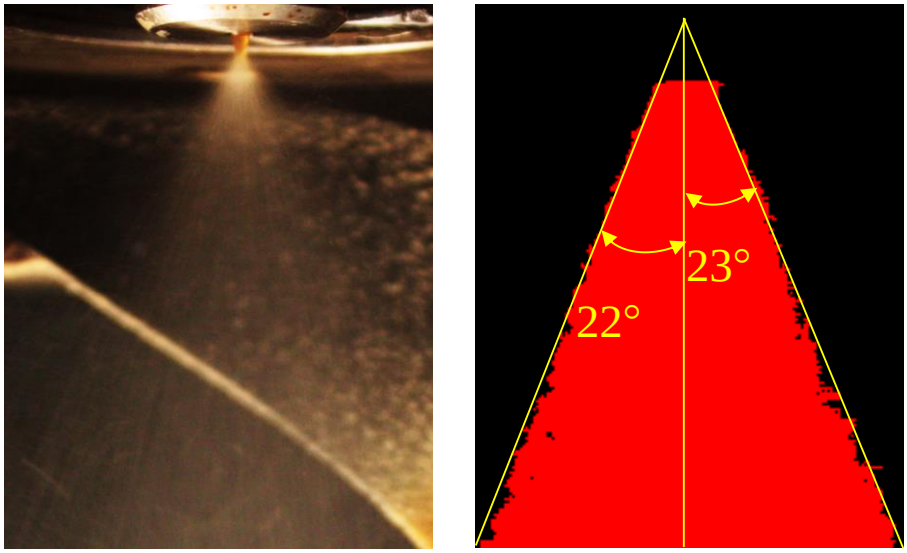

Figure 14. Example of recognition of the jet shape and aperture angle. Left: original image. Right: binary image.

Visual observation and recording of the wall layer was also accomplished by means of two progressive scan CCD video cameras. The first one (Pulnix™ 6710) was equipped with a magnifying zoom lens and a 0.02 m extension tube. This optical system permitted to perform video recordings at a distance of about 0.2 m from the reactor walls, focusing on an observation window left uncovered by the heating/insulating elements, without exposing the camera to unacceptable overheating. Images were digitized using a digital frame grabber (National Instruments™ PCI 1422 coupled with a PC). Frame-by-frame recording was accomplished at a sampling rate of 250 fps with a 0.013 m × 0.004 m recording window digitized as 648 × 198 square pixels (spatial resolution equal to about 20 μm). The temporal and spatial resolution of the video recordings did not permit to measure the particle size and particle velocity distributions at the same time. However, the video recordings were performed setting a video camera shutter time (1/250 s) long enough to apply the particle streak line technique *(Crowe et al., 2012; Sommerfeld and Huber, 1999)*. This particle tracking technique has been used to characterize the phenomenology of

particle–wall interactions, since it enables the visualization of 10 μm sized particles even having a velocity of about 2 m s^{-1} moving toward the wall and impacting the solid surface, as well as the occurrence of adhesion, rebound and resuspension of adhered particles to the main gaseous flow. The qualitative characterization of particle–wall interactions has been pursued by frame-by-frame analysis of video recordings lasting 8 s, during which a number of events (adhesion, rebound, or resuspension) in the order of thousands takes place.

The visual observation was also accomplished with another progressive scan CCD camera (Photron Ultima APX), equipped with a magnifying zoom lens and a 27.5 mm extension tube. The camera head (CMOS 10 bit-monochrome) was connected to a processor, which stored non-compressed digital data of high-speed recorded images. The processor was connected to a PC, where it was possible to visualize and save the downloaded images. The frame-by-frame recording was accomplished at a sampling rate of 2000 fps, with a 0.028 m × 0.028 m recording window digitized as 1024 × 1024 square pixels (spatial resolution equal to about 27 μm), while the shutter time was set to 42 μs.

It is noteworthy that, being the wall layer of molten wax transparent to visible radiation, the video recordings could always be performed during experiments in the *SW–SP* and *SW–NSP* regimes, whereas an extensive particle layer deposition limited the frame-by-frame analysis to the first 30 s after the spray injection during the *NSW–NSP* and *NSW–SP* experiments.

Visual observation and video recording permitted to characterize the near-wall interactions, from a phenomenological and qualitative point of view. As regarding the *NSW–SP* experiments, the video recordings were useful to evaluate the maximum spread factor $\xi = \frac{D_{max}}{D_0}$, defined in *Section 1.5*. An impact event of a droplet on the duct wall during a typical test is reported in Figure 15. As the impact is oblique, the shape of the droplet at the maximum spread will be elliptical. As a matter of fact, it is possible to see the spherical droplet which is approaching the wall (first frame on the left) and the elliptical shape at its maximum spread (frame on the right), where d_x and d_y are the minor and major ellipse axes, respectively. The elliptical splat area can be converted into an equivalent splat of circular shape and its equivalent diameter, $D_{max,eq}$, can be derived. It is possible to define the equivalent diameter $D_{max,eq} = \sqrt{d_x d_y}$ as the diameter of a circular splat with the same area as the elongated splat (Fig. 16) *(Kang and Ng, 2006)*.

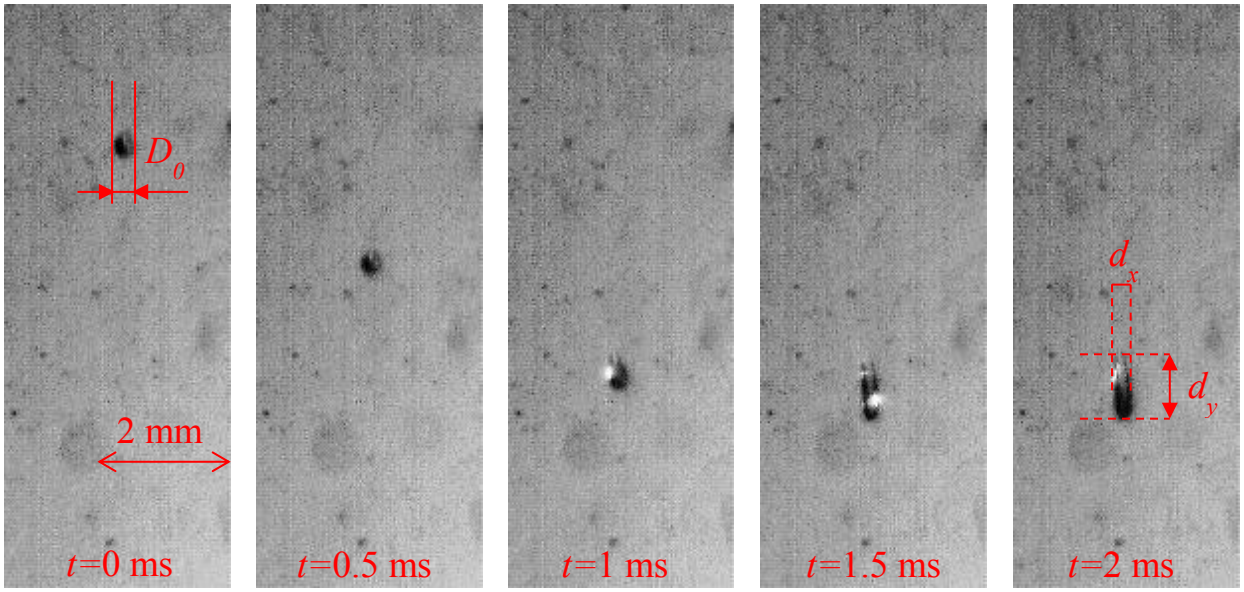

Figure 15. Impact of a wax droplet on the Pyrex duct wall.

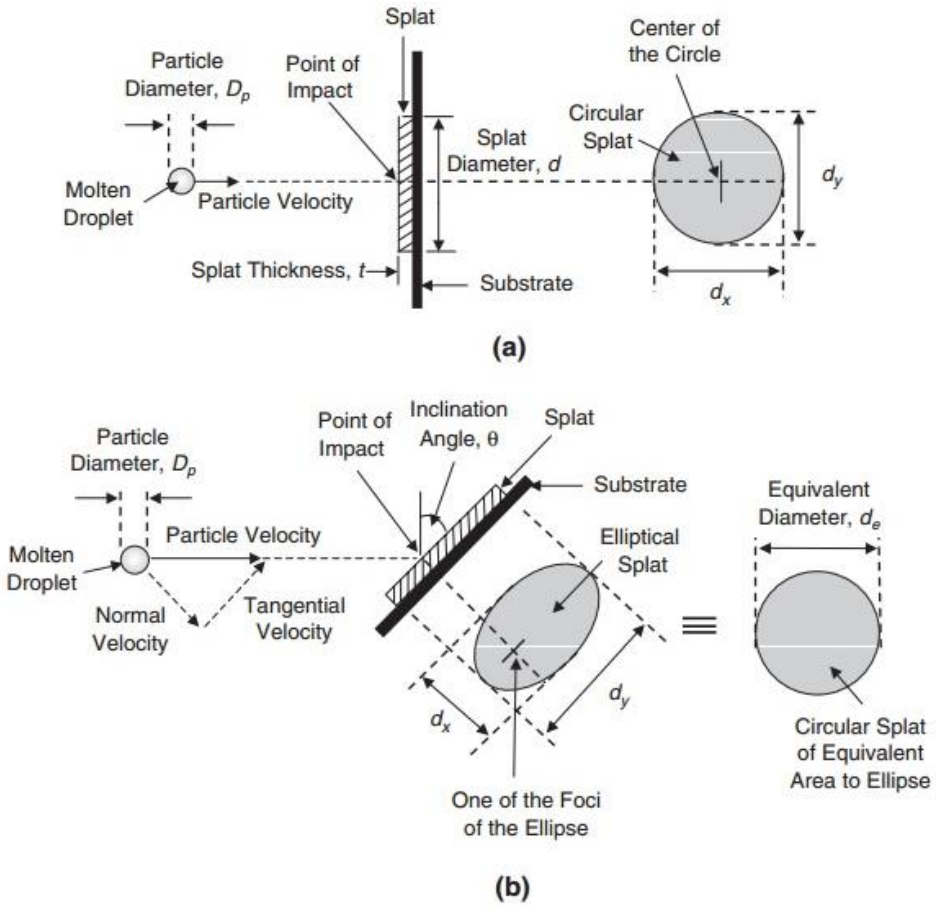

Figure 16. Idealized illustration of (a) perpendicular impact of molten particle resulting in circular splat and (b) oblique impact of molten particle resulting in elongated splat with its equivalent diameter (*Kang and Ng, 2006*).

2.3 The impact test apparatus for the micromechanical investigation of particle–wall interactions

2.3.1 Design

Particle–wall micromechanical interactions were investigated by means of a proper experimental apparatus, as depicted in Fig. 17.

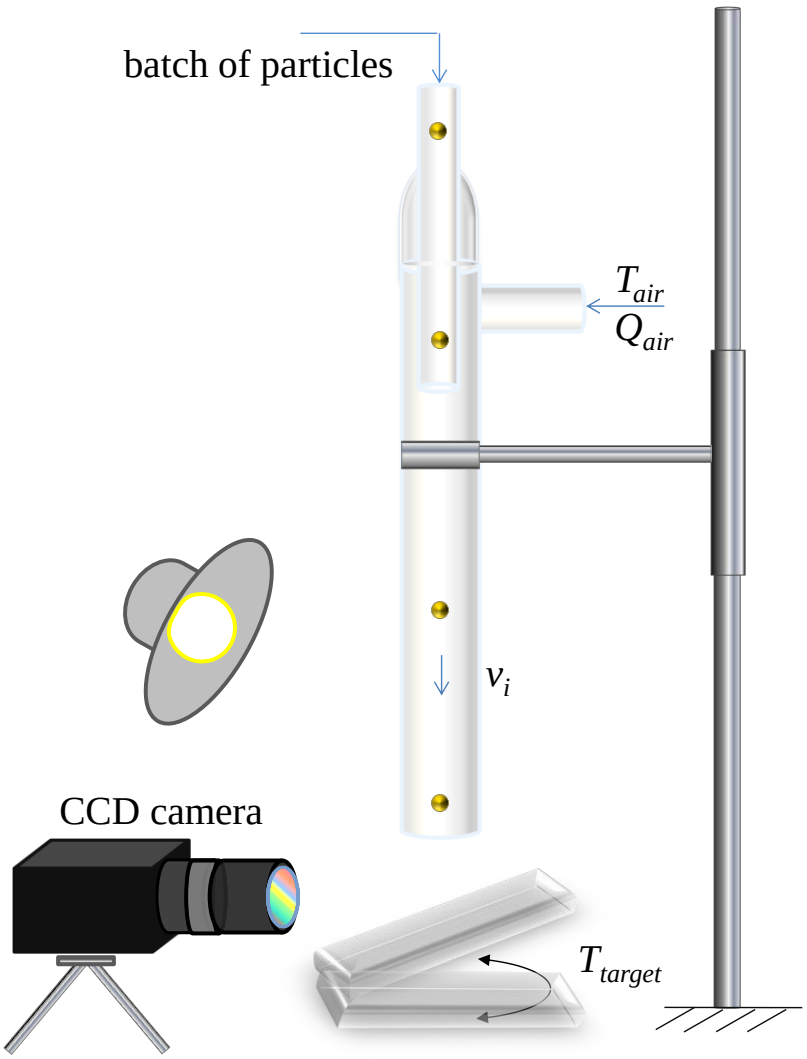

Figure 17. Outline of the particle–wall impact apparatus.

The test rig consisted of a vertical Pyrex™ tube, 0.65 m high and 0.03 m-ID, connected at the top with another Pyrex tube (0.01 m-ID and 0.013 m-OD) running coaxially for 0.08 m inside the larger tube. Batches of wax microparticles (50–100 μm) were fed into the smaller tube by means of a Pasteur pipette. Air was fed sideways at the top of the tube, and flowed downward between the

inner and outer tubes. The particles flowed through the inner tube driven by gravity, and then in the outer tube where they were entrained by the air flow. The particle impact velocity was controlled by regulating the air flow rate Q_{air}, by means of a flow meter/controller (Bronkhorst™ High-Tech). The temperature T_{air} of the air stream could be adjusted by means of a temperature controller. When the particles exited the tube, they impacted on a target plate placed around 0.05 m below the bottom end of the tube. The target could be inclined to obtain particle impact angles ranging from about 10° to about 90° with respect to the horizontal. The tube length L was chosen on the basis of the particle relaxation time τ and of the particle impact velocity. Typical values of particle impact velocity in EFG are on the order of 2 m s^{-1} *(Shannon et al., 2008)*. In order to approach similar velocities, the length L of the eductor tube was calculated from the relationship:

$$L = 10\tau v_i = 10\frac{\rho_p d_p^2}{18\mu} v_i \tag{45}$$

where μ is the fluid viscosity, and the particle relaxation time was conservatively multiplied by 10. For the typical values of the operational parameters, Eq. (45) gave L=0.65 m. Furthermore, the tube length was such that the particle residence time was about three times longer than the characteristic fusion time of the wax (about 0.11 s for a 100 μm-particle). This feature enabled the characterization of the impact dynamics of wax particles at different temperatures, i.e. with different stickiness degrees (from *NSP* to *SP*). The particle impact velocity was calculated as the sum of the gas velocity in the tube and the particle terminal velocity, and it was experimentally verified by particle tracking at the exit of the tube with a high-speed video camera (Photron Ultima APX). The particle velocities before and after the impact were determined experimentally, hence the restitution coefficient was calculated.

Four different target materials were used, in order to investigate the effect of the particle/wall interfacial energy on the rebound characteristics: Pyrex, stainless steel, montan wax Waradur E and Teflon. In particular, the wax target was obtained by solidification of melted wax, in order to have a smooth surface.

Additional experimental impact tests were carried out after the target surface (either dry or wet) was layered with wax powder (d_p=75±10 μm) of different thickness (between about 0.2 mm and 1.4 mm) and voidage around 0.5. These experiments aimed at simulating the rebound behaviour of a particle hitting adhered particles covering either a dry refractory wall or the slag layer (*NSW–NSP* regime for both cases). For this kind of tests, the dry wall was represented by the Pyrex target, while the liquid layer was represented by a syrup (μ_{syr}=0.5–1 Pa s @25°C, ρ_{syr}=1280 k m^{-3}, γ_{syr}=0.05 N m^{-1}), to mimic the slag layer at ambient conditions.

2.3.2 Operating conditions

Batches of spherical wax particles are used. They were obtained by previous melting, atomization and solidification in the lab-scale entrained-flow apparatus. As matter of fact, raw wax particles are not spherical, whereas after atomization and re-solidification it was possible to obtain spherical particles. SEM micrographs of a sample of the wax particles before (left) and after (right) the atomization process is reported in Fig. 18.

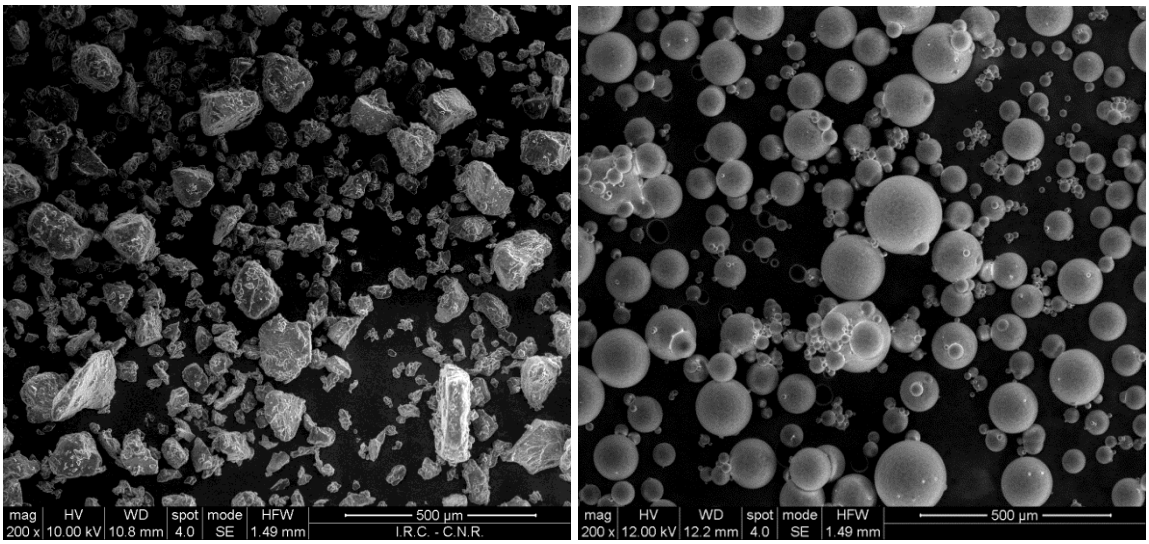

Figure 18. SEM images of wax particles before (left) and after (right) the atomization process.

The experimental tests aimed at characterizing the phenomenology of particle–wall interaction from a micromechanical point of view, in terms of restitution coefficients and capture efficiency. In particular, the *NSW–NSP* regime, the *NSW–SP* regime and the transition from the two regimes were investigated by varying different operating parameters, as reported in Table 5. The experiments probed the influence of: *(i)* increasing air temperature, which enabled to switch from non-sticky to sticky particle conditions; *(ii)* the target material and the target structures, used for the investigation of the *NSW–NSP* regime; *(iii)* the impact angle on the rebound characteristics for the *NSW–NSP* and the *NSW–SP* regimes.

Table 5. Impact tests: main reactor design and operating parameters.

	NSW–NSP	***NSP→SP* transition**	***NSW–SP***
Inner tube internal diameter *D* [m]	0.01	0.01	0.01
Outer tube internal diameter *D* [m]	0.03	0.03	0.03
Outer tube length *L* [m]	0.65	0.65	0.65
Air temperature, T_{air} (°C)	20	20–110	120
Air flow rate, Q_{air} ($m^3\ h^{-1}$ @273 K)	2–8	3–4	3–5
Particle diameter, d_p (μm)	75±10	80±15	120±20
Impact velocity, v_i ($m\ s^{-1}$)	0.5–3	2	0.7–5
Impact angle, α_i (°)	10–90	84±4	15–90
Target material	Pyrex	Pyrex	Pyrex
	Stainless steel		
	Montan wax Waradur E		
	Teflon		
Target surface	Flat polished surface	–	–
	Surface covered with 0.25 mm-thick layer of powdered wax		
	Surface covered with 1.4 mm-thick layer of powdered wax		
	Surface covered with syrup and 0.2 mm-thick layer of powdered wax		

The airstream was preheated and its temperature was measured at the exit of the tube by means of a J-type thermocouple. The air temperature was varied in the 20–120°C range, in order to perform impact events at different particle temperatures. The air flow rate ranged between 2 $m^3\ h^{-1}$ and 8 $m^3\ h^{-1}$ (at 105°C) in order to ensure particle impact velocity in the order of 1–2 $m\ s^{-1}$ at each operating temperature. The target was heated by the air flow in such a way to obtain isothermal impact events. A maximum difference of 10°C in temperature was measured between the air exiting the tube and the target during the experimental tests. Particle–air thermal equilibrium was

assumed on the basis of the Biot number (Bi«1). Furthermore, the effect of the impact angle on the rebound characteristics when testing the *NSW–NSP* and *NSW–SP* regimes was studied. In particular, the impact angle α_i ranged between 10° and 90°. Additional experimental impact tests were carried out with the presence of wax powdery layers (d_p=75±10 μm) with different thickness (about 0.2 mm and 1.4 mm) and voidage around 0.5, spread on both a dry and a wet target surface. For this kind of tests, the dry wall was represented by the Pyrex target, while the liquid layer was represented by a syrup. Figure 19 shows the viscosity of the syrup as a function of the shear rate, obtained at room temperature with the rheometer MCR 702 TwinDrive (Anton Paar).

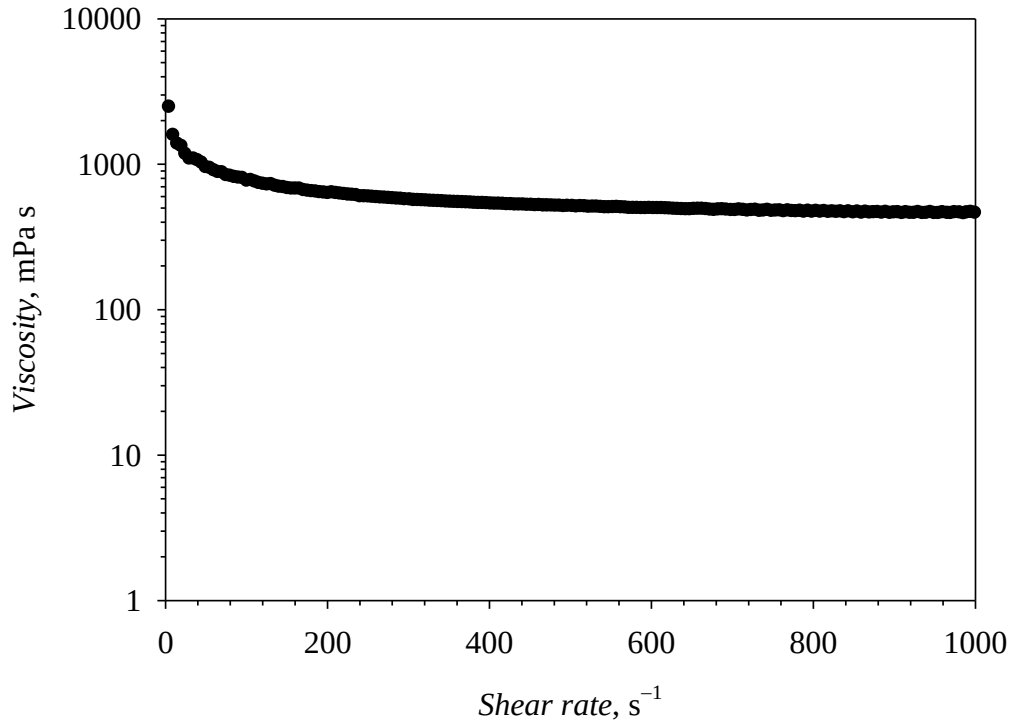

Figure 19. Viscosity vs shear rate for the syrup.

This liquid was chosen as for its properties (μ_{syr}=0.5–1 Pa s @25°C, ρ_{syr}=1280 kg m^{-3}, γ_{syr}=0.05 N m^{-1}) the entrapment and over-layering criteria are not satisfied, while the segregation or segregation–coverage regimes are likely to be established, as expected for realistic particle–slag interaction in entrained-flow gasifiers. Furthermore, syrup kinematic viscosity is $3.9\cdot10^{-4}$–$7.8\cdot10^{-4}$ m^2 s^{-1}, consistent with values commonly reported in the literature for coal slag *(Shannon et al., 2008*; *Ni et al., 2011*; *Song et al., 2011*; *Yang et al., 2011*; *Duchesne et al., 2012).*

2.3.3 Analysis of the experimental results

The rebound characteristics of a particle hitting a planar surface (*NSW–NSP* regime) were studied in terms of coefficients of restitution ε_n, ε_t and ε_g defined in *Section 1.5* by Eqs. (9)–(11) as the ratio of rebound to incidence velocities (normal, tangential and global components, respectively). In order to measure ε_n, ε_t and ε_g, the impact of the particles on the target was recorded with the progressive scan CCD camera (Photron Ultima APX), equipped with a magnifying zoom lens and a 27.5 mm extension tube. Frame-by-frame recording was accomplished at a sampling rate of 1000 fps, with a 0.028 m × 0.028 m recording window digitized as 1024 × 1024 square pixels (spatial resolution of about 27 μm), while the shutter time was set to 42 μs. Furthermore, a halogen lamp (Osram 800 W, 3200 K), a white paperboard as reflecting and diffusing surface, and a black paperboard as background were used to achieve a proper lighting of the impact zone. Each recorded frame was post-processed using the program Image-Pro Plus. In particular, it was possible to identify the position of each particle in the x and y directions, based on its x and y centers. The particle incident and rebound velocities in the x and y directions were calculated based on the frame rate and the particle distance travelled between two consecutive frames before and after the impact, respectively. Impact and rebound angles were measured from the particle position before and after a collision. All the experimental results were then grouped and classified by velocity, size, temperature and impact angle ranges, by means of an algorithm developed in Matlab language and environment. A sample of the measurements is given in Fig. 20, reporting a wax particle (d_p=70 μm) as it collides and bounces off the Pyrex target at room temperature (*NSW–NSP* regime). The time-series of the particle dimensionless coordinates, x^+ and y^+, during impact and rebound are reported in Fig. 21, where $x^+ = x(t)/x^0$ and $y^+ = y(t)/y^0$. $x(t)$, $y(t)$ and x^0, y^0 are the coordinates of the particle center at time t and at time t=0, respectively. The star (black/white) symbol represents the closest position of the particle to the target (t=4 ms, see Figure 20). The coordinate x^+ linearly increases with the time before and after collision, as the particle moves from the left to the right. The different slope before and after the impact means that the value of the tangential coefficient of restitution is not equal to 1. Also y^+ has a linear dependence on the time before and after collision, decreasing during the impact phase and increasing during the rebound phase. The distance travelled by the particle in the y direction during the rebound phase is shorter than that recorded during the impact phase, and this is a first indication that the normal restitution coefficient is smaller than 1.

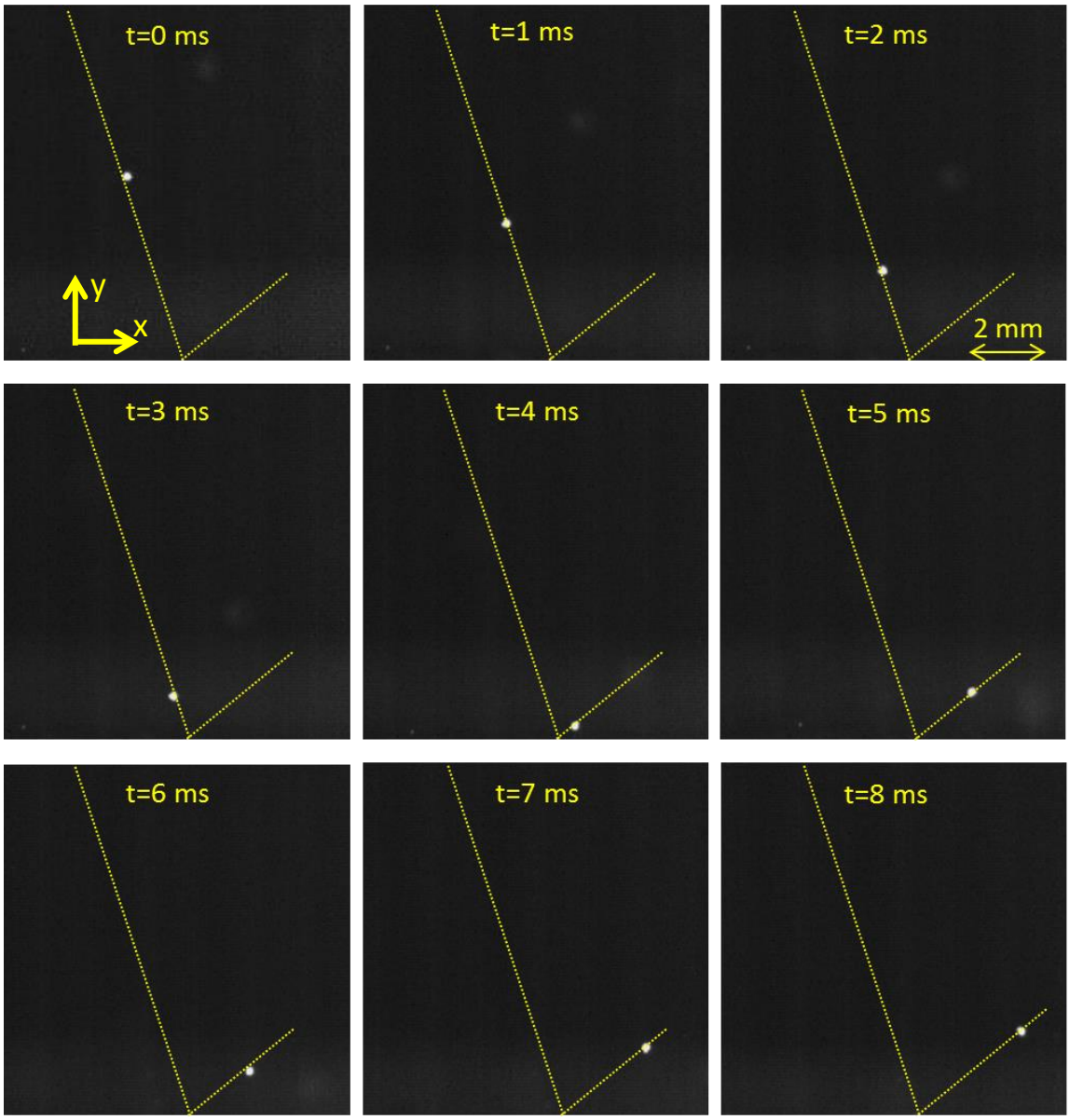

Figure 20. Snapshots captured during a typical particle impact (d_p=70 μm). The dotted lines represent the particle trajectory before and after the collision.

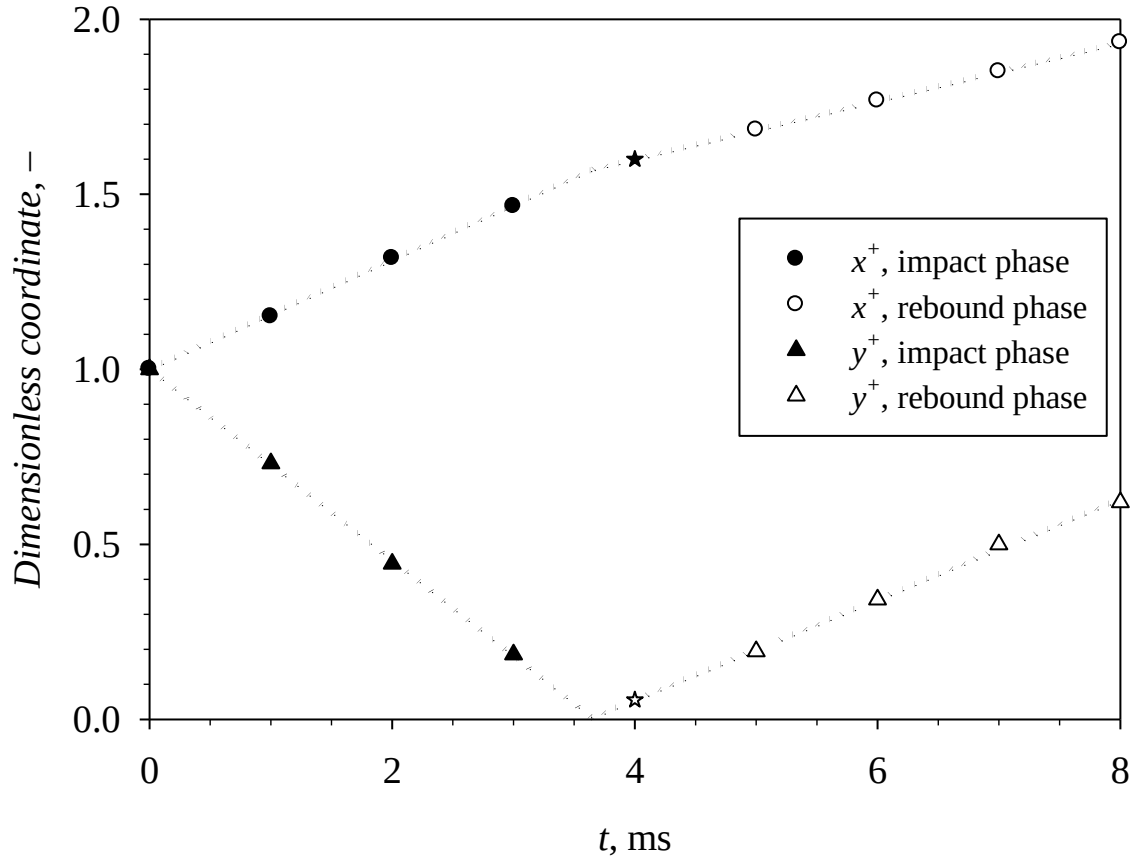

Figure 21. Time-series of the particle dimensionless coordinates, x^+ and y^+, before/after impact for the sample test reported in Fig. 20. The star marks the time (t=4 ms) corresponding to the closest particle position to the target.

In order to verify the suitability of describing this kind of collision events with theoretical models from literature *(Brach and Dunn, 1998; Gorham and Kharaz, 2000; Thornton and Ning, 1998; Wu et al., 2003; Wu et al., 2009)*, the mechanical properties of both the particles and the target are needed. The wax mechanical properties were determined by uniaxial compressive tests in accordance with ASTM D 695-10, with a dynamometer INSTRON 3360 equipped with a load cell of 10 kN (AlphaTechnologies, T 2020-DC10). Seven wax cylindrical samples, 0.025 m-height, were tested. A typical stress-strain curve for the wax samples is shown in Fig. 22, while the mean values of the mechanical properties of the wax and those for different coals *(Hobbs, 1964; Zhong et al., 2014)* are reported in the Table 6, together with their standard deviation. The mechanical properties of the wax quite well agree with the data for coal/char reported in the literature.

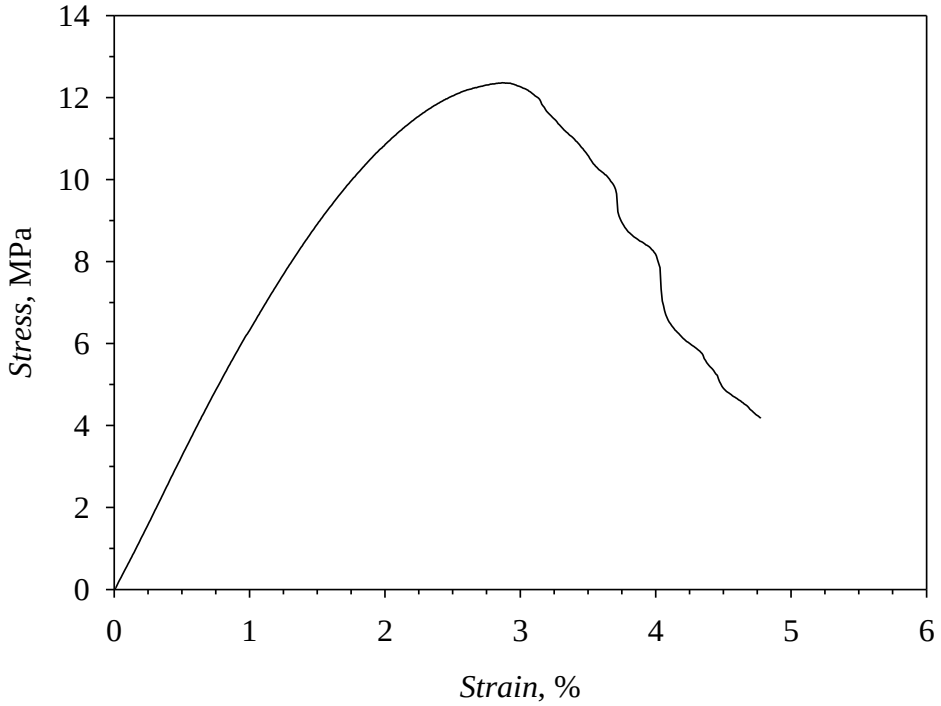

Figure 22. Typical stress–strain curve for wax samples.

Table 6. Mechanical properties of montan wax Waradur E and of different reference coals.

Material	Young's modulus, E (MPa)	Strength, (MPa)
Waradur E wax	700±66	9.5±2.5[a]
Coal (Rank Code No. 100a)	3675±545	17±2.82[b]
Coal (Rank Code No. 201)	1324±193	5.3±0.83[b]
Coal (Rank Code No. 301)	400±103	1.93±0.27[b]
Coal (Rank Code No. 801)	3805±41.37	26.54±2.07[b]
Schleenhain brown coal	43±15	2.35±0.78[c]
Schleenhain brown coal char obtained at 800 °C	206±63	11.2±5[c]

[a] 0.2% offset yield strength.
[b] After *Hobbs, 1964*, yield strength.
[c] After *Zhong et al., 2014*, compressive strength.

The mechanical properties were used to model the particle rebound characteristics in terms of the restitution coefficients ε_n, ε_t and ε_g defined in *Section 1.5* by Eqs. (6)–(8), (11) and (12). Furthermore, the effect of the particle/wall interfacial energy on the rebound characteristics was

investigated. Table 7 reports the surface energies, the mechanical properties and the critical velocities for wax particles impacting the four target materials. These parameters were used to calculate the restitution coefficients according to the theoretical models described in *Section 1.5*. The calculated coefficients of restitution were compared with those measured during the impact experiments.

Table 7. Surface energies, mechanical properties of the reference target materials and values of critical velocities.

	Pyrex	**Stainless steel**	**Wax**	**Teflon**
Surface energy, Γ (N m^{-1})	1	0.8	0.03	0.02
Young's Modulus E (GPa)	64	190	0.7	0.5
Poisson's ratio (–)	0.2	0.3	0.49	0.46
Yield velocity, v_y (m s^{-1})	$6.8 \cdot 10^{-3}$	$6.7 \cdot 10^{-3}$	$3.9 \cdot 10^{-2}$	$2.6 \cdot 10^{-2}$
Sticking velocity, v_s (m s^{-1})	$1.15 \cdot 10^{-1}$	$1.04 \cdot 10^{-1}$	$3.03 \cdot 10^{-2}$	$3.02 \cdot 10^{-2}$

The rebound characteristics for the *NSW–SP* regime were expressed in terms of capture efficiency ($C.E.$), defined as the fractional number of adhered particles over the number of total impacted particles:

$$C.E. = \frac{N_p^{\varepsilon g=0}}{N_p^{tot}} 100\% \tag{46}$$

Finally, for the transitional *NSP→SP* regimes, both the restitution coefficients and capture efficiency were measured.

Chapter 3. Investigation of near-wall particle segregation phenomena: results and discussion

In this section, the experimental results obtained with the lab-scale cold entrained-flow reactor are reported and discussed. In particular, the effect of different operating parameters on the fractional mass of wax in the lean-dispersed phase and at the wall was under investigation for all the possible particle-wall interaction regimes (*NSW–NSP*, *NSW–SP*, *SW–NSP* and *SW–SP* regimes). The near-wall particle segregation phenomena were also studied from a qualitative point of view in order to evaluate and elucidate the phenomenology of the particle−wall interactions in entrained-flow reactors. This was accomplished by visual observation and video recording at the near-wall region of the reactor for each regime.

3.1 Analysis of the Sticky Wall–Sticky Particle regime

In this section the experimental results obtained in the sticky wall–sticky particle (*SW–SP)* regime are reported. The experimental tests aimed at characterizing the general phenomenology of the interaction between the dispersed phase generated by the spray and the reactor walls. The partitioning of the atomized wax between the dispersed and the wall phases was quantitatively assessed as a function of the distance from the nozzle. The qualitative phenomenology of the dispersed phase/wall interaction and of the wall layer flow was assessed by careful analysis from close-up video recordings taken at the wall during the experiments. Furthermore, the effect of the scale of the model reactor was investigated, and the results are hereinafter reported.

3.1.1 Partitioning of the wax between the dispersed phase and the wall layer in the 0.04 m-ID reactor

The wax feeding rate was W_{wax}^{lean} (z=0)=0.2 g s^{-1}. By taking into account the gas (steam+oxygen)-to-solid feed ratios typical of industrial gasifiers *(Montagnaro et al., 2011)*, the total air flow rate (expressed as the sum of Q_{ms}, the flow rate of mainstream air, and Q_a, the flow rate of atomization air) was fixed at 1 m^3 h^{-1} (at 298 K). Q_a was treated as a parameter, ranging between 0.25 m^3 h^{-1} and 0.35 m^3 h^{-1}, with a reference case of 0.30 m^3 h^{-1}. The values of Q_a complied with the nozzle constraints, and assured a good wax atomization in terms of size and dispersion of droplets. The air streams were both preheated before entering the reactor and at about 100°C the gas hydraulic velocity was around 0.3 m s^{-1}, comparable with values typical of industrial gasifiers. T_{ms} was fixed at 120°C, while T_w was fixed at 135°C.

The reactor length L was varied to investigate the influence of the distance from the injection nozzle on the fractional mass of wax transferred form the lean-dispersed phase to the wall layer. L

ranged between 0.03 m and 0.27 m. In the following figures, experimental data are reported as average values of multiple tests (symbols), together with error bars corresponding to the standard deviation.

Figure 23 reports the values of y^{lean} measured in experiments carried out with different values of L, while keeping all the operating variables of the reference case. y^{lean} abruptly decreases from nearly 0.91 in the proximity of the nozzle (L=0.03 m) to approach 0.12 for $L \geq 0.20$ m. It is interesting to compare the experimental plot with limiting lines corresponding to the idealized *NSW–NSP* and *SW–SP* regimes (Fig. 3), both reported in Fig. 23 for comparison. In the first case (*NSW–NSP*), the wall reflects impinging particles according to a nearly elastic interaction pattern. Accordingly, y^{lean} would be 1 for any L. The other idealized limiting curve (*SW–SP*) is based on the consideration of the conical shape of the jet and of the uniform distribution of the dispersed phase across the jet which reflects the design and operational characteristics of the nozzle used in the experiments. Additional assumptions are that wax droplets approach the wall along radial trajectories departing from the nozzle (see Fig. 12); the droplets impinge the wall under the effect of inertia and are deposited thereon without rebound, as they are incorporated in the wall molten layer. According to the geometry of the nozzle and of the reactor (Fig. 12), the impact of molten wax droplets becomes significant only at a distance $z \geq z^*$ from the nozzle, the value of z^* being determined by the aperture angle of the conical jet (θ_{max}=25° and z^*=0.043 m in the present case). Simple geometrical arguments suggest that:

$$y^{lean}(z) = \begin{cases} 1 & z < z^* \\ \left(\frac{z^*}{z}\right)^2 & z \geq z^* \end{cases} \tag{47}$$

Equation (47) is plotted in Fig. 23 as the idealized limiting curve corresponding to the *SW–SP* regime.

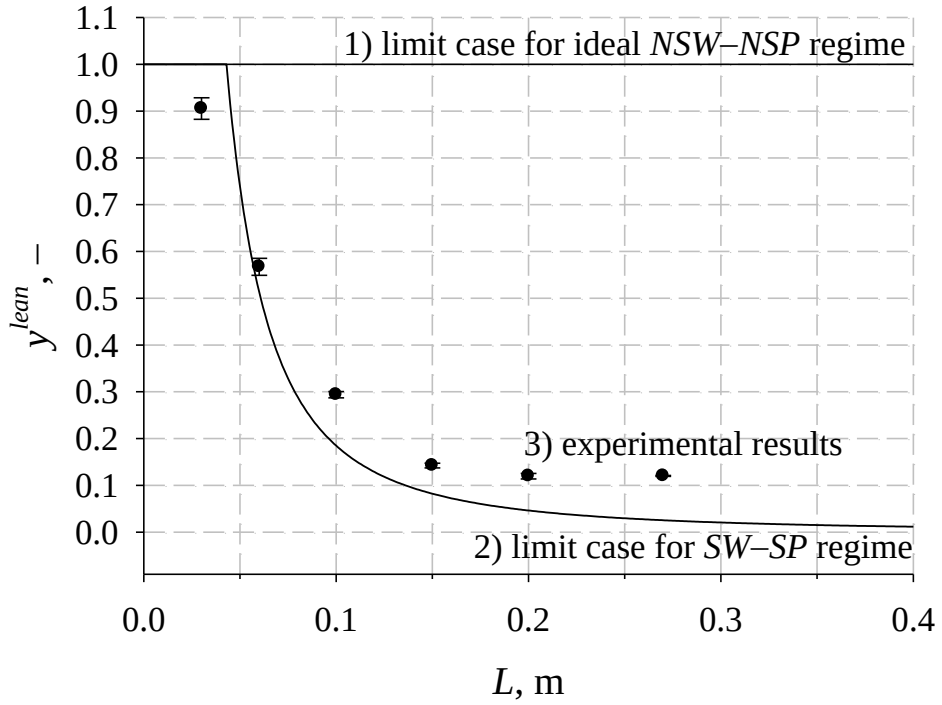

Figure 23. Effect of the axial coordinate on the wax fractional content in the lean phase. 1) ideal *NSW–NSP* regime; 2) plot of Eq. (47) for *SW–SP* regime with only nozzle-related geometrical effects & no rebound; 3) experimental results from tests carried out at Q_a=0.30 $m^3\ h^{-1}$**.**

When the experimental data points are compared with the limiting curves, the following features may be recognized:

- Experimental data points lie much closer to the *SW–SP* regime limiting curve than to the other limiting curve. This finding is fully consistent with the operating conditions of the tests, which promoted a permanently molten status of both entrained wax droplets and wall layer.

- Values of y^{lean} slightly departs from 1 already at $z < z^*$. It is likely that this behaviour is related to moderate back-mixing of the dispersed phase, associated with recirculation and mainstream gas entrainment developing close to the nozzle.

- The experimental data points lie somewhat above the theoretical *SW–SP* regime limiting curve for large values of *L*. This might result from either moderate droplet rebound at the wall followed by re-entrainment, or by a certain degree of ineffectiveness of the inertial forces in promoting impingement and entrapment of droplets as they are simultaneously invested by the mainstream flow directed parallel to the wall. It must be underlined that the transfer of droplets to the wall in the fully developed flow downstream of the nozzle, by Brownian or turbophoretic mechanisms is bound to be rather ineffective if one considers that the Reynolds

number of the fully developed flow is in the order of 500. This might justify the relative constancy of $y^{lean} \cong 0.12$ for large values of L.

The effect of the flow rate of atomizing air Q_a on y^{lean} is shown in Fig. 24a). The changes of y^{lean} are modest, comprised between 0.14 and 0.16. Also the atomization temperature did not lead to significant variations in y^{lean}, as shown in Fig. 24b): as T_a was increased from 130°C to 145°C, y^{lean} was comprised between 0.13 and 0.16. However it must be recalled that the selected range of T_a was well above the range of temperatures at which the solid–liquid transition of the wax occurs.

The mainstream gas flow rate exerted only moderate effect on y^{lean}, as reported in Fig. 25. This finding further suggests that the axial profile of y^{lean} is largely dominated by the hydrodynamics of the jet.

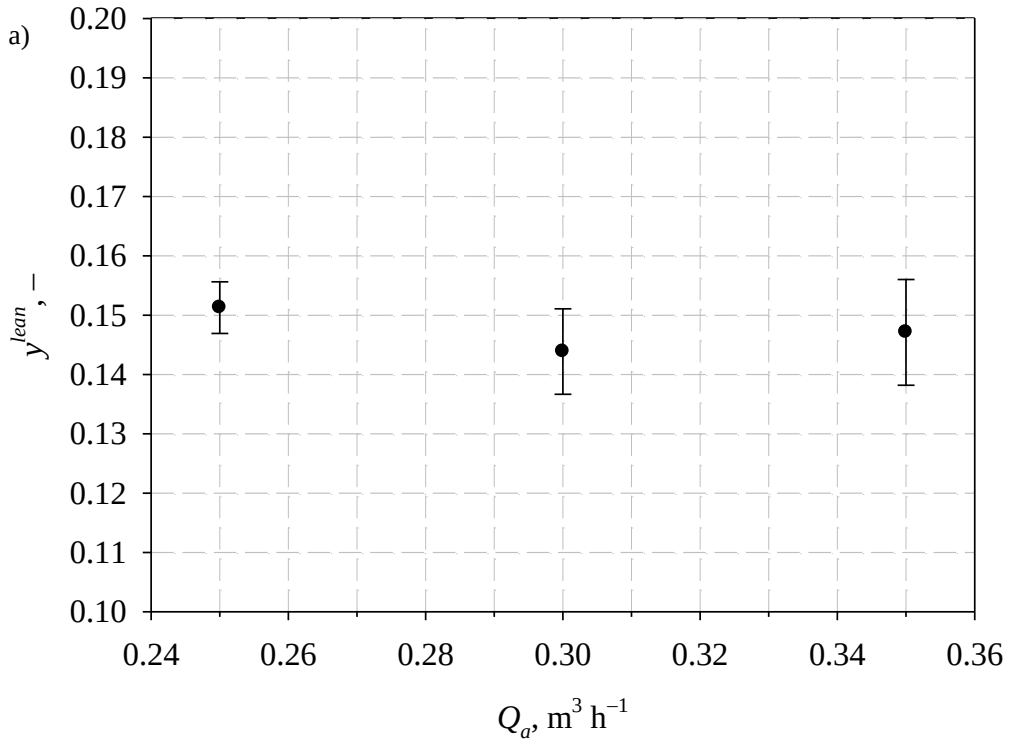

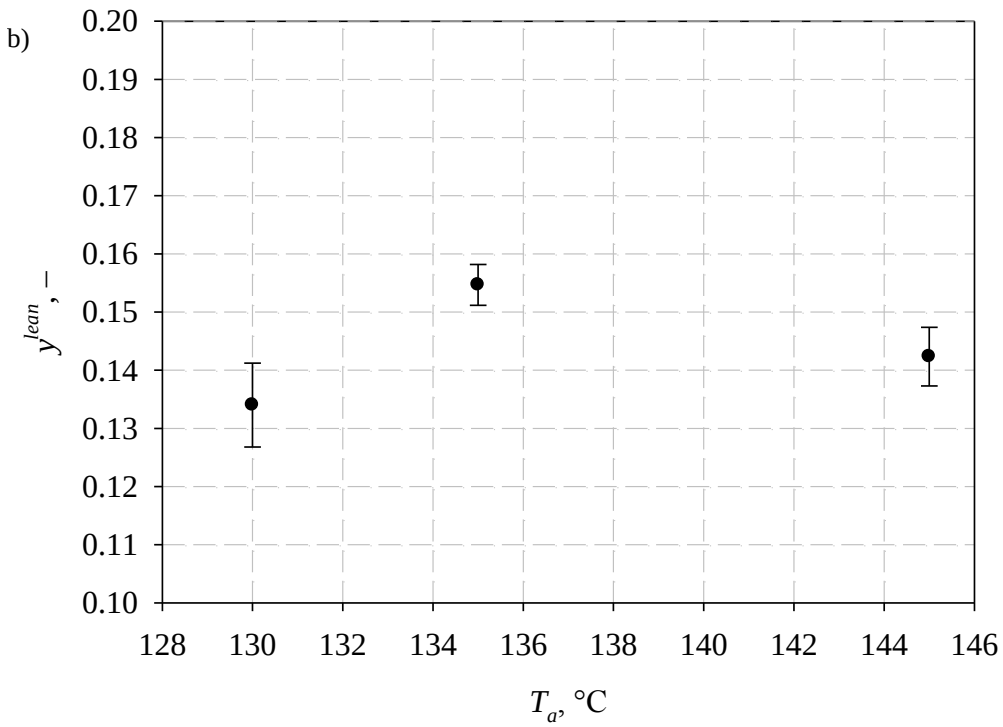

Figure 24. a) Effect of the atomization air flow rate on the wax fractional content in the lean phase. Tests carried out at T_a=145°C and L=0.15 m. b) Effect of the atomization temperature on the wax fractional content in the lean phase. Tests carried out at Q_a=0.30 m^3 h^{-1} and L=0.15 m.

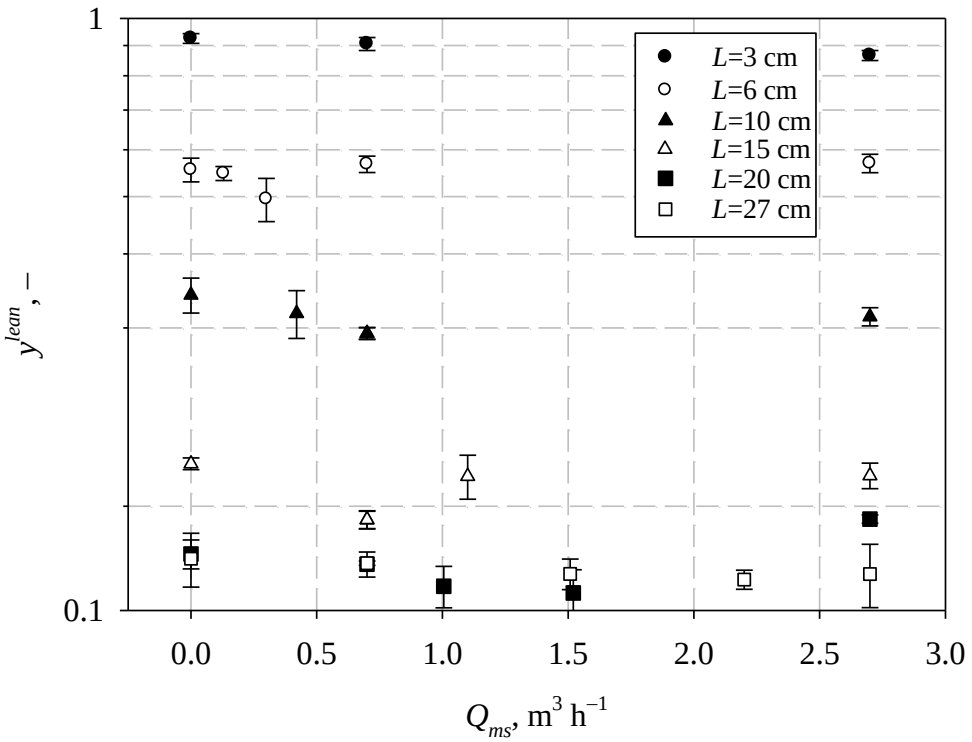

Figure 25. Effect of the mainstream gas flow rate on the wax fractional content in the lean phase. Q_a =0.30 m^3 h^{-1}.

3.1.2 Qualitative phenomenology of dispersed phase/wall interaction and wall layer flow

Two temporal sequences of snapshots captured during a typical test are reported in Fig. 26 (Q_a=0.30 $m^3 h^{-1}$, T_a=138°C and L=0.20 m). As a result of the impact of sticky particles on the sticky wall (Fig. 3), coalescence was by far the predominant process, though occasional droplet rebound and re-entrainment into the dispersed phase could be observed.

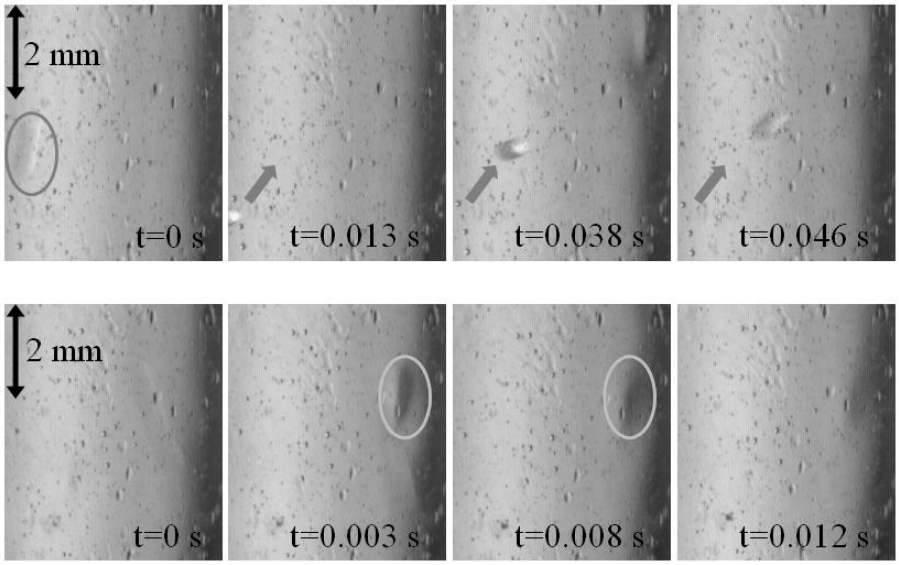

Figure 26. Rebound (up) and coalescence (down) of sticky wax droplets impinging on the sticky wax wall. Snapshots captured at a frame rate of 250 fps.

A sequence of snapshots recorded during a typical test is reported in Fig. 27 (Q_a=0.30 $m^3 h^{-1}$, T_a=120°C and L=0.10 m) displaying the motion of the wall liquid layer in the proximity of the tube discharge section. The analysis of the snapshots highlighted the presence of very fine (typically micron-sized) air bubbles entrapped in the wall molten wax layer and descending along vertical streamlines. The wall layer was characterized by laminar flow. Assuming that the air bubbles behave as a non-diffusive tracer and following their trajectories, it was possible to estimate a descending velocity of the molten wax wall layer in the order of 3–6 mm s^{-1}. On the basis of this result, and of the value of the volumetric flow rate of the wall layer phase, the thickness of the wall liquid layer was calculated and results to be in the order of 0.22 mm.

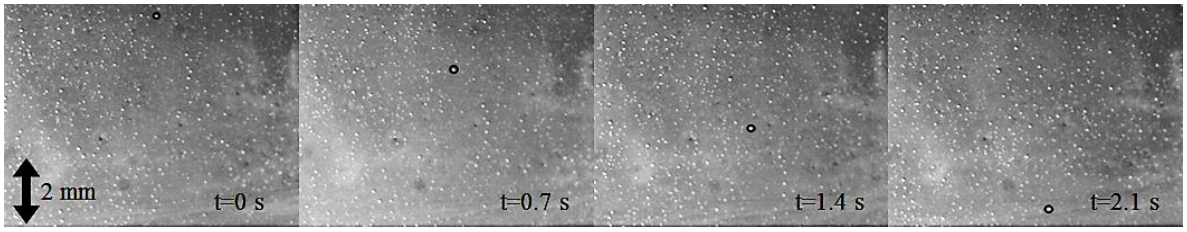

Figure 27. Snapshots captured by the CCD camera at a frame rate of 120 fps. The open circle highlights one of the descending air bubbles entrapped in the wall molten wax layer.

3.1.3 Effect of the scale of the model reactor

This section compares results obtained in the two model reactors (0.04 m-ID and 0.1 m-ID) for the *SW–SP* regime. When testing in the 0.1 m-ID reactor, the flow rate of the mainstream air was scaled as well, to keep the gas superficial velocity in the range of practical interest of 0.25–0.30 m s^{-1}. Q_a and Q_{ms} were fixed at 0.275 m^3 h^{-1} and 5 m^3 h^{-1} (at 273 K), respectively. Also in this case, the values of Q_a complied with the nozzle constraints and assured good wax atomization in terms of size and dispersion of droplets for both the investigated regimes. The reactor length L was varied, again, to study the influence of the distance from the injection nozzle on the fractional mass of wax transferred form the lean-dispersed phase to the wall layer. Different reactor tubes were used: L was varied in the 0.1–0.6 m range. All the operating parameters for both the design configurations are summarized and listed in Table 4. In the following figures, the experimental data are reported as average values of multiple tests (symbols), together with error bars corresponding to the standard deviation. The effect of the reactor length on the fractional mass of wax transferred form the lean-dispersed phase to the wall layer is shown in Fig. 28. Also the theoretical limiting curve for the *SW–SP* regime (Eq. (47)) is reported. The axial coordinate corresponding to the intersection of the conical jet and the cylindrical reactor is z^*=0.1275 m for the 0.10 m-ID reactor, z^*=0.043 m for the 0.04 m-ID reactor.

Results obtained with the two model reactors are fairly coincident, within the experimental error, and demonstrate that no significant effect of scaling-up the reactor internal diameter is appreciated as far as the *SW–SP* regime is concerned. With reference to the 0.10 m-ID reactor, in the range of z/z^* from 0.78 (z=0.10 m) to nearly 5 (z=0.6 m), y^{lean} decreases from about 0.68 to asymptotically approach nearly 0.18. When the experimental data points are compared with the theoretical limiting curve it can be recognized that: *(i)* at $z/z^*>1$, the experimental data points approach the limiting curve, as the operating conditions effectively promoted the *SW–SP* regime; *(ii)* the departure of the experimental data at $z/z^*<1$ is related to moderate backmixing of the dispersed phase associated with recirculation and mainstream gas entrainment developing close to the nozzle.

As regards the phenomenology of droplets/liquid layer interaction, it closely conforms to qualitative interaction patterns highlighted when testing in the 0.04 m-ID reactor. Coalescence was

by far the predominant process following the impact of sticky particles on the sticky wall, though occasional droplet re-suspension into the dispersed phase was observed.

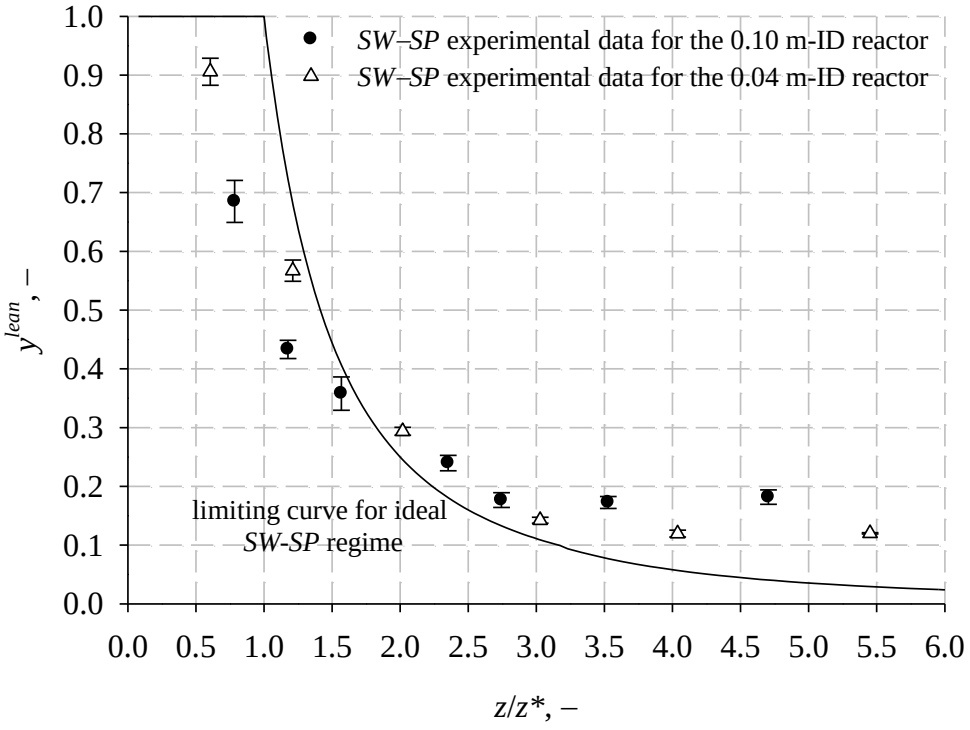

Figure 28. Effect of the reactor inner diameter on axial profiles of the fractional mass of wax in the dispersed phase (y^{lean}). The limiting curve represents the plot of the theoretical Eq. (47).

3.2 Analysis of the Non Sticky Wall–Non Sticky Particle regime

In this section, the experimental results for the Non Sticky Wall–Non Sticky Particle (*NSW–NSP)* regime are reported. Experimental results included: *(a)* the quantitative assessment of the partitioning of atomized wax between the wall layer and the lean-dispersed phase entrained in the mainstream; *(b)* the qualitative and quantitative assessment of the micromechanical interaction between impinging wax particles and the wall. The first goal was pursued by selective collection of entrained wax at the exit of the Pyrex duct, the second by careful analysis of multiple events from close-up video recordings taken at the wall during the experiments. The partitioning of the atomized wax between the dispersed and the wall phases was quantitatively assessed as a function of the distance from the nozzle. Experimental tests were carried out in the 0.1 m-ID reactor and the main operating parameters are summarized and listed in Table 4. The flow rate of mainstream air, Q_{ms}, and the flow rate of atomization air, Q_a, were treated as parameters for the purposes of

exploring, evaluating and testing their effect on the phenomenology of interaction between the lean-dispersed phase and the wall layer. In particular, Q_{ms} ranged between 1 $m^3\ h^{-1}$ and 20 $m^3\ h^{-1}$ (at 273 K), while Q_a ranged between 0.275 $m^3\ h^{-1}$ and 0.8 $m^3\ h^{-1}$ (at 273 K), with a reference case of 1 $m^3\ h^{-1}$ and 0.5 $m^3\ h^{-1}$, respectively. The reactor length L varied in the 0.1–0.45 m range.

3.2.1 Partitioning of atomized wax: SW–SP versus NSW–NSP regimes

Figure 29 shows results obtained under comparable hydrodynamic conditions (Q_a=0.275 $m^3\ h^{-1}$; Q_{ms}=5 $m^3\ h^{-1}$) when the particle–wall interaction regime is switched from *SW–SP* to *NSW–NSP*. This switch was simply accomplished by changing the mainstream temperature from 160°C to 30°C and the wall temperature from 140°C to 30°C, i.e. setting both the temperatures at values well below the softening limit of the wax. It must be underlined that even at these temperatures, the wax particles exhibited plastic behaviour upon impingement, a feature that is certainly relevant to the micromechanical interaction with the wall, as it will be discussed later.

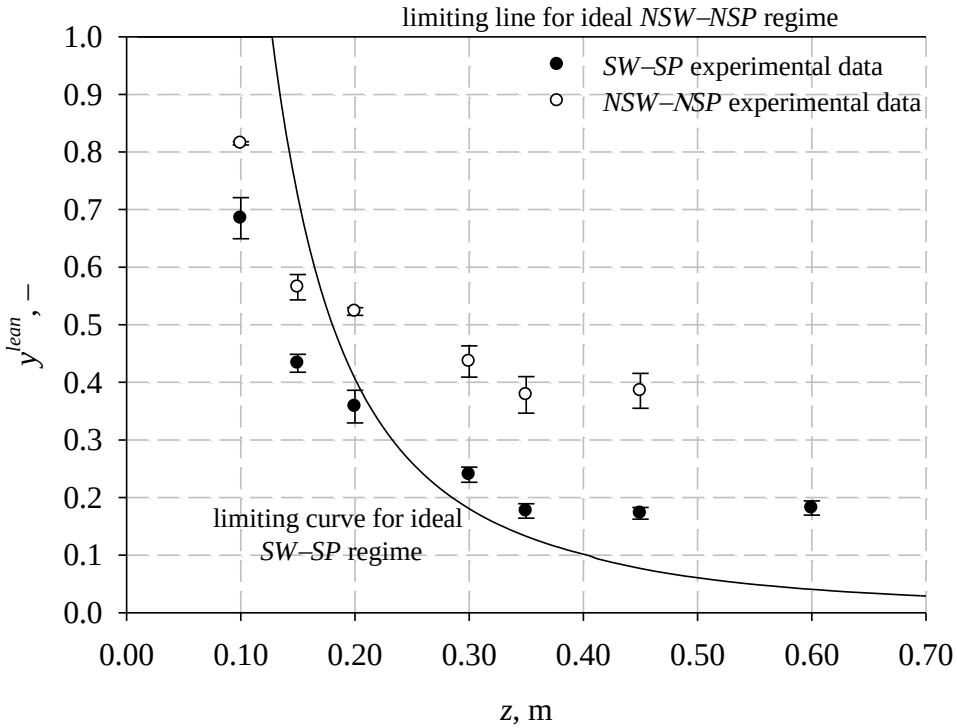

Figure 29. Partitioning of wax: *SW–SP* versus *NSW–NSP* regime. The limiting curves representing the *NSW–NSP* and the *SW–SP* regimes are plotted as a reference.

The values of y^{lean} are plotted against the axial coordinate z of the reactor. The limiting line corresponding to the idealized *NSW–NSP* regime (the wall reflects impinging particles according to a nearly elastic interaction pattern, thus y^{lean}=1 for any z) and that for the idealized *SW–SP* regime (see Eq. (47)) are reported as a reference. Switching from *SW–SP* to *NSW–NSP* regime

significantly affects the wax partitioning, highlighting how the change in the operating conditions would be able to induce the shift from a sticky–sticky regime to a regime in which the non sticky behaviour of both the wall layer and impinging particle is established. y^{lean} is systematically larger in the *NSW–NSP* regime along the reactor, approaching a value of nearly 0.4 for $z/z^*>>1$ (z^*=0.1275 m), compared with 0.18 observed in the *SW–SP* regime. It is remarkable that, though larger than for the *SW–SP* regime, y^{lean} in the *NSW–NSP* regime is still substantially smaller than 1. This finding is consistent with the establishment of a near-wall segregated particle layer under the combined effect of the hydrodynamics of the confined multiphase flow, of particle adhesion/rebound and resuspension, as it will be discussed later.

3.2.2 Partitioning in the NSW–NSP regime: effect of operating conditions

The effect of the air flow rates (Q_a and Q_{ms}) on the partitioning of wax particles is hereinafter reported and discussed. Figure 30 shows partitioning data at a fixed flow rate of mainstream air (Q_{ms}=1 $m^3\ h^{-1}$) while varying the flow rate of atomization air (Q_a) between 0.275 $m^3\ h^{-1}$ and 0.8 $m^3\ h^{-1}$. The analysis of experimental data indicates that:

- increasing the atomization air flow rate shifts the data points toward the *NSW–NSP* limiting line. A threshold value of Q_a is found at around 0.5–0.6 $m^3\ h^{-1}$, above which the limiting *NSW–NSP* line is approached, under the operating conditions adopted;
- at Q_a smaller than 0.5 $m^3\ h^{-1}$, y^{lean} decreases alongwith z as the entrained wax is deposited on the wall. At large values of z, y^{lean} approaches 0.38 (Q_a=0.275 $m^3\ h^{-1}$), 0.53 (Q_a=0.4 $m^3\ h^{-1}$) and 0.66 (Q_a=0.5 $m^3\ h^{-1}$).

The trends of data points in Fig. 30 may be explained by considering that increasing Q_a brings about a reduction of the size of the wax particles, that can therefore more easily solidify along their trajectory to the wall. Moreover, as Q_a is increased, jet–wall interference and turbulence are promoted. Both these effect enhance particle re-suspension, hence increased y^{lean}. Two SEM micrographs of the wax particles collected in the lean phase for Q_a=0.275 $m^3\ h^{-1}$ (left) and Q_a=0.4 $m^3\ h^{-1}$ (right) are reported in Fig. 31. It is shown that the mean size of the wax particles decreases with increasing Q_a.

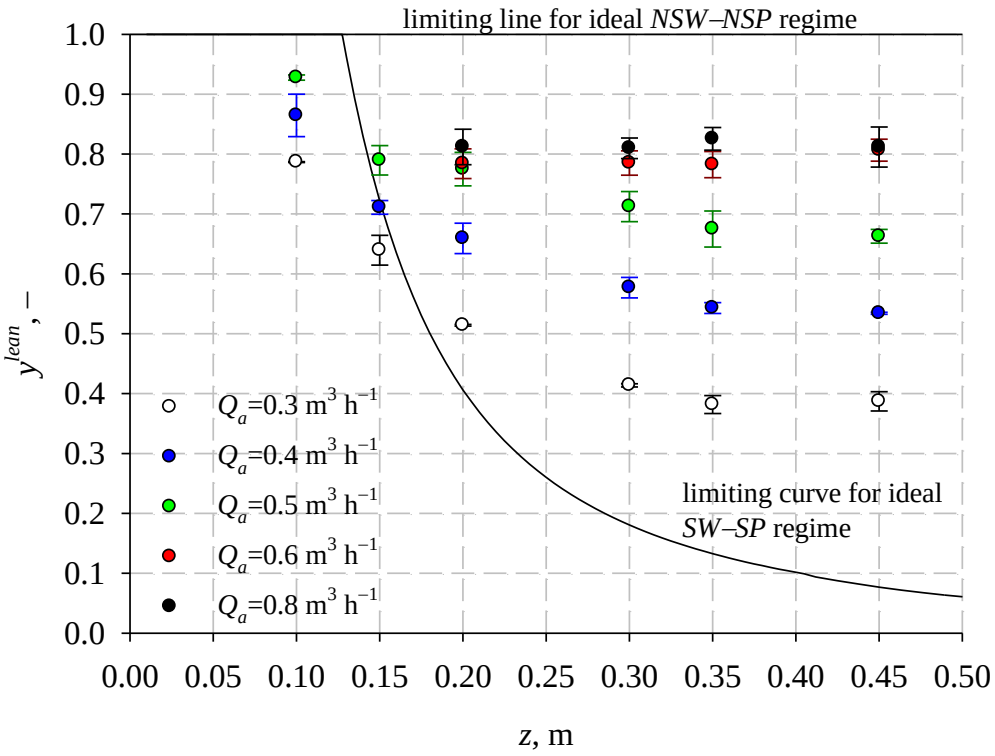

Figure 30. Effect of the atomization air flow rate (Q_a) on the axial profile of the fractional mass of wax in the dispersed phase (y^{lean}). Flow rate of mainstream air set at 1 m^3 h^{-1}. The limiting curves representing the *NSW–NSP* and the *SW–SP* regimes are plotted.

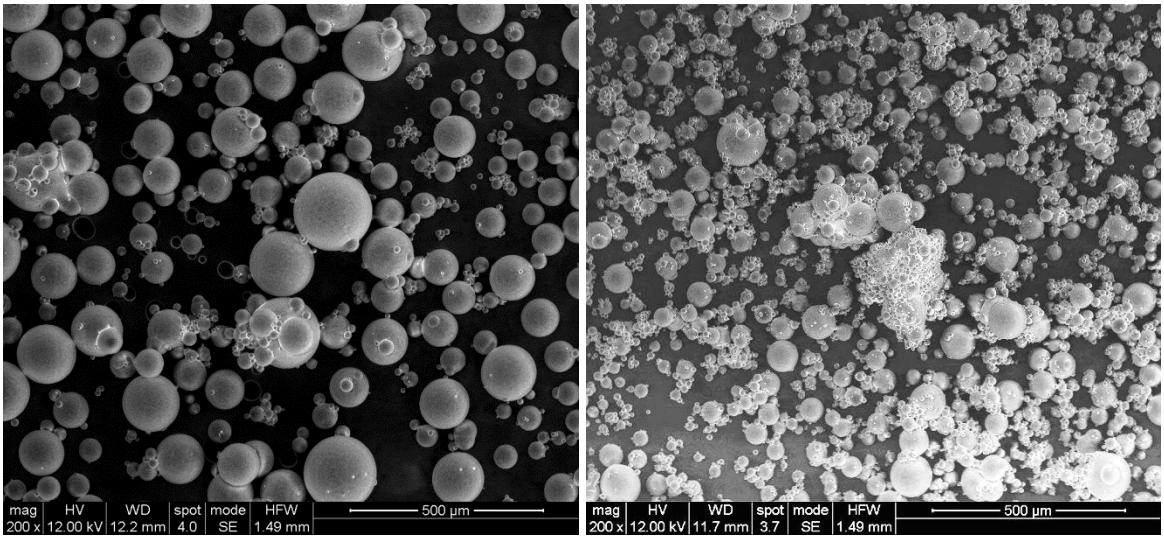

Figure 31. SEM images of the wax particles collected in the lean phase for Q_a=0.275 m^3 h^{-1} (left) and Q_a=0.4 m^3 h^{-1} (right).

Figure 32 reports pictures of the Pyrex duct of the reactor after experimental testing in the *NSW–NSP* regime at two levels of Q_a, namely 0.5 m^3 h^{-1} and 0.8 m^3 h^{-1}. The other operational parameters, namely Q_{ms} and L, were kept at 1 m^3 h^{-1} and 0.45 m, respectively. In order to improve the observation of wax deposits on the inner surface of the transparent duct, a black paper stripe has

been inserted into the tube to provide a dark background: accordingly, the darker the appearance of the surface, the smaller the surface coverage. During the tests at Q_a=0.5 $m^3\,h^{-1}$, particles accumulate nearly uniformly along the tube, except over the last 0.1–0.15 m, consistently with the finding of a nearly constant value for y^{lean}. Increasing Q_a up to 0.8 $m^3\,h^{-1}$ results in larger jet velocities and jet-induced turbulence, which contribute to prevent particle accumulation in the pre-impact zone ($z/z^*<1$). Correspondingly, the fractional mass of wax in the dispersed phase is larger, consistently with results in Fig. 30.

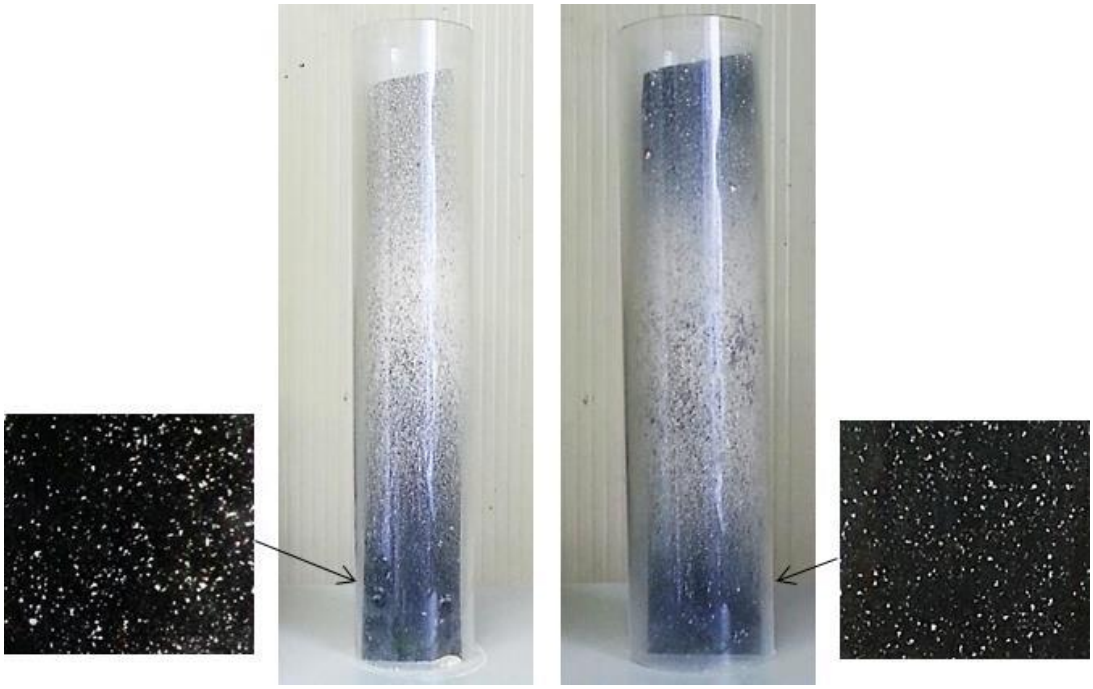

Figure 32. Effect of the atomization air flow rate Q_a on the distribution pattern of wax particles on the walls. Left: Q_a=0.5 $m^3\,h^{-1}$; right: Q_a=0.8 $m^3\,h^{-1}$. Q_{ms} was fixed at 1 $m^3\,h^{-1}$ for both the test cases. L=0.45 m. A black paper stripe provides a dark background for an improved observation of the wax deposits on the inner duct.

The effect of the mainstream gas flow rate on wax deposition is reported in Fig. 33. The plots compare y^{lean} data for Q_{ms} ranging from 1 $m^3\,h^{-1}$ to 20 $m^3\,h^{-1}$, Q_a being fixed at 0.5 $m^3\,h^{-1}$. The profiles of y^{lean} along z are shifted toward the *SW–SP* limiting curve as the flow rate of the mainstream air increases. It is likely that the following processes concur to this somewhat unexpected trend:

- increasing the mainstream rate suppresses the vortical turbulent structure establishing at the location where the jet interferes with the wall, hence reduces re-suspension of particles;

- increasing the mainstream rate may enhance near-wall particle segregation patterns of hydrodynamical nature, due to the formation of a "lean core-dense annulus" multiphase flow structure similar to the dense dispersed phase postulated by *Montagnaro and Salatino (2010)*.

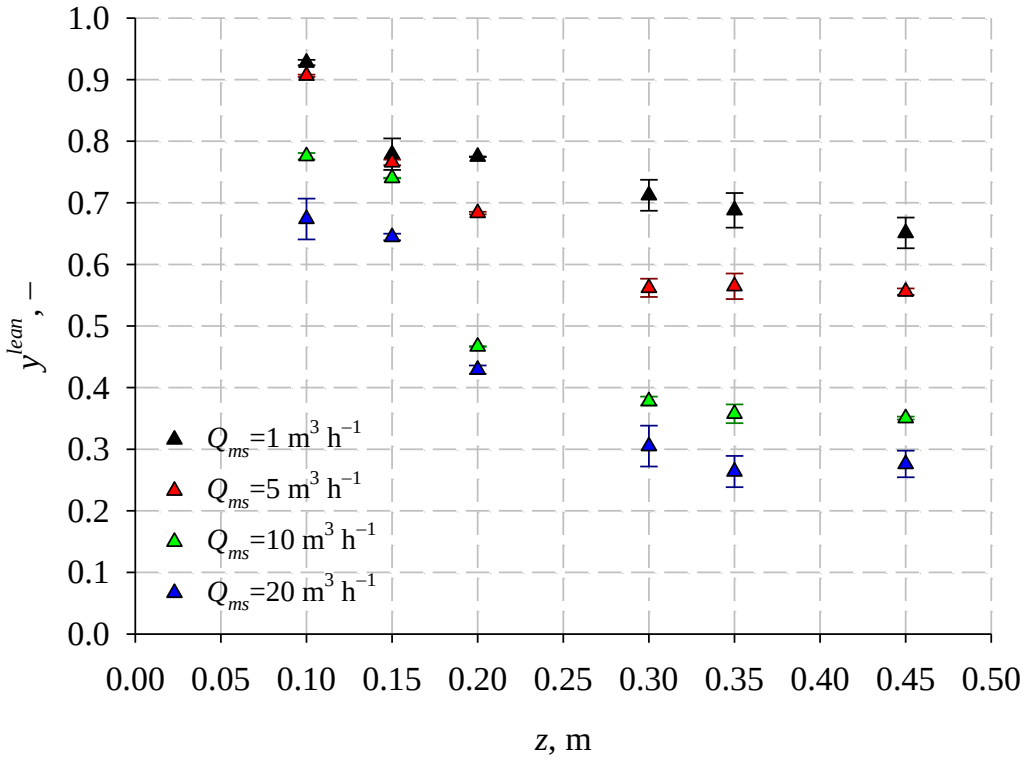

Figure 33. *NSW–NSP* regime: effect of the flow rate of mainstream air *(Q_{ms})* on the axial profile of the fractional mass of wax in the dispersed phase (y^{lean}). Flow rate of atomization air set at 0.5 m^3 h^{-1}.

The qualitative patterns of particle deposition on the Pyrex duct in the *NSW–NSP* regime are reported in Fig. 34. Patterns corresponding to different values of Q_{ms} are compared, keeping Q_a=0.5 m^3 h^{-1} and L=0.45 m. For Q_{ms}=1 m^3 h^{-1}, particles accumulate nearly uniformly along the tube length, except over the lowest 0.1 m, similarly to what reported in Fig. 32. For Q_{ms}=20 m^3 h^{-1} the deposition pattern is different. Particles accumulate in a relatively compact form in the upper part of the duct (i.e. the pre-impact/impact zone). Accumulation takes place in the lower duct too, but with a different morphology, as deposits have the appearance of loosely connected particle clusters, a feature consistent with the prevailingly hydrodynamical nature of near-wall particle segregation in this section of the duct.

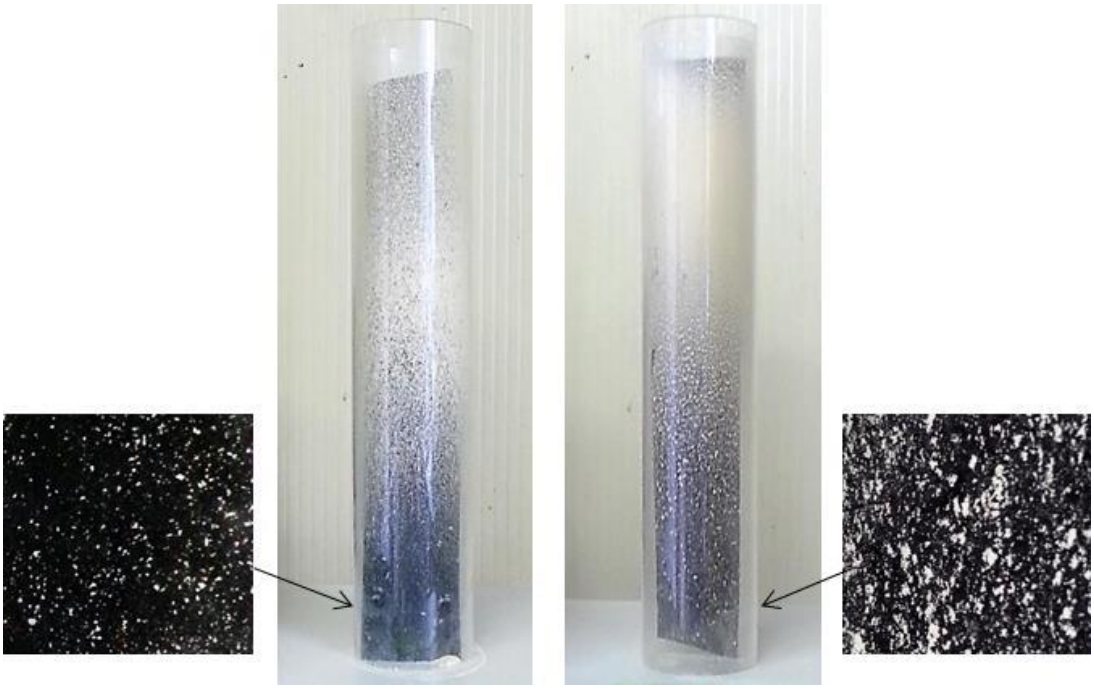

Figure 34. Effect of the mainstream air flow rate Q_{ms} on the distribution pattern of wax particles on the walls. Left: Q_{ms}=1 m^3 h^{-1}; right: Q_{ms}=20 m^3 h^{-1}. Q_a was fixed at 0.5 m^3 h^{-1} for both the test cases. L=0.45 m. A black paper stripe provides a dark background for an improved observation of the wax deposits on the inner duct.

3.2.3 Phenomenology of particle–wall micromechanical interaction and theoretical criteria of particle detachment

The qualitative phenomenology of particles/wall interactions is very complex. Video recordings were performed locating the CCD camera at three different levels, namely 0.1 m, 0.15 m and 0.2 m from the nozzle (denoted as pre-impact, impact and post-impact zone, respectively). Two mainstream gas flow rates (Q_{ms}=1 m^3 h^{-1} and Q_{ms}=10 m^3 h^{-1}) were investigated, while Q_a was fixed at 0.5 m^3 h^{-1}.

Analysis of video recordings enabled to track the fate of individual particles, to count the number of particles touching the wall, those undergoing adhesion and those being resuspended into the mainstream. Figures 35 and 36 show a particle–wall impact/rebound event following a collision, and a particle resuspension event due to entrainment in the gas flow, respectively. In particular, the pre-impact and post-impact particle streak lines, corresponding to the rebound event are shown in Fig. 35. On the other hand, Figure 36 shows how an adhered particle (frame a) rotates and/or rolls along the wall (frames b–e) and eventually is detached and resuspended into the mainstream, as made evident by the particle streak line (frame f). Particle resuspension due to impinging particles was never observed during the video recordings.

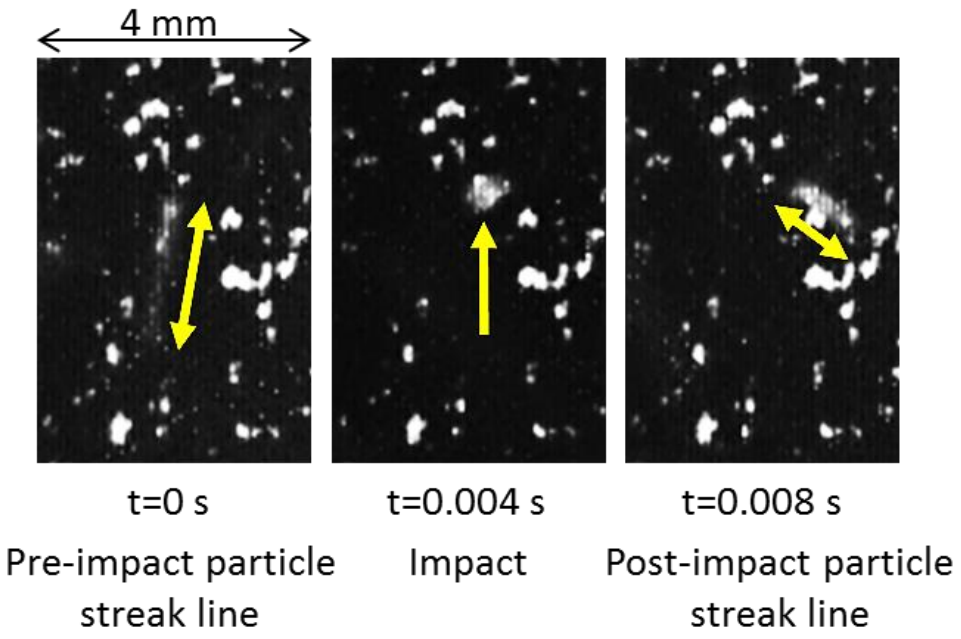

Figure 35. Evidence of an impact/rebound event captured during video recording.

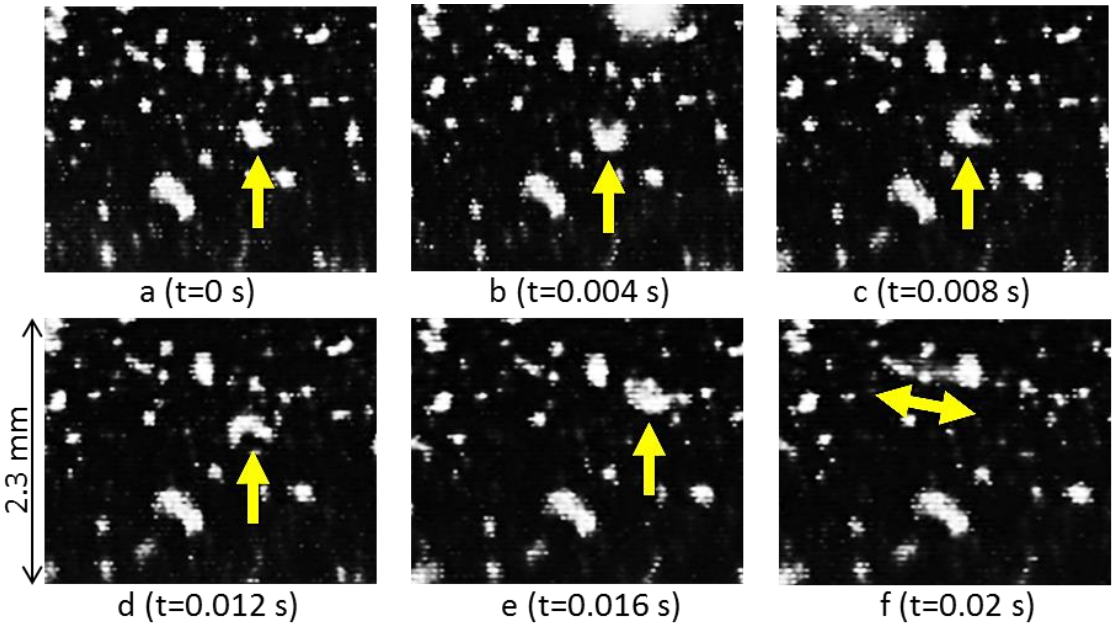

Figure 36. Evidence of a resuspension event captured during video recording. a): particle adhered on the wall surface; b)–e): the particle rotates clockwise and rolls; f) particle streak line after resuspension.

Analysis of frames captured at Q_{ms}=1 $m^3\ h^{-1}$ and at z=0.1 m from the nozzle, namely in the pre-impact zone of the duct, indicated that nearly 50% of particles hitting the wall surface adhered thereon, whereas the total fraction of particles transferred to the lean phase due to rebound and resuspension phenomena was estimated in the order of 0.5. The occurrence of rebound and

resuspension phenomena was therefore comparable. Resuspension phenomena were typically observed for larger particles and clusters of particles. Increasing z, the distance from the nozzle, namely z=0.15 m (impact zone, z nearly equal to z^*) and z=0.2 m (post-impact zone), the visual observations highlight that the frequency of particle–wall collisions and the occurrence of particle resuspension phenomena decrease. In particular, at z=0.15 m and z=0.2 m, the fraction of particle transferred back into the mainstream is 0.26 and 0.13, respectively. In particular, video recordings highlighted that the occurrence of rebound events sharply decreased with the distance from the nozzle. As a consequence, particles transfer back to the mainstream flow was mostly due to resuspension phenomena.

The phenomenology of particle–wall interactions can be analyzed in the light of the hydrodynamics of gas flow and particle trajectories outlined in Fig. 37.

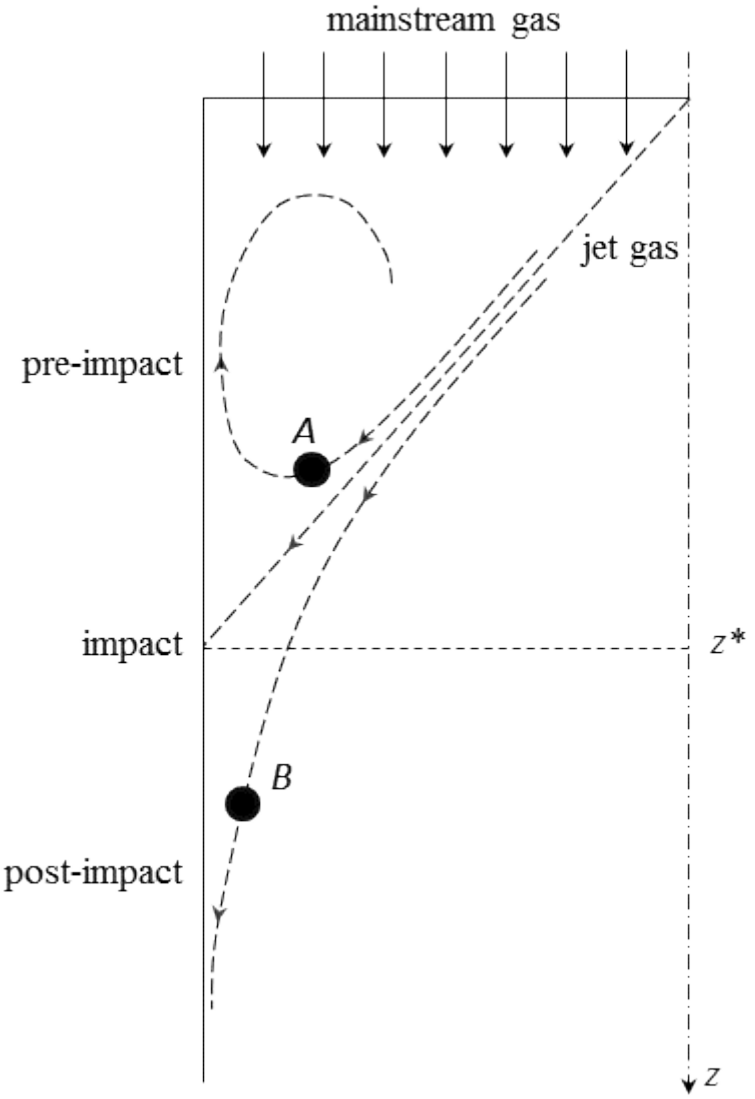

Figure 37. Hydrodynamic patterns induced by mainstream and jet gas flows and their influence on the particle trajectories.

The overall gas flow structure results from overlapping of the conical jet flow issuing from the nozzle and the parallel mainstream flow. The outer jet gives rise, upon interaction with the wall, to flow patterns resembling those of confined oblique stagnation flows *(Wang, 1985)*, with possible establishment of recirculation patterns. As atomized particles approach the reactor wall along jet trajectories, they may either be entrained in the vortical structure establishing in the pre-impact opposed flow region (particle *A*), or be swept into the mainstream gas flow (particle *B*) in the post-impact assisted flow region. The relative importance of the mainstream flow and of the oblique stagnation flow of the outer jet is determined by the ratio between the jet and mainstream gas flow rates, which rules the level of turbulence in the pre-impact, impact and post-impact regions. The oblique stagnation flow patterns prevail at small mainstream air flow rates, whereas they are suppressed at high mainstream air flow rates.

The vortical structure establishing close to the stagnation region ($z=z^*$) is relevant to particle resuspension, which can be assessed by calculation of the threshold gas velocity corresponding to particle detachment by lift-off, sliding or rolling, as described in the *Section 1.5*. The pull-off force is a function of the particle–surface thermodynamic work of adhesion, which was estimated, for wax particles on a Pyrex surface, as 0.346 kg s^{-2} *(Restagno et al., 2002; Drelich et al., 2004; Annapragada et al., 2007)*. Furthermore, the contact radius at separation is a function of the particle–surface composite Young's modulus, which is 4/3 GPa for wax particles on Pyrex surface *(Annapragada et al., 2007).*

Solving Eqs. (15), (16) and (17), the threshold velocities for lift-off, sliding and rolling were in the order of 56 m s^{-1}, 46 m s^{-1} and 1 m s^{-1}, respectively, for wax particle diameter d_p=100 μm. When these velocities are compared with peak gas velocities expected in the vicinity of the wall from the combination of mainstream and jet flow (≅4 m s^{-1}), it is concluded that lift-off and sliding are not likely to occur to any appreciable extent, while rolling is the dominant mechanism for particle detachment, in agreement with results from literature *(Ibrahim et al., 2003; Ibrahim et al., 2008)*. The effect of rolling might be further emphasized if one considers that burst-sweep events may occur in the viscous sublayer, causing occasional increase of the flow velocities *(Soltani and Ahmadi, 1994; Soltani and Ahmadi, 1995; Ziskind et al., 1995; Marchioli and Soldati, 2002)*. This phenomenon can facilitate re-suspension by lowering the detachment velocity by a factor of nearly 2. It is noteworthy that the jet velocity (≅4 m s^{-1}) near the wall at the impact zone ($z=z^*$) is larger than the threshold gas velocity for rolling, whereas the overall mean gas velocity (0.06 m s^{-1}) is smaller. This finding confirms that resuspension is mainly related to interference of the gas jet with the wall, which dominates the hydrodynamics under these operating conditions. Rebound is relevant in the pre-impact zone, due to high normal-to-wall component of velocity of the particles,

whereas it is strongly reduced in the post-impact zone where jet streamlines are deflected by the mainstream flow.

As discussed above, increasing the mainstream air flow rate suppresses the jet-induced turbulence and recirculation in the pre-impact and impact zones. This is confirmed by visual observation of wall interaction patterns as the mainstream air flow rate is increased to Q_{ms}=10 $m^3 h^{-1}$. The frequency of collisions at any z is only slightly smaller than that observed at Q_{ms}=1 $m^3 h^{-1}$. The fraction of particles transferred to the mainstream flow is 0.20, 0.28 and 0.08, at z=0.1 m, z=0.15 m and z=0.2 m, respectively. Under these operating conditions, particle transfer to the mainstream flow was largely due to the resuspension phenomenon, while only occasional rebound occurred. The comparison of these results with those observed at Q_{ms}=1 $m^3 h^{-1}$ further confirms the key role of the mainstream and oblique stagnation jet flows in the balance between deposition and resuspension phenomena that ultimately lead to near-wall particle segregation in entrained flow.

Furthermore, results obtained solving Eqs. (15), (16) and (17) show that the particle diameter significantly affects the rolling threshold velocity, resulting 2.7 m s^{-1} and 1.1 m s^{-1} for particle diameters of 10 μm and 100 μm, respectively - i.e. coarser particles require lower gas velocities to be detached from the surface, in agreement with the literature *(Ibrahim et al., 2003; Ibrahim et al., 2008; Goldasteh et al., 2013)* -.

The particle temperature also affects the rolling threshold velocity. As a matter of fact, for waxes, the elastic modulus sharply decreases with the temperature. From literature, the montan wax mechanical properties are similar to carnauba wax, for the last one the Young's modulus being 1.81 GPa and 0.77 GPa at 23°C and 37°C, respectively *(Craig et al., 1967; Annapragada et al., 2007)*. The threshold velocity for rolling mode increases from 0.8 m s^{-1} (at 23°C) to 1.1 m s^{-1} (at 37°C), stating that increasing temperature causes larger deformations and, hence, a larger contact area. This ends up into a greater adhesion moment and, thus, a larger threshold velocity.

3.3 Analysis of the Non Sticky Wall–Sticky Particle regime

In this section, the experimental results for the Non Sticky Wall–Sticky Particle (*NSW–SP)* regime are reported. The experimental tests aimed at characterizing the general phenomenology of the interaction between the dispersed phase generated by the spray and the reactor walls. The partitioning of the atomized wax between the dispersed and the wall phases was quantitatively assessed as a function of the distance from the nozzle. The experimental tests were carried out in the 0.1-m ID reactor and the main operating parameters are summarized and listed in Table 4. The flow rate of mainstream air, Q_{ms}, was treated as parameter for the purposes of evaluating and testing its effect on the phenomenology of interaction between the lean-dispersed phase and the wall layer. In particular, Q_{ms} ranged between 1 $m^3 h^{-1}$ and 10 $m^3 h^{-1}$ (at 273 K), with a reference

case of 1 $m^3 h^{-1}$, while Q_a was fixed at 0.275 $m^3 h^{-1}$ (at 273 K). The reactor length L varied in the 0.1–0.6 m range. Furthermore, the effect of the presence of a powdery layer on the wall on the partitioning of the wax between the two phases was investigated, and the results are reported and discussed hereinafter. The qualitative phenomenology of sticky particles/wall micromechanical interaction was assessed by careful analysis from close-up video recordings taken at the wall during the experiments.

3.3.1 Partitioning in the NSW–SP regime: effect of operating conditions

In the following figures, experimental data are reported as average values of multiple tests (symbols), together with error bars corresponding to the standard deviation. The effects of the mainstream air flow rate (Q_{ms}) and of the presence of a powdery layer on the partitioning of wax are reported and discussed hereinafter. The effect of Q_{ms} on y^{lean} at fixed $Q_a = 0.275$ $m^3 h^{-1}$ is shown in Fig. 38. y^{lean} decreases from nearly 0.8 in the proximity of the nozzle (L=0.1 m) to approach 0.13 for $L \geq 0.35$ m. It is possible to notice that the experimental data points are very close to the limiting curve for ideal *SW–SP* regime. This result suggests that the main micromechanical interaction pattern between a droplet and a dry wall is the deposition. Furthermore, Q_{ms} has a very slight effect on y^{lean} as in Fig. 38, and this is due to the high droplet inertia. As a matter of fact, in order to keep the molten status of the atomized wax, a slight overpressure was used for the wax feed, thus increasing the droplets size and inertia. It was not possible to investigate the effect of Q_a on y^{lean}, as an increasing atomization air flow rate would have reduced the droplets size, prejudicing the molten status of the droplets at the impact.

Figure 39 shows the effect of the roughness of the wall on the partitioning of wax between the two phases. In particular, the tests were carried out with a polished and dry wall and with the wall pre-covered with a layer of wax particles obtained in *NSW–NSP* conditions. The experiments aimed at simulating the impact of sticky particles on a dry wall or on a wall covered with non sticky particles (low carbon conversion). As depicted in Fig. 39, the presence of a solid layer does not affect the partitioning of the wax between the lean-dispersed phase and the wall layer. This outcome confirms that also in the presence of a rough surface, the main droplet-wall micromechanical interaction is the adhesion.

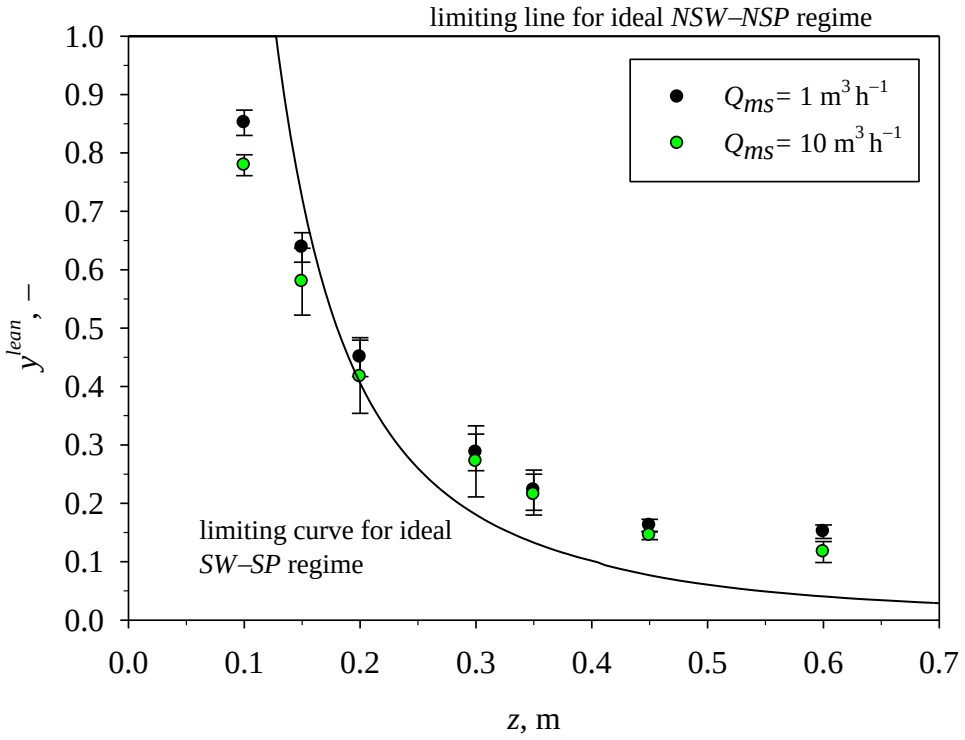

Figure 38. Effect of the mainstream air flow rate (Q_{ms}) on the axial profile of the fractional mass of wax in the dispersed phase (y^{lean}). Q_a=0.275 m^3 h^{-1}. The limiting curves representing the *NSW–NSP* and the *SW–SP* regimes are plotted as a reference.

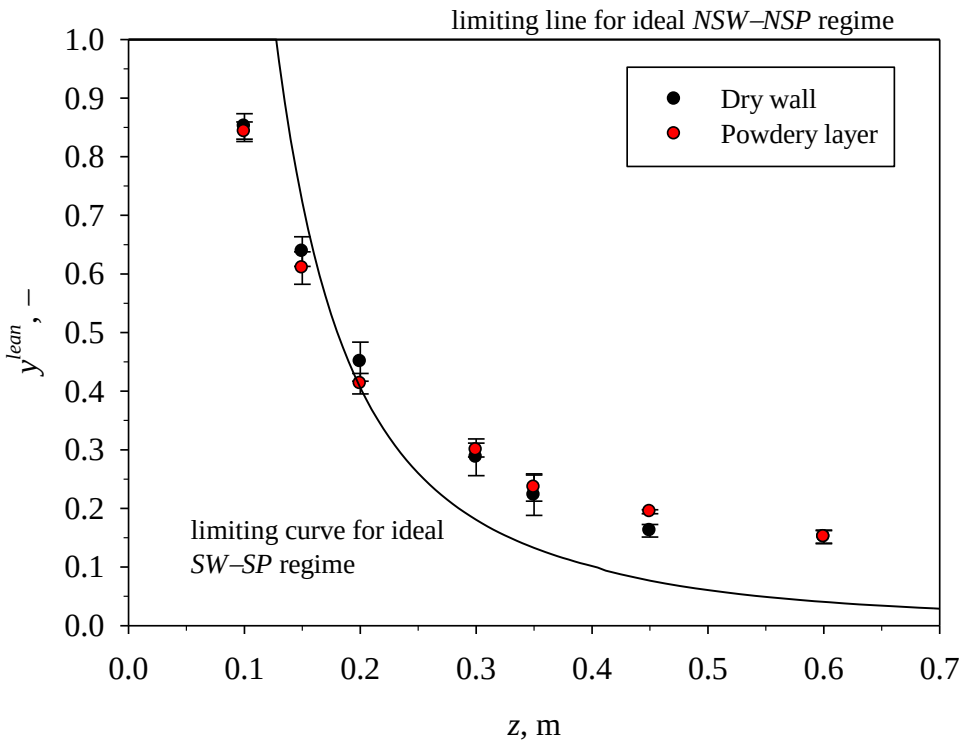

Figure 39. Effect of the roughness of the wall on the axial profile of the fractional mass of wax in the dispersed phase (y^{lean}). Q_a=0.275 m^3 h^{-1}, Q_{ms}=1 m^3 h^{-1}. The limiting curves representing the *NSW–NSP* and the *SW–SP* regimes are plotted as a reference.

3.3.2 *Phenomenology of non sticky wall–sticky particle micromechanical interaction and theoretical criteria of particle rebound and deposition*

The qualitative phenomenology of sticky particles/wall interactions was accomplished with close-up video recordings at the wall. The CCD camera (Photron Ultima APX) was located at three different levels, namely 0.1 m, 0.15 m and 0.2 m from the nozzle (denoted as pre-impact, impact and post-impact zone, respectively). Two mainstream gas flow rates (Q_{ms}=1 m^3 h^{-1} and Q_{ms}=10 m^3 h^{-1}) were investigated, while Q_a was fixed at 0.275 m^3 h^{-1}.

Analysis of video recordings enabled to track the fate of individual droplets. It was possible to see the phases of impact, spread and deposition, while no rebound occurred. Furthermore, the spreading phase was, in some events, accompanied by the phenomenon of fingering, which is the separation of a part of the liquid from the elliptical splat. The fingering is the result of an instability at the spreading edge of the splat, and it is typically unidirectional. Frames of a typical impact of a droplet with the spreading phase (top) and another impact for which fingering occurred (bottom) are reported in Fig. 40.

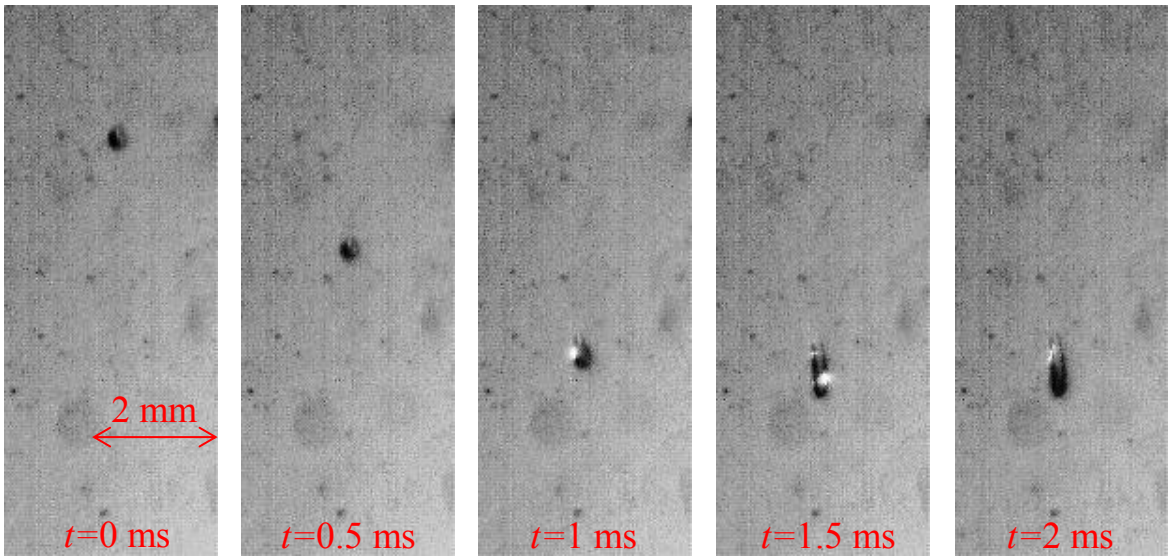

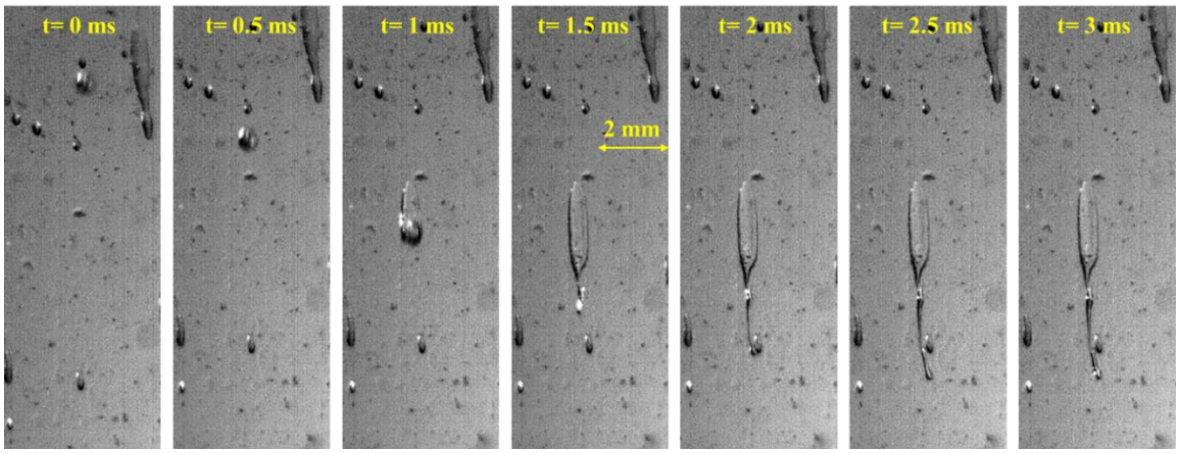

Figure 40. Evidence of an impact event captured during video recording. top): droplet impacted on the wall surface and adhered after spreading; bottom): droplet impacted on the wall surface and adhered after spreading and fingering.

Analysis of the frames allowed to determine the experimental spread factor, ξ for each tracked droplet. Figure 41 reports the spread factor ξ as a function of the Weber number We, for the two values of Q_{ms} at the three different distances from the nozzle (Figs. 41 a), b) and c)), while the atomization air flow rate was fixed at Q_a=0.275 $m^3\ h^{-1}$. ξ does not significantly vary with the axial coordinate of the reactor, and it is roughly the same value while varying Q_{ms}. Furthermore, ξ is about constant with the Weber number and it is $\xi = 1.8 \pm 0.05$. This outcome is in agreement with the results shown in Figs. 38 and 39. As a matter of fact, deposition is the main phenomenon for the *SW–NSP* regime, while varying the axial coordinate of the reactor, the mainstream air flow rate and Weber number (*We* ranging between 1 and 250).

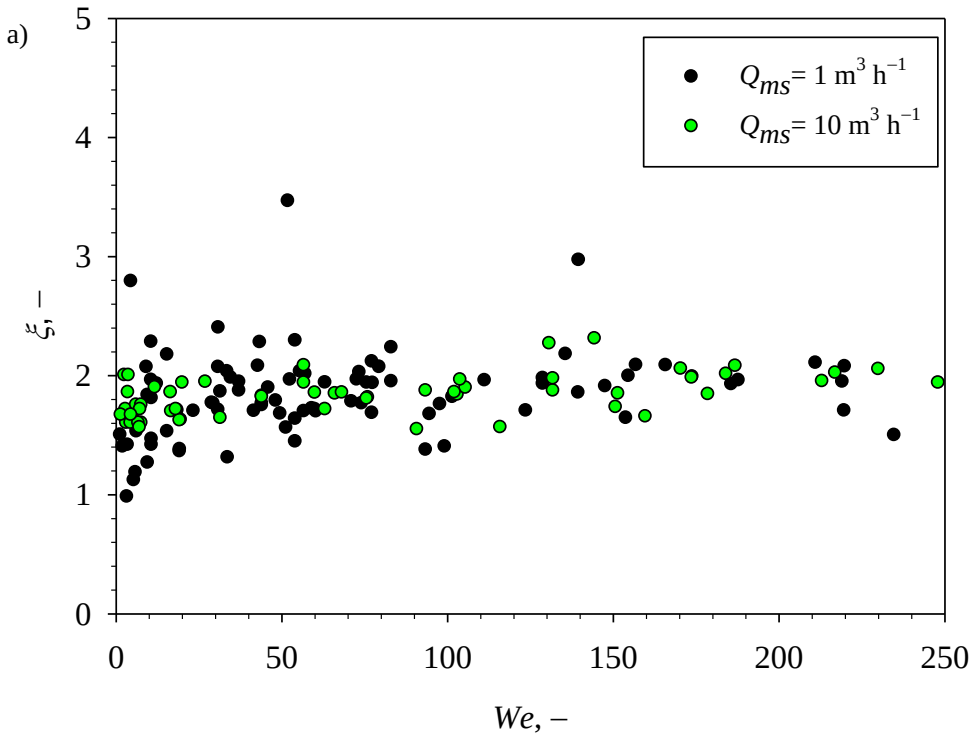
a)
Q_{ms}= 1 m^3 h^{-1}
Q_{ms}= 10 m^3 h^{-1}
ξ, –
We, –
0
1
2
3
4
5
0
50
100
150
200
250

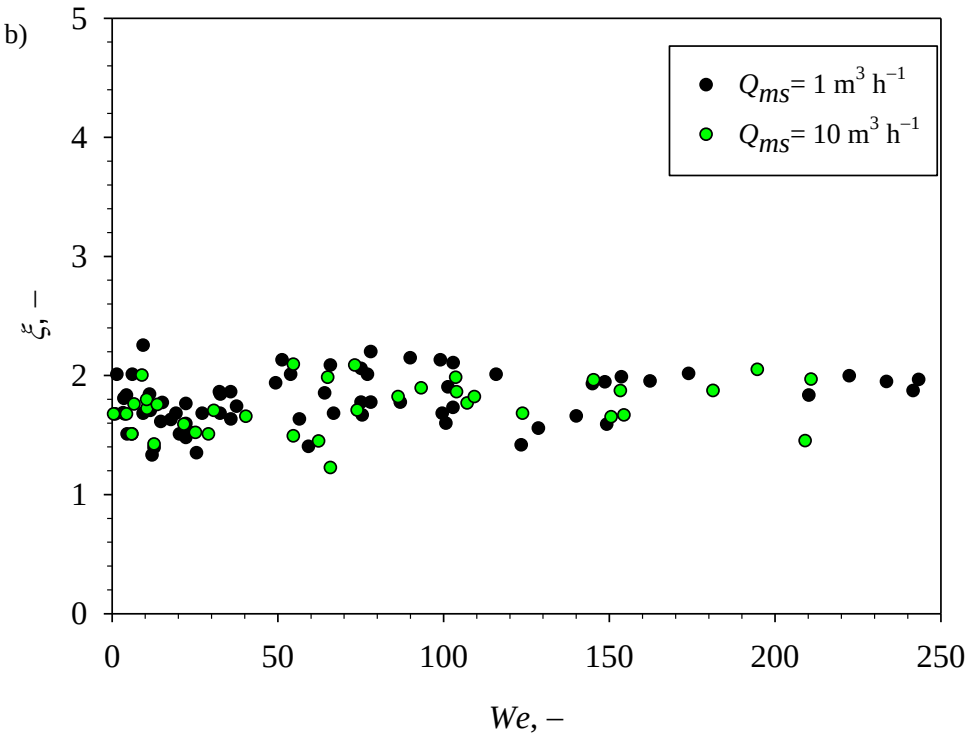
b)
Q_{ms}= 1 m^3 h^{-1}
Q_{ms}= 10 m^3 h^{-1}
ξ, –
We, –
0
1
2
3
4
5
0
50
100
150
200
250

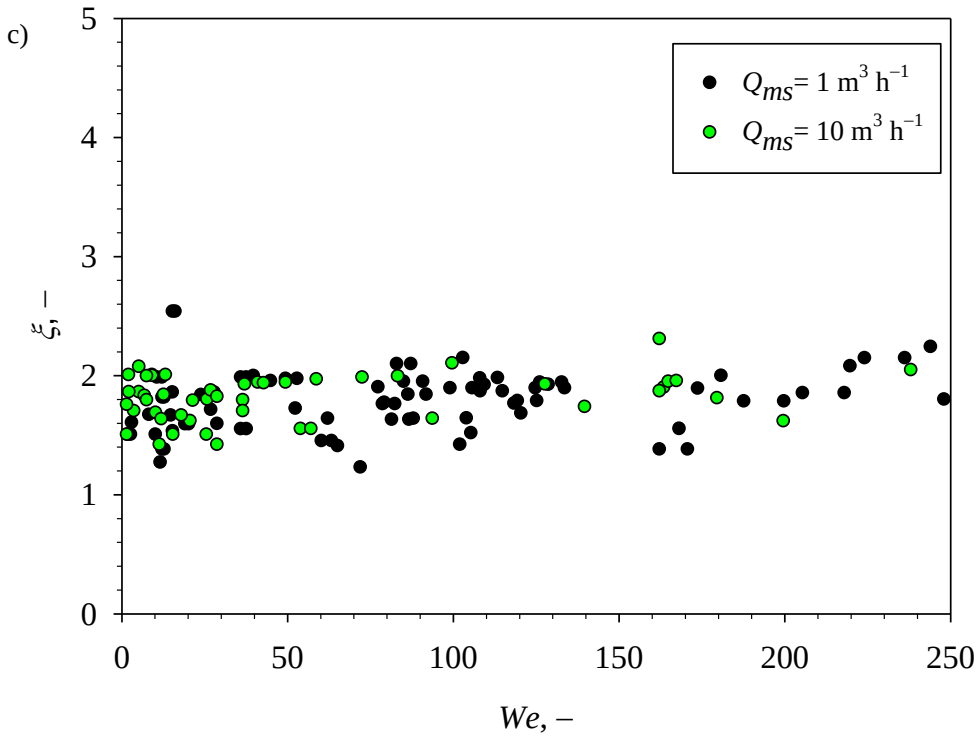

Figure 41. Effect of the mainstream air flow rate Q_{ms} on the spread factor, ξ, as a function of the Weber number, *We*, at three distances form the nozzle. Video recording taken at a) *z*=0.1 m from the nozzle; b) *z*=0.15 m from the nozzle; c) *z*=0.2 m from the nozzle.

The experimental data points of ξ were compared with the theoretical model described in *Section 1.5 (Mao et al., 1997)*. In the theoretical calculation of ξ, the droplet viscosity was set equal to $\mu_D = 0.02$ Pa s, while the contact angle was θ_c=85$\pm$2° and the effect of the solidification was negligible. Figures 42 a), b) and c) report the comparison of the values of the spread factor obtained by experimental test with those derived from the theory (Eq. 34). Theoretical and experimental values agree fairly well for each distance from the nozzle and for both the values of Q_{ms}. However, the experimental data points are about constant with the Weber number, whereas the theoretical values slightly increase with *We*. The difference may be due to the assumption, in the theoretical model, of a circular splat. As a matter of fact, the model was proposed for normal impacts. For oblique impacts, the splat can be better approximated by an ellipse. The equivalent elliptical-to-circular diameter was calculated to compare the experimental results with the theoretical model. Thus, the discrepancy between the experimental and theoretical values could be due to this correction of the spread factor. Furthermore, the video recording system did not allow to measure the impact angle for each droplet, while a constant value was used, equal to the jet aperture angle. A difference in the impact angle could lead to different impact velocity and, thus, to different spread factors.

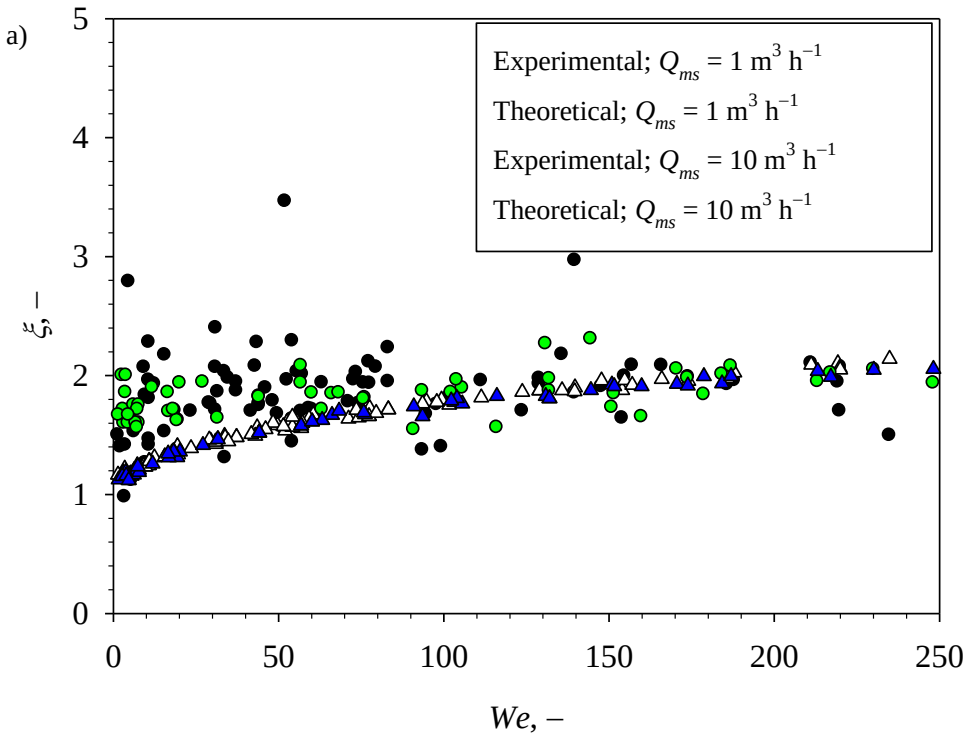
a)
Experimental; Q_{ms} = 1 m^3 h^{-1}
Theoretical; Q_{ms} = 1 m^3 h^{-1}
Experimental; Q_{ms} = 10 m^3 h^{-1}
Theoretical; Q_{ms} = 10 m^3 h^{-1}
ξ, –
0
1
2
3
4
5
0
50
100
150
200
250
We, –

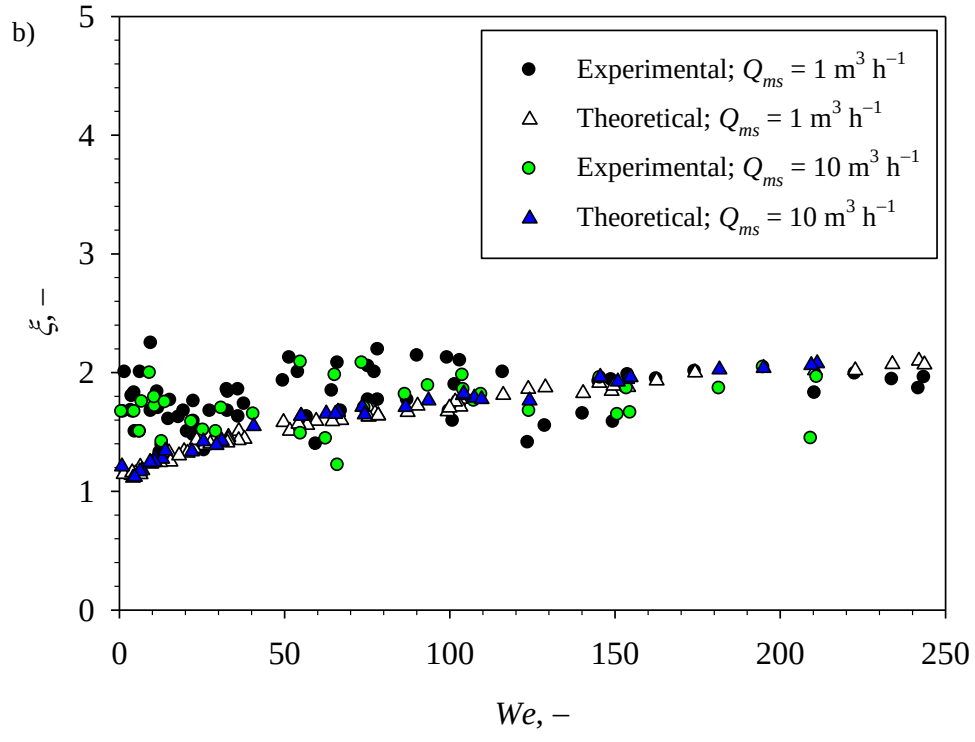
b)
Experimental; Q_{ms} = 1 m^3 h^{-1}
Theoretical; Q_{ms} = 1 m^3 h^{-1}
Experimental; Q_{ms} = 10 m^3 h^{-1}
Theoretical; Q_{ms} = 10 m^3 h^{-1}
ξ, –
0
1
2
3
4
5
0
50
100
150
200
250
We, –

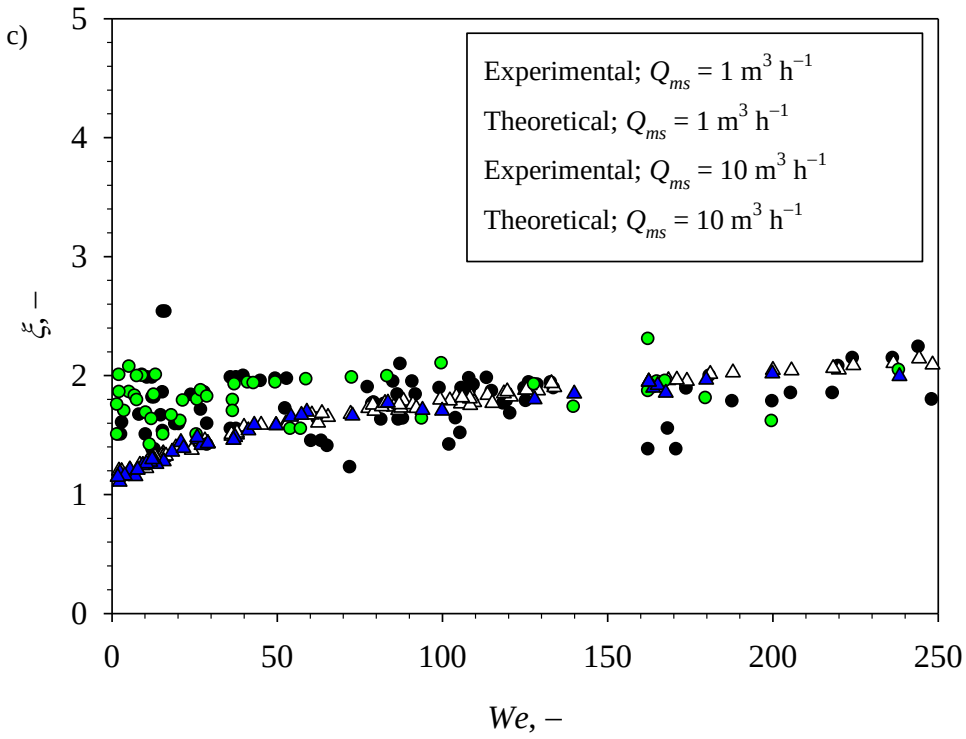

Figure 42. Comparison of experimental and theoretical results. Effect of the mainstream air flow rate Q_{ms} on the spread factor, ξ, as a function of the Weber number, *We*, at three distances form the nozzle. Video recording taken at a) z=0.1 m from the nozzle; b) z=0.15 m from the nozzle; c) z=0.2 m from the nozzle.

The experimental values of the spread factor were also used to evaluate the tendency of a droplet to rebound upon the impact, in terms of the excess rebound energy *ERE*, defined in *Section 1.5* (Eq. (39)). Figures 43 a), b) and c) report the trend of the excess rebound energy, as a function of the initial droplet diameter D_0, for the two values of Q_{ms} (1 m^3 h^{-1} and 10 m^3 h^{-1}) and for the three distances from the nozzle (z=0.1 m, 0.15 m and 0.2 m). For each case the experimental values of *ERE* are smaller than 0 for D_0 ranging between 120 μm and 480 μm. This outcome (*ERE* <0) confirms that adhesion is the phenomenon which characterizes this kind of particle–wall interaction, in agreement with the results obtained by visual observation and partitioning tests (Figs. 38–39).

a)

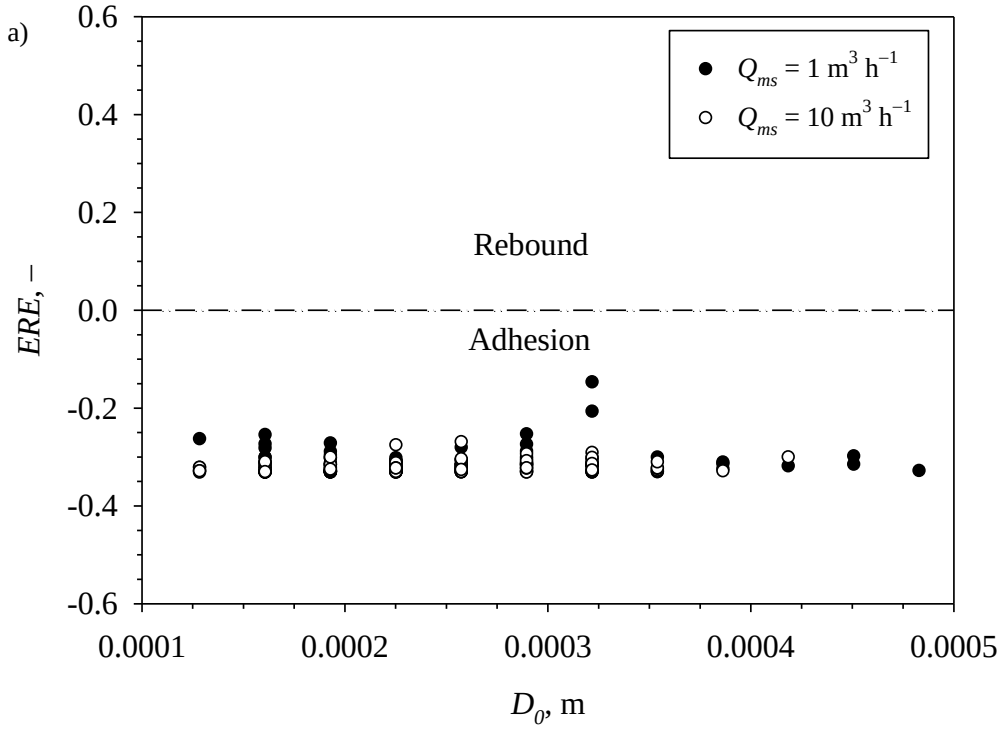
0.6
0.4
0.2
0.0
-0.2
-0.4
-0.6
ERE, –
Rebound
Adhesion
Qms = 1 m3 h–1
Qms = 10 m3 h–1
0.0001
0.0002
0.0003
0.0004
0.0005
D0, m

b)

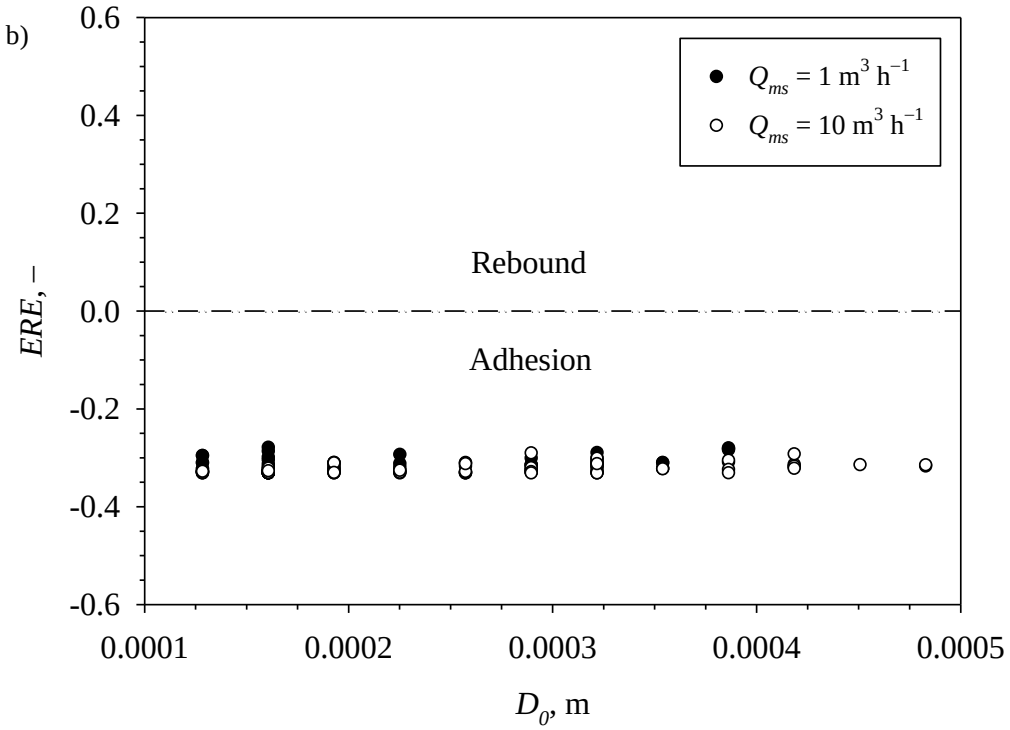
0.6
0.4
0.2
0.0
-0.2
-0.4
-0.6
ERE, –
Rebound
Adhesion
Qms = 1 m3 h–1
Qms = 10 m3 h–1
0.0001
0.0002
0.0003
0.0004
0.0005
D0, m

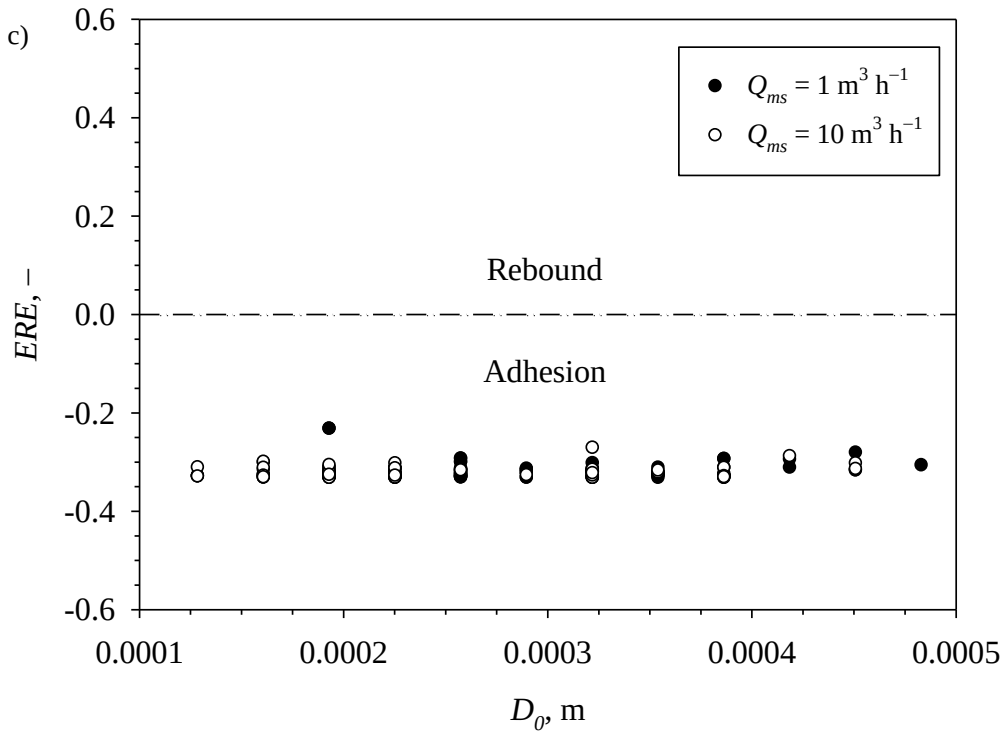

Figure 43. Excess Rebound Energy, *ERE* versus the initial droplet diameter, D_0. Effect of the mainstream air flow rate Q_{ms} at three distances form the nozzle. a): video recording taken at z=0.1 m from the nozzle; b) video recording taken at z=0.15 m from the nozzle; c) video recording taken at z=0.2 m from the nozzle.

Ni et al. (2011) used the model proposed by *Mao et al. (1997)* to predict the slag–wall interaction in entrained-flow slagging gasifiers. Results obtained by the experimental tests with wax can be compared with those obtained by *Ni et al. (2011)*. Physical properties of wax and Shenfu coal slag are reported in Table 8.

Table 8. Physical properties of wax Waradur E and Shenfu coal slag.

	Waradur E wax	**Shenfu coal slag**
ρ_D (kg m^{-3})	1000	2715
μ_D (Pa s)	0.02 (at 110°C)	0.65 (at 1500°C)
γ (N m^{-1})	0.029	0.4
θ_c (°)	85	56

Figures 44 a), b) and c) report the comparison of the *ERE* as a function of D_0 for the wax and the Shenfu coal slag, at three different impact velocities: v_i =1.5 m s^{-1}, 3 m s^{-1}, 4.5 m s^{-1}, respectively.

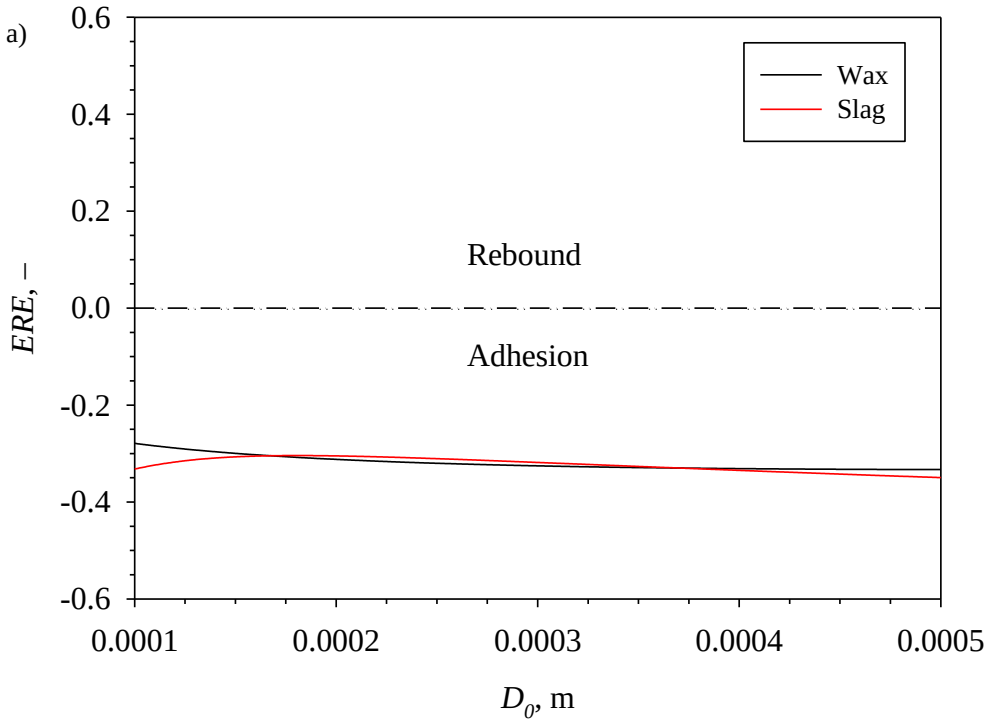
a)
0.6
0.4
0.2
0.0
-0.2
-0.4
-0.6
ERE, –
Wax
Slag
Rebound
Adhesion
0.0001
0.0002
0.0003
0.0004
0.0005
D0, m

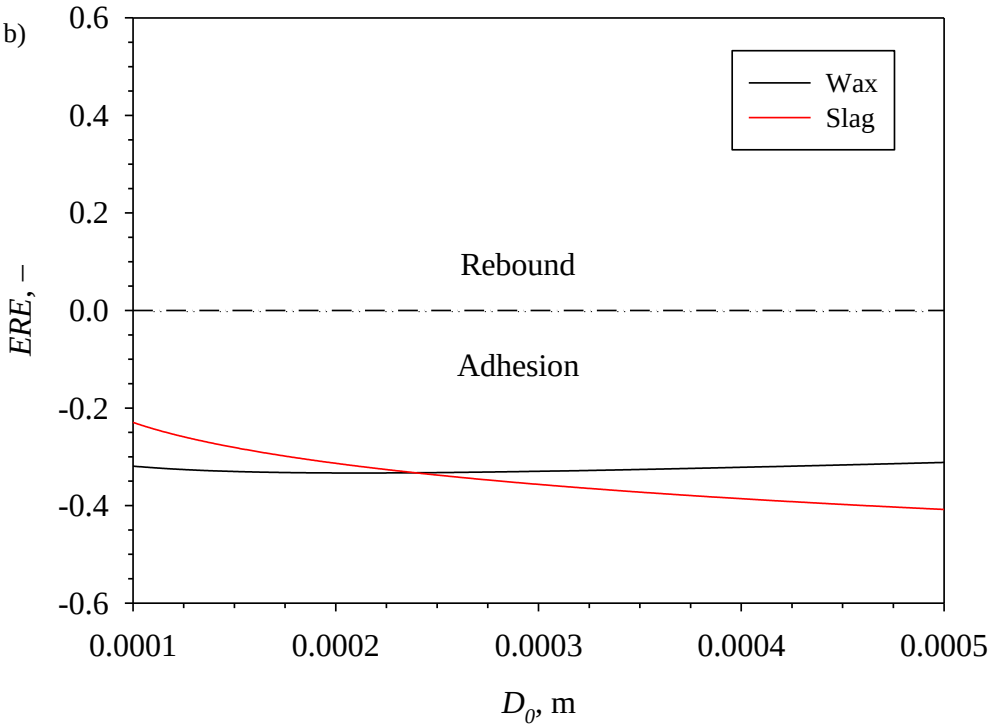
b)
0.6
0.4
0.2
0.0
-0.2
-0.4
-0.6
ERE, –
Wax
Slag
Rebound
Adhesion
0.0001
0.0002
0.0003
0.0004
0.0005
D0, m

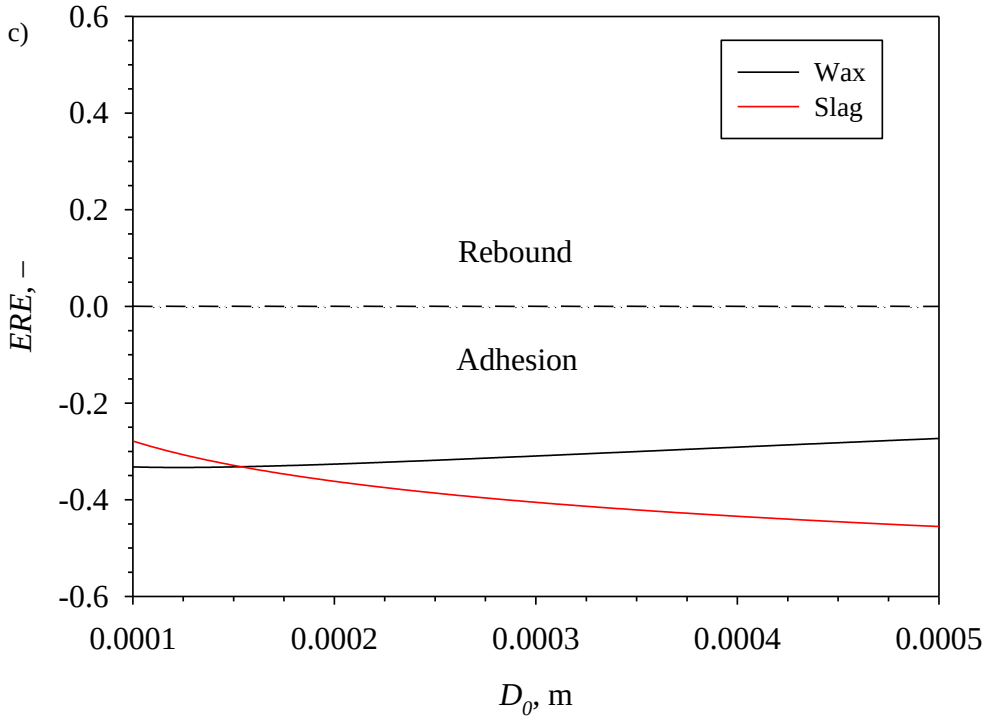

Figure 44. Excess Rebound Energy, *ERE* versus the initial droplet diameter, D_0. Comparison of results for wax and Shenfu coal slag droplets at three different impact velocities. a): v_i=1.5 m s^{-1}; b) v_i =3 m s^{-1}; c) v_i 4.5 m s^{-1}.

It is possible to notice that for each case the excess rebound energy *ERE* is lower than 0 for both wax and slag droplets at the three different impact velocities. From a qualitative point of view, the curves obtained for the wax and the slag are different. The reason lies in the different contact angle, i.e. the wettability, between the droplets and the wall, which is fairly poor for wax droplets on Pyrex, while it is very good for the slag on the refractory wall. Finally, it is possible to conclude that both wax and slag droplets adhere on the surface without rebound (*ERE* <0), and that wax mimics very well the build-up of the slag layer on the walls of the gasifier.

3.4 Analysis of the Sticky Wall–Non Sticky Particle regime

In this section, the experimental results for the Sticky Wall–Non Sticky Particle (*SW–NSP)* regime are reported. Experimental tests aimed at characterizing the general phenomenology of the interaction between the dispersed phase generated by the spray and the reactor walls. The partitioning of the atomized wax between the dispersed and the wall phases was quantitatively assessed as a function of the distance from the nozzle. Experimental tests were carried out in the 0.1-m ID reactor and the main operating parameters are summarized and listed in Table 4. The flow rate of mainstream air, Q_{ms} was treated as parameter for the purposes of evaluating and testing its effect on the phenomenology of interaction between the lean-dispersed phase and the wall layer. In

particular, Q_{ms} ranged between 2 $m^3 h^{-1}$ and 10 $m^3 h^{-1}$ (at 273 K) with a reference case of 2 $m^3 h^{-1}$, while Q_a was fixed at 0.5 $m^3 h^{-1}$ (at 273 K). The reactor length L varied in the 0.15–0.6 m range. The qualitative phenomenology of non sticky particles–sticky wall micromechanical interaction was assessed by careful analysis from close-up video recordings taken at the wall during the experiments.

3.4.1 Partitioning in the SW–NSP regime: effect of operating conditions

In the following figures, the experimental data are reported as average values of multiple tests (symbols), together with error bars corresponding to the standard deviation. The effect of the mainstream air flow rate (Q_{ms}) on the partitioning of wax is reported and discussed hereinafter. The influence of Q_{ms} on y^{lean} at fixed Q_a =0.5 $m^3 h^{-1}$ is shown in Fig. 45. The curve at Q_{ms} =2 $m^3 h^{-1}$ reports that y^{lean} decreases from nearly 0.7 to approach 0.17 for L≥0.35 m, while at Q_{ms} =10 $m^3 h^{-1}$, y^{lean} decreases from nearly 0.55 to approach 0.18 for L≥0.35 m. It is possible to compare the experimental data points with those obtained when testing in the other regimes. The partitioning of the atomized wax between the dispersed and the wall phases as a function of the distance from the nozzle is reported in Fig. 46 for all the interaction regimes, at fixed Q_{ms} (1 $m^3 h^{-1}$ for *SW–SP*, *NSW–SP* and *NSW–NSP* regimes, 2 $m^3 h^{-1}$ for the *SW–NSP* regime). It is possible to notice that y^{lean} reaches maximum values for the *NSW–NSP* regime, minimum values for the *SW–SP* regime, while its values in the *SW–NSP* regime lie between those for the *NSW–NSP* and *NSW–SP* regimes, as expected. As a matter of fact, the interaction of a non sticky particle with a liquid layer can lead to segregation and segregation–coverage regimes. Therefore, the fractional content of wax in the lean-dispersed phase is lower than that obtained in the *NSW–NSP* regime. On the other hand, the interaction of the particles with the liquid layer and with other particles makes the fractional content of wax in the lean phase larger than that obtained for the *NSW–SP* and *SW–SP* regimes, for which the main interaction pattern is the deposition.

Figure 47 reports the partitioning of the atomized wax between the dispersed and the wall phases, as a function of the distance from the nozzle for the *NSW–SP*, *NSW–NSP* and *SW–NSP* regimes, at fixed Q_{ms}=10 $m^3 h^{-1}$. The values of y^{lean} are lower for all the investigated regimes (compared to the results shown in Fig. 46). Data points obtained in the *SW–NSP* regime are very close to those obtained in the *NSW–SP* regime. It is possible to conclude that larger mainstream air flow rates reduce the fractional content of wax in the dispersed phase, enhancing particle deposition/segregation phenomena, as highlighted and discussed previously, for the *NSW–NSP* regime (*Section 3.3.1*).

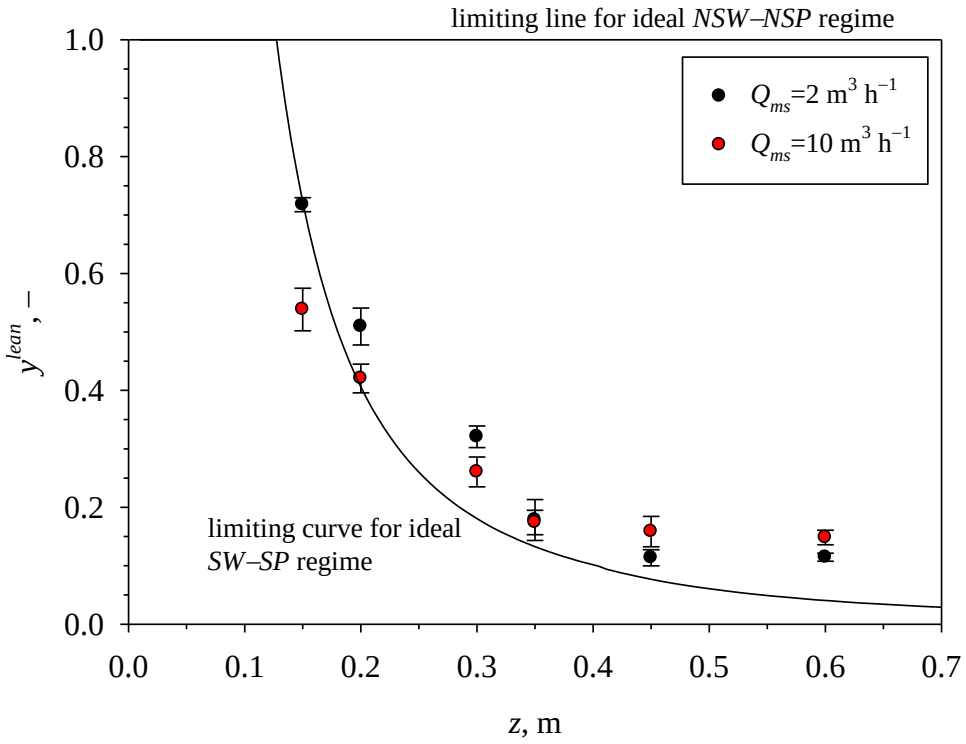

Figure 45. Effect of the mainstream air flow rate (Q_{ms}) on the axial profile of the fractional mass of wax in the dispersed phase (y^{lean}). Q_a=0.5 m^3 h^{-1}. The limiting curves representing the *NSW–NSP* and the *SW–SP* regimes are plotted as a reference.

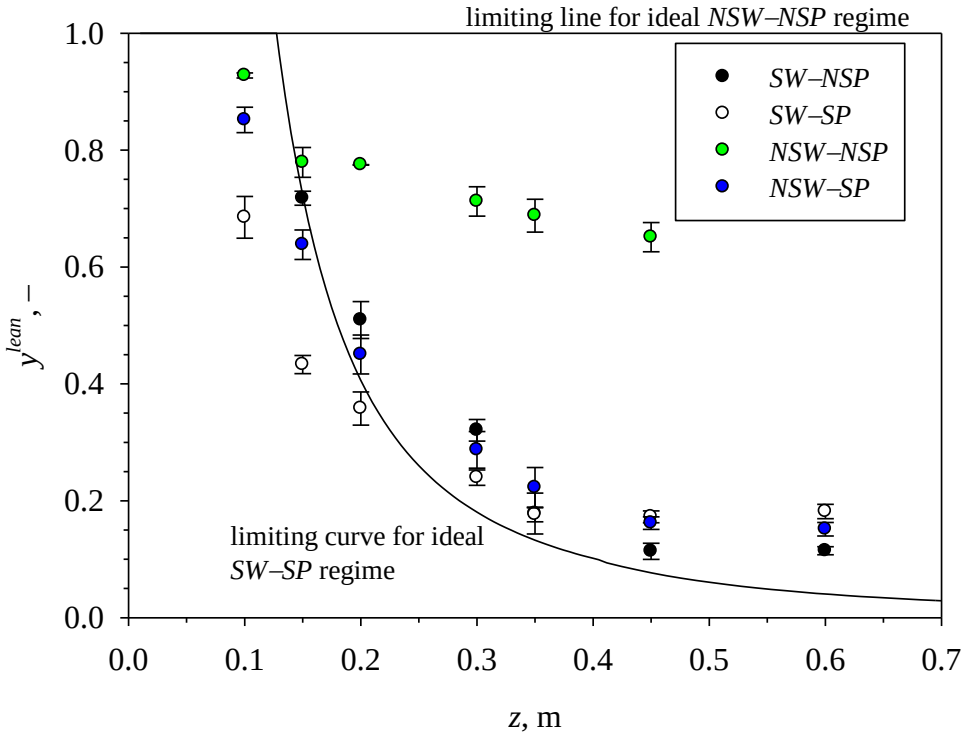

Figure 46. Partitioning of wax for all the interaction regimes. Q_{ms}=1–2 m^3 h^{-1}. The limiting curves representing the *NSW–NSP* and the *SW–SP* regimes are plotted as a reference.

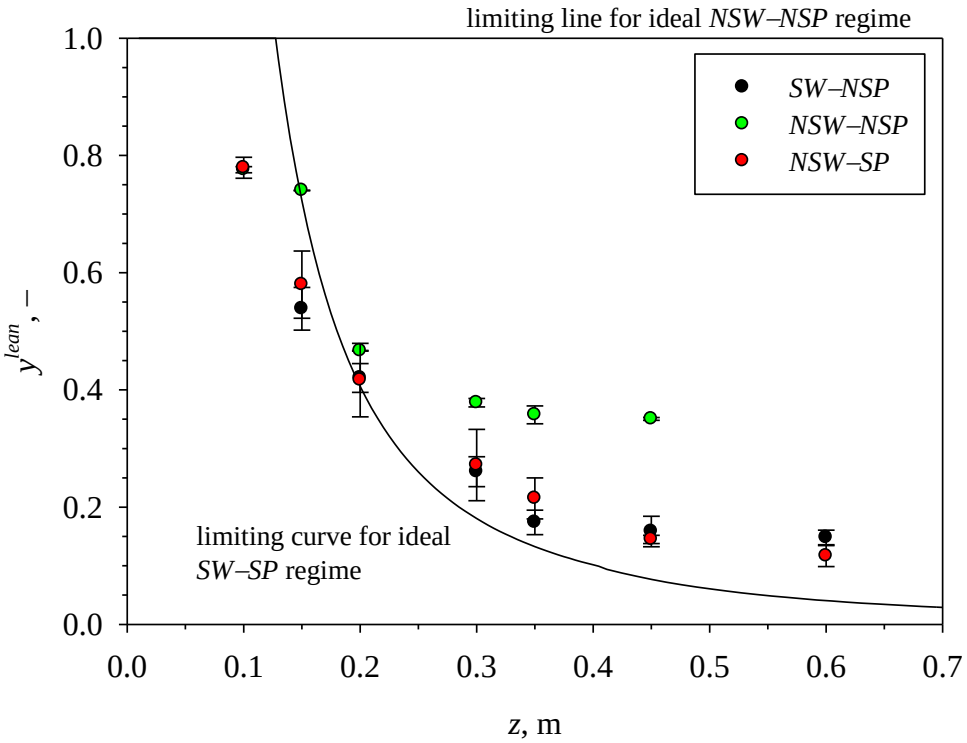

Figure 47. Partitioning of wax for all the interaction regimes. Q_{ms} =10 m^3 h^{-1}. The limiting curves representing the *NSW–NSP* and the *SW–SP* regimes are plotted as a reference.

3.4.2 Phenomenology of sticky wall–non sticky particle micromechanical interaction

The qualitative phenomenology of non sticky particles–sticky wall interactions was accomplished with close-up video recordings at the wall. The CCD camera (Photron Ultima APX) was located at 0.45 m from the nozzle at two radial positions (approximately at the center of the tube and at 0.001 m from the wall, respectively). The effect of the mainstream gas flow rate (Q_{ms}=2 m^3 h^{-1} and Q_{ms}=10 m^3 h^{-1}) was investigated (Reynolds number around 560 and 2350, respectively), while Q_a was fixed at 0.5 m^3 h^{-1}.

Analysis of video recordings enabled to visualize the descending liquid layer and to track the fate of individual particles at the exhaust of the duct in the near-wall region and at the center of the duct. As example, some frames of a typical particle (d_p=100 μm) moving in proximity of the liquid layer and leaving the duct are shown in Fig. 48. Furthermore, the figure shows a portion of the liquid layer about ready to drop from the reactor.

Image analysis and particle tracking techniques enabled to measure the particle velocity for each location and operating condition. In particular, video recordings taken at the near-wall region showed that the particle trajectories were streak lines in the axial direction. On the other hand,

particle trajectories and velocities at the centre of the tube were calculated as the sum of the measured axial and radial components. The imaging system did not allow to measure the particles tangential velocity.

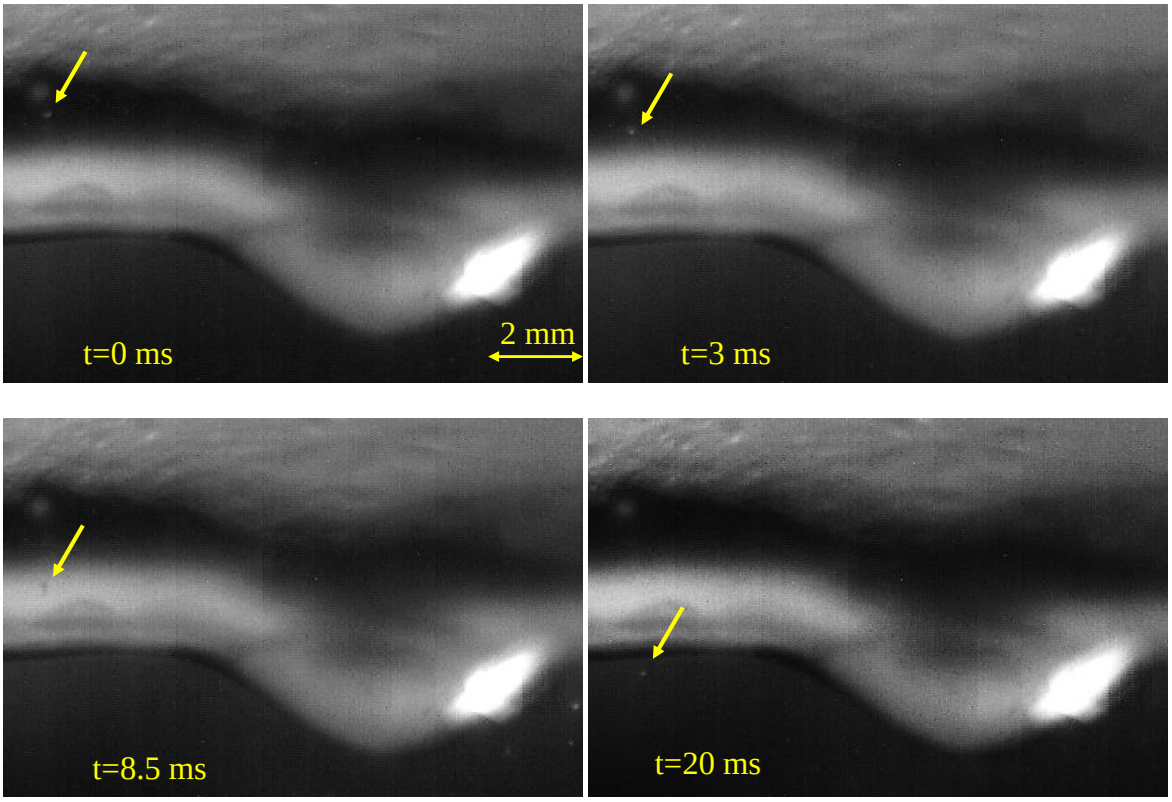

Figure 48. Evidence of a particle moving in proximity of the liquid layer in the near-wall region (0.001 m distant from the wall) and exiting the duct captured during video recording.

Figure 49 shows the cumulative particle velocity distribution obtained at the two radial positions (0.001 m distant from the wall and at the center of the duct) and for two values of the mainstream air flow rate, Q_{ms}=2 m^3 h^{-1} and Q_{ms}=10 m^3 h^{-1} (Figs. 49 a) and b)). The particle velocity distributions are reported as a function of the relative particle–gas velocity (v–u). For each radial position, gas velocity was calculated from the theoretical laminar profile in pipes when Q_{ms}=2 m^3 h^{-1}, while for Q_{ms}=10 m^3 h^{-1} the 1/7th-*power velocity-distribution law* was used *(Schlichting and Gersten, 2000)*. The solid line in Figs. 49 a) and b) represents the terminal particle velocity for the particles mean size (d_p=100 μm), which corresponds to the particle–gas relative velocity for a dilute solid–gas phase. Figure 49 a) shows that, at Q_{ms}=2 m^3 h^{-1}, regardless of the radial position, more than 60% of the particles are characterized by a velocity lower than the terminal particle velocity. Moreover, the two cumulative distributions, measured under laminar conditions, are quite sharp around the terminal velocity These results indicate that particles follow the gaseous streamlines as expected in dilute particle-laden flows. The cumulative distributions

measured in the near-wall region and at the center of the duct for Q_{ms}=10 $m^3 h^{-1}$ are reported in Fig. 49 b). At the center of the duct, the particle–gas relative velocity corresponding to 50% is very close to the terminal particle velocity, indicating that particles follow the gaseous streamlines as expected in dilute particle-laden flows, although the cumulative distribution appears much broader than that obtained under laminar conditions (Fig. 49 a)), as a consequence of gas velocity fluctuations (*Re*≈2350). On the other hand, in the near-wall region, the relative particle–gas velocity is much smaller than the terminal velocity. Furthermore, more than 70% of the particles show a negative relative particle–gas velocity, indicating that particles are slower than the gas flow. These results highlight that the particle flow pattern at near-wall region is deeply influenced by the gas flow, which induces particle segregation and accumulation phenomena, under transitional turbulent conditions. As a consequence, the tendency to reach a segregation–coverage regime with the formation of a dense-dispersed phase in the near-wall region of the reactor is enhanced. Furthermore, these results are in good agreement with those obtained during the partitioning tests reported and discussed in *Section 3.4.1*.

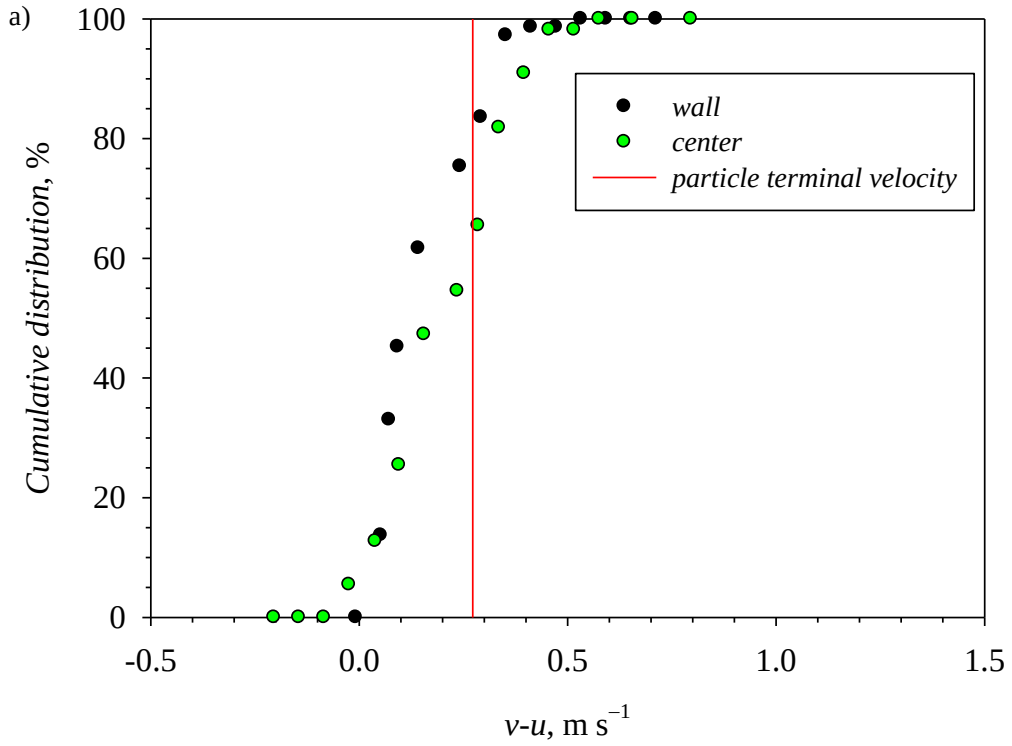

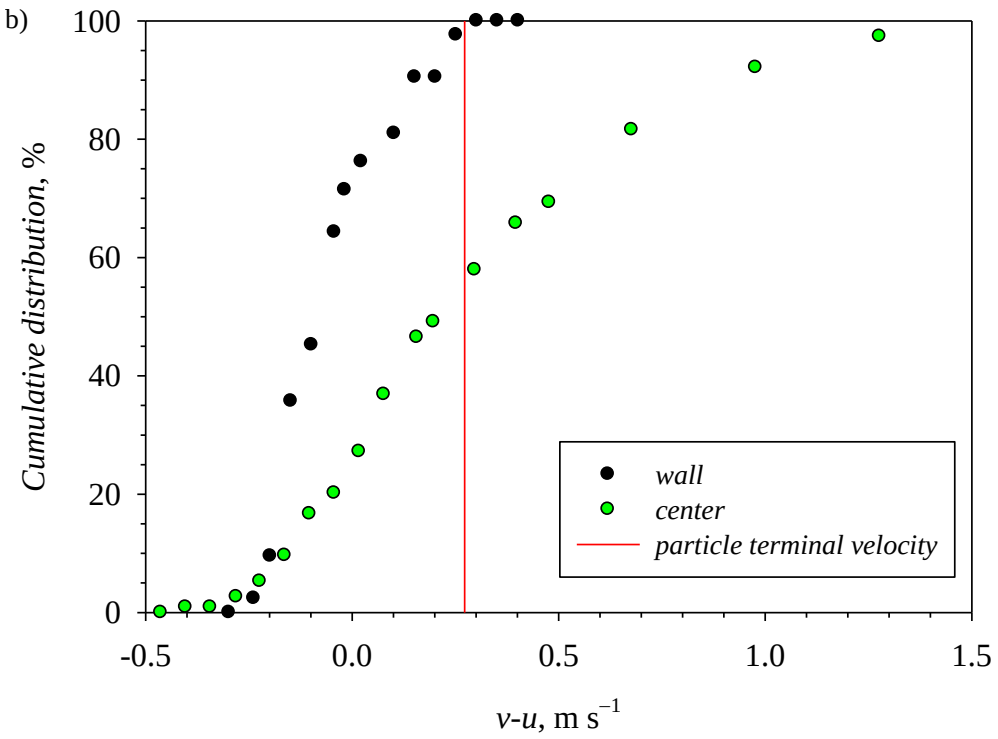

Figure 49. Effect of the mainstream air flow rate (Q_{ms}) on the particle velocity distribution for two radial positions (at the center of the tube and 0.001 m distant from the wall) as a function of the particle–gas relative velocity. a) Q_{ms} =2 m^3 h^{-1}; b) Q_{ms} =10 m^3 h^{-1}. Q_a =0.5 m^3 h^{-1}. The solid line represents the particle terminal velocity.

3.5 General comments on the four investigated regimes

An investigation of near-wall segregation phenomena in entrained-flow slagging gasifiers was accomplished with a lab-scale cold entrained-flow reactor (see Fig. 13), which allowed to study the general phenomenology of the interaction between the dispersed phase generated by the spray and the reactor walls. The four particle–wall interaction regimes were investigated, on the basis of the stickiness of the wall layer and of the impinging char particle (namely *sticky wall–sticky particle*, *non sticky wall–non sticky particle*, *non sticky wall–sticky particle* and *sticky wall–non sticky particle* regimes).

The experimental results included: *(a)* the quantitative assessment of the partitioning of atomized wax between the wall layer and the lean-dispersed phase entrained in the mainstream; *(b)* the qualitative and quantitative assessment of the micromechanical interaction between impinging wax particles and the wall. The first goal was pursued by selective collection of entrained wax at the exit of the Pyrex duct, the second by careful analysis of multiple events from close-up video recordings taken at the wall during the experiments. The partitioning of the atomized wax between the dispersed and the wall phases was quantitatively assessed as a function of the distance from the nozzle. The flow rate of mainstream air, Q_{ms}, and the flow rate of atomization air, Q_a, were treated

as parameters for the purposes of exploring, evaluating and testing their effect on the phenomenology of interaction between the lean-dispersed phase and the wall layer.

Results showed that the particle–wall interaction mechanisms and segregation patterns are deeply affected by the stickiness of both the wall layer and the impinging particle. In particular, in the *SW–SP* and *NSW–SP* regimes, the experimental trends of the fractional mass of wax in the lean-dispersed phase, y^{lean}, are very close to the *SW–SP* regime limiting curve. These results indicated that sticky particles mainly adhere on the wall surface, regardless the stickiness of the wall. A careful analysis of multiple events from close-up video recordings taken at the wall during the experiments in the *SW–SP* and *NSW–SP* regimes also confirmed the deposition as the main micromechanical droplet/wall interaction pattern. On the other hand, non sticky particles may rebound, deposit and be resuspended into the main flow upon the impact on a dry wall, depending also from the local hydrodynamic conditions. The mainstream gas flow rate exerted a remarkable influence on the extent of the wax deposition. In particular, the wax fractional content in the lean-dispersed phase decreased as the mainstream flow rate increased. This somewhat unexpected result was explained by considering the interaction between the mainstream flow and the oblique stagnation flow typical of the outer jet. Increasing the mainstream rate moderates the stagnation effects and suppresses the local turbulence which is largely responsible for particle resuspension, thus favoring the stratification and segregation of particles in the near-wall region of the duct. This hypothesis is confirmed by close-up observation of particle–wall interaction patterns. A simple analysis of particle resuspension suggests that lift-off and sliding are not relevant to particle resuspension, whereas the rolling mechanism may be active under the experimental conditions tested even for the finer particles, and be responsible for resuspension when a strong jet–wall interference takes place. Finally, as regards the interaction of non sticky particles with a sticky wall, the partitioning results lie between those obtained for the other regimes. Moreover, from a phenomenological point of view, particles follow the gaseous streamlines at the center of the duct, as expected in dilute particle-laden flows. On the other hand, the particle flow pattern in the near-wall region is deeply influenced by the gas flow. In particular, increasing the mainstream air flow rate induces particle segregation and accumulation phenomena. Furthermore, the micromechanical interaction of a particle with a sticky wall enhances particle transport to the wall and the tendency to reach a segregation–coverage regime with the formation of a dense-dispersed phase in the near-wall region of the reactor.

Chapter 4. Micromechanical investigation of particle-wall interactions: results and discussion

In this section, the results on the micromechanical particle–wall interactions are reported and discussed. The experimental tests were carried out using the apparatus depicted in Fig. 17. The operating conditions are summarized and reported in Table 5. The experimental results included: *i)* the restitution coefficients of wax particles colliding against the target surface in the *NSW–NSP* regime (operated at 20°C), while varying the impact velocity (from 0.5 to 3 m s^{-1}) and angle (from 10° to 90°) and for different target materials and surface structures *(Section 4.1)*; *ii)* the restitution coefficients and capture efficiencies of wax particles colliding against the Pyrex target during the transition from the *NSW–NSP* to the *NSW–SP* regime, while varying the particle impact temperature (from 20° to 110°C) whereas the impact velocity and angle were kept at 2 m s^{-1} and 84°, respectively *(Section 4.2)*; *iii)* the capture efficiency of wax droplets colliding against the Pyrex target in the *NSW–SP* regime (operated at 120°C), while varying the impact velocity (from 0.7 to 5 m s^{-1}) and angle (from 15° to 90°) *(Section 4.3)*. The experimental data for the coefficients of restitution are reported as values averaged over multiple tests (symbols). Error bars corresponding to the standard error are also reported. In order to ensure experimental reproducibility, each point is the average of at least 50 measurements.

4.1 Rebound characteristics in the NSW–NSP regime

The effect of the impact angle α_i on the restitution coefficients is reported in Fig. 50, for wax particles in the size range 75 ± 10 μm with a normal impact velocity, $v_{n.i}$, of 1 ± 0.1 m s^{-1}. The experimental data points show a slight effect of the impact angle on the normal restitution coefficient. The largest value was obtained at small impact angle (ε_n around 0.41 when α_i=35°), while the smallest value corresponds to near-normal impact angle (ε_n around 0.28). These values indicate that the rebound behaviour is plastic, as the restitution coefficients are well below 1. The effect of the impact angle on ε_n has been discussed in several studies. *Broom (1979)* found a 5–10% increase of the normal coefficient of restitution while varying the impact angle from 0° to 45° for the impact of 11-μm glass particles on an aluminium surface. However, for finer glass particles, 8.6 and 4.7 μm, the trend was opposite. Other researchers *(Gorham and Kharaz, 2000; Brauer, 1980)* concluded that ε_n is nearly constant over the full range of impact angles tested, $0°<\alpha_i<90°$. *Sommerfeld and Huber* (1999) reported that the normal coefficient of restitution is larger for small impact angles, while it approaches an almost constant value for large angles. This effect may be caused by a slight non-sphericity of the particles and, probably, by some residual wavy structures on the wall. In the present work, it is likely that ε_n is about constant with α_i if the hydrodynamic

effect of the air flow is taken into account. The air flow rate used to impact particles ($v_{n,i}$=1 m s^{-1}) at small impact angles was around 4-times larger than that used for normal impacts tests. This could enhance the particles lift from the surface at glancing impacts. This aspect is a disadvantage for the accuracy of the data from a mechanistic point of view, but it represents a more realistic condition when compared to what is likely to happen in an EF gasifier.

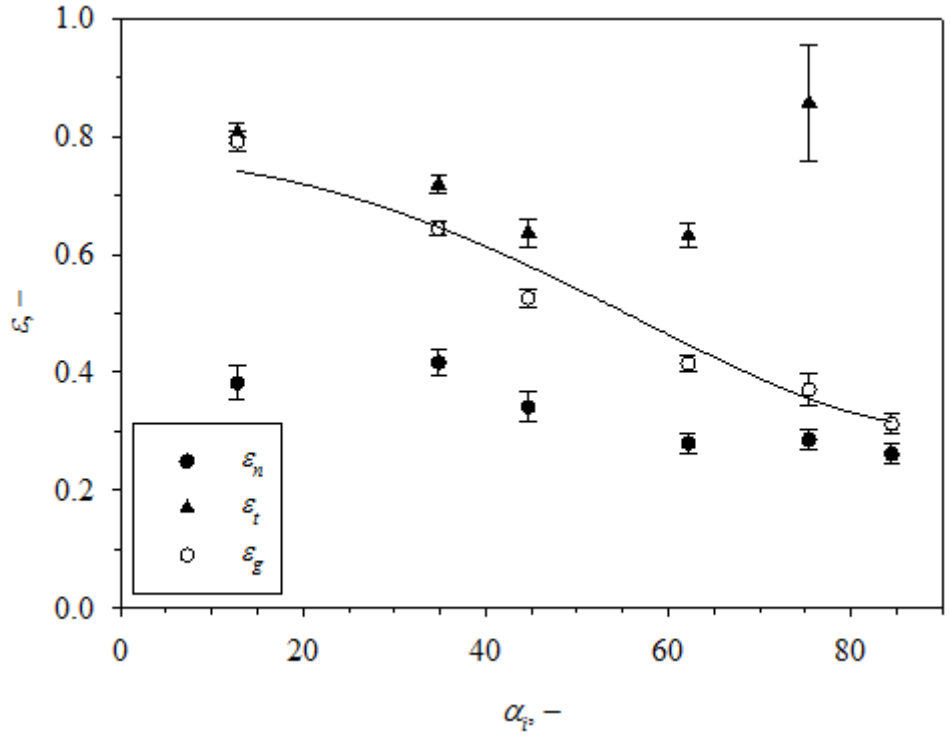

Figure 50. Effect of the impact angle on the coefficients of restitution. The line represents the fitting of the ε_g experimental data points by using Eq. (11). Operating conditions: *NSW–NSP* regime (T_{air}=20°C), v_i=1 m s^{-1}, Pyrex target.

The trend of the data points for the tangential restitution coefficient reported in Fig. 50 is non monotonic with the impact angle. In particular, it is around 0.8 at 13°, then it decreased to a minimum (for α_i≈40°), to increase thereafter, in agreement with trends reported in the literature *(Gorham and Kharaz, 2000; Wu et al., 2003)*. These variations can be attributed to the changing history of sliding (at low impact angles) and rolling (at high impact angles) regimes, as the impact angle is varied. The experimental apparatus did not permit to accurately mark the particles to measure the rotational speed before and after the collisions (i.e. rolling motion), while it allowed to characterize the sliding regime by means of the tangential coefficient of restitution. If sliding is described by a tangential-to-normal impulse ratio, f, it is possible to derive ε_t from Eq. (12). Figure 51 reports values of ε_t plotted against $(1+\varepsilon_n)\tan\alpha_i$. The measured points for impact angles between 10° and 45° are fitted fairly well by a straight line corresponding to $f = 0.28$,

whereas the data points significantly deviate for $(1+\varepsilon_n)\tan\alpha_i$>1.31, corresponding to α_i>45°. This finding is in very good agreement with the rigid body theory, as the critical impact angle for the transition from sliding to rolling regime is α_i^{cr}=43°, according to Eq. (13). It is possible to conclude that the rigid body theory well describes the measured variation of ε_t during the sliding regime.

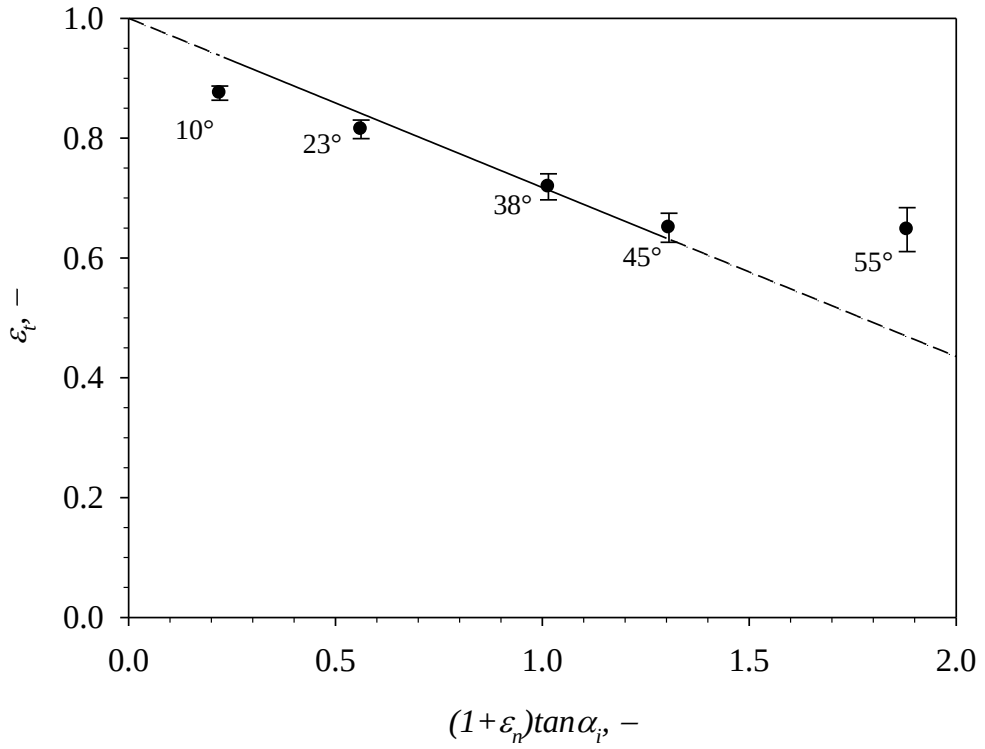

Figure 51. Tangential coefficient of restitution: plot based on Eq. (12). Symbols represent experimental data points; the solid line represents the linear data fitting for impact angles between 10° and 45°. Operating conditions: *NSW–NSP* regime (T_{air}=20°C), v_i =1 m s^{-1}, Pyrex target.

As regards the effect of α_i on the global restitution coefficient ε_g (affected by both ε_n and ε_t, see Eq. (11) and Fig. 50), ε_g tends to ε_t at small impact angles, and to ε_n at large ones. It is possible to fit the experimental data points with Eq. (11) by considering ε_n and ε_t as constant values. The result of this operation is shown in Fig. 50, as well. The qualitative trend of the theoretical ε_g agrees fairly well with the experimental data points. The best fit was obtained for ε_n=0.31 and ε_t=0.76.

The trend of ε_n, obtained when testing in *NSW–NSP* regime at different normal impact velocities (d_p=75±10 μm, α_i=84±1°), is shown in Fig. 52. The experimental data are compared with those obtained by application of the *Thornton and Ning* model *(Thornton and Ning, 1998)* for impact of adhesive elasto–plastic spheres. The values of the mechanical properties and of the critical

velocities v_s and v_y are reported in Table 7, with particular reference to the case under investigation (Pyrex target material). It was $v_y<v_s$; this means that the wax particle plastically deforms for each normal impact velocity investigated, and that the maximum value of ε_n is less than 1. This finding agrees with the experimental results shown in Fig. 52 (ε_n~0.3). Furthermore, the calculation of v_y and, as a consequence, of ε_n, required the knowledge of the cut-off pressure p_y, which is generally expressed as $p_y = c \times \sigma_y$, where c is a constant (around 2.6–3 for hard-sphere models *(Tabor, 1948)*) and σ_y the yield stress. The impact of wax particles, instead, can be properly described by a soft-sphere model, for which the collision is not instantaneous *(Stevens and Hrenya, 2005)*. The best fit of the experimental data points was obtained for c=0.7, which describes an incipient plastic deformation when the contact pressure is the 70% of the yield stress.

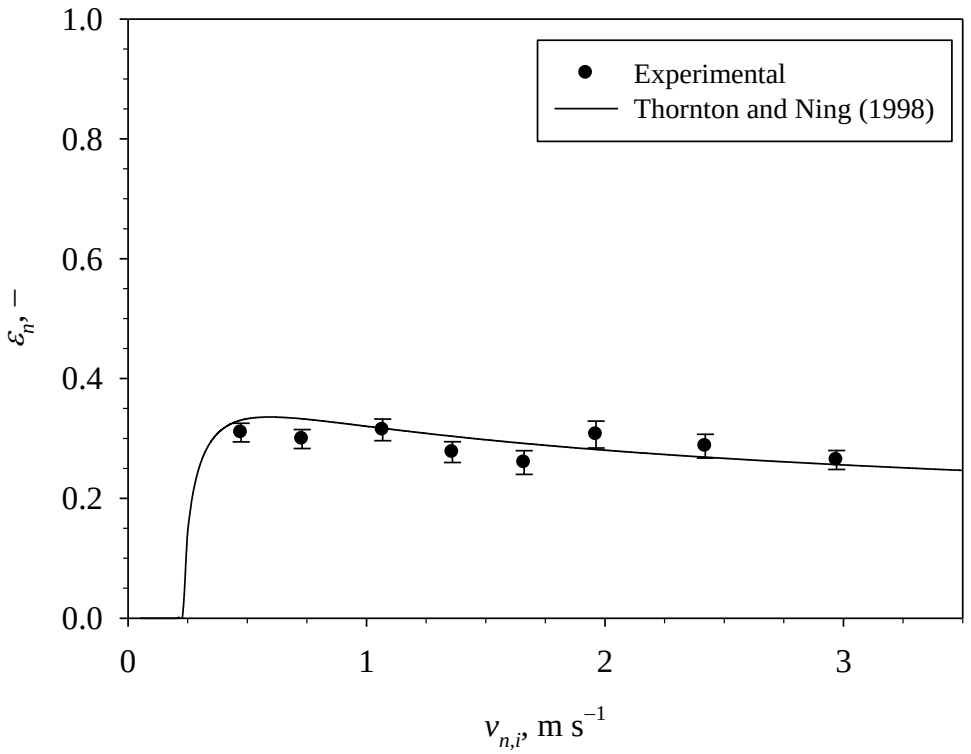

Figure 52. Effect of the normal impact velocity on the normal coefficient of restitution. Operating conditions: *NSW–NSP* regime (T_{air}=20°C), α_i=84°, Pyrex target.

This results in a damping effect of the normal restitution coefficient at each impact velocity investigated, due to the particles softness *(Kim and Dunn, 2007)*. In such a scenario, a char particle could be seen as a soft particle, too, especially during the pyrolysis and latest stage of reaction.

The plastic rebound nature is also confirmed by results obtained in the *NSW–NSP* regime using different target materials, characterized (see Table 7) by different mechanical properties, especially

in terms of surface energy and elastic modulus. Figure 53 reports the trends of ε_n and ε_g for 75±10 μm particles colliding against Pyrex, stainless steel, montan wax Waradur E and Teflon targets, at fixed α_i=84±4° and v_i=1.25±0.1 m s^{-1}. It is quite evident that the nature of the substrate material exerts negligible influence on the particle rebound. As a matter of fact, when the impact energy far exceeds the adhesion energy, the coefficient of restitution is primarily a function of the energy losses due to plastic deformation, as described by Eqs. (6), (8) and (11). Accordingly, the restitution coefficient decreases with an increasing impact velocity, and it is a function of the yield velocity only *(Wall at al., 1990)*. The small difference in ε_n observed among the different targets indicates that the elastic yield limit velocity was the same in each case, consistent with the plastic deformation occurring only in the particle. This behaviour agrees with previous investigations, confirming that the target surface energy does not affect the restitution coefficients during plastic impacts *(Wall at al., 1990)*.

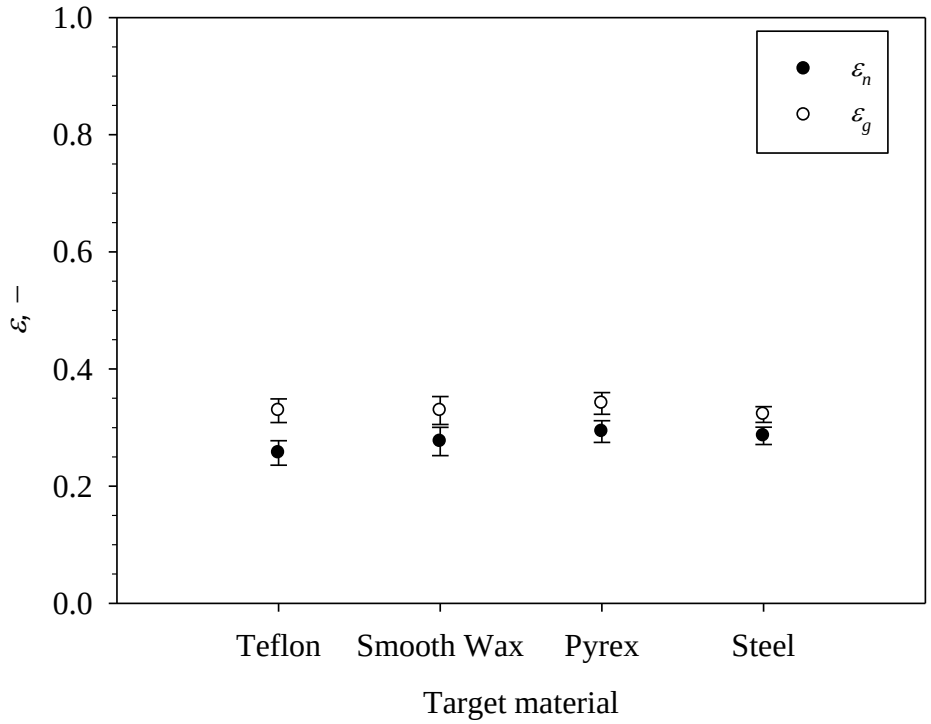

Figure 53. Effect of the target material on the normal and global coefficient of restitution. Operating conditions: *NSW–NSP* regime (T_{air} =20°C), v_i =1.25 m s^{-1}, α_i=84°.

Figures 54 and 55 report the effect of the target structure on the normal and global coefficients of restitution, respectively for different normal impact velocities. Other parameters were d_p=75±10 μm and α_i=84±4°. The Pyrex and smooth wax surfaces are shown as reference, where ε_n and ε_g are about constant with the impact velocity. Moreover, the two figures report results

obtained for the Pyrex target covered by: *i)* two wax powder layers with different thickness; *ii)* a syrup layer spotted with wax powder. Both ε_n and ε_g decrease in the presence of a powder layer, and they are smaller for a thicker powder layer. In particular, ε_n (Fig. 54) has a mean value equal to 0.28 for the Pyrex and smooth wax targets, while it decreases to around 0.1 for the thin powder layer, and to around 0.07 for the thick powder layer. A similar result is obtained for ε_g in Fig. 55. These results may be explained by taking into account the different surface roughness in the presence of the powder layer, which acts as a damper during the rebound phase. This damping effect is proportional to the thickness of the powder layer. It is remarkable that this damping effect is the same regardless of whether a dry (Pyrex) or wet (syrup-layered Pyrex) target is used. This finding may be explained on the basis of the fact that the powder layer separates the incoming particles from the wall substrates, and the particles partially penetrate the powdery layer. These phenomena determine energy losses, hence smaller coefficients of restitution, as reported in the literature *(Abd-Elhady et al., 2006; van Beek et al., 2006)*. This finding is very relevant to the assessment of the fate of char/ash particles in EF slagging gasifiers. Smaller restitution coefficients as the target is covered by a powder layer promote the establishment of segregation–coverage regimes, with, in turn, may be responsible for the formation of a dense–dispersed phase in the near-wall zone *(Montagnaro and Salatino, 2010)*.

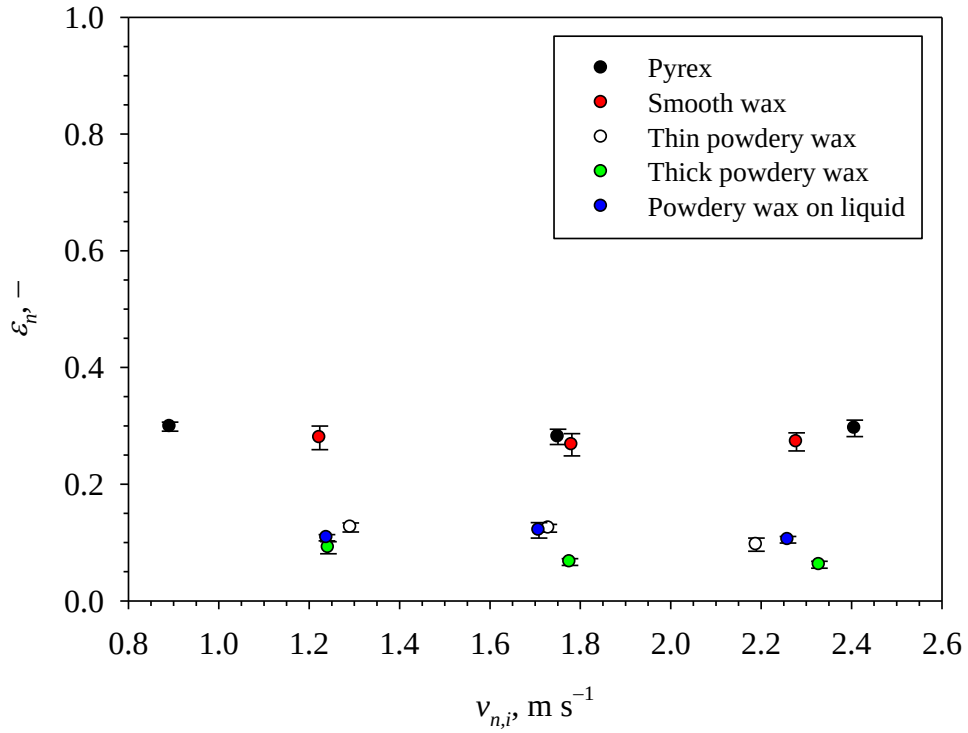

Figure 54. Effect of the target surface on the normal coefficient of restitution. Operating conditions: *NSW–NSP* regime (T_{air} =20°C), α_i=84°. Key to symbols: black) Pyrex; red) Wax, smooth surface; white) Pyrex surface covered with 0.25 mm-thick layer of powdered wax; green) Surface covered with 1.4 mm-thick layer of powdered wax; blue) Surface covered with syrup and 0.2 mm-thick layer of powdered wax.

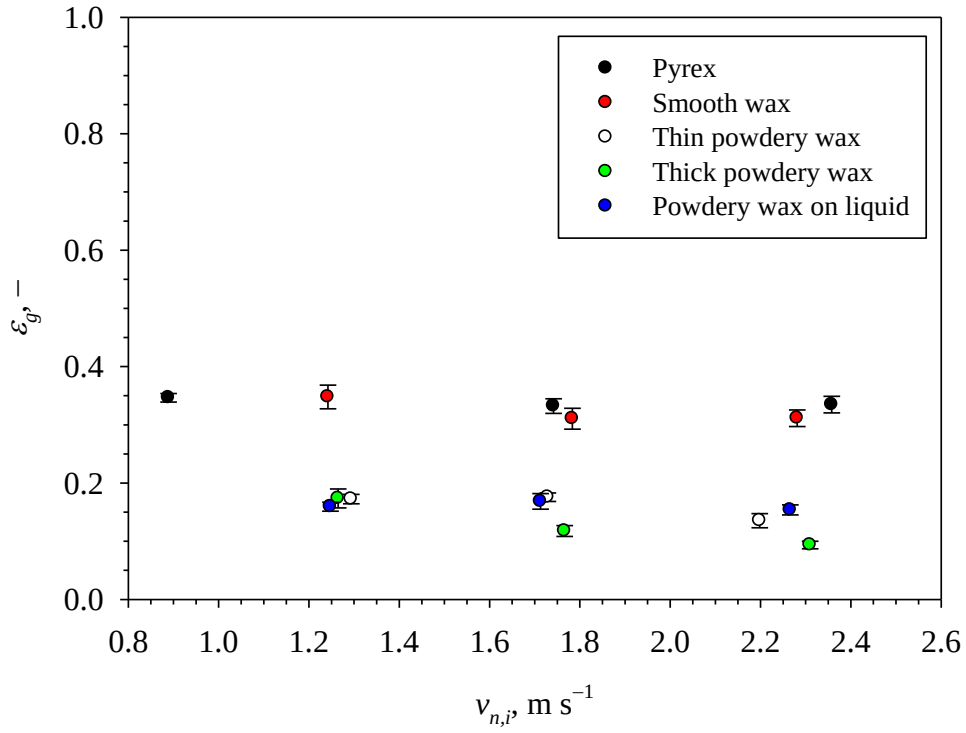

Figure 55. Effect of the target surface on the global coefficient of restitution. Operating conditions and key to symbols as reported in Fig. 54.

4.2 *Rebound characteristics in the transitional NSW–NSP→NSW–SP regime*

The effect of the particle temperature on the capture efficiency (d_p=80±15 μm, α_i=84±4°, v_i=2±0.1 m s^{-1}), defined in Eq. (46), is reported in Fig. 56. Notably, due to the operating conditions in the impactor, the particle temperature could be considered equal to the temperature of the mainstream air. The capture efficiency increased from 0 to 93% when temperature was increased from 20°C to 105°C. The capture efficiency was practically zero at temperatures below 50°C. At these temperatures the montan wax is solid (its melting range is 75–85°C), thus the particles did not adhere on the target surface. *Craig et al. (1965)* measured the temperatures at which 1%, 50%, and 70% flow occurred, for the montan wax. These temperatures were 65°C, 71.1°C and 74.6°C, respectively. This is in agreement with the experimental points reported in Fig. 56, where the capture efficiency was around 8% at 70°C, as a consequence of the incipient solid–liquid transition of the wax. As the temperature is increased even further, there is a sharp rise in the capture efficiency, up to 93% at 105°C. The behaviour of the wax during its solid–liquid transition resembles that occurring during the char–slag transition in gasification processes.

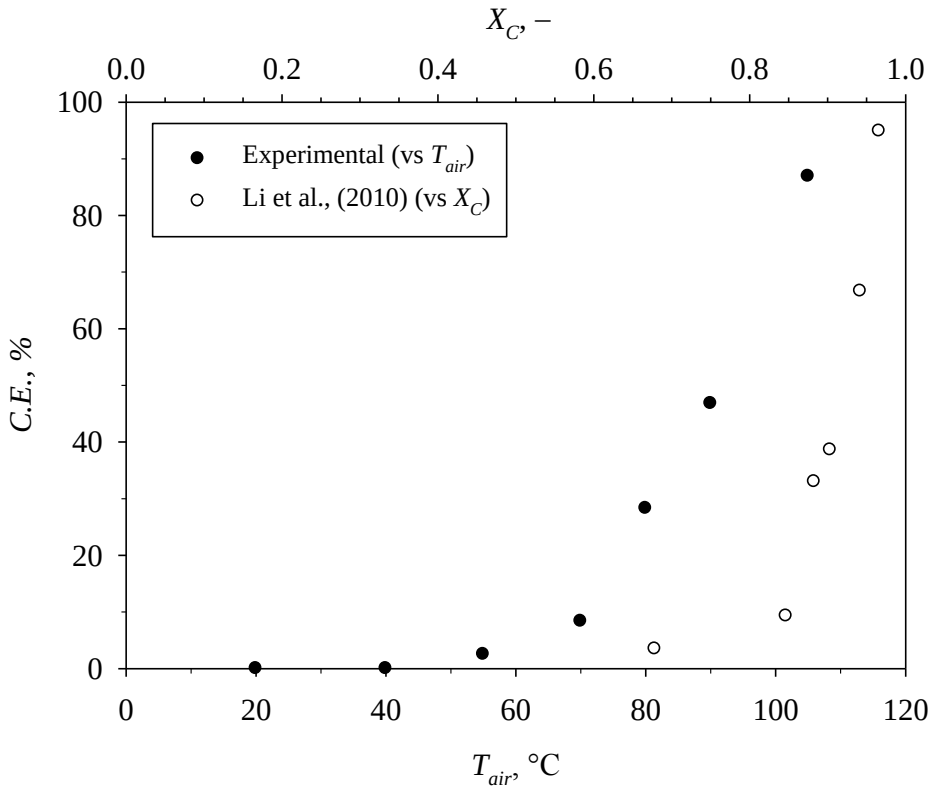

Figure 56. Effect of the particle temperature (present study) and of the fractional carbon conversion (after *Li et al., 2010*) on the particle capture efficiency. Operating conditions: *NSW* and *NSP→SP* transition, v_i=2 m s^{-1}, α_i=84°, Pyrex target.

To better appreciate this, the capture efficiencies measured by *Li et al. (2010)* in tests with 43–63 μm coal particles impacting a deposition plate in a laminar EFG at different carbon conversions are reported in Fig. 56 for comparison. The capture efficiency was fairly small for coal conversion smaller than a threshold value (around 88%), whereas it sharply increased for larger coal conversion. This behaviour is related to the transition from a porous char particle, in which the molten mineral matter is encapsulated by the refractory carbon matrix, to a particle in which the residual carbon is enclosed by the mineral slag. As a consequence, for coal conversion larger than about 90%, the particles become sticky and the capture efficiency sharply increases. The close resemblance of the two plots in Fig. 56 suggests the usefulness of the physical modelling tool to characterize the *NSP→SP* transition occurring in realistic conditions by experiments with wax impacted at near ambient conditions.

Figure 57 reports the effect of the temperature on both the global and normal coefficients of restitution.

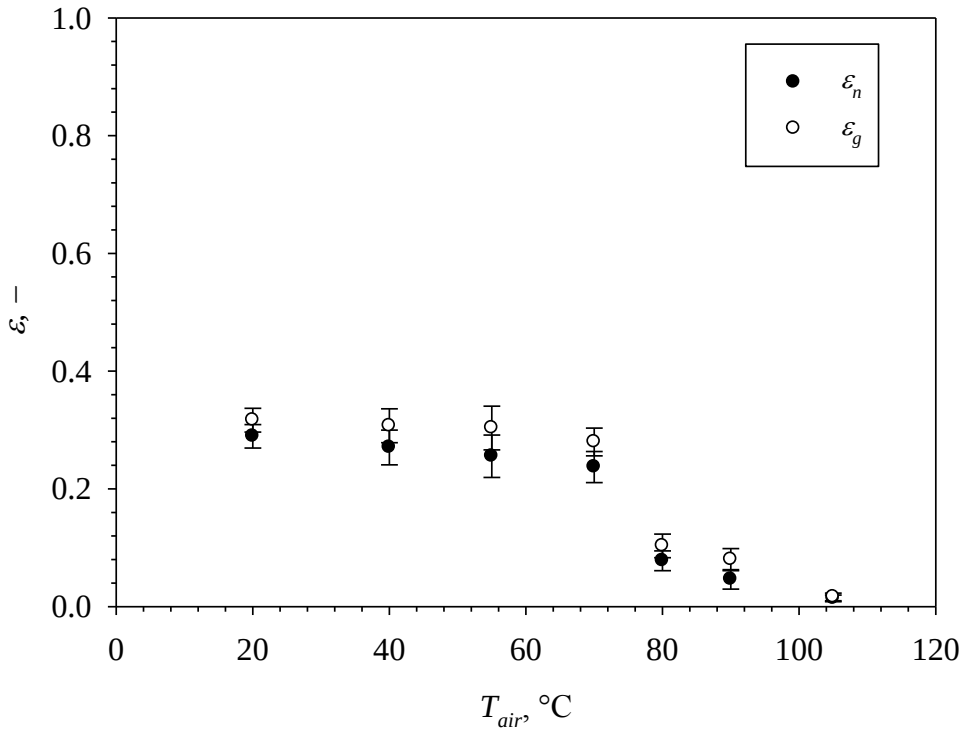

Figure 57. Effect of the particle temperature on the normal and global coefficients of restitution. Operating conditions: *NSW* and *NSP→SP* transition, v_i=2 m s^{-1}, α_i=84°, Pyrex target.

Results show that both ε_n and ε_g are constant, as the temperature increases from 20°C to 55°C, whereas at higher temperatures both the restitution coefficients decrease, becoming vanishingly small at 105°C. These experimental results are in agreement with those reported in Fig. 56. Furthermore, these results suggest that ε_n, ε_t and ε_g to be used as boundary conditions in CFD codes should not be set as constant values, but as a decreasing function of the temperature and carbon content of the fuel particle.

4.3 Rebound characteristics in the NSW–SP regime

Table 9 reports the *C.E.* for droplets of 120±20 μm size upon collision against the Pyrex target at 110°C, while varying α_i and v_i. The capture efficiency is always larger than 85%, highlighting that the deposition is by far the key phenomenon occurring for such impact experiments. At small values of α_i, *C.E.* slightly decreases with increasing impact velocities. This result can be explained by taking into account sliding and slipping phenomena *(Šikalo and Ganić, 2006)*, occurring more frequently at larger velocities. Figure 58 shows a sliding event upon the impact of a droplet (α_i =29°, v_i =4.46 m s^{-1}). The droplet adheres on the surface and slides, as it is possible to notice from the droplet coordinates, *x* and *y*, also reported in Fig. 58. This sliding motion leads to a global restitution coefficient which is not zero, thus, the *C.E.* decreases.

On the other hand, at large impact angles, the capture efficiency slightly increased with the incident velocity, as at larger impact velocities the viscous dissipation overtakes the inertial energy *(Šikalo and Ganić, 2006)*. This transition from rebound to adhesion can be described in terms of the parameter K_D defined in *Section 1.5* (Eq. (40)), as a function of the Ohnesorge and Reynolds numbers *(Sommerfeld and Tropea, 1994; Šikalo and Ganić, 2006)*. Figure 59 reports the values of the Ohnesorge number, *Oh*, as a function of the Reynolds number, *Re* for the impacts of droplets at large impact angles. The results are compared with the limiting theoretical curve obtained for $K_D = 3$ *(Sommerfeld and Tropea, 1994).* Both the curves are obtained considering the normal impact velocity. The experimental data points lie in the region of adhesion, especially those at larger *Re* number, confirming the large *C.E.* shown in Table 9.

It is possible to conclude that, in the *NSW–SP* regime, the coefficients of restitution are about zero while varying impact angles and velocities in the ranges investigated.

Table 9. Effect of the impact angle and impact velocity on the particle capture efficiency in the *NSW–SP* regime. Operating conditions: T_{air}=120°C, Pyrex target.

$C.E.$ (%)	α_i (15–45°)	α_i (45–75°)	α_i (75–90°)
v_i (m s^{-1}) 0.7–2.3	98	93	89
v_i (m s^{-1}) 2.3–3.5	97.5	98	97.5
v_i (m s^{-1}) 3.5–5	94	97	100

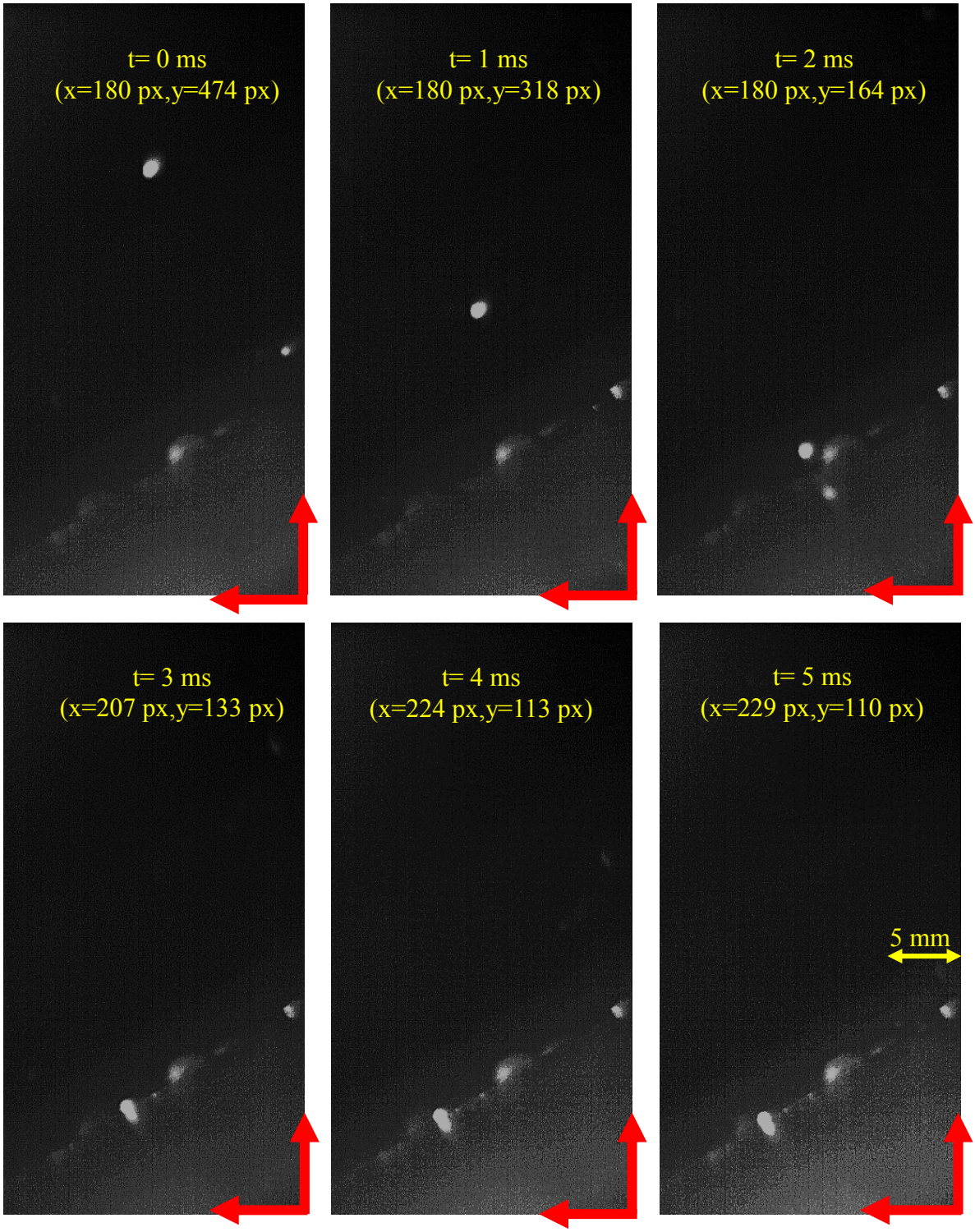

Figure 58. A Sliding event upon an impact in *NSW–SP* regime. Operating conditions: v_i=4.46 m s^{-1}, α_i=29°, Pyrex target.

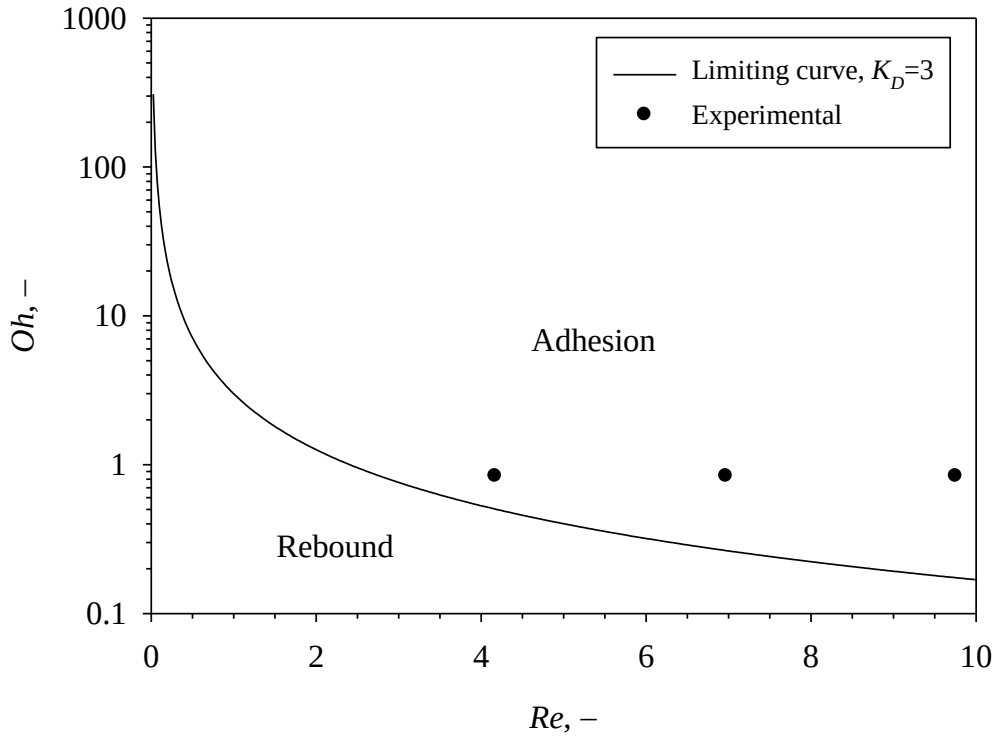

Figure 59. Rebound criterion for a droplet impacting a dry wall. Comparison of the experimental data points with the theoretical curve *(Sommerfeld and Tropea, 1994)*.

4.4 General comments on the investigated regimes

Micromechanical particle–wall interaction was investigating using a devoted lab-scale apparatus (see Fig. 17). High speed imaging and tracking of wax particles impacted onto a flat surface at near-ambient conditions were carried out. Particle–wall collision was described in terms of normal and lateral restitution coefficients and capture efficiency. The influence of the particle stickiness, impact velocity and angle, and surface properties and structure of the target on the rebound patterns was studied.

Results indicate that the elastic–plastic adhesive model provides an adequate representation of the non sticky particle–wall collisions. The coefficients of restitution are well below unity, as a consequence of the plastic behaviour of the impacting particle. In the *non sticky wall–non sticky particle* regime, the coefficients of restitution are affected by impact angle and velocity, whereas, for such plastic impacts, the nature of the target material exerts a negligible influence on the particle rebound. Moreover, a significant decrease of the restitution coefficients was observed when the particles were impacted against a powder-covered target. This finding may be explained on the basis of the fact that the powder layer separates the incoming particles from the wall substrates, and the particles partially penetrate the powdery layer, determining larger energy dissipation. These

conditions favour the accumulation of particles close to the surface and, thus, the establishment of a segregation–coverage regime in a slagging entrained-flow gasifier, with the formation of a dense-dispersed phase in the near-wall reactor zone. Increasing the temperature, particles shift from the solid/plastic to the fluid state. During this transitional regime the coefficient of restitution drops to vanishingly small values. This outcome is confirmed in the *non sticky wall – sticky particle* regime, while varying impact velocity and angle. Thus, it is possible to conclude that deposition is the prevailing phenomenon during the collision of sticky particles on a wall.

Chapter 5. Conclusions and future developments

Near-wall phenomena in entrained-flow gasifiers were studied on the basis of three scales of investigation, i.e. compartments scale, near-wall segregation scale, and micromechanical interactions scale, using the tool of physical modeling. Two kinds of experiments were carried out, in order to assess particle segregation and micromechanical interaction patterns in an entrained-flow reactor. The first objective was pursued using a lab-scale cold entrained-flow reactor, optically accessible, and equipped with a nozzle whence molten wax atomized into a mainstream of air to simulate the near-wall fate of char/ash particles in a real hot environment. Particle–wall interaction was investigated while varying the stickiness of both the particles and the wall layer. The four possible scenarios (*sticky wall–sticky particle*, *non sticky wall–non sticky particle*, *non sticky wall–sticky particle* and *sticky wall–non sticky particle* regimes) were investigated. Results obtained from the partitioning tests indicated that wax loading in the lean-dispersed phase decreased with increasing distance from the atomizing nozzle, as increasingly large amounts of wax were deposited onto the wall. The fractional wax content in the lean-dispersed phase at the exhaust was minimum in the *SW–SP* regime, whereas it was maximum in the *NSW–NSP* regime. The mainstream gas flow rate exerted a remarkable influence on the extent of wax deposition, especially for the *NSW–NSP* regime. The fractional wax content in the lean-dispersed phase decreased as the mainstream flow rate increased. This somewhat unexpected result was explained by considering the interaction between the mainstream flow and the oblique stagnation flow typical of the outer jet. Increasing the mainstream rate moderates the stagnation effects and suppresses the local turbulence, which is largely responsible for particle resuspension, thus favoring the stratification and segregation of particles in the near-wall region of the duct. This hypothesis was confirmed by close-up observation of particle–wall interaction patterns. A simple analysis of the particle resuspension phenomenon suggested that lift-off and sliding are not relevant to the particle resuspension, whereas the rolling mechanism may be active under the experimental conditions tested even for the finer particles, and responsible for the resuspension when a strong jet–wall interference takes place. Sticky particles mainly adhere on the wall surface, regardless the stickiness of the wall, whereas non sticky particles may rebound, deposit, segregate and be resuspended into the main gaseous flow. As regards the interaction of non sticky particles with a sticky wall, the partitioning results lie between those obtained for the other regimes, indicating that a dense-dispersed phase in the near-wall region of the reactor may establish. Moreover, from a phenomenological point of view, particles follow the gaseous streamlines at the center of the duct, as expected in dilute particle-laden flows. On the other hand, the particle flow pattern in the near-wall region is deeply influenced by the gas flow. In particular, increasing the mainstream air flow rate induces particle segregation and accumulation phenomena. Furthermore, the micromechanical interaction of a particle with a sticky wall enhances particle transport to the wall and the tendency

to reach a segregation–coverage regime with the formation of a dense-dispersed phase in the near-wall region of the reactor.

The micromechanical particle–wall interaction was investigated using another lab-scale apparatus. High speed imaging and tracking of wax particles impacted onto a flat surface at near-ambient conditions were carried out. Particle–wall collision was described in terms of normal and lateral restitution coefficients and capture efficiency. The influence of the particle stickiness, impact velocity and angle, and surface properties and structure of the target on the rebound patterns was studied. Results indicate that the elastic–plastic adhesive model provides an adequate representation of the non sticky particle–wall collisions. The coefficients of restitution are well below unity, as a consequence of the plastic behaviour of the impacting particle. In the *non sticky wall–non sticky particle* regime, the coefficients of restitution are affected by impact angle and velocity. For such plastic impacts, the nature of the target material exerts a negligible influence on the particle rebound. Moreover, a significant decrease of the restitution coefficients was observed when the particles were impacted against a powder-covered target, as a consequence of larger energy dissipation. These conditions favour the accumulation of particles close to the surface and, thus, the establishment of a segregation–coverage regime in a slagging entrained-flow gasifier, with the formation of a dense-dispersed phase in the near-wall reactor zone. Increasing the temperature, particles shift from the solid/plastic to the fluid state and the coefficient of restitution drops to vanishingly small values, confirming that deposition is the prevailing phenomenon during the collision of sticky particles on a wall.

Future work could be useful to the development of a phenomenological model of the fate of coal/ash particles in entrained-flow gasifiers. Under practical operation conditions, the strong swirl/vortex flow plays a significant role in the transport of particles from the dispersed phase to the walls, and in the build-up of the slag layer. Therefore, it is useful to provide the lab-scale cold entrained-flow reactor with a swirl generator in order to investigate the effect of a swirl flow field on the particle–wall interaction.

In addition, the restitution coefficient is an important parameter when modelling the multiphase flow in the gasification chamber, e.g. by the tools of CFD–DPM, as it critically affects the boundary condition for particle–wall collisions. The experimental results indicated that the elastic–plastic adhesive model provides an adequate representation of the non sticky particle–wall collisions. It is essential to investigate the suitability of this model for char particles in real hot conditions, aiming to develop user-defined functions to be embedded into CFD–DPM codes for the prediction of multiphase flow and particle–wall interaction in EF slagging gasification.

Chapter 6. Towards better understanding and control of the fate of char/ash particles in entrained-flow gasifiers

The slagging conditions establishing during combustion/gasification of solid fuels play a key role in the design of modern entrained-flow reactors. The residence time in these processes is short (a few seconds), hence, high temperatures are required to ensure a good conversion; for this reason, almost all the entrained-flow gasifiers operate in the slagging mode. These operating temperatures ensure the destruction of tars and oils and, if the gasifier is appropriately designed and operated, a very high carbon conversion may be reached *(Higman and van der Burgt, 2008)*.

The slagging behavior of ash plays a key role in the performance of entrained-flow gasifiers. At temperatures above the ash-softening point, the ash becomes sticky and agglomerates, causing blockage of the beds or fouling of the heat exchange equipment. Once above the slagging temperature (about 1300-1500°C), ash has a fully liquid behavior with a relatively low viscosity, hence, it is possible to remove it from the system. Entrained-flow gasifiers have become the preferred technology for hard coals, and have been selected for the majority of commercial-sized IGCC applications. The current development in next generation of coal-fired power stations uses IGCC technologies in order to address a number of problems related to the increase of the emissions of NOx, SOx, and particulates from conventional pulverized coal-fired power stations *(Kitto and Stultz, 2005)*. One advantage of a slagging reactor over a non-slagging combustor is the fact that the collected slag has in general a higher economic value compared with the bottom ash, because of its longer durability and resistance to surface wear. In addition, the slag layer results in a molten protective coating and reduces the heat loss to the wall, generally increasing the cold gas efficiency of the gasifier *(Yong and Ghoniem, 2012)*. However, the increasing slag layer can bring about gasifier plugging, and the slag deposition on the wall membrane reduces the overall heat-transfer coefficient. The molten ash flows through the bottom of the gasifier and is quenched in a water bath, whence it can be typically divided into coarse slag and fine slag *(Li and Whitty, 2009)*. Both the coarse and fine slag may have a relatively large content of unburned carbon. Coarse slag is derived from the slag which accumulates on and flows down the reactor wall before entering the slag quench chamber (which may also serve as gas quench depending on the gasifier design). Finer particles of mineral matter also enter the slag quench and are designated as fine slag. A third stream is the fly slag, which leaves the gasifier with the syngas *(Higman and Tam, 2014)*. The presence of unburned carbon within the slag is a result of the incomplete gasification of the coal, which is the major determinant of the gasification efficiency in entrained-flow processes. The carbon content in fine and coarse slags can reach 60% and 30–35% respectively *(Xu et al., 2009; Zhao et al., 2010; Montagnaro et al., 2011)*, and this is a crucial key also in coal gasification modeling. Char and ash particle deposition flux depends on the flow field and char trajectories, wall temperature, as well as

on char properties such as carbon conversion, ash composition, particle diameter and velocity. Furthermore, under slag flow conditions, the extent of coverage of the slag layer by carbon particles must also be taken into account given the relevance of the stiffness and surface roughness to the micromechanics of a particle impinging a refractory wall, a layer of adhered particles, or a layer of molten slag. The extent of surface coverage by carbon particles is governed by carbon impingement on the slag layer, convective transport of flowing slag, and gasification of carbon deposited on the slag. Different near-wall carbon-slag segregation regimes (*entrapment*, *segregation*, *segregation–coverage*) can occur *(Montagnaro and Salatino, 2010)*, as a function of the reactor axial coordinate and of the progress of X_C (as depicted in Figs. 3,4). Also local hydrodynamic conditions influence the particle–wall interaction and, thus, the extent of carbon coverage onto the slag layer. Micromechanical interaction patterns and local hydrodynamics can determine the contributions of ash and slag within the gasifier.

On the basis of the results obtained in this project, the fate of coal/ash particles can be elucidated taking into account the variety of possible particle−wall micromechanical interaction patterns (namely *sticky wall–sticky particle*, *non sticky wall–non sticky particle*, *non sticky wall–sticky particle* and *sticky wall–non sticky particle* regimes) *(Yong et al., 2012)*.

As regards the interaction of a sticky particle with the wall (*SW–SP* and *NSW–SP* regimes), deposition is clearly the prevailing phenomenon of particle-wall interaction, regardless of the stickiness of the wall layer , the local hydrodynamics and impact velocity. This outcome confirms that char particles with high carbon conversion mainly contribute to the formation of the slag layer, in the near-injection zone of the gasifier, and to the built-up of the slag layer throughout the reactor length.

On the other hand, in the *non sticky wall–non sticky particle* interaction regime (typical of char particles characterized by large carbon content impinging on either a dry wall or on a carbon-covered slag layer), rebound, adhesion and resuspension can occur. In particular, rebound may occur upon a non sticky particle−wall collision, even when particles are in a plastic state. In this case, the restitution coefficient upon the impact is lower than unity and a further decrease of the restitution coefficients occurs when segregation regime is established. As a matter of fact, the presence of a particle layer results in a damping of the restitution coefficient, thus, the segregation−coverage regime can establish, with the formation of a dense-dispersed phase in the near-wall region of the reactor. Particle deposition patterns are also affected by the local hydrodynamics, which can either favour the stratification and segregation of particles in the near-wall region of the duct or the near-wall turbulence, which is largely responsible for particle resuspension. This kind of interaction can be encountered in the near-injection zone, where the gaseous flow field promotes particle deposition onto the internal walls of the reactor in such a way

to guarantee the formation and the proper built-up of the slag layer onto the reactor walls. Furthermore, the interaction of char particles with other particles covering the slag layer is likely to occur and should be promoted throughout the reactor length, except the tap hole zone, where temperature and slag viscosity have to ensure a continuous discharge of the wall phase.

As regards the interaction of char (non sticky) particles with a sticky wall, rebound can occur, although deposition without plunging is likely to be the most important phenomenon. In this case, the particle flow pattern in the near-wall region is deeply influenced by the gas flow field. In particular, a proper tuning of the local hydrodynamic conditions in the near-wall region of the gasifier is able to favour particle deposition and accumulation onto the slag layer (*segregation–coverage* regime). This annular phase is characterized by a velocity that is intermediate between that of the fast lean-dispersed particle phase and that of the slowly moving molten ash wall layer. This feature is beneficial to the carbon conversion, as it gives rise to a longer mean residence time of the carbon particles belonging to this dense phase (with respect to the particle mean residence time in the lean phase) and it has to be promoted throughout the reactor length.

Altogether, the phenomenological and quantitative characterization of char-wall interaction in entrained flow that has been gained in the present study lays the path for the development of more accurate constitutive submodels of particle-wall interaction. The predictive ability of computational fluid-dynamics may be considerably improved by combining this tool with better description of the micromechanics of multiphase flow in the near–wall region of the gasifiers. Reliability of key process variables like carbon burn-off and slag build-up prediction can be improved, and this will positively impact the assessment of important associated properties, like process efficiency, temperature fields and energy dissipation at the wall, durability of refractory linings, fate of ash material.

Nomenclature

A	area [m^2]
a	contact radius [m]
C	ratio of rough-to-smooth pull-off forces [–]
C.E.	capture efficiency [–]
C_s	heat capacity [J kg^{-1} K^{-1}]
D	reactor inner diameter [m]
D_0	initial droplet diameter [m]
D_{max}	maximum spread droplet diameter [m]
d_p	particle diameter [m]
d_x	minor ellipse axis [m]
d_y	major ellipse axis [m]
$\bar{d}$	mean diameter of the solidified droplet [m]
E	Young's modulus [kg m^{-1} s^{-2}]
E_{diss}	viscous dissipation energy [kg m^2 s^{-2}]
E_K	kinetic energy [kg m^2 s^{-2}]
ER	Equivalence ratio [–]
ERE	excess rebound energy [–]
E_S	surface energy [kg m^2 s^{-2}]
f	tangential-to-normal impulse ratio [–]
F_D	drag force [kg m s^{-2}]
F_G	gravitational force [kg m s^{-2}]
F_L	lift force [kg m s^{-2}]
F_{PO}	adhesion force [kg m s^{-2}]
$F_{PO,s}$	adhesion force for a smooth surface [kg m s^{-2}]
f_s	correlation factor in Table 3 [–]
f_w	correcting factor in Eq. (22) [–]
G	shear modulus [kg m^{-1} s^{-2}]

H	latent heat [kJ kg^{-1}]
h	height [m]
HT	hemispherical temperature [°C]
IT	initial deformation temperature [°C]
K	composite Young's modulus [kg m^{-1} s^{-2}]
K_D	parameter in Eq. (37) [–]
k	stiffness ratio [–]
k_s	static coefficient of friction [–]
k_t	thermal conductivity [W m^{-1} K^{-1}]
L	reactor length [m]
m	mass flow rate [kg s^{-1}]
p_y	cut-off pressure [kg m^{-1} s^{-2}]
Q	gas volumetric flow rate [m^3 s^{-1}]
$\bar{s}$	mean thickness of the solidified droplet [m]
T	temperature [°C]
t	time [s]
U	overall heat transfer coefficient [W m^{-2} K^{-1}]
u	gas velocity [m s^{-1}]
u_{fr}	friction velocity [m s^{-1}]
v	particle/droplet velocity [m s^{-1}]
W	wax mass flow rate [kg s^{-1}]
x	distance/coordinate [m]
X_C	carbon conversion degree [–]
x_s	solidified fraction [–]
y	coordinate [m]
y^{lean}	fractional mass in the dispersed phase [–]
z	axial distance from the nozzle [m]

Greek symbols

α	angle [°]
Γ	surface energy per unit area [kg s^{-2}]
γ	surface tension [kg s^{-2}]
ε	coefficient of restitution [–]
θ	aperture angle of the jet [°]
θ_c	static liquid-solid contact angle [°]
μ	viscosity [kg m^{-1} s^{-1}]
ν	Poisson's ratio [–]
ξ	maximum spread factor [–]
ρ	density [kg m^{-3}]
τ	particle relaxation time [s]
φ	parameter in Eq. (32) [J^2 s^{-1} m^{-4} K^{-2}]
Ψ	factor accounting for burst event [–]
ω	slag thermal diffusivity [m^2 s^{-1}]

Subscripts

1	referred to the particle
2	referred to the surface
250	corresponding to a viscosity of 250 poise
10000	corresponding to a viscosity of 10000 poise
A	referred to stage (a)
a	atomization
air	air
B	referred to stage (b)
C	referred to stage (c)
D	droplet

eq	equivalent
fuel	fuel
g	global
i	impact
LV	liquid-vapor
m	melting
max	maximum value
ms	mainstream
n	normal
p	particle
r	rebound
s	sticking
SL	solid-liquid
st	stoichiometric
SV	solid-vapor
syr	syrup
t	tangential
target	target
w	wall
wax	wax
y	yield

Superscripts

*	geometrical condition of droplet impingement
cr	critical
lean	lean (dispersed) phase
oxid	in oxidizing atmosphere
red	in reducing atmosphere

th	threshold value
+	dimensionless
0	at initial time

Dimensionless Numbers

Bi	Biot number
Oh	Ohnesorge number
Pe	Peclet number
Re	Reynolds number
Ste	Stefan number
We	Weber number

References

Abani N, Ghoniem AF, *Large eddy simulations of coal gasification in an entrained flow gasifier*, Fuel 104 (2013) 664–680.

Abd-Elhady MS, Rindt CCM, Wijers JG, van Steenhoven AA, *Modelling the impaction of a micron particle with a powdery layer*, Powder Technol 168 (2006) 111–124.

Ambrosino F, Aprovitola A, Brachi P, Marra FS, Montagnaro F, Salatino P, *Investigation of char-slag interaction regimes in entrained-flow gasifiers: linking experiments with numerical simulations*, Combust Sci Technol 184 (2012) 871–887.

Ambrosino F, Aprovitola A, Brachi P, Marra FS, Montagnaro F, Salatino P, *Entrained-flow gasification of coal under slagging conditions: Relevance of fuel–wall interaction and char segregation to the properties of solid wastes*, Fuel 114 (2013) 44–55.

Annapragada SR, Sun D, Garimella SV, *Prediction of effective thermo-mechanical properties of particulate composites*, Comp Mater Sci 40 (2007) 255–266.

Antonyuk S, Heinrich S, Deen N, Kuipers H, *Influence of liquid layers on energy absorption during particle impact*, Particuology 7 (2009) 245–259.

Aziz SD, Chandra S, *Impact, recoil and splashing of molten metal droplets*, Int J Heat Mass Transfer 43 (2000) 2841–2857.

Basu P, *Combustion and gasification in fluidized beds* (2006), Taylor & Francis.

Baxter LL, *Ash deposition during biomass and coal combustion: A mechanistic approach*, Biomass Bioenerg 4 (1993) 85–102.

Baxter LL, Desollar RW, *A mechanistic description of ash deposition during pulverized coal combustion: Predictions compared with observations*, Fuel 72 (1993) 1411–1418.

Bockelie MJ, Denison MK, Chen Z, Linjewile T, Senior CL, Sarofim AF, *CFD Modeling for entrained flow gasifiers in Vision 21 systems*, Proceedings of the 19th Annual International Pittsburgh Coal Conference, Pittsburgh, PA, 2002.

Bool LE, Johnson SA, American Society of Mechanical Engineers, Environmental Control Division Publication, EC, 1, Environmental Control/Fuels and Combustion Technologies (1995) 305–312.

Brach RM, Dunn PF, *Models of rebound and capture for oblique microparticle impacts*, Aerosol Sci Tech 29 (1998) 379–388.

Brauer H, *Report on investigations on particle movement in straight horizontal tubes, particle/wall collision and erosion of tubes and tube bends*, J Powder Bulk Solids Technol 4 (1980) 3–12.

Broom GP, *Adhesion of particles in fibrous air filters*, Filtr Separat 16 (1979) 661–669.

Caporaloni M, Tampieri F, Trombetti F, Vittori O, *Transport of particles in nonisotropic air turbulence*, J Atmos Sci 32 (1975) 565–568.

Carbone R, *Analysis of the wall effects and occurrence of segregated phases in the fluid-dynamics of entrained-flow gas-solid reactors*, Thesis (2012).

Chen L, Ghoniem AF, *Development of a three–dimensional computational slag flow model for coal combustion and gasification*, Fuel 113 (2013) 357–366.

Chen C, Horio M, Kojima T, *Numerical simulation of entrained flow coal gasifiers. Part I: modeling of coal gasification in an entrained flow gasifier*, Chem Eng Sci 55 (2000) 3861–3874.

Chen C, Horio M, Kojima T, *Use of numerical modeling in the design and scale-up of entrained flow coal gasifiers*, Fuel 80 (2001) 1513–1523.

Chen L, Yong SZ, Ghoniem AF, *Modeling the slag behavior in three dimensional CFD simulation of a vertically-oriented oxy-coal combustor*, Fuel Process Technol 112 (2013) 106–117.

Cheng W, Dunn PF, Brach RM, *Surface roughness effects on microparticle adhesion*, J Adhesion 78 (2002) 929–965.

Ching B, Golay MW, Johnson TJ, *Droplet impacts upon liquid surfaces*, Science 226 (1984) 535–537.

Coda B, Cieplik MK, Wild PJ, Kiel JHA, *Slagging behavior of wood ash under entrained-flow gasification conditions*, Energy Fuel 21 (2007) 3644–3652.

Cossali GE, Coghe A, Marengo M, *The impact of a single drop on a wetted solid surface*, Exp Fluids 22 (1997) 463–472.

Craig, RG, Eick JD, Peyton FA, *Properties of natural waxes used in dentistry*, J Dent Res 44 (1965) 1308–1316.

Craig, RG, Eick JD, Peyton FA, *Strength properties of waxes at various temperatures and their practical application*, J Dent Res 46 (1967) 300–305.

Crowe CT, Schwarzkopf JD, Sommerfeld M, Tsuji Y, *Multiphase flows with droplets and particles, second ed.* (2012), CRC Press, Boca Raton.

Dong M, Li S, Xie J, Han J, *Experimental studies on the normal impact of fly ash particles with planar surfaces*, Energies 6 (2013) 3245–3262.

Drelich J, Tormoen GW, Beach ER, *Determination of solid surface tension from particle–substrate pull-off forces measured with the atomic force microscope*, J Colloid Interf Sci 280 (2004) 484–497.

Duchesne MA, Ilyushechkin AY, Hughes RW, Lu DY, McCalden DJ, Macchi A, Anthony EJ, *Flow behaviour of slags from coal and petroleum coke blends*, Fuel 97 (2012) 321–328.

Erickson TA, Allan SE, McCollor DP, Hurley JP, Srinavasachar S, Kang SG, Baker JE, Morgan ME, Johnson SA, Borio R, *Modeling of fouling and slagging in coal-fired utility boilers*, Fuel Process Technol 44 (1995) 155–171.

Eskin D, Ratulowski J, Akbarzadeh K, *Modeling of particle deposition in a vertical turbulent pipe flow at a reduced probability of particle sticking to the wall*, Chem Eng Sci 66 (2011) 4561–4572.

Fries L, Antonyuk S, Heinrich S, Dopfer D, Palzer S, *Collision dynamics in fluidised bed granulators: a DEM-CFD study*, Chem Eng Sci 86 (2013) 108–123.

Gibson LM, Gopalan B, Pisupati SV, Shadle LJ, *Image analysis measurements of particle coefficient of restitution for coal gasification applications*, Powder Technol. 247 (2013) 30–43.

Goldasteh I, Ahmadi G, Ferro AR, *Monte Carlo simulation of micron size spherical particle removal and resuspension from substrate under fluid flows*, J Aerosol Sci 66 (2013) 62–71.

Goldman SR, *A technique for computer simulation of time varying slag flow in coal gasification reactor*, AIChE J 27 (1981) 869–872.

Gorham DA, Kharaz AH, *The measurement of particle rebound characteristics*, Powder Technol 112 (2000) 193–202.

Govind R, Shah J, *Modeling and simulation of an entrained flow coal gasifier*, AIChE J 30 (1984) 79–92.

Greb SF, Eble CF, Peters DC, Papp AR, *Coal and the environment* (2006), American Geological Institute.

Guha A, *Transport and deposition of particles in turbulent and laminar flow*, Annu Rev Fluid Mech 40 (2008) 311–341.

Guingo M, Minier JP, *A new model for the simulation of particle resuspension by turbulent flows based on a stochastic description of wall roughness and adhesion forces*, J Aerosol Sci 39 (2008) 957–973.

Gupta RP, Wall TF, Baxter L, *Impact of Mineral Impurities in Solid Fuel Combustion* (2002), Kluwer Academic Publisher: New York.

Hertz H, On the contact of elastic solids, *Miscellaneous Papers by H. Hertz, Eds. D.E. Jones, and G.A. Schott* (1896), *Macmillan, London*, 146–162.

Higman C, Tam S, *Advances in Coal Gasification, Hydrogenation, and Gas Treating for the Production of Chemicals and Fuels*, Chem Rev 114 (2014) 1673–1708.

Higman C, van der Burgt M, *Gasification 2nd edition* (2008), Gulf Professional Publishing.

Hobbs DW, *The strength and the stress-strain characteristics of coal in triaxial compression*, J Geol 72 (1964) 214–231.

Ibrahim AH, Dunn PF, Brach RM, *Microparticle detachment from surfaces exposed to turbulent air flow: Controlled experiments and modeling*, J Aerosol Sci 34 (2003) 765–782.

Ibrahim AH, Dunn PF, Qazi MF, *Experiments and validation of a model for microparticle detachment from a surface by turbulent air flow*, J Aerosol Sci 39 (2008) 645–656.

Isaak, P, Tran HN, Barham D, Reeve DW, *Stickiness of fireside deposits in kraft recovery units*, J Pulp Pap Sci 12 (1986) 84–88.

Jain D, Deen NG, Kuipers JAM, Antonyuk S, Heinrich S, *Direct numerical simulation of particle impact on thin liquid films using a combined volume of fluid and immersed boundary method*, Chem Eng Sci 69 (2012) 530–540.

Jayaratne OW, Mason BJ, *The coalescence and bouncing of water drops at an air/water interface*, Proc R Soc London A 280 (1964) 545–565.

Johnson KL, Kendall K, Roberts AD, *Surface energy and the contact of elastic solids*, Proc Roy Soc A 324 (1971) 301–313.

Kang CW, Ng HW, *Splat morphology and spreading behavior due to oblique impact of droplets onto substrates in plasma spray coating process*, Surf Coat Technol 200 (2006) 5462–5477.

Kim OV, Dunn PF, *A microsphere-surface impact model for implementation in computational fluid dynamics*, J Aerosol Sci 38 (2007) 532–549.

Kitto JB and Stultz SC, *Steam/Its generation and use, 41st edition* (2005), The Babcock & Wilcox Company, Barberton, Ohio, U.S.A.

Kumar M and Ghoniem AF, *Multiphysics simulations of entrained flow gasification. Part II: Constructing and validating the overall model*, Energy Fuels 26 (2012) 464–479.

Leighton D, Acrivos A, *The lift on a small sphere touching a plane in the presence of a simple shear flow*, J Appl Math Phys 36 (1985) 174–178.

Li B, Brink A, Hupa M, *Simplified model for determining local heat flux boundary conditions for slagging wall*, Energy Fuels 23 (2009**)** 3418–3422.

Li R, Ashgriz N, Chandra S, Andrews JR, *Shape and surface texture of molten droplets deposited on cold surfaces*, Surf Coat Technol 202 (2008) 3960–3966.

Li S, Whitty KJ, *Investigation of coal char-slag transition during oxidation: effect of temperature and residual carbon*, Energy Fuels 23 (2009) 1998–2005.

Li S, Wu Y, Whitty KJ, *Ash deposition behavior during char-slag transition under simulated gasification condition*, Energy Fuels 24 (2010) 1868–1876.

Li S, Whitty KJ, *Physical phenomena of char-slag transition in pulverized coal gasification*, Fuel Process Technol 95 (2012) 127–136.

Losurdo M, Spliethoff H, Kiel J, *Ash deposition modeling using a visco-elastic approach*, Fuel 102 (2012) 145–155.

Lunkad SF, Buwa VV, Nigam KDP, *Numerical simulations of drop impact and spreading on horizontal and inclined surfaces*, Chem Eng Sci 62 (2007) 7214–7224.

Mao T, Kuhn DCS, Tran H, *Spread and rebound of liquid droplets upon impact on flat surfaces*, AIChE J 43 (1997) 2169–2179.

Marchioli C, Soldati A, *Mechanisms for particle transfer and segregation in a turbulent boundary layer*, J Fluid Mech 468 (2002) 283–315.

Melchior T, Putz G, Muller M, *Surface Tension Measurements of Coal Ash Slags under Reducing Conditions at Atmospheric Pressure*, Energy Fuels 23 (2009) 4540–4546.

Montagnaro F, Salatino P, *Analysis of char-slag interaction and near-wall particle segregation in entrained-flow gasification of coal*, Combust Flame 157 (2010) 874–883.

Montagnaro F, Brachi P, Salatino P, *Char-wall interaction and properties of slag waste in entrained-flow gasification of coal*, Energy Fuels 25 (2011) 3671–3677.

Mundo CHR, Sommerfeld M, Tropea C, *Droplet-wall collisions: experimental studies of the deformation and breakup process*, Int J Multiphas Flow 21 (1995) 151–173.

Ni J, Zhou Z, Yu G, Liang Q, Wang F, *Molten Slag Flow and Phase Transformation Behaviors in a Slagging Entrained-Flow Coal Gasifier*, Ind. Eng. Chem. Res. 49 (2010) 12302–12310.

Ni J, Yu G, Guo Q, Zhou Z, Wang F, *Submodel for predicting slag deposition formation in slagging gasification systems*, Energy Fuels 25 (2011) 1004–1009.

Niksa S, Liu G, Hurt RH, *Coal conversion submodels for design applications at elevated pressures. Part I. Devolatilization and char oxidation*, Progress in Energy and Combustion Science 29 (2003) 425–477.

Noda R, Naruse I, Ohtake K, *Fundamentals on combustion and gasification behaviour of coal particle trapped on molten slag layer***,** J. Chem. Eng. Jpn. 29 (1996) 235–241.

O'Neill ME, *A sphere in contact with a plane wall in a slow linear shear flow*, Chem Eng Sci 23 (1968) 1293–1298.

Pan KL, Law CK, *Dynamics of droplet-film collision*, J Fluid Mech 587 (2007) 1–22.

Pasandideh-Fard M, Qiao YM, Chandra S, Mostaghimi J, *Capillary effects during droplet impact on a solid surface*, Phys Fluids 8 (1996) 650–659.

Patterson JH, Hurst HJ, *Ash and slag qualities of Australian bituminous coals for use in slagging gasifiers*, Fuel 79 (2000) 1671–1678.

Pedel J, Thornock JN, Smith PJ, *Large eddy simulation of pulverized coal jet flame ignition using the direct quadrature method of moments*, Energy Fuels 26 (2012) 6686–6694.

Poirier DR, Poirier EJ, *Heat transfer fundamentals for metal casting*, Second Edition (1994), The Minerals, Metals and Materials Society, Warrendale, PA.

Raask E, *Mineral Impurities in Coal Combustion* (1985), Hemisphere Publishing Corporation, Washington.

Reeks MW, *The transport of discrete particles in inhomogeneous turbulence*, J Aerosol Sci 14 (1983) 729–739.

Rein M, *Phenomena of liquid drop impact on solid and liquid surfaces*, Fluid Dyn Res 12 (1993) 61–93.

Restagno F, Crassous J, Cottin-Bizonne C, Charlaix E, *Adhesion between weakly rough beads*, Phys Rev E 65 (2002) 042301.

Richards GH, Slater PN, Harb JH, *Simulation of ash deposit growth in a pulverized coal-fired pilot scale reactor*, Energy Fuel 7 (1993) 774–781.

Rioboo R, Marengo M, Tropea C, *Time evolution of liquid drop impact onto solid, dry surfaces*, Exp Fluids 33 (2002) 112–124.

Rioboo R, Bauthier C, Conti J, Voue M, De Coninck J, *Experimental investigation of splash and crown formation during single drop impact on wetted surfaces*, Exp Fluids 35 (2003) 648–652.

Rogers LN, Reed J, *The adhesion of particles undergoing an elastic-plastic impact with a surface*, J Phys D Appl Phys 17 (1984) 677–689.

Schlichting H, Gersten K, *Boundary layer theory*, 8th Edition (2000), Springer.

Seggiani M, *Modeling and simulation of time varying slag flow in a Prenflo entrained-flow gasifier*, Fuel 77 (1998) 1611–1621.

Shannon GN, Rozelle PL, Pisupati SV, Sridhar S, *Conditions for entrainment into a FeOx containing slag for a carbon-containing particle in an entrained coal gasifier*, Fuel Process Technol 89 (2008) 1379–1385.

Shimizu T, Haga D, Mikami G, Takahashi T, Horinouchi K, *Heat recovery from melted blast furnace slag using fluidized* bed, Proc. 13th Int. Conf. Fluidization (2010), Gyeong-ju, Korea, Paper #83.

Shimizu T, Tominaga H, *A model of char capture by molten slag surface under high-temperature gasification condition*, Fuel 85 (2006) 170–178.

Šikalo Š, Ganić EN, *Phenomena of droplet-surface interactions*, Exp Therm Fluid Sci 31 (2006) 97–110.

Šikalo Š, Tropea C, Ganić EN, *Impact of droplets onto inclined surfaces*, J Colloid Interf Sci 286 (2005) 661–669.

Silaen A, Wang T, *Effect of turbulence and devolatilization models on coal gasification simulation in an entrained-flow gasifier*, Int J Heat Mass Tran 53 (2010) 2074–2091.

Slater SA, Leeming AD, Young JB, *Particle deposition from two-dimensional turbulent gas flows*, Int J Multiphas Flow 29 (2003) 721–750.

Soltani M, Ahmadi G, *On particle adhesion and removal mechanisms in turbulent flows*, J Adhes Sci Technol 8 (1994) 763–785.

Soltani M, Ahmadi G, *Direct numerical simulation of particle entrainment in turbulent channel flow*, Phys Fluids 7 (1995) 647–657.

Sommerfeld M, Huber N, *Experimental analysis and modelling of particle-wall collisions*, Int J Multiphas Flow 25 (1999) 1457–1489.

Sommerfeld M, Tropea C, *Experimental studies of deposition and splashing of small liquid droplets impinging on a flat surface*, Proceedings of the Sixth International Conference on Liquid Atomization and Spray Systems (1994) I-18.

Song W, Sun Y, Wu Y, Zhu Z, *Measurement and simulation of flow properties of coal ash slag in coal gasification*, AIChE J 57 (2011) 801–818.

Song W, Tang L, Zhu X, Wu Y, Rong Y, Zhu Z, Koyama S, *Fusibility and flow properties of coal ash and slag*, Fuel 88 (2009) 297–304.

Song W, Tang L, Zhu X, Wu Y, Zhu Z, Koyama S, *Flow properties and rheology of slag from coal gasification*, Fuel 89 (2010) 1709–1711.

Stevens AB, Hrenya CM, *Comparison of soft-sphere models to measurements of collision properties during normal impacts*, Powder Technol 154 (2005) 99–109.

Tabor D, *A simple theory of static and dynamic hardness*, Proc Roy Soc Lond 192 (1948) 247–274.

Thornton C, Ning Z, *A theoretical model for the stick/bounce behavior of adhesive, elastic-plastic spheres*, Powder Technol 99 (1998) 154–162.

Tominaga H, Yamashita T, Ando T, Asahiro N, *Simulator development of entrained flow coal gasifiers at high temperature and high pressure atmosphere*, IFRF Comb J, 200004 (2000).

Tran HN, Mao X, Kuhn DCS, Backman R, Hupa M, *The sticky temperature of recovery boiler fireside deposits*, Pulp Pap Can 103 (2002) 29–33.

van Beek MC, Rindt CCM, Wijers JG, van Steenhoven AA, *Rebound characteristics for 50-µm particles impacting a powdery deposit*, Powder Technol 165 (2006) 53–64.

van Dyk JC, Waanders FB, Benson SA, Laumb ML, Hack K, *Viscosity predictions of the slag composition of gasified coal, utilizing FactSage equilibrium modelling*, Fuel 88 (2009) 67–74.

Vascellari M, Arora R, Pollack M, Hasse C, *Simulation of entrained flow gasification with advanced coal conversion submodels. Part 1: Pyrolysis*, Fuel 113 (2013) 654–669.

Vascellari M, Arora R, Hasse C, *Simulation of entrained flow gasification with advanced coal conversion submodels. Part 2: Char conversion*, Fuel 118 (2014) 369–384.

Wall S, John W, Wang HC, Goren SL, *Measurements of kinetic energy loss for particles impacting surfaces*, Aerosol Sci Tech 12 (1990) 926–946.

Wang AB, Chen CC, *Splashing impact of a single drop onto very thin liquid films*, Phyis Fluids 12 (2000) 2155–2158.

Wang CY. *The unsteady oblique stagnation point flow*, Phys Fluids 28 (1985) 2046–2049.

Wang J, Liu H, Liang Q, Xu J, *Experimental and numerical study on slag deposition and growth at the slag tap hole region of Shell gasifier*, Fuel Process Technol 106 (2013) 704–711.

Wang XH, Zhao DQ, He LB, Jiang LQ, He Q, Chen Y, *Modeling of a coal-fired slagging combustor: development of a slag submodel*, Combust Flame 149 (2007) 249–260.

Watanabe H, Otaka M, *Numerical simulation of coal gasification in entrained flow coal gasifier*, Fuel 85 (2006) 1935–1943.

Wen CY, Chaung TZ, *Entrainment coal gasification modeling*, Ind Eng Chem Process Des Dev 18 (1979) 684–695.

Worthington AM, *A study of splashes* (1908), London, New York, Bombay, Calcutta: Longmans, Green, and Co.

Wu CY, Thornton C, Li LY, *Coefficients of restitution for elastoplastic oblique impacts*, Adv Powder Technol 14 (2003) 435–448.

Wu CY, Thornton C, Li LY, *A semi-analytical model for oblique impacts of elastoplastic spheres*, P Roy Soc A-Math Phy 465 (2009) 937–960.

Wu Y, Zhang J, Smith PJ, Zhang H, Reid C, Lv J, Yue G, *Three-dimensional simulation for an entrained flow coal slurry gasifier*, Energy Fuels 24 (2010) 1156–1163.

Xu S, Zhou Z, Gao X, Yu G, Gong X, *The gasification reactivity of unburned carbon present in gasification slag from entrained-flow gasifier*, Fuel Process Technol 90 (2009) 1062–1070.

Yang Z, Wang Z, Wu Y, Wang J, Lu J, Li Z, Ni W, *Dynamic model for an oxygen-staged entrained flow gasifier*, Energy Fuels 25 (2011) 3646–3656.

Yarin AL, *Drop impact dynamics: splashing, spreading, receding, bouncing…*, Annu Rev Fluid Mech 38 (2006) 159–192.

Yong SZ, Gazzino M, Ghoniem A, *Modeling the slag layer in solid fuel gasification and combustion – Formulation and sensitivity analysis*, Fuel 92 (2012) 162–170.

Yong SZ, Ghoniem A, *Modeling the slag layer in solid fuel gasification and combustion – Two-way coupling with CFD*, Fuel 6 (2012) 457–466.

Yoon SS, DesJardin PE, Presser C, Hewson JC, Avedisian CT, *Numerical modeling and experimental measurements of water spray impact and transport over a cylinder*, Int J Multiphas Flow 32 (2006)132–157.

Young GC, *Municipal solid waste to energy conversion processes: economic, technical, and renewable comparisons* (2010), John Wiley & Sons.

Zhao X, Zeng C, Mao Y, Li W, Peng Y, Wang T, Eiteneer B, Zamansky V, Fletcher T, *The surface characteristics and reactivity of residual carbon in coal gasification slag*, Energy Fuels 24 (2010) 91–94.

Zhbankova SL, Kolpakov AV, *Collision of water drops with a plane water surface*, Fluid Dyn 25 (1990) 470–473.

Zhong S, Baitalow F, Nikrityuk P, Gutte H, Meyer B, *The effect of particle size on the strength parameters of German brown coal and its chars*, Fuel 125 (2014) 200–205.

Zimmermann S, Taghipour F, *CFD modeling of the hydrodynamics and reaction kinetics of FCC fluidized-bed reactors*, Ind Eng Chem Res 44 (2005) 9818–9827.

Ziskind G, Fichman M, Gutfinger C, *Resuspension of particulates from surfaces to turbulent flows-Review and analysis*, J Aerosol Sci 26 (1995) 613–644.

Ziskind G, Fichman M, Gutfinger C, *Adhesion moment model for estimating particle detachment from a surface*, J Aerosol Sci 28 (1997) 623–634.

Appendix

The papers published by the author referring to this Ph. D. research program are reported.

XXXV Meeting of the Italian Section of the Combustion Institute

XXXV Meeting of the Italian Section of the Combustion Institute

PHYSICAL MODELLING OF ENTRAINED-FLOW SLAGGING COAL GASIFIERS

R. Carbone*, R. Solimene*, F. Montagnaro,**
M. Troiano*, P. Salatino*****
solimene@irc.cnr.it; fabio.montagnaro@unina.it
* Istituto di Ricerche sulla Combustione, Consiglio Nazionale delle Ricerche,
Piazzale Vincenzo Tecchio 80, 80125 Napoli, Italy
** Dipartimento di Scienze Chimiche, Università degli Studi di Napoli Federico II,
Complesso Universitario di Monte Sant'Angelo, 80126 Napoli, Italy
*** Dipartimento di Ingegneria Chimica, Università degli Studi di Napoli Federico II,
Piazzale Vincenzo Tecchio 80, 80125 Napoli, Italy

Abstract
This paper reports a theoretical and experimental study which aims to give a contribution in the development of a phenomenological model of the fate of coal/ash particles which considers the establishment of a particle segregated phase in the near-wall region of the gasifier. Mechanistic understanding of particle-wall interaction patterns in entrained-flow gasifiers has been carried out using the tool of the physical modelling, implemented by rational downscaling of the real system into a lab-scale cold entrained-flow reactor. Hydrodynamics of sticky wall-sticky particle regime has been characterized by partitioning measurements between simulated segregated phases and by visual observation of wall-layer phase.

1. Introduction

Modern entrained-flow coal gasifiers are characterized by operating conditions that promote ash migration/deposition onto the reactor walls whence the molten ash is drained and quenched at the bottom of the gasifier as a vitrified slag [1-3]. The recent literature has addressed the fate of char particles as they impinge on the wall slag layer [3-5]. This research group has contributed [6-8] to develop a phenomenological model of the fate of coal/ash particles which considers the establishment of a particle segregated phase in the near-wall region of the gasifier. This configuration can lead to an extensive coverage of the slag layer with carbon particles (segregation and coverage regime) beneficial to carbon conversion, as it gives rise to a longer mean residence time of carbon particles belonging to this segregated phase [6]. The phenomenological model has received some qualitative validation from analysis of the properties of ash streams generated in a full-scale entrained-flow gasification plant [7]. Moreover, the complex phenomenology associated with interaction of a particle-laden turbulent flow with the inelastic slag-covered wall of the gasifier has been the subject of numerical simulations [8], that confirmed both a possible near-wall accumulation of particles and the relevance of such phenomenon on the performance of entrained-flow gasifiers.

In the gasification chamber, coal particles are fed in such a way to form a lean-

dispersed particle-laden gas flow. This stream is characterized by inertia and turbulence, due to the centrifugal forces associated to the swirl or tangential flow and to the 'turbophoretic' transport near the reactor walls, respectively [6]. Other authors [5] described different particle-wall interaction patterns on the basis of the stickiness of both impinging particles and wall:

i) Sticky Wall-Sticky Particle (SW-SP), in which char particles with high carbon conversion impinge on the slag layer (Fig. 1a);
ii) Sticky Wall-No Sticky Particle (SW-NSP), for particles with a low carbon conversion impinging on the slag layer [3,6] (Fig. 1b);
iii) No Sticky Wall-Sticky Particle (NSW-SP), when high carbon conversion char particles impinge on either dry wall or a carbon-covered ash layer (Fig. 1c);
iv) No Sticky Wall-No Sticky Particle (NSW-NSP), referring to low carbon conversion char particles impinging on either dry wall or a carbon-covered ash layer (Fig. 1d).

The particle or the wall is considered sticky when both the particle carbon conversion is above a certain critical (threshold) value (as explained by Li et al. [4], who set this value around 88%) and the temperature is above the ash melting point.

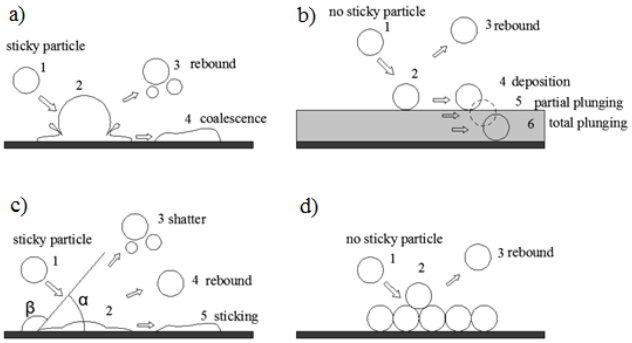

Figure 1. Micromechanical interaction patterns: a) SW-SP; b) SW-NSP; c) NSW-SP; d) NSW-NSP. (1) pre-impact, (2) impact, (3-6) post-impact.

This study aims at implementing a physical modelling by rational downscaling of the real gasifier into a lab-scale cold entrained-flow reactor. The operation of the downscaled reactor ensures the formation of two phases: a dispersed phase and a near-wall layer to reproduce and characterize the four micromechanical interaction patterns depicted in Fig. 1. The present work, in particular, is focused on the study of the first regime (SW-SP) for which, after the droplets impact on the liquid layer, it is possible to have rebound and/or coalescence of droplets, as shown in Fig. 1a.

2. Downscaled cold flow model reactor and experimental features

A downscaled lab-scale cold flow model reactor has been designed, built-up and developed in order both to avoid the difficulties related to the 'hard' operating conditions of entrained-flow slagging gasifiers in terms of pressure and

temperature and to ensure the optical accessibility of the reactor walls. The design regarded the choice of a suitable material to simulate, at atmospheric conditions and at low temperature, the slag phase behavior of an actual entrained-flow gasifier. In this respect, the use of melted wax (1-hexadecanol) has been reported by Shimizu et al. [9], even if for a different application. Following this path, Waradur E© wax has been selected (Vöelpker, Germany) (Table 1) after a comparison of the properties of different waxes with those typical of slag [2,3]. Choice criteria were inspired to have: i) similar wax-vs.-slag kinematic viscosity to ensure laminar flow of the melted phase along the wall; ii) peculiar wax properties, such as the plunging and overlayering criteria are not satisfied, as it is expected during particle-slag interaction in entrained-flow gasifiers [6].

Table 1. Comparison between wax and slag properties (viscosity, density, kinematic viscosity).

	Wax	*Slag*
μ (Pa s)	0.02-0.1 (at 130°C-90°C)	0.05-1 (at about 1200-1500°C)
ρ (kg m^{-3})	1000	2500-3000
ν (m^2 s^{-1})	2×10^{-5}-10^{-4}	1.7×10^{-5}-3.3×10^{-4}

The operating conditions have been set on the basis of the ratio between the reactor volume and the fuel inlet mass flow rate commonly found for industrial gasifiers. This ratio is around 5 m^3 s kg^{-1}. Assuming as lab-scale model reactor a cylindrical tube of 0.04 m ID and 1 m high, the fuel inlet mass flow rate is around 0.3 g s^{-1}. The inlet wax and air mass flow rates are 0.2 g s^{-1} and 1 m^3 h^{-1} (at 298 K), respectively. To simulate char particles in a slagging gasifier, the wax has been fed with a mean particle size of about 50–100 µm. The nozzle was chosen to give a full cone spray that ensures the formation of two phases: a dispersed phase and a wax layer on the internal wall of the reactor. The schematic representation of the experimental apparatus is reported in Fig. 2. Once the wax, collected in a storage vessel, is heated to the liquid state, a three-way valve is opened to convey it to the atomizer. The atomization section provides for two inlet air streams: an atomization air stream (0.3 m^3 h^{-1}) and a main air stream (0.7 m^3 h^{-1}). A 0.04 m ID Pyrex tube has been utilized as experimental reactor, to ensure the optical accessibility. The atomization air stream is fed to the nozzle, while the main air stream is uniformly conveyed, sideways to the nozzle after passing through a distribution plate, to the Pyrex tube.

In order to correctly operate the lab-scale reactor, three different temperatures have to be taken in account: the atomization temperature, i.e. the nozzle exit temperature, the main stream temperature, the wall temperature. The first one has to be set in such a way to ensure the complete liquid state of the wax droplets at the Pyrex tube inlet. Different aggregation states and viscosity values of wax in the

dispersed phase can be reached by varying the main stream temperature. The wall temperature can be varied to assure the desired aggregation state and viscosity value of the wall-layer wax. Thus, by tuning these three temperatures, it is possible to obtain the different micromechanical interaction patterns above discussed.

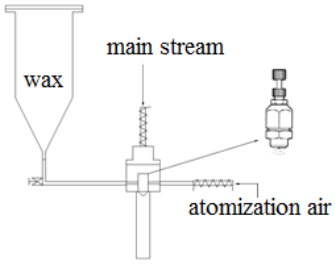

Figure 2. Experimental apparatus with a zoom of the atomization nozzle.

An experimental campaign has been carried out setting these temperatures to obtain the Sticky Wall-Sticky Particle (SW-SP) regime. Hydrodynamics has been characterized by partitioning measurements of the wax droplets into a dilute-dispersed phase, a dense-dispersed phase and the layered material on the wall at the exhaust and by visual observation of wall-layer phase at Pyrex tube exit. Partitioning measurements were carried out by measuring the mass fractions of wax exiting the reactor in the dispersed phase and in the wall-layer phase. To this end, the apparatus was equipped with a system (consisting by a vacuum flask, a trap, a filter and a pump) for the two phases wax collection at the bottom of the Pyrex tube. The dispersed phase wax mass fraction y^{lean} was used to evaluate a bulk-to-wall flux, thus, the mean bulk-to-wall mass-transfer coefficient k_m:

$$k_m = -\frac{1}{\tau} ln \frac{W_{WAX}^{lean}(z=L)}{W_{WAX}^{lean}(z=0)} = -\frac{1}{\tau} ln \left(1 - \frac{W_s}{W_{WAX}^{lean}(z=0)}\right) = -\frac{1}{\tau} ln(y^{lean}) \quad (1)$$

where τ is the mean gas residence time, while W_{wax}^{lean} and W_s are the wax mass flow rates in the lean phase and in the wall-layer phase, respectively. Furthermore, a CCD camera (Pulnix, 120 fps) equipped with a magnifying zoom lens was positioned at the bottom of the Pyrex tube to acquire images to estimate, by an image analysis technique, the mean velocity of the near-wall liquid layer. The experiments have been characterized by varying the atomization temperature, the atomization air flow rate, and Pyrex tube length.

3. Results and discussion

Partitioning measurements: Figure 3 reports the dilute dispersed phase fraction measured at the exhaust (wax droplets) and the mean bulk-to-wall mass transfer coefficient as functions of the atomization air flow rate (Q_a), the atomization temperature (T_a) and the Pyrex tube length (L).

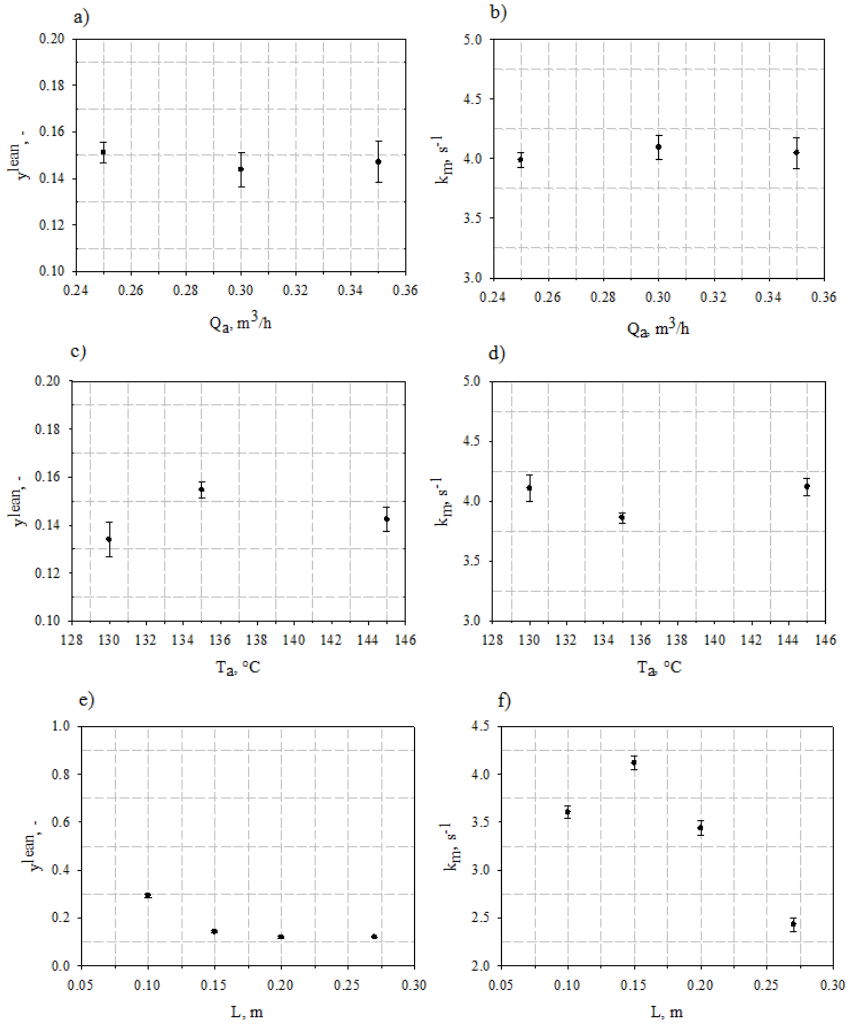

Figure 3. Effect of the atomization air flow rate Q_a, the atomization temperature T_a and the tube length L on: (a)-(c)-(e) the wax lean phase fraction and (b)-(d)-(f) the average mass transfer coefficient.

It can be observed that: i) Q_a slightly influences y^{lean} and k_m (Figs. 3a and 3b) at fixed τ, T_a and L (0.474 s, 145°C and 0.15 m, respectively); ii) y^{lean} and k_m (Figs. 3c and 3d) do not significantly vary with the atomization temperature (Q_a=0.3 m^3 h^{-1}, L=0.15 m). It is noteworthy that the wax viscosity at 145°C is about twice than that at 130°C; thus, at least for the range exploited, viscosity variations do not significantly affect the partitioning results. For these operating conditions, y^{lean} and k_m results to be in the order of 0.15 and 4s^{-1}, respectively. As regards the effect of tube length, the experiments were carried out at four different Pyrex tube lengths and the results are reported in Fig. 3e and 3f. The y^{lean}-vs.-L curve shows a strong

decay of y^{lean} with tube length, until it reaches a nearly constant value of about 0.12 at 0.2 m. Figure 3f shows the k_m-vs.-L curve: it is characterized by a non-monotonous trend, confirming what described by Montagnaro and Salatino [6]. Altogether, taking into account the whole set of experimental runs, y^{lean} varied between 0.3 and 0.12, and k_m between 2.3 and 4.2 s^{-1}.

Visual observations: Figure 4 shows a sequence of snapshots of wall liquid layer captured nearby the tube exit by the CCD camera at frame rate of 120fps. The analysis of the snapshots highlights the presence of micron-sized air bubbles entrapped in the wall melted wax layer and descending along vertical streamlines. Assuming that air bubbles behave as seeding "particles", the wall liquid layer is characterized by laminar flow as expected. Beside following the air bubbles trajectory in the wall layer, it is possible to estimate a descending velocity of wall melted-wax layer in the order of 3-6 mm s^{-1} for each tube length. Further investigations are necessary to determine the velocity profile and the wall layer thickness.

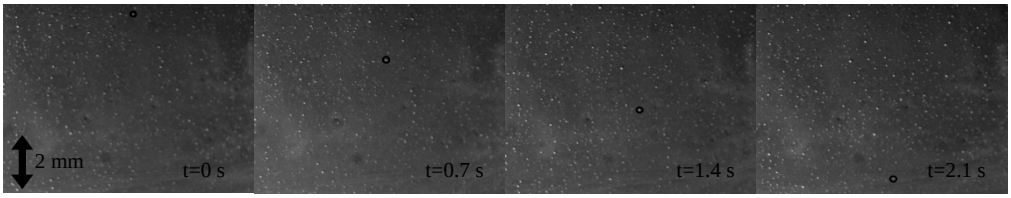

Figure 4. Images sequence captured by CCD camera. Open circle: a descending air bubble entrapped in the wall melted-wax layer.

References

[1] Shimizu, T., Tominaga, H., *Fuel* 85:170–178 (2006).
[2] Ni, J., Yu, G., Guo, Q., Zhou, Z., Wang, F., *Energy Fuels* 25:1004–1009 (2011).
[3] Shannon, G.N., Rozelle, P.L., Pisupati, S.V., Sridhar, S., *Fuel Process. Technol.* 89:1379–1385 (2008).
[4] Li, S., Wu, Y., Whitty, K.J., *Energy Fuels* 24:1868–1876 (2010).
[5] Yong, S.Z., Ghoniem, A., *Fuel* 97:457–466 (2012).
[6] Montagnaro, F., Salatino, P., *Combust. Flame* 157:874–883 (2010).
[7] Montagnaro, F., Brachi, P., Salatino, P., *Energy Fuels* 25:3671–3677 (2011).
[8] Ambrosino, F., Aprovitola, A., Brachi, P., Marra, F.S., Montagnaro, F., Salatino, P., *Combust. Sci. Technol.* 184:871–887 (2012).
[9] Shimizu, T., Haga, D., Mikami, G., Takahashi, T., Horinouchi, K., *Proc. 13th Int. Conf. Fluidization*, Gyeong-ju, Korea, Paper #83 (2010).

10.4405/35proci2012.VIII2

Proceedings

XXXVI Meeting of the Italian Section of The Combustion Institute

XXXVI Meeting of the Italian Section of The Combustion Institute

AN EXPERIMENTAL INVESTIGATION ON NEAR-WALL PARTICLE SEGREGATION IN ENTRAINED-FLOW SLAGGING COAL GASIFIERS

Ramona Carbone*, Roberto Solimene*, Fabio Montagnaro, Maurizio Troiano***, Piero Salatino*****

solimene@irc.cnr.it; fabio.montagnaro@unina.it

*Istituto di Ricerche sulla Combustione, Consiglio Nazionale delle Ricerche, Piazzale Vincenzo Tecchio 80, 80125 Napoli (Italy)

**Dipartimento di Scienze Chimiche, Università degli Studi di Napoli Federico II, Complesso Universitario di Monte Sant'Angelo, 80126 Napoli (Italy)

*** Dipartimento di Ingegneria Chimica, dei Materiali e della Produzione Industriale, Università degli Studi di Napoli Federico II, P.le V. Tecchio 80, 80125 Napoli (Italy)

Abstract

This paper reports on preliminary results of an experimental investigation aimed at the development of a phenomenological model of the fate of coal/ash particles in entrained-flow slagging coal gasifiers, which considers the establishment of a particle segregated phase in the near-wall region of the gasifier. Mechanistic understanding of particle-wall interaction patterns has been carried out using the tool of the physical modeling. To this end, a cold flow model reactor has been designed and set up, where molten wax is air-atomized into a mainstream of air to simulate the fate of char/ash particles in a real hot environment. Sticky wall-sticky particle regime has been characterized, from a hydrodynamic point of view, by partitioning measurements between simulated segregated phases and by visual observation of the impact of sticky particles on the sticky wall.

1. Introduction

Modern entrained-flow coal gasifiers are characterized by operating conditions that promote ash migration/deposition onto the reactor walls, whence the molten ash is drained and quenched at the bottom of the gasifier as a vitrified slag [1-3]. The recent literature has addressed the fate of char particles as they impinge on the wall slag layer [3-5]. This research group has contributed [6-9] to develop a phenomenological model of the fate of coal/ash particles, which considers the establishment of a particle segregated phase in the near-wall region of the gasifier. This configuration can lead to an extensive coverage of the slag layer with carbon particles (segregation and coverage regime) beneficial to carbon conversion, as it gives rise to a longer mean residence time of carbon particles belonging to this segregated phase [6]. The phenomenological model has received some qualitative validation from analysis of the properties of ash streams generated in a full-scale entrained-flow gasification plant [7]. Moreover, the complex phenomenology

associated with interaction of a particle-laden turbulent flow with the inelastic slag-covered wall of the gasifier has been the subject of numerical simulations [8,9], that confirmed both a possible near-wall accumulation of particles and the relevance of such phenomenon on the performance of entrained-flow gasifiers. In the gasification chamber, coal particles are fed through nozzles as a lean-dispersed particle-laden gas flow. Inertial and turbophoretic mechanisms seem to be predominant, the first being enhanced by swirled or tangential flow, and the latter being active near the reactor walls. Moreover, inertia is relevant to coarser particles, turbophoresis to finer ones [6]. It is possible to classify all the possible particle-wall interaction patterns on the basis of the stickiness of both impinging particles and wall [5]:

i) Sticky Wall-Sticky Particle (SW-SP), in which char particles with high carbon conversion impinge on the slag layer (Fig. 1a);
ii) Sticky Wall-No Sticky Particle (SW-NSP), for particles with a low carbon conversion impinging on the slag layer [3,6] (Fig. 1b);
iii) No Sticky Wall-Sticky Particle (NSW-SP), when high carbon conversion char particles impinge on either dry wall or a carbon-covered ash layer (Fig. 1c);
iv) No Sticky Wall-No Sticky Particle (NSW-NSP), referring to low carbon conversion char particles impinging on either dry wall or a carbon-covered ash layer (Fig. 1d).

The particle or the wall is considered sticky when both the particle carbon conversion is above a certain critical (threshold) value (as explained by Li et al. [4], who set this value around 90%) and the temperature is above the ash melting point.

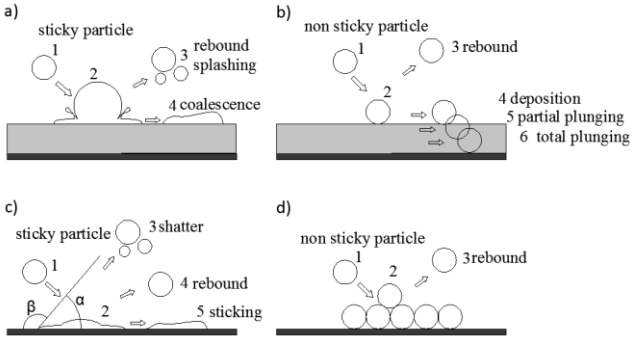

Figure 1. Micromechanical interaction patterns: a) SW-SP; b) SW-NSP; c) NSW-SP; d) NSW-NSP. (1) pre-impact, (2) impact, (3-6) post-impact.

This study aims at investigating near-wall particle segregation by using a lab-scale cold entrained-flow reactor. The cold flow model reactor ensures the formation of a dispersed phase and a near-wall layer to reproduce and characterize the four micromechanical interaction patterns depicted in Fig. 1. The present work, in particular, is focused on the study of the first regime (SW-SP) for which, after the droplets impact on the liquid layer, it is possible to have rebound and/or

coalescence of droplets, as shown in Fig. 1a.

2. Cold flow model reactor and experimental features

Industrial entrained-flow slagging gasifiers operate at 'hard' conditions in terms of pressure and temperature, thus, a lab-scale cold flow model reactor has been designed, built-up and developed in order to permit the optical accessibility of the reactor walls. The plastic/fluid behaviour of softened or molten ash and of the wall slag layer has been simulated, at nearly ambient conditions, by molten wax as a surrogate of fuel ash. In this respect, the use of melted wax (1-hexadecanol) has been reported by Shimizu et al. [10], even if for a different application. After a screening of different candidates, Waradur E^{TM} (Völpker, Germany) was selected, as the rheological/mechanical properties of this wax resembled those of a typical coal slag. Wax viscosity lies in the range 0.02-0.1 kg m^{-1}s^{-1} as the temperature ranges between 130°C and 90°C, and wax density is around 1000 kg m^{-3}. Accordingly, the kinematic viscosity is in the order of 10^{-5}-10^{-4} m^2 s^{-1}, consistent with values reported in the literature for coal slag [2,3]. The kinematic viscosities of the wax are consistent with the establishment of laminar flow of the molten phase along the reactor walls. Besides, taking into account the surface tension (0.03 kg s^{-2} at 100°C), wax properties are such that the entrapment and over-layering criteria are not satisfied, and the segregation or segregation-coverage regime are likely to be established, as expected for realistic particle-slag interaction in entrained-flow gasifiers [6,7]. The wax was liquified and stored in a 9 L heated vessel. A three-way valve could be opened to convey the wax to the atomization vessel, consisting of air distribution and atomizer positioning sections. The atomization system generated a spray of molten wax in the model reactor which gave rise, upon deposition onto the wall, to a layer of molten wax. The nozzle was a commercial Delavan^{TM} atomizer (AL model), designed so as to generate a spray of conical shape with an aperture angle of θ_{max}=25° and a uniform cross-sectional distribution of the atomized dispersed phase. Air-assisted atomization of wax resulted into droplets of 50-100 μm size. The reactor consisted of a Pyrex^{TM} tube (D=0.04 m-ID). A mainstream of air was fed at the top of the air section, while the atomization air was fed directly to the nozzle. The schematic representation of the experimental apparatus and the parameters of the nozzle jet are reported in Fig. 2.

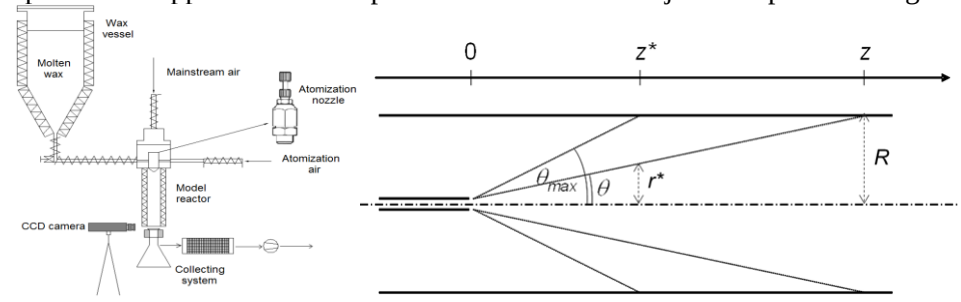

Figure 2. Experimental apparatus with a zoom of the atomization nozzle (left); geometrical parameters of the jet in the model reactor (right).

The operating conditions have been set on the basis of the ratio between the reactor volume and the fuel inlet mass flow rate commonly found for industrial gasifiers. This ratio is around 5 m^3 s kg^{-1}. Assuming as lab-scale model reactor a cylindrical tube of 0.04 m-ID and 1 m high, the fuel inlet mass flow rate is around 0.3 g s^{-1}. The inlet wax and air mass flow rates are 0.2 g s^{-1} and 1 m^3 h^{-1} (Q_a=0.3 m^3 h^{-1} for atomization air and Q_{ms}=0.7 m^3 h^{-1} for main air stream, both measured at 298 K), respectively.

In order to correctly operate the lab-scale reactor, three different temperatures have to be taken in account: the atomization temperature (T_a), i.e. the nozzle exit temperature, the main stream temperature, the wall temperature. The first one has to be set in such a way to ensure the complete liquid state of the wax droplets at the Pyrex tube inlet. Different aggregation states and viscosity values of wax in the dispersed phase can be reached by varying the main stream temperature. The wall temperature can be varied to assure the desired aggregation state and viscosity value of the wax wall layer. Thus, by tuning these three temperatures, it is possible to obtain the different micromechanical interaction patterns above discussed.

Experimental tests aimed at characterizing the phenomenology of the interaction between the dispersed phase generated by the spray and the reactor walls. For the SW-SP regime, partitioning measurements of the atomized wax between the dispersed and the wall phases were quantitatively assessed as a function of the distance from the nozzle. To accomplish this task, the reactor was equipped with a system (consisting by a vacuum flask, a trap, a filter and a pump) for the two phases wax collection at the bottom of the Pyrex tube. The mass flow rates in the dispersed phase and in the wall layer phase were obtained by dividing the amounts of wax cumulatively collected by the duration of the test. Visual observation and recording of the impact of sticky particles on the sticky wall was also accomplished by means of a CCD camera (Pulnix™ 6710) equipped with a magnifying zoom lens. The experiments were characterized by varying the main stream air flow rate and the Pyrex tube length.

3. Results and discussion

Partitioning measurements: Figure 3 reports the dilute-dispersed phase fraction of wax (y^{lean}) measured at the exhaust as a function of the reactor length (L) and of the main stream air flow rate. Figure 3a) reports values of y^{lean} measured in experiments carried out with different L-values, at fixed Q_a, Q_{ms} and T_a (0.3 m^3 h^{-1}, 0.7 m^3 h^{-1} and 145°C, respectively). It shows that y^{lean} abruptly decreases from nearly 0.91 in the proximity of the nozzle (L=0.03 m) to approach 0.12 for $L \geq 0.20$ m. Figure 3a) also compares the experimental plot with limiting lines corresponding to idealized NSW-NSP and SW-SP regimes. In the first case (NSW-NSP), the wall reflects impinging particles according to a nearly elastic interaction pattern. Accordingly, y^{lean} would be 1 for any L. The other idealized limiting curve (SW-SP) is obtained by considering the conical shape of the jet and the uniform distribution of the dispersed phase across the jet (Fig. 2). Additional assumptions

are that droplets impinging the wall under the effect of inertia are deposited thereon without rebound.

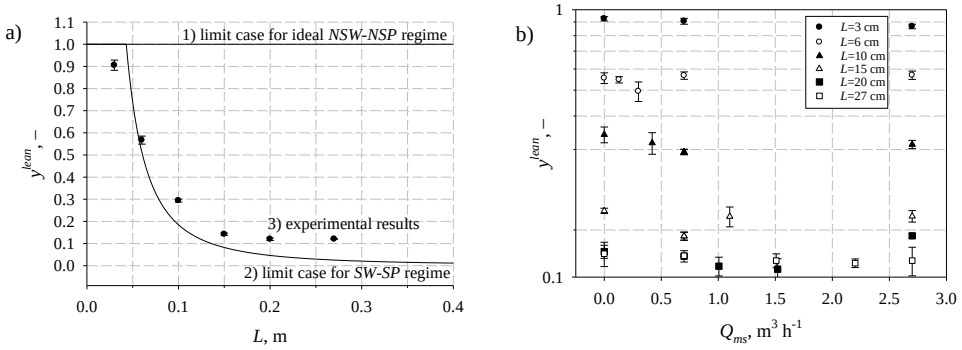

Figure 3. Effect of the tube length (a) and of the main stream gas flow rate (b) on the wax lean phase fraction.

According to the geometry of the nozzle and of the reactor (Fig. 2), the impact of molten wax droplets becomes significant only at a distance $z \geq z^*$ from the nozzle, the value of z^* being 0.043 m in the present case. Geometrical arguments suggest that:

$$y^{lean}(z) = \begin{cases} 1 & for \quad z < z^* \\ \dfrac{q\pi(r^*)^2}{q\pi R^2} = \left(\dfrac{r^*}{R}\right)^2 = \left(\dfrac{z^*}{z}\right)^2 & for \quad z \geq z^* \end{cases} \qquad (1)$$

where q is the axial wax mass flux at $z=z^*$, and r^* and R are represented in Fig. 2. Equation (1) is plotted in Fig. 3a) as the idealized limiting curve corresponding to the SW-SP regime. Comparing the experimental data points with the limiting curves, the following features may be recognized: i) experimental data points lie much closer to the SW-SP regime limiting curve than to the other one, consistently with the operating conditions of the tests which promoted a molten status of both entrained wax droplets and of the wall layer; ii) values of y^{lean} slightly depart from 1 already at $z<z^*$. This behaviour is related to moderate backmixing of the dispersed phase associated with recirculation and main stream gas entrainment developing close to the nozzle; iii) the experimental data points lie somewhat above the theoretical SW-SP regime limiting curve for large values of L. This might result from either moderate droplet rebound at the wall followed by re-entrainment, or by a certain degree of ineffectiveness of inertial forces in promoting impingement and entrapment of droplets as they are simultaneously invested by the main stream flow directed parallel to the wall. It must be underlined that the transfer of droplets to the wall in the fully-developed flow downstream of the nozzle by Brownian or turbophoretic mechanisms is bound to be rather ineffective considering that the Reynolds number is in the order of 500.
Figure 3b) shows the effect of the main stream gas flow rate on y^{lean}: when L was

fixed and varying Q_{ms} up to 2.7 m^3 h^{-1} at fixed T_a and Q_a (145°C and 0.3 m^3 h^{-1}, respectively), y^{lean} did not significantly vary. On the other hand, y^{lean} decreased as L increased at fixed Q_{ms}, in line with what observed in Fig. 3a). These findings further suggest that the axial profile of y^{lean} is largely dominated by the hydrodynamics of the jet.

Visual observations: Figure 4 reports two temporal sequences of snapshots captured by the CCD camera during a typical test (Q_a=0.3 m^3 h^{-1}, T_a=138°C and L=0.20 m). As a result of the impact of sticky particles on the sticky wall, coalescence was by far the predominant process, though occasional droplet rebound and re-entrainment into the dispersed phase could be observed.

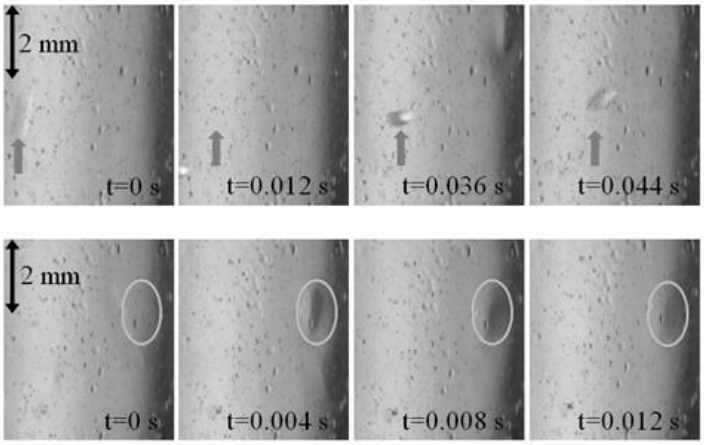

Figure 4. Rebound (up) and coalescence (down) of sticky wax droplets impinging on the sticky wax wall. Snapshots captured at a frame rate of 250 fps.

References

[1] Shimizu, T., Tominaga, H., *Fuel* 85:170–178 (2006).
[2] Ni, J., Yu, G., Guo, Q., Zhou, Z., Wang, F., *Energy Fuels* 25:1004–1009 (2011).
[3] Shannon, G.N., Rozelle, P.L., Pisupati, S.V., Sridhar, S., *Fuel Process. Technol.* 89:1379–1385 (2008).
[4] Li, S., Wu, Y., Whitty, K.J., *Energy Fuels* 24:1868–1876 (2010).
[5] Yong, S.Z., Ghoniem, A., *Fuel* 97:457–466 (2012).
[6] Montagnaro, F., Salatino, P., *Combust. Flame* 157:874–883 (2010).
[7] Montagnaro, F., Brachi, P., Salatino, P., *Energy Fuels* 25:3671–3677 (2011).
[8] Ambrosino, F., Aprovitola, A., Brachi, P., Marra, F.S., Montagnaro, F., Salatino, P., *Combust. Sci. Technol.* 184:871–887 (2012).
[9] Ambrosino, F., Aprovitola, A., Brachi, P., Marra, F.S., Montagnaro, F., Salatino, P., *Fuel* http://dx.doi.org/10.1016/j.fuel.2013.03.040 (2013).
[10] Shimizu, T., Haga, D., Mikami, G., Takahashi, T., Horinouchi, K., *Proc. 13th Int. Conf. Fluidization*, Gyeong-ju, Korea, Paper #83 (2010).

2013 International Conference on Coal Science and Technology Proceedings

September 29-October 3, 2013
State College, PA, USA
Penn Stater Hotel & Conference Center

Published by EMS Energy Institute, The Pennsylvania State University

PENNSTATE
1855

EARTH AND MINERAL SCIENCES
ENERGY INSTITUTE
COLLEGE OF EARTH AND MINERAL SCIENCES

Modeling and Experiments (in a Cold Flow Model Reactor) to Study Char-Wall Interaction and Segregation Phenomena During Slagging Entrained-Flow Coal Gasification

Maurizio Troiano[1], Andrea Aprovitola[2], Fiorenzo Ambrosino[3], Francesco Saverio Marra[4], Piero Salatino[1], Fabio Montagnaro[5], Roberto Solimene[4]

[1]*Dipartimento di Ingegneria Chimica, dei Materiali e della Produzione Industriale, Università degli Studi di Napoli Federico II, Piazzale Vincenzo Tecchio 80, 80125 Napoli, Italia*
[2]*Istituto di Calcolo e Reti ad Alte Prestazioni, Consiglio Nazionale delle Ricerche, Via Pietro Castellino 111, 80131 Napoli, Italia*
[3]*ENEA, CR Portici, Piazzale Enrico Fermi 1, 80055 Portici, Italia*
[4]*Istituto di Ricerche sulla Combustione, Consiglio Nazionale delle Ricerche, Piazzale Vincenzo Tecchio 80, 80125 Napoli, Italia*
[5]*Dipartimento di Scienze Chimiche, Università degli Studi di Napoli Federico II, Complesso Universitario di Monte Sant'Angelo, 80126 Napoli, Italia*
fabio.montagnaro@unina.it

Abstract

Aim of this communication is to report on the recent findings by this research group on modeling and experiments, the latter carried out in a cold flow model reactor, to study char-wall interaction and segregation phenomena during slagging entrained-flow coal gasification. This work illustrates how different modeling approaches can be jointly used to understand segregation patterns of char particles. RANS-based simulations of the full-scale geometry with coal particle injection and tracking aimed to obtain the behaviour of the flow field and particle trajectories. Simulations enabled to estimate the effect of swirl and tangential flow on the bulk-to-wall char particle deposition rate. Then, RANS results were adopted in a more detailed model based on the solution of the filtered Navier-Stokes equations, where a turbulence LES approach for the Eulerian gas phase was applied. This enabled the assessment of the char particle deposition rates and the nature of char-slag interaction. This paper also reports on preliminary results of an experimental investigation aimed at the development of a phenomenological model of the fate of coal/ash particles. The study specifically addresses the interaction between the lean-dispersed particle phase and the reactor walls, and the establishment of a particle segregated phase in the near-wall region of the gasifier. A lab-scale cold flow reactor has been designed and set up, where molten wax is air-atomized into a mainstream of air to simulate the fate of char/ash particles in a real hot environment. Characterization of the hydrodynamics of the lean-dispersed phase, of its interaction with the wall, of the build-up of the liquid wall layer has been accomplished with a focus on the 'sticky wall-sticky particle' subregime. The particle deposition rate at the wall and the wax droplets partitioning between the lean-dispersed phase and the wall liquid layer have been assessed under a range of operating conditions.

Brief Introduction

Entrained-flow (EF) coal gasifiers are characterized by operating conditions that promote ash migration/deposition onto the reactor walls, whence the molten ash is drained and quenched at the bottom of the gasifier as a vitrified slag [1,2]. The fate of char particles as they impinge on the wall slag layer has been recently addressed [3–7]. In one of these works [4], it has been developed a phenomenological model of the fate of coal/ash particles, which considers the establishment of a particle segregated phase in the near-wall region of the gasifier. It has been highlighted that char particles impinging on the wall slag layer can be either entrapped inside the melt (this prevents further progress of combustion/gasification) or adhere onto the slag layer's surface. In the latter case, and if the coverage of the slag layer with carbon particles is extensive, a dense-dispersed annular phase may establish in the close proximity of the wall ash layer, where the excess impinging char particles that cannot be accommodated on the slag surface accumulate. The establishment of this annular phase, slower than the fast lean-dispersed particle phase, is beneficial to carbon conversion since the mean residence time of char particles belonging to this dense phase would be longer, with respect to what happens in the lean phase. In another paper [8], this phenomenological model has received qualitative validation from analysis of the properties of ash streams generated in a full-scale plant.

Nonetheless, modeling coal gasification under EF conditions is still a challenging goal with broad areas un uncertainty [9–13]. Almost all of the CFD-models related to the topic rely on the Reynolds average Navier-Stokes (RANS) approach to take into account the effect of the turbulence on the flow field (solving for field variables averaged in time). The RANS approach can limit the predictive capabilities of the simulations, because several closure models have to be adopted to introduce the effects of the unresolved time scales on the averaged fields. Despite such drawbacks, the adoption of the RANS approach is unavoidable to limit the computational power required to simulate full scale configurations, since EF gasifiers are characterized by a wide range of turbulence scales.

Micromechanics of Particle-Slag Interaction

Coal particles are fed to the gasification chamber through nozzles as a lean-dispersed particle-laden gas flow. Particle transport to the wall is controlled by inertial forces, possibly enhanced by swirled or tangential flow, and by the "turbophoretic" component which becomes particularly active near the reactor walls. Both mechanisms play a significant role in the transport of particles from the dispersed phase to the walls, and in the build-up of a slag layer. In this context, the stickiness of the particle and of the wall layer play a major role. Plastic behaviour and stickiness are emphasized as the content of the inherently refractory carbon decreases, i.e. as the carbon conversion degree X_C increases and as the temperature is beyond the ash melting point. Yong et al. [14] described different particle-wall interaction patterns on the basis of the stickiness of the impinging particles and of the wall layer. These patterns are outlined in Fig. 1 (left). *Sticky wall - sticky particle* (*SW-SP*): char particles with low carbon content (large X_C) impinge on the slag layer; *sticky wall - non sticky particle* (*SW-NSP*): particles characterized by large carbon content impinge on the slag layer; *non sticky wall - sticky particle* (*NSW-SP*): char particles characterized by low carbon content impinge on either a dry wall or on a carbon-covered slag layer; *non sticky wall - non sticky particle* (*NSW-NSP*): char particles with large carbon content impinge on either a dry wall or on a carbon-covered ash layer.

Figure 1 (right) shows how the different near-wall char-slag segregation regimes can occur as a function of the reactor axial coordinate and of the progress of X_C. For the first regime (*SW-SP*), sticky particles impinging on the slag layer can either rebound or be entrapped by the liquid surface, contributing, in the latter case, to the wall layer build-up. *SW-NSP* interactions were also studied to establish entrapment, coverage and rebound criteria. Montagnaro and Salatino [4] developed theoretical criteria for particles plunging into the slag layer and for full carbon-coverage of the wall ash layer. Shannon et al. [3] developed a detailed analysis of the dynamics of a carbon particle after impact on the wall slag layer. The possibility that a particle deposited on the slag layer's surface can subsequently suffer partial/total

plunging as the particle gasification degree increases (thus letting the particle itself transform from non sticky to sticky) was postulated and experimentally verified by Montagnaro et al. [8]. *NSW-SP* interactions have also been the subject of investigation in different contexts. Ni et al. [2] proposed a sub-model for predicting slag droplets interaction with the wall, hence slag layer formation. Shimizu and Tominaga [1] developed a model (valid for the *NSW-NSP* case) for char capture by a slag layer covered, at least partially, by other char particles. In their model, a char particle impinging the slag surface will rest, whereas it will be repelled if it reaches the part of the slag layer which is covered by unreacted or partly reacted carbon-rich char particles.

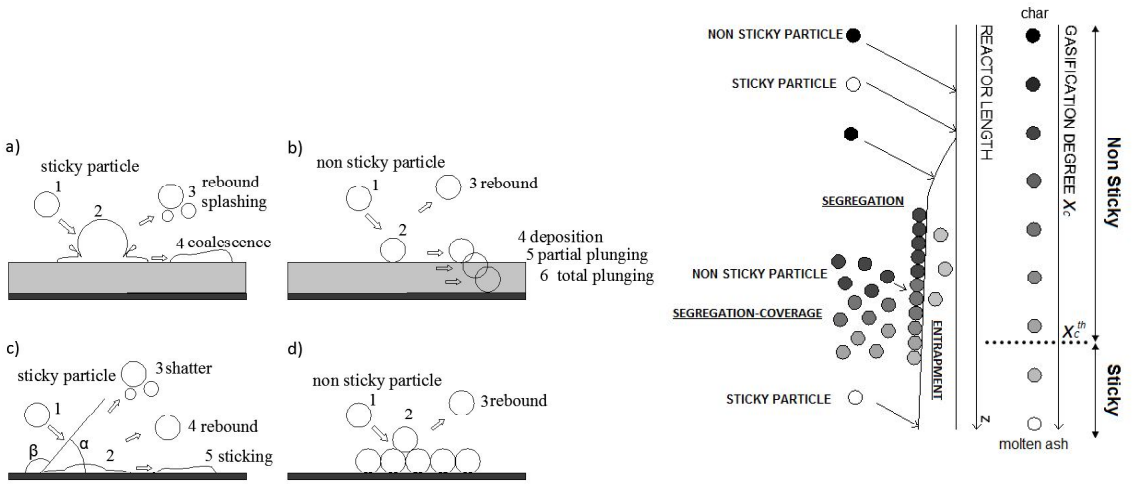

***Figure 1**. Left: micromechanical interaction patterns; regimes a) SW-SP; b) SW-NSP; c) NSW-SP; d) NSW-NSP. (1) pre-impact, (2) impact, (3-6) post-impact. Right: particle-wall micromechanical interactions and near-wall segregation regimes along the reactor axial coordinate (X_C^{th} is the threshold X_C-value).*

Structure and Aim of This Work

Aim of this communication is to report on the recent findings by this research group on modeling and experiments, the latter carried out in a cold flow model reactor, to study char-wall interaction and segregation phenomena during slagging EF coal gasification.

On the modeling side, a particular emphasis is devoted to the char-slag interaction, for which a very detailed model, based on the discrete element method (DEM) for the solid phase and the large eddy simulation (LES) approach for the gas phase, has been adopted. More in particular, particle velocities and trajectories as they impinge the confining walls covered by the slag are provided by the adoption of a DEM-RANS CFD model. At this level, the focus is on the assessment of the distribution of particles in the gasifier, on the identification of the average particles load in the different zones of the gasifier and of their velocity and angle of impact onto the confining surface. Therefore, an approach based on a RANS model for the gas phase and on a Lagrangian particle tracking (LPT) algorithm to evaluate the particle movement is considered pertinent. A further level of modeling addresses the detailed simulation of the particle-wall interaction, using an accurate DEM-LES model where the real particles trajectories are affected by the interaction with an unsteady turbulent field and with the confining surface. Properties of this surface are varied to take into account the different mechanisms of particle deposition due to the presence of a bare wall, a molten slag, or a slag already covered by a layer of particles. This latter level enables the assessment of the particle deposition regimes that are likely to occur under the assigned boundary conditions.

On the experimental side, the tool is that of the physical modeling. Features of particle-wall interaction have been investigated in a lab-scale cold EF reactor. The reactor is equipped with a nozzle whence

molten wax is air-atomized into a mainstream of air. The temperature of the mainstream is adjusted to tune the viscosity (and the stickiness) of the wax droplets. The temperature of the wall may also be adjusted to control the formation, viscosity and stickiness of the liquid wall layer. Assessment of the flow and segregation patterns in the reactor is based on direct visual observation, as the reactor is optically accessible. The partitioning of the wax droplets into the different phases is characterized by their selective collection at the reactor exhaust. The model reactor and the test protocol aim at providing insight into the detailed mechanisms of interaction between dispersed particles and the wall liquid layer.

Basis for the Modeling Part: Development of the Gasifier Model

Both modeling levels are based on a CFD Eulerian-Lagrangian approach. The Eulerian gas phase is treated with a RANS approach at the first level, while a LES approach is adopted at the second level. In both levels the DEM is used to describe the fate of the solid phase, following a LPT method where the gas phase velocities are those obtained with the RANS and LES approaches, respectively. To optimize the performances of RANS computations, the parcel numerical object is used instead of the particle. A parcel is a group of identical particles considered to be coincident so they all have the same trajectory. Tracked particles are considered point-wise and supposed to be spherical, rigid and non rotating. The OpenFOAM (Open Field Operation and Manipulation) code is adopted to compute the numerical solutions in the two CFD levels of modeling procedure. The OpenFOAM CFD Toolbox is a free, open source CFD software package released and supported by EsiCFD, developed in the framework of finite volume (FV) methods. The core technology of OpenFOAM is a flexible set of efficient C++ modules. These are used to build the flow solvers. The domain decomposition parallelism is intrinsic to the design of OpenFOAM and integrated at a low level so that solvers can generally be developed without the need for any parallel-specific coding. In OpenFOAM, the spatial discretization of the gas phase equations is performed with a FV discretization on arbitrary 3D domains, partitioned through unstructured meshes of polyhedral cells. The algorithm implemented in OpenFOAM for the LPT is the so-called TrackToFace method described in Macpherson et al. [15]. It solves the equations of particles motion detecting the face where the particle trajectory intersects the cell's faces, to avoid the need for a time-consuming search algorithm of the cell where the particle locates during its movement. A one-way coupling approach is considered in this work: the particle phase motion is affected by fluid phase flow conditions but the contrary does not hold. This is considered a valid assumption if the particle volumetric concentration is not too high (dispersed regime). Therefore, the effective structure of the dense but very thin film of solid particles in the dense-dispersed phase cannot be reproduced, limiting the present analysis to the incipient formation of such a layer.

At the first level, a U-RANS (Unsteady-RANS) simulation method for the Eulerian phase has been applied to simulate the gasification chamber investigated by Sommerfeld and Qiu [16]. The char particles migration on the slag layer is influenced by the turbulent motion induced by the swirl applied at the incoming streams. Induced flow structures, whose dimensions are on the order of the swirler diameter, are inherently unsteady. Accordingly, a time-dependent description of their dynamics is preferred to a time-averaged approach to investigate the deposition mechanisms.

The second level is based on the adoption of the LES method to solve the model equations of the Eulerian continuous phase. The LES method relies on the separation of turbulent flow spatial scales among resolved and non-resolved ones, provided by a low-pass filtering procedure applied to the governing equations. The effect of the unresolved scales on the resolved ones is recovered through the adoption of the sub grid scale (SGS) models in the filtered equations [17]. Since the LES approach does not introduce an explicit time average of the model equations, it contains a larger amount of time frequencies with respect to the case of U-RANS simulation. For variable-density flows, the Favre filter is usually adopted, which corresponds to a volume average in a FV method. The filter width in the present formulation is kept equal to the control volume measure, hence it is implicitly defined in the domain discretization. Therefore, a very fine grid has to be used in order to correctly locate the cut-off frequency of the filter at the tail of the inertial range of the kinetic energy spectrum. As commonly done in LES using FV methods,

the equations are discretized starting from the integral counterparts, that can therefore be interpreted as the evolution equations for the filtered variables. The built-in OpenFOAM compressible version of localized dynamic model LDKM developed by Kim et al. [18] is used to compute the subgrid viscosity. The model is supposed to tune the effects of the SGS on the resolved field during the computation. The reader is referred to the previous work by Ambrosino et al. [13,19] for a detailed description of the model.

Basis for the Experimental Part: the Model Reactor

A physical downscaled cold flow model of an EF gasifier has been designed and set up, Fig. 2 (left). Downscaling did not conform to rigorous rules, but rather aimed at reproducing the general features of the interaction between a lean-dispersed particle phase and a confining wall. The plastic/fluid behaviour of softened or molten ash and of the wall slag layer has been simulated, at nearly ambient conditions, by molten wax as a surrogate of fuel ash. After a screening of different candidates, Waradur E^{TM} (Völpker, Germany) was selected, as the rheological/mechanical properties of this wax resembled those of a typical coal slag. Wax viscosity lies in the range 0.02-0.1 kg m^{-1} s^{-1} as the temperature ranges between 130°C and 90°C [20], and wax density is around 1000 kg m^{-3}. Accordingly, the kinematic viscosity is in the order of 10^{-5}-10^{-4} m^2 s^{-1}, consistent with values commonly reported in the literature for coal slag. Taking into account the surface tension (0.03 kg s^{-2} at 100°C), wax properties are such that the segregation or segregation-coverage regimes (Fig. 1) are likely to be established, as expected for realistic particle-slag interaction in EF gasifiers [4,8].

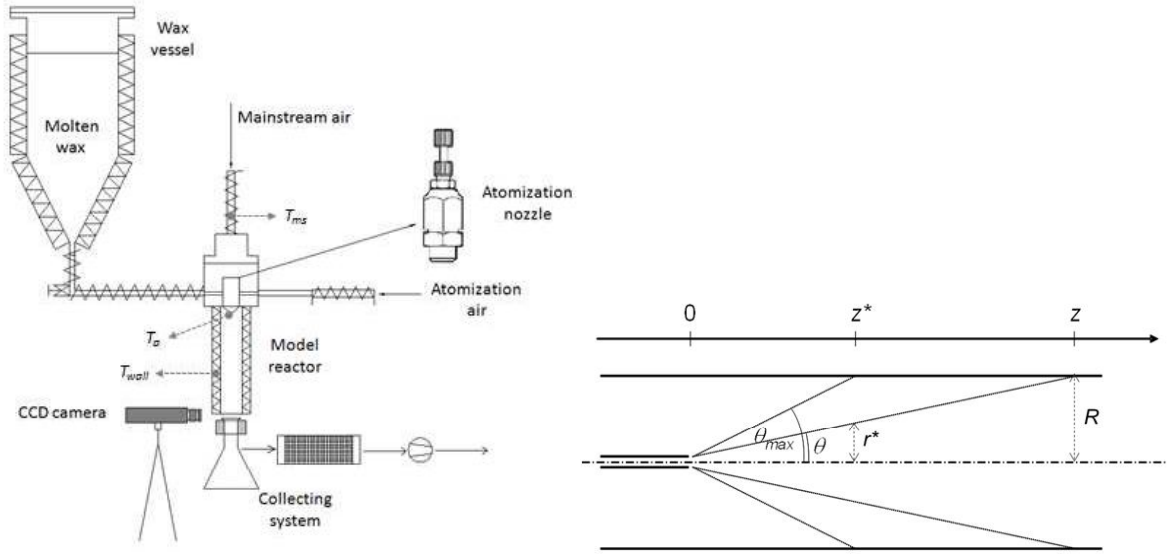

***Figure 2**. Left: scheme (not to scale) of the downscaled cold flow model reactor with a detailed view of the atomization nozzle (T_a=atomization temperature; T_{ms}=mainstream temperature; T_w=wall temperature). Right: geometrical parameters of the jet in the model reactor.*

The wax was liquefied and stored in a 9 L heated vessel. A three-way valve could be opened to convey the wax to the atomization vessel through a heated horizontal tube. The atomization vessel consisted of a plenum chamber, a distributor plate, an atomizer positioning section and a nozzle. The atomization system generated a spray of molten wax in the model reactor which eventually gave rise, upon deposition onto the wall, to a layer of molten wax. The nozzle was a commercial Delavan^{TM} atomizer (AL model), designed so as to generate a spray of conical shape with an aperture angle of θ_{max}=25° and a uniform cross-sectional distribution of the atomized dispersed phase, Fig. 2 (right). Air-assisted atomization of wax resulted into droplets of 50-100 μm size. The atomization air was fed directly to the nozzle. The reactor consisted of a Pyrex^{TM} tube (D=0.04 m-ID) on which the atomizing system is fitted. A mainstream of air was fed at the top of the plenum chamber, flowing through a distributor plate in order to equalize

distribution of the air mainstream across the reactor.

The partitioning of the atomized wax between the dispersed and the wall phases was quantitatively assessed as a function of the distance from the nozzle. To accomplish this task, the reactor was equipped with a system for the collection of wax issuing from the reactor in either phase. This consisted of a vacuum flask with a 0.03 m-OD inlet tube, collecting wax issuing in the lean phase, that was fitted with an outer annular section where wax flowing in the wall layer was collected. The collection system was equipped with a filter and a suction pump. The mass flow rates in the dispersed phase and in the wall layer phase were obtained by dividing the amounts of wax cumulatively collected by the duration of the test. The actual status of the dispersed wax and of the wall layer could be controlled by adjusting the values of three temperatures. Atomization temperature (T_a), i.e. the nozzle temperature. This temperature must be set at values large enough to ensure good flowability and effective atomization of the wax. T_a ranged between 120°C and 155°C in the experiments, with a reference value of 145°C. Mainstream temperature (T_{ms}), that determines the status of the wax immediately after atomization. Adjusting T_{ms} with respect to the wax critical temperature at which the liquid-solid transition occurs (around 85°C for the wax used in the present study) enables accurate control of the physical status (liquid vs. solid) of the wax, as well as its viscosity. In this work, T_{ms} was fixed at 120 °C. Wall temperature (T_w), that can be varied to control the physical status and the viscosity of the wax accumulated on the wall. In this work, T_w was fixed at 135 °C.

In the present study operating conditions of the reactor were selected so as to reproduce the sticky wall/sticky particle (*SW-SP)* regime. The wax feeding rate was $W_{wax}^{lean}(z=0)$=0.2 g s^{-1}. The total air flow rate (expressed as the sum of Q_{ms}, the flow rate of mainstream air, and Q_a, the flow rate of atomization air) was fixed at 1 m^3 h^{-1} (at 298 K). Q_a was treated as a parameter, ranging between 0.25 m^3 h^{-1} and 0.35 m^3 h^{-1}, with a reference case of 0.30 m^3 h^{-1}. The air streams were both preheated before entering the reactor, and at about 100°C the gas hydraulic velocity was around 0.3 m s^{-1}, comparable with values typical of industrial gasifiers. The reactor length L was varied to investigate the influence of the distance from the injection nozzle on the fractional mass of wax transferred form the lean-dispersed phase to the wall layer. L ranged between 0.03 m and 0.27 m.

Modeling: Results and Discussion

RANS model

In order to develop and validate the proposed procedure, a prototype gasifier configuration has been chosen as benchmark for all the simulations. A sketch of its geometry is reported in Fig. 3 (top), where all lengths are non-dimensionalized using the radius R=0.032 m of the outer wall of the external annular jet as the reference length. Two gas streams are coaxially injected into the main cylindrical chamber. The outer stream feeds gas, while the inner stream feeds gas loaded with particles. The main chamber extends for 0.96 m, corresponding to 5-times the diameter of the main chamber (0.192 m). It is followed by a second, larger chamber to minimize the effects of outflow boundary conditions. The mass flow rates of the feeding are 9.9 g s^{-1} and 38.3 g s^{-1} related to the central gas jet and the annular swirled gas jet, respectively. The swirl number, computed as the ratio of the axial flux of angular momentum to the axial flux of linear momentum, is set at 0.47 for all the computations.

A sketch of the geometry and computational mesh used for simulations at the RANS level is shown in Fig. 4. The computational mesh adopted is multi-block and structured, and it is composed of about 15×10^4 cells. An additional volume is added at the outlet section of the gasifier, to allow a better reproduction of the recirculation region. The discretization scheme adopted is backward Euler for time-derivative terms. All divergence and Laplacian terms are discretized assuming second-order numerical

schemes. Simulations are conducted considering two different clouds of particles, each made of identical particles. All clouds have particle density equal to 2500 kg m^{-3}, that is the same value of the reference simulation [16]. In the first cloud, parcels are made of 100 particles having diameter d_P = 45 μm. In the second cloud, parcels are made of 10 particles having d_P = 102 μm. The two particle diameters (45 μm and 102 μm, corresponding to Stokes numbers of 5 and 25 for the first and the second cloud, respectively) were selected so as to represent different patterns of particle-wall interaction. Particles are injected at the centre of the axial inlet of the gasifier with a 30° conical injection. Particle mass flow rate at the injection is 0.34 g s^{-1}, that is the same for all the clouds and the same of the reference simulation [16]. Particle injection velocity equals the fluid velocity. All particles rebound at gasifier walls according to either inelastic (a coefficient of restitution ε = 0.2 was assumed in this case) or fully elastic (ε = 1) impacts.

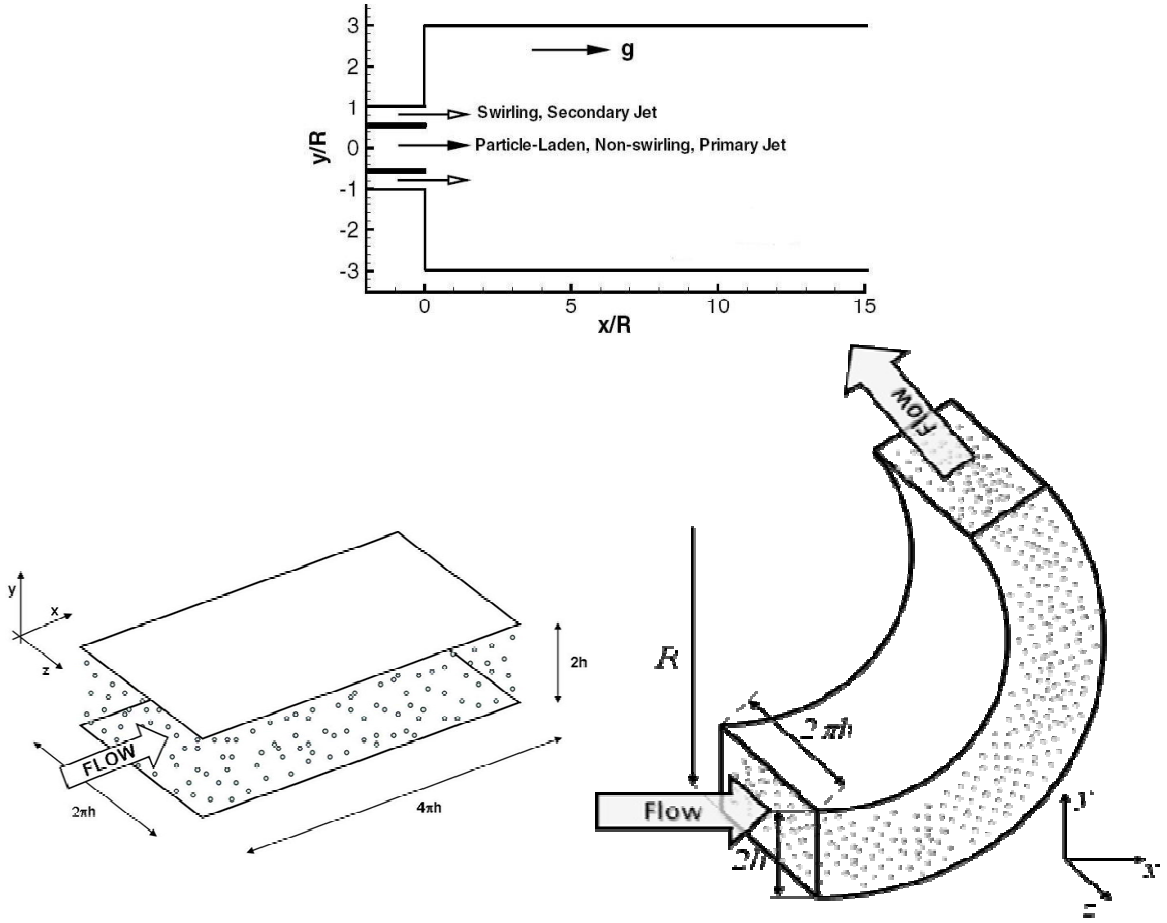

Figure 3. *Top: sketch of the domain used for the RANS level of computation (only a portion of the gasifier is reported). Bottom: periodic planar channel (left) and periodic curved channel (right) configurations adopted at the LES level of the computational procedure. h=0.02 m and R=0.096 m.*

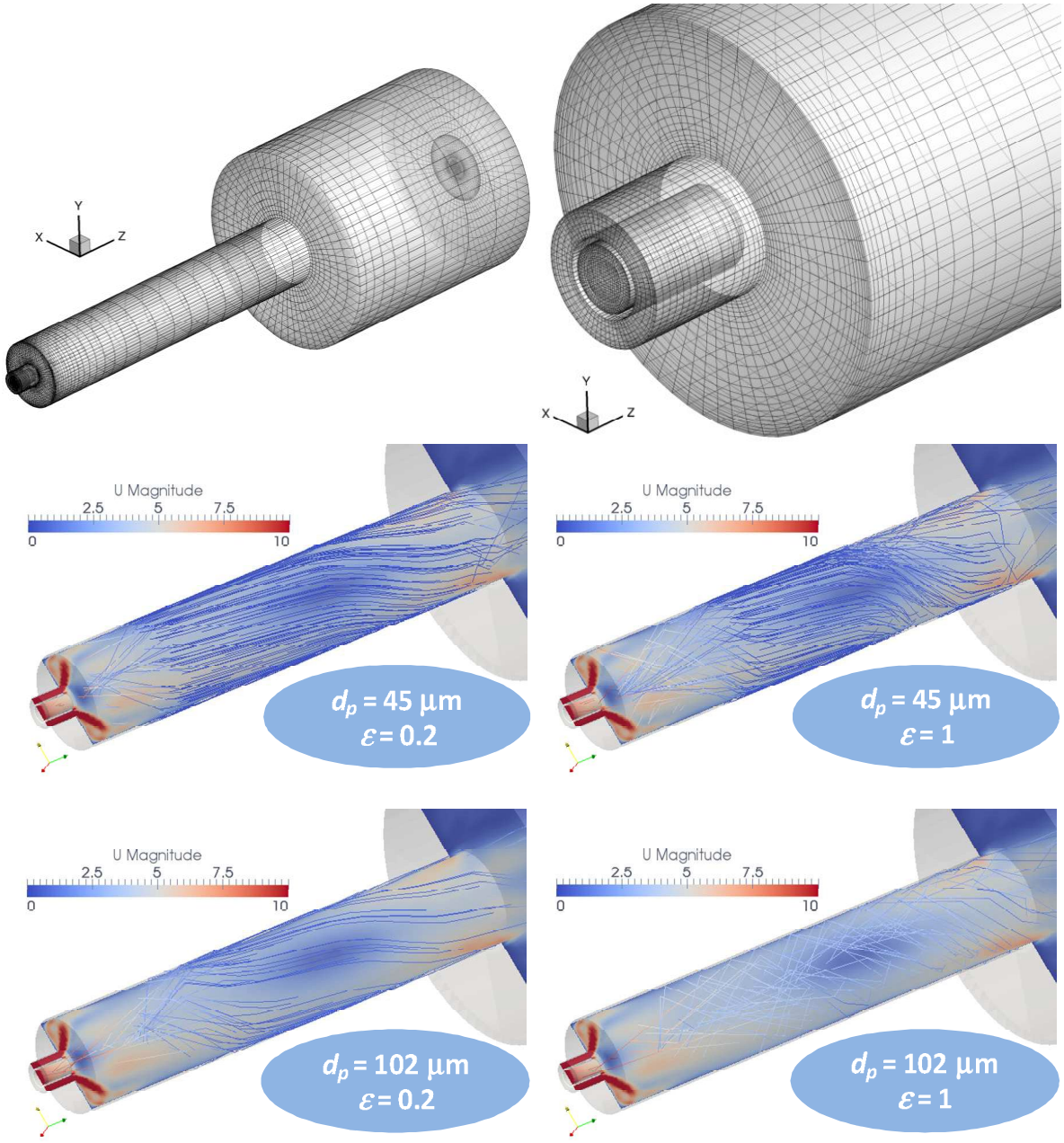

Figure 4. *Top: computational domain and grid for 3D RANS computations. Centre (d_P=45 µm) and bottom (d_P=102 µm): particles pathlines in the gasifier for ε=0.2 (left) and ε=1 (right). U magnitude scale (m s^{-1}) refers to particle velocity.*

In Fig. 4 the particles pathlines, obtained by post-processing the computed particle positions for several time steps from 6 s to 9 s and colored according to the velocity magnitude of the tracing particles, are shown together with the contour of the gas axial velocity component in the midplane section. Figure 4 makes it possible to appreciate the influence of the coefficient of restitution of particle-wall collisions and of the particle size on the qualitative patterns of particle flow. Switching from inelastic to elastic impacts and changing particle size are clearly reflected by quantitative and qualitative features of particle trajectories. Lighter particles are drawn by the flow field after few rebounds when they first impinge the

walls (the fewer, the smaller the coefficient of restitution). Heavier particles are much less affected by drag, undergoing multiple rebounds all along the gasifier length, again with a pronounced influence of the coefficient of restitution. Different zones of the gasifier with respect to particle migration to the wall can be (at least qualitatively) identified, depending on particle diameter. The first zone, close to the inlet section, is in shadow with respect to the particle trajectories. The second zone is characterized by an intense particle deposition rate, mainly due to the centrifugal motion induced by the swirl flow. The characterization of the third, longer zone, is more difficult, being quite different when the two different dimensions of particles are considered. Detailed simulation results (not shown here for brevity) indeed show that in the third region particles are confined within a thin zone close to the walls: smaller particles remain substantially deposited on the walls, moving very slowly well inside the boundary layer; coarser particles maintain a substantial level of inertia and continue to rebound at the walls, following spiral-like trajectories close to the walls. Eventually, a fourth zone is identified at the end of the gasifier, where disturbances induced by the approaching outlet section lift the particles from the wall. RANS results strengthen the hypothesis of establishment of char particles accumulation near the wall, beneficial to carbon gasification as previously discussed.

LES model

Inspection of the pathlines reported in Fig. 4 reveals that the particles, after the very first few impacts against the walls, are dragged by the air flow and are unable to be embodied again into the core of the gasifier: they in fact preferentially travel close to the walls. For finer particles, accumulation toward the walls is very fast and these particles remain confined into a thin layer, becoming therefore almost unaffected by the swirling component of the flow field. They travel almost parallel to the axis of the cylinder. On the other hand coarser particles, having a larger inertia, continue to bounce hitting the walls several times along the entire cylinder length so that they travel into a thicker region close to the walls. In this case the swirling component of the gas phase flow continues to exert a significant influence, preserving a tangential component of the particles motion. When the near-wall flow of the dispersed particle phase is addressed, two idealized configurations may be considered based on these findings. The first, aiming at reproducing the multiphase turbulent flow of particles moving parallel to the walls, i.e. almost without sensing the walls' curvature, is the periodic planar channel, Fig. 3 (bottom left). The second configuration, aiming at characterizing a swirled turbulent flow where particles continuously hit the walls along their path, is the periodic curved channel, Fig. 3 (bottom right). In this work, a simple representation of the wall properties, and consequently of the particle-wall interaction, is considered: only the normal restitution coefficient is varied to reproduce different levels of normal momentum exchange during the collision of particles with the wall (representative of a fully- or partially-molten slag having different values of elasticity, or a fully-covered slag over which a thin layer of deposited solid particles may induce elastic behaviour). Two different clouds of 10^5 particles have been considered, both with parcels made of one particle each. In the first cloud, particles have $d_P = 45$ μm (St = 5) while, in the second cloud, particles have $d_P = 102$ μm (St = 25). These clouds are the same adopted in a reference simulation [21]. After the establishment of the fully-developed turbulent flow, particles are simultaneously injected at random positions in the channel, all with zero velocity. Particles do not leave the domain, because they are returned from the side walls of the channel by the periodicity of the boundary condition. Four different values of the coefficient of restitution were tested: $\varepsilon = 0.2$, 0.5, 0.8 and 1.

Detailed results for these configurations solved adopting the LES model for the gas phase are illustrated in Ambrosino et al. [13] and show that local particle clustering is present and clearly emphasized when ε is reduced. In the planar channel case, smaller particles remain distributed over the surface forming a layer extending along the whole viscous sub-layer and characterized by a somewhat more pronounced clustering at contact with the surface, with a dimension that increases with ε. For coarser particles the

layering is less pronounced. In this case, at lower values of ε the tendency to cluster close to the wall to form large-scale structures is much more pronounced. This result is consistent with the experimental observation of a layer of slag fines that is formed above the molten slag layer and separately collected at the bottom of the gasifier [8]. In the curved channel case, it is instead more relevant to observe the evolution of the particle distribution patterns as they form starting from the initial, fully random distribution, being this configuration more relevant to the initial rapid migration of particles injected in the gasifier toward the slagging surface. It clearly emerges a strong dependency upon the main two parameters here investigated, i.e. the particle size and the wall softness. A snapshot of particle position for different St numbers and restitution coefficients after 0.5 s from fully random particle injection is reported in Fig. 5. This figure clearly shows that the particles very rapidly cluster into the stagnation flow regions close to the outer wall, but the structures change for different particle size and wall restitution coefficients. For the smaller particles, a less pronounced accumulation close to the stagnation flow regions arises. It is interesting the effect of the inelastic impact ($\varepsilon = 0.2$) of the particles that results in the appearing of periodic structures along the azimuth direction, more marked for particles at St = 25. This effect reduces the tendency of particles to accumulate into the regions of stagnation flow.

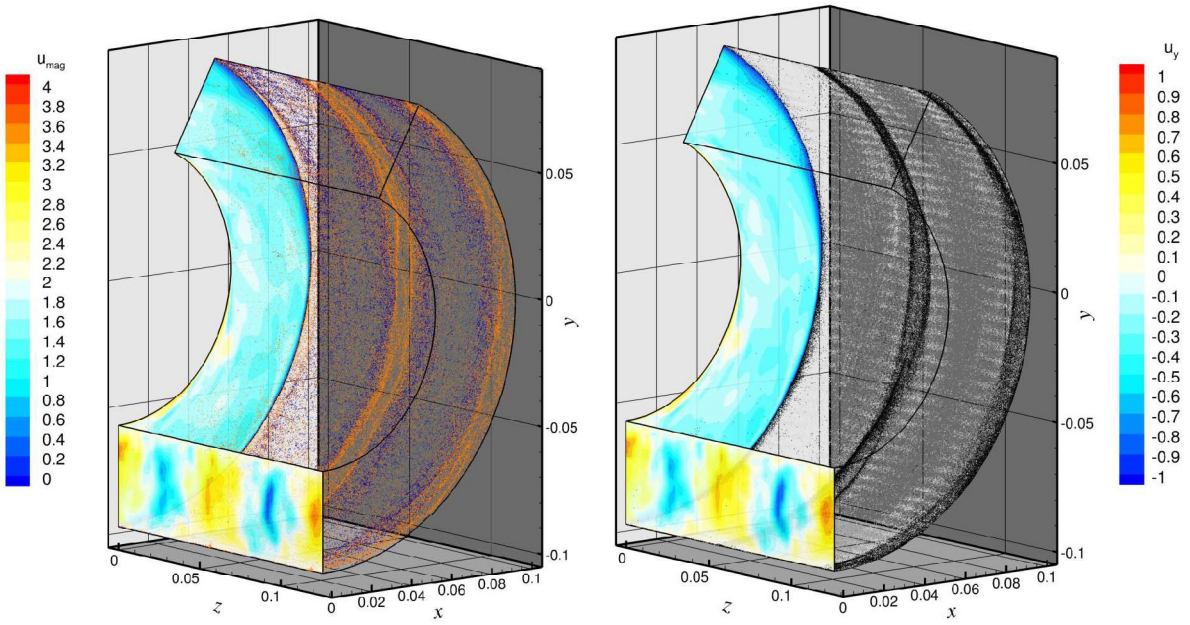

***Figure 5**. Snapshots of the particles distribution after 0.5 s from injection. LES level, curved channel flow case. Comparison between different values of Stokes and restitution coefficient. Coloured contours of velocity magnitude is shown over the cut z=0. Coloured contours of radial velocity is shown over the cut x=0.*

Results of numerical simulation do confirm the establishment of a region near the wall slag layer (the dense-dispersed annular phase), in which several particles accumulate before adhering to the slag to an extent that depends on the system fluid-dynamics and on parameters such as particles Stokes number and restitution coefficient. Interestingly, the segregation of char particles near the wall is more evident for the curved channel flow geometry, a more realistic case, and is enhanced for coarser particles. Particle accumulation appears to take place within a relatively short time since particle injection.

Experiments in the Model Reactor: Results and Discussion

Temporal sequences of snapshots captured during a typical test (obtained by a CCD camera and not

reported here for brevity) show that, as a result of the impact of sticky particles on the sticky wall, Fig. 1 (left), coalescence was by far the predominant process, though occasional droplet rebound and re-entrainment into the dispersed phase could be observed. Moreover, the analysis of the snapshots highlighted the presence of very fine (typically micron-sized) air bubbles entrapped in the wall molten wax layer and descending along vertical streamlines. The wall layer was characterized by laminar flow. Assuming that air bubbles behave as a non-diffusive tracer and following their trajectories, it was possible to estimate a descending velocity of the molten wax wall layer in the order of 3-6 mm s^{-1}. On the basis of this result and of the value of volumetric flow rate of wall layer phase, the thickness of the wall liquid layer was calculated and results to be in the order of 0.22 mm.

The mass flow rate of wax conveyed in the dispersed phase $W_{wax}^{lean}(z = L)$ was worked out to calculate the fractional mass of wax in the dispersed phase at $z = L$, defined as:

$$y^{lean}(z = L) = \frac{W_{wax}^{lean}(z = L)}{W_{wax}^{lean}(z = 0)} \tag{1}$$

Figure 6 (left) reports values of y^{lean} measured in experiments carried out with different values of L, while keeping all the operating variables of the reference case. y^{lean} abruptly decreases from nearly 0.91 in the proximity of the nozzle ($L = 0.03$ m) to approach 0.12 for $L \geq 0.20$ m. It is interesting to compare the experimental plot with limiting lines corresponding to idealized *NSW-NSP* and *SW-SP* regimes, Fig. 1 (right), both reported in Fig. 6 (left) for comparison. In the first case (*NSW-NSP*), the wall reflects impinging particles according to a nearly elastic interaction pattern. Accordingly, y^{lean} would be 1 for any L. The other idealized limiting curve (*SW-SP*) is based on the consideration of the conical shape of the jet and of the uniform distribution of the dispersed phase across the jet which reflects the design and operational characteristics of the nozzle used in the experiments. Additional assumptions are that wax droplets approach the wall along radial trajectories departing from the nozzle, Fig. 2 (right). Droplets impinge the wall under the effect of inertia and are deposited thereon without rebound as they are incorporated in the molten wall layer. According to the geometry of the nozzle and of the reactor, the impact of molten wax droplets becomes significant only at a distance $z \geq z^*$ from the nozzle, the value of z^* being determined by the aperture angle of the conical jet ($\theta_{max} = 25°$ and $z^* = 0.043$ m in the present case). Simple geometrical arguments suggest that:

$$y^{lean}(z) = \begin{cases} 1 & for\, z < z^* \\ \dfrac{q\pi(r^*)^2}{q\pi R^2} = \left(\dfrac{r^*}{R}\right)^2 = \left(\dfrac{z^*}{z}\right)^2 & for\, z \geq z^* \end{cases} \tag{2}$$

taking into account Eq. (1) and defining q as the axial wax mass flux at $z = z^*$, while r^* and R are depicted in Fig. 2 (right). Equation (2) is plotted in Fig. 6 (left) as the idealized limiting curve corresponding to the *SW-SP* regime.

When the experimental data points are compared with the limiting curves, the following features may be recognized. Experimental data points lie much closer to the *SW-SP* regime limiting curve than to the other limiting curve. This finding is fully consistent with the operating conditions of the tests which promoted a permanently molten status of both entrained wax droplets and of the wall layer. Values of y^{lean} slightly departs from 1 already at $z < z^*$. It is likely that this behaviour is related to moderate backmixing of the dispersed phase associated with recirculation and mainstream gas entrainment developing close to the nozzle. The experimental data points lie somewhat above the theoretical *SW-SP* regime limiting curve for large values of L. This might result from either moderate droplet rebound at the wall followed by re-entrainment, or by a certain degree of ineffectiveness of inertial forces in promoting impingement and entrapment of droplets as they are simultaneously invested by the mainstream flow directed parallel to the wall. It must be underlined that transfer of droplets to the wall in the fully developed flow downstream of

the nozzle by Brownian or turbophoretic mechanisms is bound to be rather ineffective if one considers that the Reynolds number of the fully developed flow is in the order of 500. This might justify the relative constancy of y^{lean} (around 0.12) for large values of L.

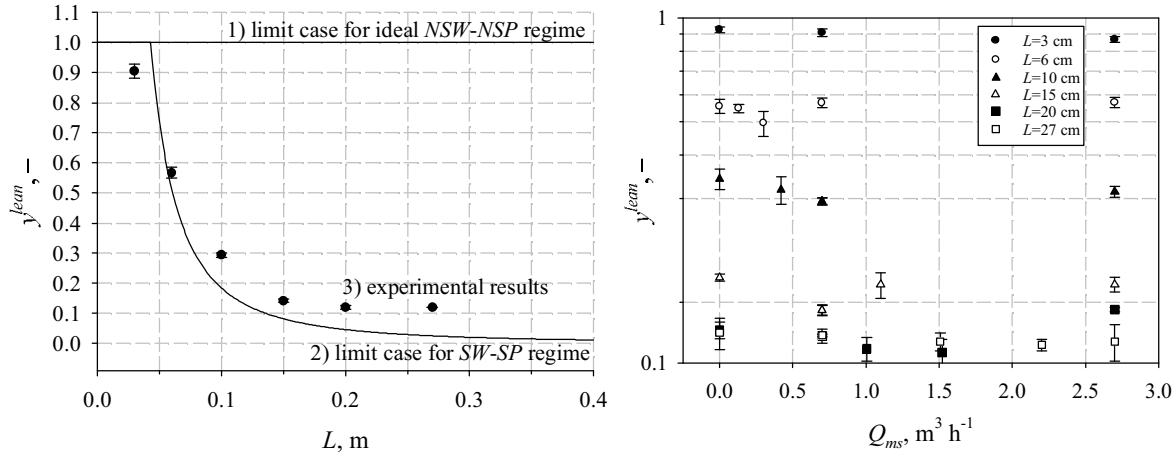

***Figure 6**. Left: effect of the axial coordinate on the fractional wax content in the lean phase. 1) ideal NSW-NSP regime; 2) plot of Eq. (2) for SW-SP regime with only nozzle-related geometrical effects & no rebound; 3) experimental results from tests carried out at Q_a=0.30 m^3 h^{-1}. Right: effect of the mainstream gas flow rate on the fractional wax content in the lean phase (Q_a=0.30 m^3 h^{-1}).*

As far as the effect of the flow rate of atomizing air Q_a on y^{lean} is concerned, results suggest that changes of y^{lean} are modest, comprised between 0.14 and 0.16. Also the atomization temperature did not lead to significant variations in y^{lean}: as T_a was increased from 130°C to 145°C, y^{lean} was comprised between 0.13 and 0.16. However it must be recalled that the selected range of T_a was well above the range of temperatures at which solid-liquid transition of the wax occurs. The mainstream gas flow rate exerted only moderate effect on y^{lean}, as reported in Fig. 6 (right). It is in fact observed that, when L was fixed and varying Q_{ms} up to 2.7 m^3 h^{-1}, y^{lean} did not suffer significant variations. On the other hand, y^{lean} decreased as L increased at fixed Q_{ms}, from about 0.90 (L = 0.03 m) to about 0.12 (L = 0.27 m), in line with what observed in Fig. 6 (left). These findings further suggest that the axial profile of y^{lean} is largely dominated by the hydrodynamics of the jet.

Conclusions

The use of RANS- and LES-based CFD computations provide powerful tools for the detailed characterization of near-wall flow patterns and for the development of constitutive submodels to be implemented in design-oriented compartmental models. The multilevel approach was effectively directed to analyze the segregation of char particles in the near-wall region of the gasification chamber and to assess its influence on the performance of the gasifier. The relevance of near-wall particle segregation on the performance of entrained-flow gasifiers was confirmed. Computations demonstrated the criticality of key parameters, namely the size of particles and the coefficient of restitution of particle-wall interaction, to the establishment and the stability of the segregated dense-dispersed particle phase close to the gasifier walls. Detailed CFD computations lay the path to implementation of constitutive equations and parameters expressing bulk-to-wall particle migration and near-wall flow of the segregated particle phase in design-oriented compartmental models.

In a parallel investigation, the dispersed flow of atomized molten wax in a circular pipe has been investigated. The experimental set-up and procedure aimed at characterizing the interaction of droplet- or particle-laden flows and confining walls, with special emphasis on conditions that promote the formation and flow of a liquid layer on the reactor wall. This phenomenology is relevant to the performance of

entrained-flow coal gasifier operating in the slagging regime. Operating conditions of the experiments were such that droplets were permanently kept in the molten status, either in the disperse phase or after impingement on the reactor wall. Accordingly, the dispersed flow/wall interaction corresponded to the sticky wall-sticky particle regime. Key variable of the flow is represented by the fractional content of wax remaining in the dispersed phase as a function of the distance travelled downstream the injection nozzle. Axial profiles of this variable measured along the reactor closely conformed to values predicted by assuming idealized radial droplet trajectories in the jet and inertial impact on the wall. The preliminary set-up and tuning of the procedure reported in the present study will provide the ground for more extensive characterization of dispersed phase/wall interactive patterns in the sticky wall-sticky particle regime, and for extension to other regimes of potential interest in slagging entrained-flow gasification of solid fuels.

Acknowledgments

The Authors wish to express their gratitude to VölpkerSpezialprodukte GmbH, Germany, for supplying the raw wax Waradur E™. Mrs. Ramona Carbone is gratefully acknowledged for her experimental work, and for useful discussion. The modeling part of this work has been supported by the 'Accordo di Programma CNR – MiSE 2009-2011' Research Fund for the Electric System. The computing resources and the related technical support used for this work have been made provided by CRESCO/ENEAGRID High Performance Computing infrastructure and its staff (www.cresco.enea.it). CRESCO/ENEAGRID High Performance Computing infrastructure is funded by ENEA ('Italian National Agency for New Technologies, Energy and Sustainable Economic Development') and by National and European research programs.

References

[1] Shimizu, T.; Tominaga, H., A model of char capture by molten slag surface under high-temperature gasification conditions. *Fuel* **2006,** 85, 170-178.
[2] Ni, J.; Yu, G.; Guo, Q.; Zhou, Z.; Wang, F., Submodel for predicting slag deposition formation in slagging gasification systems. *Energy Fuels* **2011,** 25, 1004-1009.
[3] Shannon, G. N.; Rozelle, P. L.; Pisupati, S. V; Sridhar, S., Conditions for entrainment into a FeO_x containing slag for a carbon-containing particle in an entrained flow gasifier. *Fuel Process Technol* **2008,** 89, 1379-1385.
[4] Montagnaro, F.; Salatino, P., Analysis of char-slag interaction and near-wall particle segregation in entrained-flow gasification of coal. *Combust Flame* **2010,** 157, 874-883.
[5] Li, S.; Whitty, K. J., Physical phenomena of char-slag transition in pulverized coal gasification. *Fuel Process Technol* **2012,** 95, 127-136.
[6] Losurdo, M.; Spliethoff, H.; Kiel, J., Ash deposition modeling using a visco-elastic approach. *Fuel* **2012,** 102, 145-155.
[7] Yong, S. Z.; Ghoniem, A., Modeling the slag layer in solid fuel gasification and combustion – Two-way coupling with CFD. *Fuel* **2012,** 97, 457-466.
[8] Montagnaro, F.; Brachi, P.; Salatino, P., Char-wall interaction and properties of slag waste in entrained-flow gasification of coal. *Energy Fuels* **2011,** 25, 3671-3677.
[9] Seggiani, M., Modelling and simulation of time varying slag flow in a Prenflo entrained-flow gasifier. *Fuel* **1998,** 77, 1611-1621.
[10] Chen, C.; Horio, M.; Kojima, T., Use of numerical modeling in the design and scale-up of entrained flow coal gasifiers. *Fuel* **2001,** 80, 1513-1523.
[11] Watanabe, H.; Otaka, M., Numerical simulation of coal gasification in entrained flow coal gasifier. *Fuel* **2006,** 85, 1935-1943.
[12] Silaen, A.; Wang, T., Effect of turbulence and devolatilization models on coal gasification simulation in an entrained-flow gasifier. *Int J Heat Mass Tran* **2010,** 53, 2074-2091.
[13] Ambrosino, F.; Aprovitola, A.; Brachi, P.; Marra, F. S.; Montagnaro, F.; Salatino, P., Investigation of

char-slag interaction regimes in entrained-flow gasifiers: linking experiments with numerical simulations. *Combust Sci Technol* **2012,** 184, 871-887.
[14] Yong, S. Z.; Gazzino, M.; Ghoniem, A., Modeling the slag layer in solid fuel gasification and combustion – Formulation and sensitivity analysis. *Fuel* **2012,** 92, 162-170.
[15] Macpherson, G. B.; Nordin, N.; Weller, H. G., Particle tracking in unstructured, arbitrary polyhedral meshes for use in CFD and molecular dynamics. *Commun Numer Meth Eng* **2009,** 25, 263-273.
[16] Sommerfeld, M.; Qiu, H. H., Characterization of particle-laden, confined swirling flows by phase-doppler anemometry and numerical calculation. *Int J Multiphas Flow* **1993,** 19, 1093-1127.
[17] Sagaut, P., Large eddy simulation for incompressible flows. Springer; **2001**.
[18] Kim, W. W.; Menon, S.; Mongia, H. C., Large-eddy simulation of a gas turbine combustor flow. *Combust Sci Technol* **1999,** 143, 25-62.
[19] Ambrosino, F.; Aprovitola, A.; Brachi, P.; Marra, F. S.; Montagnaro, F.; Salatino, P., Open source codes for the development of multilevel modelling of entrained-flow coal gasifiers, *Open Source CFD Int Conf* **2011**, 3-4 November, Paris-Chantilly, France, available online at https://www.opensourcecfd.com/conference2011/posters.
[20] Li, R.; Ashgriz, N.; Chandra, S.; Andrews, J. R., Shape and surface texture of molten droplets deposited on cold surfaces. *Surf Coat Technol* **2008,** 202, 3960-3966.
[21] Marchioli, C.; Soldati, A.; Kuerten, J. G. M.; Arcen, B.; Tanière, A.; Goldensoph, G.; Squires, K. D.; Cargnelutti, M. F.; Portela, L. M., Statistics of particle dispersion in direct numerical simulations of wall-bounded turbulence: results of an international collaborative benchmark test. *Int J Multiphas Flow* **2008,** 34, 879-893.

Volume 117, Part B, 30 January 2014 ISSN 0016-2361

ELSEVIER

FUEL

the science and technology of Fuel and Energy

Special Section:
3rd International Symposium on Gasification and its Applications

Guest Editors:
John R. Grace, Jun-ichiro Hayashi, Chun-Zhu Li

Fuel 117 (2014) 1267–1273

Contents lists available at SciVerse ScienceDirect

Fuel

journal homepage: www.elsevier.com/locate/fuel

A lab-scale cold flow model reactor to investigate near-wall particle segregation relevant to entrained-flow slagging coal gasifiers

Maurizio Troiano [b], Ramona Carbone [a], Fabio Montagnaro [c], Piero Salatino [b,*], Roberto Solimene [a]

[a] Istituto di Ricerche sulla Combustione, Consiglio Nazionale delle Ricerche, Piazzale Vincenzo Tecchio 80, 80125 Napoli, Italy
[b] Dipartimento di Ingegneria Chimica, dei Materiali e della Produzione Industriale, Università degli Studi di Napoli Federico II, Piazzale Vincenzo Tecchio 80, 80125 Napoli, Italy
[c] Dipartimento di Scienze Chimiche, Università degli Studi di Napoli Federico II, Complesso Universitario di Monte Sant'Angelo, 80126 Napoli, Italy

HIGHLIGHTS

- Understanding of particle–wall interactions in entrained gasifiers is pursued.
- The real system was downscaled into a lab-scale cold entrained-flow reactor.
- Molten wax was air-atomized into a mainstream of air.
- Insights into the interaction particles/wall liquid layer were provided.
- The fractional mass of dispersed phase ranged from 91% to 12% along the reactor.

ARTICLE INFO

Article history:
Received 23 November 2012
Received in revised form 16 May 2013
Accepted 21 June 2013
Available online 4 July 2013

Keywords:
Slagging gasifiers
Particle-wall interaction
Segregation
Wax

ABSTRACT

This paper reports on preliminary results of an experimental investigation aimed at the development of a phenomenological model of the fate of coal/ash particles in entrained-flow slagging coal gasifiers. The study specifically addresses the interaction between the lean-dispersed particle phase and the reactor walls, and the establishment of a particle segregated phase in the near-wall region of the gasifier. Better mechanistic understanding of particle–wall interaction patterns in entrained-flow gasifiers is pursued using the tool of physical modeling. To this end a lab-scale cold flow reactor (0.04 m-ID) has been designed and set up, where molten wax is air-atomized (droplets of 50–100 μm size) into a mainstream of air to simulate the near-wall fate of char/ash particles in a real hot environment. Preliminary characterization of the hydrodynamics of the lean-dispersed phase, of its interaction with the wall, of the build-up of the liquid wall layer has been accomplished with a focus on the "sticky wall–sticky particle" sub-regime.

The particle deposition rate at the wall and the partitioning of wax droplets between the lean-dispersed phase and the wall liquid layer have been assessed under a range of operating conditions. Temperatures of the atomized wax, of the mainstream air and of the reactor wall have been set in a range of values (120–155 °C) at which the wax was fluid. Experiments with wax feeding rate of 0.2 g s^{-1} and flow rate of atomizing air in the order of 0.30 m^3 h^{-1} demonstrated that the fractional mass of wax in the dispersed phase decreased from 91% to 12% as the reactor length increased from 0.03 m to 0.27 m. The velocity of the descending wall liquid layer, whose thickness was in the order of 0.2 mm, ranged between 3 mm s^{-1} and 6 mm s^{-1}. The effects of the flow rate of atomization air and of the nozzle temperature were limited.

1. Introduction

Modern entrained-flow coal gasifiers are characterized by operating conditions that promote ash migration/deposition onto the reactor walls, whence the molten ash is drained and quenched at the bottom of the gasifier as a vitrified slag [1–7]. The recent literature on entrained-flow gasification has addressed the fate of char particles as they impinge on the wall slag layer [8–15]. This research group has recently contributed to develop a phenomenological model of the fate of coal/ash particles, which considers the establishment of a particle segregated phase in the near-wall region of the gasifier [16]. More specifically, it has been highlighted that char particles impinging on the wall slag layer can: (i) be entrapped inside the melt, and this prevents further progress of combustion/gasification (*entrapment* regime, Fig. 1); (ii) adhere onto the slag layer's surface without being fully engulfed, and this permits further progress of combustion/gasification (*segregation*

* Corresponding author. Tel.: +39 0817682258.
E-mail address: salatino@unina.it (P. Salatino).

0016-2361/$ - see front matter © 2013 Elsevier Ltd. All rights reserved.
http://dx.doi.org/10.1016/j.fuel.2013.06.026

Nomenclature

D	reactor inner diameter (m)
L	reactor length (m)
Q	gas volumetric flow rate ($m^3\ s^{-1}$)
q	axial wax mass flux ($kg\ m^{-2}\ s^{-1}$)
R	reactor inner radius (m)
r	radial coordinate (m)
T	temperature (°C)
W	wax mass flow rate ($kg\ s^{-1}$)
X_C	carbon conversion degree (–)
y	fractional mass of wax (–)
z	axial distance from the nozzle (m)

Greek symbols

θ	spray angle (°)

Subscripts

a	atomization
max	maximum value
ms	mainstream
w	wall
wax	wax

Superscripts

*	geometrical condition of droplet impingement
lean	lean (dispersed) phase
th	threshold value

regime, Fig. 1). In the latter case, and if the coverage of the slag layer with carbon particles is extensive, a dense-dispersed annular phase may establish in the close proximity of the wall ash layer, where the excess impinging char particles that cannot be accommodated on the slag surface accumulate (*segregation–coverage* regime, Fig. 1). This annular phase is likely to be characterized by a velocity that is intermediate between that of the fast lean-dispersed particle phase and that of the slowly moving molten ash wall layer (Fig. 1). This feature is beneficial to C conversion, as it gives rise to a longer mean residence time of carbon particles belonging to this dense phase (with respect to what happens in the lean phase). This phenomenological model has received qualitative validation from analysis of the properties of ash streams generated in a full-scale entrained-flow gasification plant [17]. Moreover, the complex phenomenology associated with the interaction of a particle-laden turbulent flow with the inelastic slag-covered wall of the gasifier has been the subject of numerical simulation [18,19]. These studies confirmed that near-wall accumulation of particles may be extensive and that particle segregation is relevant to the performance of slagging entrained-flow gasifiers, as it affects the course of heterogeneous combustion/gasification reactions and the properties of the syngas.

The present study aims at improving the mechanistic understanding of particle–wall interactions and segregation patterns in entrained-flow gasifiers. The tool is that of physical modeling. Phenomenological and quantitative features of particle–wall interaction have been investigated in a lab-scale cold entrained-flow reactor equipped with a nozzle whence molten wax is air-atomized into a mainstream of air. The temperature of the mainstream is adjusted so as to tune the solid vs liquid state and the viscosity (and "stickiness") of the wax droplets. The temperature of the wall may also be adjusted to control the formation, viscosity and stickiness of the liquid wall layer. Assessment of the flow and segregation patterns in the reactor is based on direct visual observation, as the reactor is optically accessible. Moreover, the partitioning of the wax droplets/particles into a dilute-dispersed phase, a dense-dispersed phase and the layered liquid material flowing on the wall is characterized by selective collection of the different phases at the exhaust of the reactor. The model reactor and the test protocol aim at providing insight into the detailed mechanisms of interaction between dispersed particles, in the molten, plastic or solid state, and the wall liquid layer.

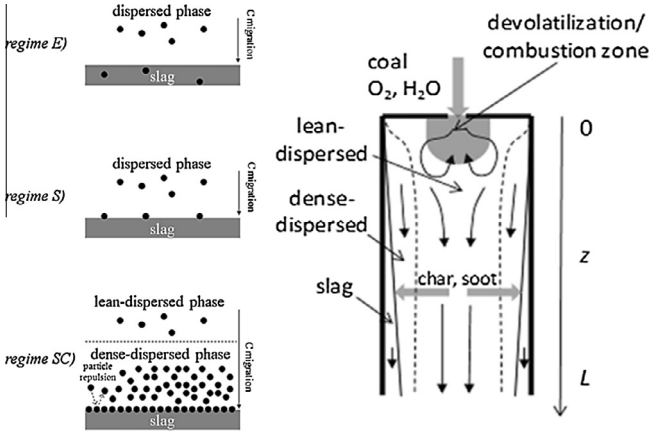

Fig. 1. Left: near-wall segregation regimes (*E* = *entrapment*; *S* = *segregation*; and SC = *segregation-coverage*). Right: schematic diagram of the entrained-flow gasifier.

2. Micromechanics of particle–slag interaction

Coal particles are fed to the gasification chamber through nozzles as a lean-dispersed particle-laden gas flow. Particle transport to the wall is controlled by inertial forces, possibly enhanced by swirled or tangential flow, and by the "turbophoretic" component related to the interaction between turbulent flow structures and the reactor walls (turbulence-promoted dispersive transport) [16]. In particular, inertia is relevant to coarser particles, turbophoresis to finer ones. Both mechanisms play a significant role in transport of particles from the dispersed phase to the walls and in the build-up of a slag layer [16].

A further key to the establishment of regimes outlined in Fig. 1 is represented by the stickiness of the particle and of the wall layer. Plastic behaviour and stickiness are emphasized as the content of the inherently refractory carbon decreases, i.e. as the carbon conversion degree X_C increases (Whitty and co-workers [9–11] set the threshold for plastic or viscous behaviour around $X_C = 90\%$ for chars derived from subbituminous and bituminous coals) and as the temperature is beyond the ash melting point. Yong et al. [14] described different particle–wall interaction patterns on the basis of the stickiness of the impinging particles and of the wall layer. These patterns are outlined in Fig. 2:

(i) *Sticky wall–sticky particle (SW–SP)*: char particles with low carbon content (large X_C) impinge on the slag layer (Fig. 2a).
(ii) *Sticky wall–non sticky particle (SW–NSP)*: particles characterized by large C content impinge on the slag layer (Fig. 2b).

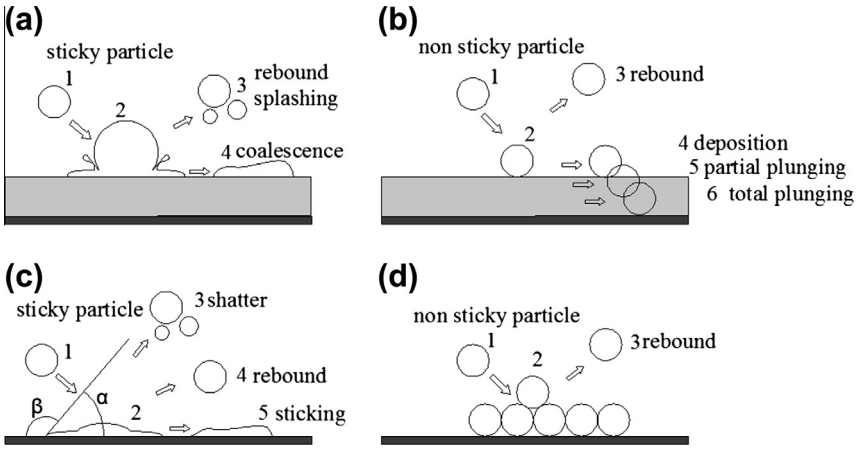

Fig. 2. Micromechanical interaction patterns: regimes (a) *SW–SP*; (b) *SW–NSP*; (c) *NSW–SP*; and (d) *NSW–NSP*. (1) Pre-impact, (2) impact, and (3–6) post-impact.

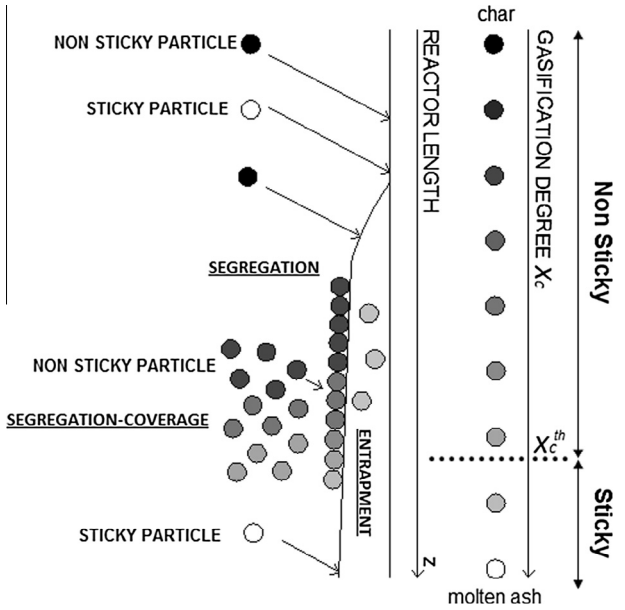

Fig. 3. Particle–wall micromechanical interactions and near-wall segregation regimes along the reactor axial coordinate (X_C^{th} is the threshold X_C-value).

(iii) *Non sticky wall–sticky particle (NSW–SP)*: char particles characterized by low C content impinge on either a dry wall or on a carbon-covered slag layer (Fig. 2c).
(iv) *Non sticky wall–non sticky particle (NSW–NSP)*: char particles with large C content impinge on either a dry wall or on a carbon-covered ash layer (Fig. 2d).

Fig. 3 shows how the different near-wall C-slag segregation regimes (entrapment, segregation and segregation-coverage) can occur as a function of the reactor axial coordinate and of the progress of X_C. The fate of char particles depends on the complex mechanics of liquid–solid, liquid–liquid and solid–solid interphase interaction. For the first regime (*SW–SP*), sticky particles impinging on the slag layer can either rebound or be entrapped by the liquid surface, contributing, in the latter case, to the wall layer build-up. Jayaratne and Mason [20], Ching et al. [21] and Pan and Law [22] have studied the impact of droplets upon liquid surfaces and have shown that droplet diameter, velocity, impact angle and liquid layer thickness all affect rebound and coalescence. *SW–NSP* interactions were also studied to establish entrapment, coverage and rebound criteria. Montagnaro and Salatino [16] developed theoretical criteria for particles plunging into the slag layer and for full carbon-coverage of the wall ash layer. Shannon et al. [8] developed a detailed analysis of the dynamics of a carbon particle after impact on the wall slag layer. The possibility that a particle deposited on the slag layer's surface can subsequently suffer partial/total plunging as the particle gasification degree increases (thus letting the particle itself transform from non sticky to sticky) was postulated and experimentally verified by Montagnaro et al. [17]. *NSW–SP* interactions have also been the subject of investigation in different contexts. Ni et al. [5] proposed a sub-model for predicting slag droplets interaction with the wall, hence slag layer formation. They specifically investigated the effects of slag viscosity, impact velocity, impact angle, molten slag surface tension and particle size on the maximum spread diameter and on the rebound criterion, as developed by Pasandideh-Fard et al. [23] and Mao et al. [24]. Yoon et al. [25] developed a criterion to discriminate whether shattering, rebound and sticking occur, based on results obtained by Mundo et al. [26]. Shimizu and Tominaga [2] developed a model for char capture by a slag layer covered, at least partially, by other char particles, valid for the *NSW–NSP* case. In their model, a char particle impinging the slag surface will rest, whereas it will be repelled if it reaches the part of the slag layer which is covered by unreacted or partly reacted C-rich char particles.

The present study aims at gaining better understanding of the micromechanics of particle–wall interaction in entrained-flow reactors. A cold flow lab-scale reactor and an experimental protocol are developed to scrutinize the interaction of wax particles entrained in air with the reactor wall. Wax can be kept in either the solid or the liquid state (at tunable viscosity) by properly setting the temperature of the entraining gas, and the wall temperature can also be adjusted to promote or prevent the formation of a liquid wall layer and to tune its viscosity. The reactor and the operating conditions do not conform to rigorous scaling rules, but rather aim at capturing the basic phenomenological and quantitative features of particle–wall interaction in a simple, manageable and optically accessible experimental setup. The first experimental campaign, documented hereinafter, referred to the simplest interaction pattern between the dispersed phase and the reactor wall: the sticky wall–sticky particle (*SW–SP*) subregime. This simple pattern provided a reference case to tune and setup the experimental procedure which is now ready for application to the investigation of more complex particle–wall interaction regimes.

3. The model reactor

A physical downscaled cold flow model of an entrained-flow gasifier has been designed and set up. It must be underlined that

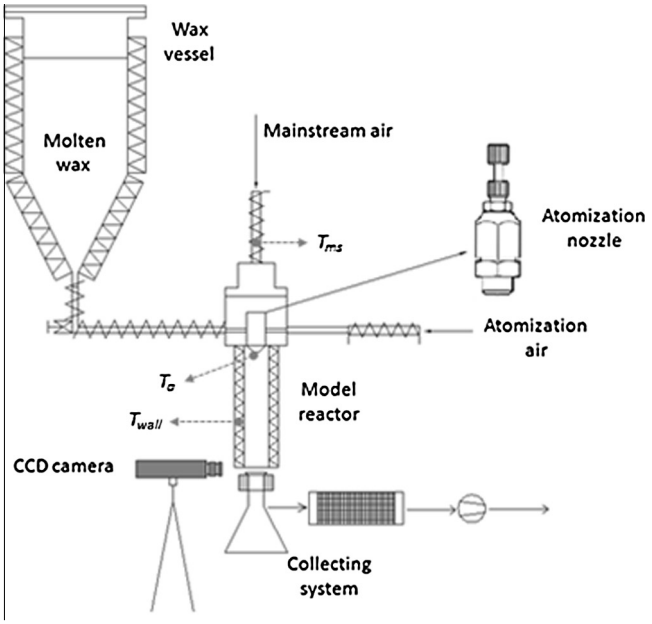

Fig. 4. Up: scheme (not to scale) of the downscaled cold flow model reactor with a detailed view of the atomization nozzle (T_a = atomization temperature; T_{ms} = mainstream temperature; T_{wall} = wall temperature). Down: picture of the experimental apparatus.

downscaling did not conform to rigorous scaling rules, but rather aimed at reproducing the basic general features of the interaction between a lean-dispersed particle/droplet phase and a confining wall, with special emphasis on conditions that promote the formation of a liquid layer on the reactor wall. The model reactor is schematized in Fig. 4.

The plastic/fluid behaviour of softened or molten ash and of the wall slag layer has been simulated, at nearly ambient conditions, by molten wax as a surrogate of fuel ash. After a screening of different candidates, Waradur E™ (Völpker, Germany) was selected, as the rheological/mechanical properties of this wax resembled those of a typical coal slag. Wax viscosity lies in the range 0.02–0.1 kg m^{-1} s^{-1} as the temperature ranges between 130 °C and 90 °C [27] and wax density is around 1000 kg m^{-3}. Accordingly, the kinematic viscosity is in the order of 10^{-5}–10^{-4} m^2 s^{-1}, consistent with values commonly reported in the literature for coal slag [5,6,8,28] (viscosity and density on the order of 0.01–1 kg m^{-1} s^{-1} and 1000 kg m^{-3}, respectively). The kinematic viscosities of the wax are consistent with the establishment of laminar flow of the molten phase along the reactor walls. Besides, taking into account the surface tension (0.03 kg s^{-2} at 100 °C), wax properties are such that the entrapment and over-layering criteria are not satisfied, and the segregation or segregation-coverage regime are likely to be established, as expected for realistic particle–slag interaction in entrained-flow gasifiers [16,17].

The wax was liquefied and stored in a 9 L heated vessel. A three-way valve could be opened to convey the wax to the atomization vessel through a heated horizontal tube. The atomization vessel consisted of a plenum chamber, a distributor plate, an atomizer positioning section and a nozzle. The atomization system generated a spray of molten wax in the model reactor which eventually gave rise, upon deposition onto the wall, to a layer of molten wax. The nozzle was a commercial Delavan™ atomizer (AL model), designed so as to generate a spray of conical shape with an aperture angle of θ_{max} = 25° and a uniform cross-sectional distribution of the atomized dispersed phase (Fig. 5). Air-assisted atomization of wax resulted into droplets of 50–100 μm size. The atomization air was fed directly to the nozzle.

The reactor consisted of a Pyrex™ tube (D = 0.04 m-ID) on which the atomizing system is fitted. A mainstream of air was fed at the top of the plenum chamber, flowing through a distributor plate in order to equalize distribution of the air mainstream across the reactor. The main reactor design and operating parameters are listed in Table 1.

Experimental tests aimed at characterizing the general phenomenology of the interaction between the dispersed phase generated by the spray and the reactor walls. The partitioning of the atomized wax between the dispersed and the wall phases was quantitatively assessed as a function of the distance from the nozzle. To accomplish this task, the reactor was equipped with a system for the collection of wax issuing from the reactor in either phase. This consisted of a vacuum flask with a 0.03 m-OD inlet tube, collecting wax issuing in the lean phase, that was fitted with an outer annular section where wax flowing in the wall layer was collected. The collection system was equipped with a filter and a suction pump. The mass flow rates in the dispersed phase and in the wall layer phase were obtained by dividing the amounts of wax cumulatively collected by the duration of the test.

Visual observation and recording of the wall layer was also accomplished by means of a CCD camera (Pulnix™ 6710) equipped with a magnifying zoom lens and located in the proximity of the reactor discharge section.

The actual status of the dispersed wax and of the wall layer could be controlled by adjusting the values of three temperatures:

- Atomization temperature (T_a), i.e. the nozzle temperature. This temperature must be set at values large enough to ensure good flowability and effective atomization of the wax. T_a ranged between 120 °C and 155 °C in the experiments, with a reference value of 145 °C.

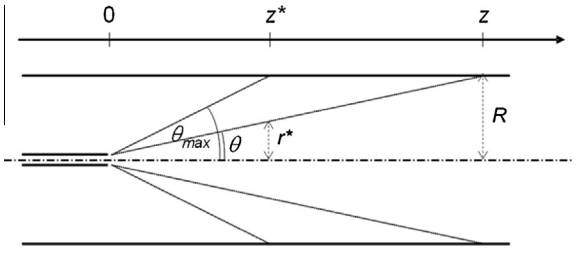

Fig. 5. Geometrical parameters of the jet in the model reactor.

Table 1
Main reactor design and operating parameters for reference tests.

Reactor internal diameter (m)	0.04
Reactor length (m)	0.03–0.27
Atomization temperature (°C)	120–155
Mainstream temperature (°C)	120
Wall temperature (°C)	135
Wax feeding rate (g s^{-1})	0.2
Total air flow rate (m^3 h^{-1} at 298 K)	1
Flow rate of atomization air (m^3 h^{-1} at 298 K)	0.25–0.35

- Mainstream temperature (T_{ms}). This temperature determines the status of the wax immediately after atomization. In fact, an energy balance around a single droplet in the dispersed phase, based on the assumption that Bi « 1, indicates that the temperature of the droplet closely approaches the temperature of the mainstream gas over about 10^{-4} s, far shorter than the typical residence times of droplets in the reactor. Accordingly, it can be assumed that droplets instantaneously reach thermal equilibrium with the mainstream air. Adjusting T_{ms} with respect to the wax critical temperature at which the liquid–solid transition occurs (around 85 °C for the wax used in the present study), enables accurate control of the physical status (liquid vs solid) of the wax, as well as its viscosity. In this work, T_{ms} was fixed at 120 °C.
- Wall temperature (T_w). This temperature can be varied to control the physical status and the viscosity of the wax accumulated on the wall. In this work, T_w was fixed at 135 °C.

In the present study operating conditions of the reactor were selected so as to reproduce the sticky wall–sticky particle (*SW–SP*) regime. The wax feeding rate was W_{wax}^{lean} ($z = 0$)=0.2 g s^{-1}. By taking into account the gas (steam + oxygen)-to-solid feed ratios typical of industrial gasifiers [17], the total air flow rate (expressed as the sum of Q_{ms}, the flow rate of mainstream air, and Q_a, the flow rate of atomization air) was fixed at 1 m^3 h^{-1} (at 298 K). Q_a was treated as a parameter, ranging between 0.25 m^3 h^{-1} and 0.35 m^3 h^{-1}, with a reference case of 0.30 m^3 h^{-1}. Values of Q_a complied with the nozzle constraints and assured good wax atomization in terms of size and dispersion of droplets. The air streams were both preheated before entering the reactor and at about 100 °C the gas hydraulic velocity was around 0.3 m s^{-1}, comparable with values typical of industrial gasifiers.

The reactor length L was varied to investigate the influence of the distance from the injection nozzle on the fractional mass of wax transferred form the lean-dispersed phase to the wall layer. L ranged between 0.03 m and 0.27 m.

4. Experimental results

4.1. Qualitative phenomenology of dispersed phase/wall interaction and wall layer flow

Fig. 6 reports two temporal sequences of snapshots captured during a typical test (Q_a = 0.30 m^3 h^{-1}, T_a = 138 °C and L = 0.20 m). As a result of the impact of sticky particles on the sticky wall (Fig. 2a), coalescence was by far the predominant process, though occasional droplet rebound and re-entrainment into the dispersed phase could be observed.

Fig. 7 reports a sequence of snapshots recorded during a typical test (Q_a = 0.30 m^3 h^{-1}, T_a = 120 °C and L = 0.10 m) displaying the motion of the wall liquid layer in the proximity of the tube discharge section. The analysis of the snapshots highlighted the presence of very fine (typically micron-sized) air bubbles entrapped in the wall molten wax layer and descending along vertical streamlines. The wall layer was characterized by laminar flow. Assuming that air bubbles behave as a non-diffusive tracer and following their trajectories, it was possible to estimate a descending velocity of the molten wax wall layer in the order of 3–6 mm s^{-1}. On the basis of this result and of the value of volumetric flow rate of wall layer phase, the thickness of the wall liquid layer was calculated and is in the order of 0.22 mm.

4.2. Partitioning of the wax between the dispersed phase and the wall layer

The mass flow rate of wax conveyed in the dispersed phase W_{wax}^{lean} ($z = L$) was worked out to calculate the fractional mass of wax in the dispersed phase at $z = L$, defined as:

$$y^{lean}(z = L) = \frac{W_{wax}^{lean}(z = L)}{W_{wax}^{lean}(z = 0)} \quad (1)$$

Fig. 8 reports values of y^{lean} measured in experiments carried out with different values of L, while keeping all the operating variables of the reference case. y^{lean} abruptly decreases from nearly 0.91 in the proximity of the nozzle (L = 0.03 m) to approach 0.12 for $L \geqslant 0.20$ m. It is interesting to compare the experimental plot with limiting lines corresponding to idealized *NSW–NSP* and *SW–SP* regimes (Fig. 2), both reported in Fig. 8 for comparison. In the first case (*NSW–NSP*), the wall reflects impinging particles according to a nearly elastic interaction pattern. Accordingly y^{lean} would be 1 for any L. The other idealized limiting curve (*SW–SP*) is based on the consideration of the conical shape of the jet and of the uniform distribution of the dispersed phase across the jet which reflects the design and operational characteristics of the nozzle used in the experiments (see Section 3). Additional assumptions are that wax droplets approach the wall along radial trajectories departing from the nozzle (see Fig. 5). Droplets impinge the wall under the effect of inertia and are deposited thereon without rebound as they are incorporated in the molten wall layer. According to the geometry of the nozzle and of the reactor (Fig. 5), the impact of molten wax droplets becomes significant only at a distance $z \geqslant z^*$ from the nozzle, the value of z^* being determined by the aperture angle of the conical jet (θ_{max} = 25° and z^*=0.043 m in the present case). Taking into account Eq. (1), simple geometrical arguments suggest that:

$$y^{lean}(z) = \begin{cases} 1 & \text{for} \quad z < z^* \\ \frac{q\pi(r^*)^2}{q\pi R^2} = \left(\frac{r^*}{R}\right)^2 = \left(\frac{z^*}{z}\right)^2 & \text{for} \quad z \geqslant z^* \end{cases} \quad (2)$$

where q is the axial mass flux of wax at $z = z^*$, and r^* and R are represented in Fig. 5. Eq. (2) is plotted in Fig. 8 as the idealized limiting curve corresponding to the *SW–SP* regime.

When the experimental data points are compared with the limiting curves, the following features may be recognized:

- Experimental data points lie much closer to the *SW–SP* regime limiting curve than to the other limiting curve. This finding is fully consistent with the operating conditions of the tests which promoted a permanently molten status of both entrained wax droplets and of the wall layer.
- Values of y^{lean} slightly depart from 1 already at $z < z^*$. It is likely that this behaviour is related to moderate backmixing of the dispersed phase associated with recirculation and mainstream gas entrainment developing close to the nozzle.
- The experimental data points lie somewhat above the theoretical *SW–SP* regime limiting curve for large values of L. This might result from either moderate droplet rebound at the wall followed by re-entrainment, or by a certain degree of ineffectiveness of inertial forces in promoting impingement and entrapment of droplets as they are simultaneously invested by the mainstream flow directed parallel to the wall. It must

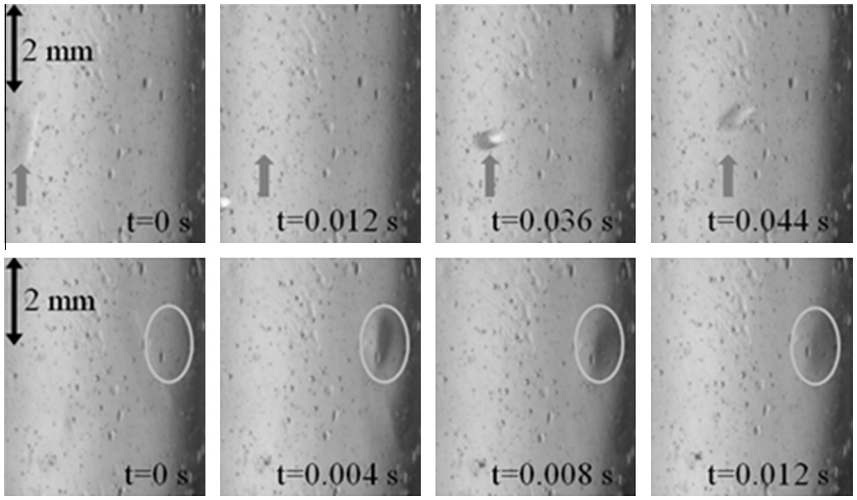

Fig. 6. Rebound (up) and coalescence (down) of sticky wax droplets impinging on the sticky wax wall. Snapshots captured at a frame rate of 250 fps. Arrows show the droplet rebound (up). Ovals show the droplet coalescence (down).

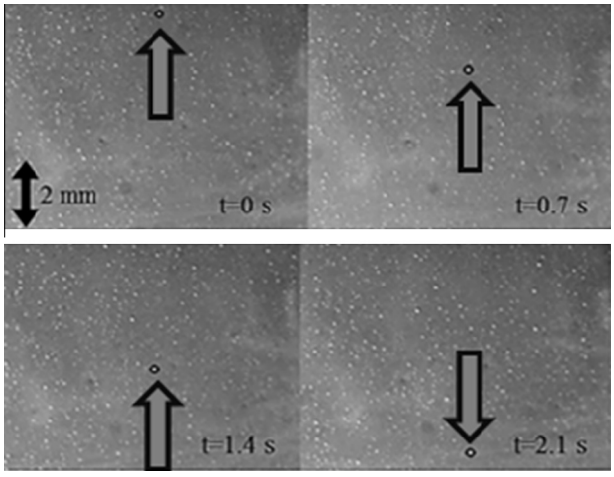

Fig. 7. Snapshots captured by the CCD camera at frame rate of 120 fps. The open circles (see arrows) highlight one of the descending air bubbles entrapped in the wall molten wax layer.

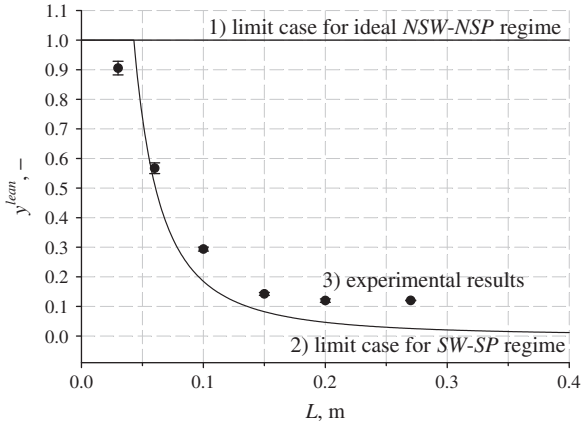

Fig. 8. Effect of the axial coordinate on the fractional wax content in the lean phase. (1) Ideal *NSW–NSP* regime; (2) plot of Eq. (2) for *SW–SP* regime with only nozzle-related geometrical effects & no rebound; and (3) experimental results from tests carried out at $Q_a = 0.30\ m^3\ h^{-1}$.

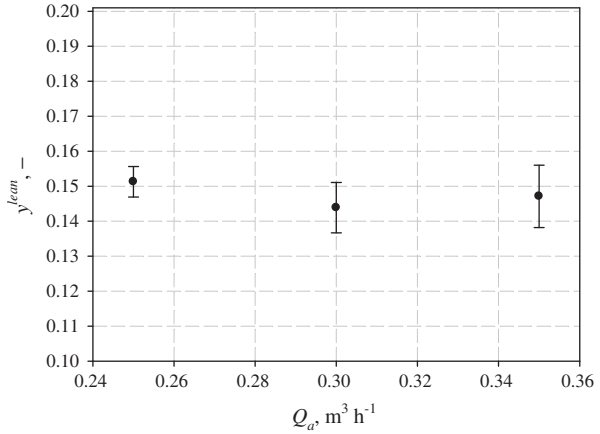

Fig. 9. Effect of the atomization air flow rate on the fractional wax content in the lean phase. Tests carried out at $T_a = 145$ °C and $L = 0.15$ m.

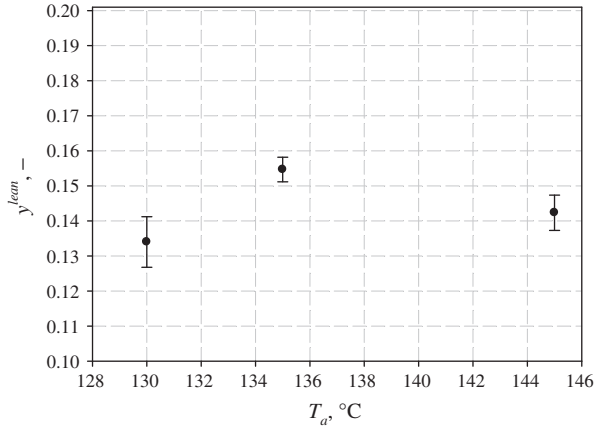

Fig. 10. Effect of the atomization temperature on the fractional wax content in the lean phase. Tests carried out at $Q_a = 0.30\ m^3\ h^{-1}$ and $L = 0.15$ m.

be underlined that transfer of droplets to the wall in the fully developed flow downstream of the nozzle by Brownian or turbophoretic mechanisms is bound to be rather ineffective if one

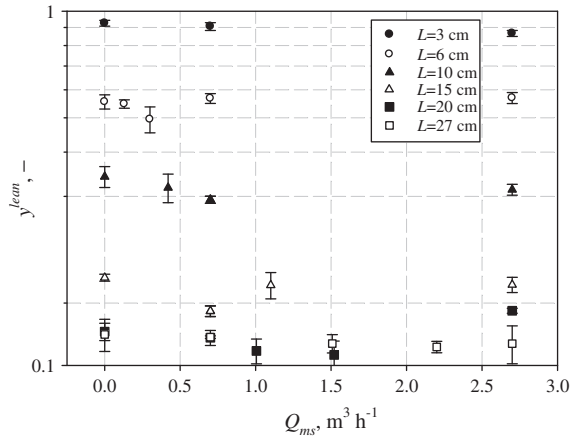

Fig. 11. Effect of the mainstream gas flow rate on the fractional wax content in the lean phase. $Q_a = 0.30$ m^3 h^{-1}.

considers that the Reynolds number of the fully developed flow is in the order of 500. This might justify the relative constancy of $y^{lean} \cong 0.12$ for large values of L.

Fig. 9 shows the effect of the flow rate of atomizing air Q_a on y^{lean}. Changes of y^{lean} are modest, comprised between 0.14 and 0.16. Also the atomization temperature did not lead to significant variations in y^{lean}, as shown in Fig. 10: as T_a was increased from 130 °C to 145 °C, y^{lean} was comprised between 0.13 and 0.16. However it must be recalled that the selected range of T_a was well above the range of temperatures at which solid–liquid transition of the wax occurs. The mainstream gas flow rate exerted only moderate effect on y^{lean}, as reported in Fig. 11. Actually, y^{lean} did not change appreciably as Q_{ms} was increased up to 2.7 m^3 h^{-1} while keeping L fixed. On the other hand, y^{lean} decreased as L increased, for given Q_{ms}, from about 0.90 ($L = 0.03$ m) to about 0.12 ($L = 0.27$ m), consistently with results reported in Fig. 8. These findings further suggest that the axial profile of y^{lean} is largely dominated by the hydrodynamics of the jet.

5. Conclusions

The dispersed flow of atomized molten wax in a circular pipe has been investigated. The experimental set-up and procedure aimed at characterizing the interaction of droplet- or particle-laden flows and confining walls, with special emphasis on conditions that promote the formation and flow of a liquid layer on the reactor wall. This phenomenology is relevant to the performance of entrained-flow coal gasifier operating in the slagging regime. Operating conditions of the experiments were such that droplets were permanently kept in the molten status, either in the disperse phase or after impingement on the reactor wall. Accordingly, the dispersed flow/wall interaction corresponded to the sticky wall–sticky particle (*SW–SP*) regime.

Key variable of the flow is represented by the fractional content of wax remaining in the dispersed phase as a function of the distance travelled downstream the injection nozzle. Axial profiles of this variable measured along the reactor closely conformed to values predicted by assuming idealized radial droplet trajectories in the jet and inertial impact on the wall. The preliminary set-up and tuning of the procedure reported in the present study will provide the ground for more extensive characterization of dispersed phase/wall interactive patterns in the *SW–SP* regime, and for extension to other regimes of potential interest in slagging entrained-flow gasification of solid fuels.

Acknowledgments

The Authors wish to express their gratitude to VölpkerSpezialprodukte GmbH, Germany, for supplying the raw wax Waradur E™. One of the Authors (RC) has been awarded an education grant in the framework of the Project "PON 01-000761 – SOLTESS" funded by the Italian Ministry of Education, University and Research (MIUR).

References

[1] Walsh PM, Sarofim AF, Beér JM. Fouling of convection heat exchangers by lignitic coal ash. Energy Fuels 1992;6:709–15.
[2] Shimizu T, Tominaga H. A model of char capture by molten slag surface under high-temperature gasification conditions. Fuel 2006;85:170–8.
[3] Ni J, Zhou Z, Yu G, Liang Q, Wang F. Molten slag flow and phase transformation behaviors in a slagging entrained-flow coal gasifier. Ind Eng Chem Res 2010;49:12302–10.
[4] Melchior T, Bläsing M, Pütz G, Müller M. Surface tension measurements of coal ash slags under reducing conditions at elevated pressures. Fuel 2011;90:280–7.
[5] Ni J, Yu G, Guo Q, Zhou Z, Wang F. Submodel for predicting slag deposition formation in slagging gasification systems. Energy Fuels 2011;25:1004–9.
[6] Song W, Sun Y, Wu Y, Zhu Z, Koyama S. Measurement and simulation of flow properties of coal ash slag in coal gasification. AIChE J 2011;57:801–18.
[7] Yang Z, Wang Z, Wu Y, Wang J, Lu J, Li Z, et al. Dynamic model for an oxygen-staged slagging entrained flow gasifier. Energy Fuels 2011;25:3646–56.
[8] Shannon GN, Rozelle PL, Pisupati SV, Sridhar S. Conditions for entrainment into a FeO_x containing slag for a carbon-containing particle in an entrained flow gasifier. Fuel Process Technol 2008;89:1379–85.
[9] Li S, Whitty KJ. Investigation of coal char–slag transition during oxidation: effect of temperature and residual carbon. Energy Fuels 2009;23:1998–2005.
[10] Li S, Wu Y, Whitty KJ. Ash deposition behavior during char–slag transition under simulated gasification conditions. Energy Fuels 2010;24:1868–76.
[11] Li S, Whitty KJ. Physical phenomena of char–slag transition in pulverized coal gasification. Fuel Process Technol 2012;95:127–36.
[12] Losurdo M, Spliethoff H, Kiel J. Ash deposition modeling using a visco-elastic approach. Fuel 2012;102:145–55.
[13] Yong SZ, Ghoniem A. Modeling the slag layer in solid fuel gasification and combustion – two-way coupling with CFD. Fuel 2012;97:457–66.
[14] Yong SZ, Gazzino M, Ghoniem A. Modeling the slag layer in solid fuel gasification and combustion – formulation and sensitivity analysis. Fuel 2012;92:162–70.
[15] Yu G, Zhu Q, Chi G, Guo Q, Zhou Z. Study on slag composition and flow property in a bench-scale OMB gasifier. Fuel Process Technol 2012;104:136–43.
[16] Montagnaro F, Salatino P. Analysis of char–slag interaction and near-wall particle segregation in entrained-flow gasification of coal. Combust Flame 2010;157:874–83.
[17] Montagnaro F, Brachi P, Salatino P. Char–wall interaction and properties of slag waste in entrained-flow gasification of coal. Energy Fuels 2011;25:3671–7.
[18] Ambrosino F, Aprovitola A, Brachi P, Marra FS, Montagnaro F, Salatino P. Investigation of char–slag interaction regimes in entrained-flow gasifiers: linking experiments with numerical simulations. Combust Sci Technol 2012;184:871–87.
[19] Ambrosino F, Aprovitola A, Brachi P, Marra FS, Montagnaro F, Salatino P. Entrained-flow gasification of coal under slagging conditions: relevance of fuel–wall interaction and char segregation to the properties of solid wastes. Fuel 2013;114:44–55.
[20] Jayaratne OW, Mason BJ. The coalescence and bouncing of water drops at an air/water interface. Proc R Soc London A 1964;280:545–65.
[21] Ching B, Golay MW, Johnson TJ. Droplet impacts upon liquid surfaces. Science 1984;226:535–7.
[22] Pan KL, Law CK. Dynamics of droplet-film collision. J Fluid Mech 2007;587:1–22.
[23] Pasandideh-Fard M, Qiao YM, Chandra S, Mostaghimi J. Capillary effects during droplet impact on a solid surface. Phys Fluids 1996;8:650–9.
[24] Mao T, Kuhn DCS, Tran H. Spread and rebound of liquid droplets upon impact on flat surfaces. AIChE J 1997;43:2169–79.
[25] Yoon SS, DesJardin PE, Presser C, Hewson JC, Avedisian CT. Numerical modeling and experimental measurements of water spray impact and transport over a cylinder. Int J Multiphas Flow 2006;32:132–57.
[26] Mundo CHR, Sommerfeld M, Tropea C. Droplet-wall collisions: experimental studies of the deformation and breakup process. Int J Multiphas Flow 1995;21:151–73.
[27] Li R, Ashgriz N, Chandra S, Andrews JR. Shape and surface texture of molten droplets deposited on cold surfaces. Surf Coat Technol 2008;202:3960–6.
[28] Duchesne MA, Ilyushechkin AY, Hughes RW, Lu DY, McCalden DJ, Macchi A, et al. Flow behaviour of slags from coal and petroleum coke blends. Fuel 2012;97:321–8.

Powder Technology 266 (2014) 282–291

Contents lists available at ScienceDirect

Powder Technology

journal homepage: www.elsevier.com/locate/powtec

Wall effects in entrained particle-laden flows: The role of particle stickiness on solid segregation and build-up of wall deposits

Maurizio Troiano [a], Piero Salatino [a], Roberto Solimene [b,*], Fabio Montagnaro [c]

[a] Dipartimento di Ingegneria Chimica, dei Materiali e della Produzione Industriale, Università degli Studi di Napoli Federico II, Piazzale Vincenzo Tecchio 80, 80125 Napoli, Italy
[b] Istituto di Ricerche sulla Combustione, Consiglio Nazionale delle Ricerche, Piazzale Vincenzo Tecchio 80, 80125 Napoli, Italy
[c] Dipartimento di Scienze Chimiche, Università degli Studi di Napoli Federico II, Complesso Universitario di Monte Sant'Angelo, 80126 Napoli, Italy

ARTICLE INFO

Article history:
Received 19 March 2014
Received in revised form 18 June 2014
Accepted 22 June 2014
Available online 28 June 2014

Keywords:
Particle–wall interaction
Entrained-flow
Slagging gasifiers
Wax
Resuspension phenomena

ABSTRACT

Particle–wall interaction is relevant to the performance of entrained-flow slagging gasifiers. Different micromechanical char–slag interaction patterns may establish, depending on the stickiness of the wall layer and of the impinging char particle. The main goal of this study is to improve the mechanistic understanding of particle–wall interactions, by using the tool of physical modeling. The idea behind this research campaign is to use molten wax as a surrogate of fuel ash. The wax had rheological/mechanical properties resembling those of a typical coal slag. Experiments have been carried out in a 0.10 m-ID lab-scale cold entrained-flow reactor, optically accessible, and equipped with a nozzle whence molten wax atomized into a mainstream of air. Reactor lengths in the range 0.1–0.6 m were investigated, while the wax was atomized at a temperature of 100–110 °C. Two interaction regimes were investigated: the "sticky wall–sticky particle" regime was simulated by setting the air mainstream and the wall temperatures at values beyond the wax melting range (160 °C and 140 °C, respectively); the "nonsticky wall–nonsticky particle" regime was simulated by setting both temperatures at 30 °C, i.e. well below the wax softening range. Assessment of the flow and segregation patterns was based on direct visual observation by means of a progressive scan CCD video camera, while the partitioning of the wax droplets into the different phases was characterized by their selective collection at the reactor exhaust. The micromechanics of particle–wall interactions in the "nonsticky–nonsticky" regime was analyzed on the basis of particle impact and of hydrodynamics of gas mainstream and jet flows. Threshold gas velocities for particle detachment were evaluated for the characterization of particle resuspension phenomena.

1. Introduction

Combustion and gasification under slagging conditions are key aspects of the design of modern entrained-flow reactors for thermal conversion of solid fuels, aimed at increasing the overall energy efficiency. In these systems, solid particles migrate toward the reactor walls, due to swirled/tangential flow induced in the reaction chamber and to turbophoresis, generating, thanks to the very high operating temperatures, a slag layer that flows along the reactor internal walls and is drained to the bottom of the reactor [1–6]. Understanding the phenomenology and proper design of slagging entrained-flow reactors requires the assessment of the fate of char particles as they impinge on the wall slag layer [7–10].

In a previous study, Montagnaro and Salatino [11] developed a phenomenological model that considers the establishment of a particle segregated phase in the near-wall region of the gasifier. In fact, it was highlighted that char particles impinging on the wall slag layer can either be entrapped inside the melt (a condition that hampers further progress of combustion/gasification), or adhere onto the slag layer's surface (progress of combustion/gasification is still possible in this case). In the latter case, and if the slag layer is extensively covered by char particles, a particle segregated phase may establish in the close proximity of the wall ash layer, where the excess impinging char particles that cannot be accommodated on the slag surface accumulate. This annular phase is slower than the lean particle-laden gas phase (that characterizes the entrained flow), so that the residence times of char particles are longer than the average gas space time, with a positive impact on carbon burn-off. Further studies, both experimental and theoretical, confirmed the soundness of this phenomenological framework [12–14].

Different micromechanical char–slag interaction patterns may establish, depending on the particle and the wall temperatures, on the solid/molten status of the particles impinging the slag layer or making up the slag itself, on the char conversion degree, on the particle kinetic energy, and on the surface tension [8,10,11,15]. In the present study,

* Corresponding author. Tel.: +39 081 7682248; fax: +39 081 5936936.
E-mail address: solimene@irc.cnr.it (R. Solimene).

http://dx.doi.org/10.1016/j.powtec.2014.06.039
0032-5910/

four different patterns are envisaged on the basis of the "stickiness degree" of the wall layer and of the impinging char particle:

- the material laying on the wall (prevailingly, inorganic ash) is "sticky" when the wall temperature is so high that ash is permanently kept in a molten status, generating a liquid slag layer. An additional condition for the slag layer to be sticky is that it must not be extensively covered by "nonsticky" char particles;
- the char particle is sticky when its temperature is beyond a critical value and the carbon conversion is beyond a given threshold, as the plastic behavior is emphasized when the content of refractory carbon decreases.

The four regimes are represented in Fig. 1: (*i*) sticky particle (*SP*) impinging on a sticky wall (*SW*); (*ii*) nonsticky particle (*NSP*) impinging on a sticky wall; (*iii*) sticky particle impinging on a nonsticky wall (*NSW*); (*iv*) nonsticky particle impinging on a nonsticky wall. Fig. 1 is complemented by Fig. 2, that shows how the different near-wall char–slag segregation regimes can occur along the reactor as carbon conversion increases. The fate of char particles depends on the complex mechanics of liquid–solid interphase interactions [1,3,11,16,17], that can determine rebound, splashing, coalescence, deposition, plunging, shattering, sticking and adhesion phenomena.

The present study lays along the path set by Troiano et al. [18] and aims at improving the mechanistic understanding of particle–wall interactions in entrained-flow systems, by using the tool of physical modeling. Particle–wall interactions are investigated in a lab-scale cold entrained-flow reactor, equipped with a nozzle whence molten wax atomized into a mainstream of air. The operating temperatures can be adjusted so as to tune the sticky–nonsticky behavior of both impinging wax droplets and wall layer. Assessment of flow and segregation patterns is based on a direct visual observation, as the reactor is optically accessible. The partitioning of the wax droplets/particles into the different phases is characterized by selective collection of ash leaving the reactor at the exhaust.

Troiano et al. [18] investigated the sticky wall–sticky particle (*SW–SP*) regime in a 0.04 m-ID reactor. They observed that the axial profiles of the fractional content of wax entrained in the dispersed phase closely conformed to values predicted by assuming idealized radial droplet trajectories in the jet and inertial impaction on the wall. In the present study the *SW–SP* regime is implemented in a larger reactor (0.10 m-ID) and the results are compared with those obtained in the *NSW–NSP* regime. A theoretical assessment of particle resuspension phenomena is developed for *NSW–NSP* regime, based on a quasi-static approach (force/moment balance), to determine threshold gas velocities that induce particle detachment from the wall surface.

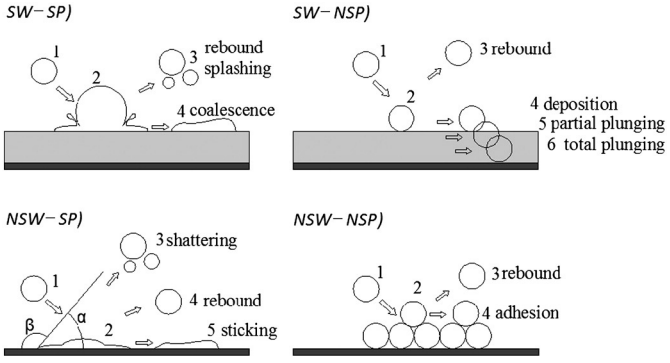

Fig. 1. Different micromechanical interaction patterns (*SW* stands for "sticky wall", *SP* for "sticky particle", *NSW* for "nonsticky wall" and *NSP* for "nonsticky particle"). (1) pre-impact, (2) impact, (3–6) post-impact.

2. Mechanistic background of particle adhesion and resuspension

Particle–wall interactions occurring during the *NSW–NSP* regime can be analyzed by considering the micromechanics of the impact of solid particles on a solid flat surface, on one side, and the mechanics of resuspension of attached particles from the wall, on the other.

Particle–wall collisions are generally characterized in terms of a restitution coefficient e, defined as the ratio between the rebound and the impact velocities. The coefficient takes the value $e = 1$ when the rebound is perfectly elastic, whereas $e \to 0$ when the particles dissipate their kinetic energy at the impact and adhere on the surface. The restitution coefficient embodies phenomena like elastic and plastic deformation of solid materials, surface contact forces and particle–wall friction. For collisions normal to a flat surface, the normal restitution coefficient is zero at impact velocities lower than a threshold value: the particles adhere on the surface as the impact energy is smaller than the adhesion energy [19]. The threshold impact velocity for particle capture, also called "capture velocity", is a function of particle size and density, particle surface energy and elastic properties of both particle and surface (Young's moduli and Poisson's ratios) [20]. For impact velocity larger than the capture velocity, rebound occurs. For elastic materials the normal restitution coefficient tends to approach 1, whereas for elastic–plastic materials the restitution coefficient increases with the impact velocity as far as the material shows elastic behavior. When the impact velocity is further increased, plastic deformation begins, inducing additional energy losses during the impact and a decrease of the normal restitution coefficient. The limiting velocity, above which plastic deformation occurs, is determined by the bulk properties of the particles and the wall and is independent of particle size [19–21]. When an oblique impact is considered, particle–wall friction expressed by the tangential restitution coefficient has to be taken into account [22,23]. Moreover, particle rolling and sliding may be active in this case.

Once adhered to the wall, particles may eventually be resuspended under the action of gas flow in the near-wall region. When the hydrodynamic forces overcome adhesion, the particle is detached from the wall and eventually dragged into the bulk gas flow. Three different mechanisms of particle detachment from a wall surface, namely lift-off, sliding and rolling [24], can be considered on the basis of force balances along the normal and tangential direction of wall surface and of a moment balance on a particle embedded in a viscous sublayer, respectively [25–28]. The threshold velocity for particle detachment from a vertical flat surface can be calculated by considering:

- normal force balance (lift-off mechanism)

$$F_L = F_{PO} \tag{1}$$

- tangential force balance (sliding mechanism)

$$F_D + F_G = k_S(F_{PO} - F_L) \tag{2}$$

- moment balance (rolling mechanism)

$$1.4\frac{d_p}{2}F_D + \frac{d_p}{2}F_G > a(F_{PO} - F_L) \tag{3}$$

where F_L is the lift force, F_{PO} the adhesion force, F_D the drag force and F_G the force due to gravity. Furthermore, k_s is the static coefficient of friction (a coefficient of 0.6 can be assumed), d_p is the particle diameter and a the contact radius between the particle and the surface. In the moment balance equation (Eq. (3)), the factor 1.4 accounts for the non-uniformity of the flow field [29]. F_L may be calculated as reported by Ziskind et al. [25] and Leighton and Acrivos [30] for a particle fully embedded in the viscous sublayer. F_{PO}, also called pull-off force, may be defined as the opposite of the force required to separate two bodies and it can be calculated according to the JKR model [31], revised for a rough

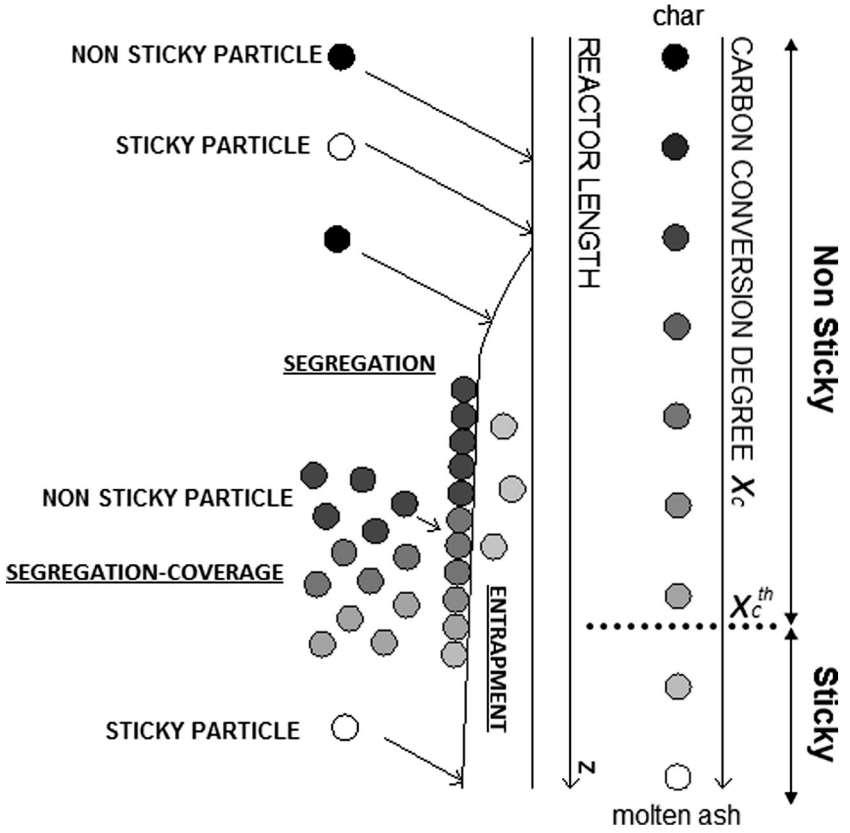

Fig. 2. Particle–wall micromechanical interactions and near-wall segregation regimes along the reactor axial coordinate z (X_C^{th} is the threshold value of the carbon conversion X_C).

surface (a ratio of rough-to-smooth pull-off forces was assumed equal to 0.06) [27,32]. F_D can be considered as the Stokes drag force, as the particle is completely embedded in the viscous sublayer, also taking into account the wall effect [29].

3. Experimental

3.1. The cold flow model reactor

A lab-scale cold flow model reactor has been designed and set up, aiming at reproducing the basic general features of the interaction between a lean-dispersed particle/droplet phase and a confining wall. The model reactor is outlined in Fig. 3.

The plastic/fluid behavior of softened or molten ash and of the wall slag layer has been simulated, at nearly ambient conditions, by molten wax as a surrogate of fuel ash. Waradur E™ (Völpker Spezialprodukte, Germany) was selected, as the rheological/mechanical properties of this wax (a refined material made from black raw montan wax) resembled those of a typical coal slag. Wax viscosity lies in the range 0.02–0.1 kg m^{-1} s^{-1} as the temperature ranges between 130 °C and 90 °C [33], and wax density is around 1000 kg m^{-3}. Accordingly, the kinematic viscosity is in the order of 10^{-5}–10^{-4} m^2 s^{-1}, consistent with values commonly reported in the literature for coal slag (viscosity and density on the order of 0.01–1 kg m^{-1} s^{-1} and 2500–3000 kg m^{-3}, respectively, in the temperature range 1200–1500 °C) [3,4,7,34]. The values of the kinematic viscosity of the wax are such to reproduce laminar flow of the molten phase along the reactor walls, as experienced during the operation of entrained-flow slagging gasifiers. Besides, taking into account the surface tension (0.03 kg s^{-2} at 100 °C), wax properties are such that the entrapment and over-layering criteria are not satisfied, and the segregation or segregation–coverage regimes are likely to be established, as expected for realistic particle–slag interaction in entrained-flow gasifiers [11,12].

The wax was liquefied and stored in a 9 L heated vessel. A three-way valve could be opened to convey the wax to the atomization nozzle through a heated horizontal tube. The atomization zone consisted of a plenum chamber, including a distributor plate, an atomizer positioning section and the nozzle. The atomization system generated a spray of molten wax in the model reactor which eventually gave rise, upon deposition onto the wall, to a layer of molten wax. The nozzle was a commercial Delavan™ air-assisted atomizer (AL model), designed so as to generate a spray of conical shape with an aperture angle of θ_{max} = 22–25° and a uniform cross-sectional distribution of droplets of 10–100 μm size (Fig. 4). The atomization air was fed directly to the nozzle, while a mainstream of air was fed sideways the atomization zone, flowing through a plenum chamber and a distributor plate in order to equalize the distribution of the mainstream air across the reactor. Both air streams can be preheated before entering the reactor.

The reactor consisted of a Pyrex™ tube (D = 0.10 m-ID) on which the atomizing system was fitted. The internal diameter of the reactor was chosen so that the atomized droplets could be given enough time to solidify during their flight toward the walls under *NSP* operating conditions. Accordingly, the impact of a fully solidified particle on a particle-covered dry wall could effectively be simulated. Moreover, the reactor could be heated and insulated to promote the establishment of a molten wax layer when investigation of the interaction of wax particles with a sticky wall was in order.

The features of the atomizer have been experimentally checked in ad hoc tests by operating the experimental rig without the Pyrex tube: (*i*) the jet aperture angle was characterized by analysis of images captured just below the atomizer nozzle; (*ii*) the size range of the generated droplets was determined by scanning electron microscopy (SEM) of

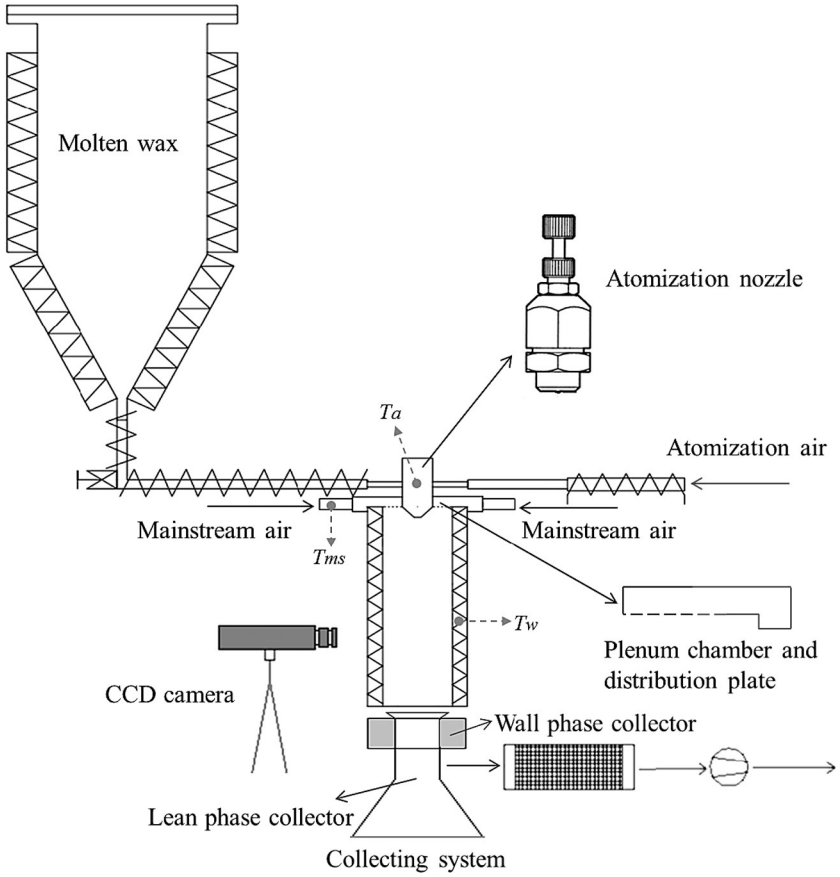

Fig. 3. Scheme (not to scale) of the downscaled cold flow model reactor with a detailed view of the atomization nozzle (T_a = atomization temperature; T_{ms} = mainstream temperature; T_w = wall temperature).

atomized wax particles collected by means of a beaker in *NSP* conditions. Experimental data obtained in these tests were consistent with the nozzle specifications.

3.2. Operating conditions

Experimental tests aimed at characterizing the general phenomenology of the interaction between the dispersed phase generated by the spray and the reactor walls, for the two extreme cases of *SW–SP* and *NSW–NSP* regimes. The main reactor design and operating parameters to simulate *SW–SP* and *NSW–NSP* regimes are listed in Table 1. The partitioning of the atomized wax between the dispersed and the wall phases was quantitatively assessed as a function of the distance from the nozzle. To accomplish this task, the reactor was equipped with a system for the collection of wax issuing from the reactor in either phase. This consisted, for testing in *SW–SP* regime, of a vacuum flask with a 0.09 m-OD inlet tube, collecting wax issuing in the lean phase, that was fitted with an outer annular section where wax flowing in the wall layer was collected. The collection system was equipped with a filter and a suction pump (Fig. 3). The mass flow rates in the dispersed phase and in the wall layer phase were obtained by dividing the amounts of wax cumulatively collected by the duration of the test. Measurements of partitioning in the *NSW–NSP* regime were carried out by means of a vacuum flask (0.12 m-OD) collecting wax in the lean phase, while the amount of wax on the walls was obtained by weighing the reactor before and after each experimental test. In any regime, the mass flow rate of wax conveyed in the dispersed phase ${W^{lean}}_{wax}(z = L)$ was worked out to calculate the fractional mass of wax in the dispersed phase at $z = L$, defined as:

$$y^{lean}(z = L) = \frac{W^{lean}_{wax}(z = L)}{W^{lean}_{wax}(z = 0)} \tag{4}$$

where L is the reactor length.

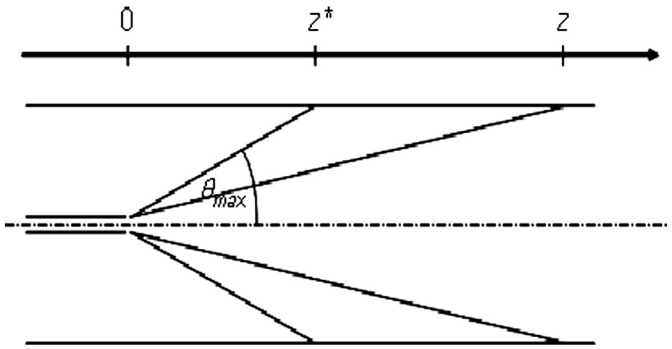

Fig. 4. Geometrical parameters of the jet in the model reactor.

Table 1
Main reactor design and operating parameters.

	SW–SP	*NSW–NSP*
Reactor internal diameter D [m]	0.1	0.1
Reactor length L [m]	0.1–0.6	0.1–0.45
Atomization temperature T_a [°C]	110	100
Mainstream temperature T_{ms} [°C]	160	30
Wall temperature T_w [°C]	140	30
Wax feeding rate ${W^{lean}}_{wax}(z = 0)$ [g s^{-1}]	0.6	0.2–0.3
Flow rate of mainstream air Q_{ms} [m^3 h^{-1} at 273 K]	5	1–20
Flow rate of atomization air Q_a [m^3 h^{-1} at 273 K]	0.275	0.275–0.8

Visual observation and recording of the wall layer was also accomplished by means of a progressive scan CCD video camera (Pulnix™ 6710) equipped with a magnifying zoom lens and a 0.02 m extension tube. This optical system permitted to perform video recordings at a distance of about 0.2 m from the reactor walls, focusing on an observation window left uncovered by the heating/insulating elements, without exposing the camera to unacceptable overheating. Images were digitized using a digital frame grabber (National Instruments™ PCI 1422 coupled with a PC). Frame-by-frame recording was accomplished at a sampling rate of 250 fps with a 0.013 m × 0.004 m recording window digitized as 648 × 198 square pixels (spatial resolution equal to about 20 μm). The temporal and spatial resolution of the video recordings did not permit to measure particle size and particle velocity distributions at the same time. However, video recordings were performed setting a video camera shutter time (1/250 s) long enough to apply the particle streak line technique [35,36]. This particle tracking technique has been used to characterize the phenomenology of particle–wall interactions since it enables the visualization of 10 μm sized particles even having a velocity of about 2 m s^{-1} moving toward the wall and impacting the solid surface, as well as the occurrence of adhesion, rebound and resuspension of adhered particles to the main gaseous flow. The qualitative characterization of particle–wall interactions has been pursued by frame-by-frame analysis of video recordings lasting 8 s during which a number of events (adhesion, rebound, or resuspension) in the order of thousands take place. It is noteworthy that, being the wall layer of molten wax transparent to visible radiation, the video recordings could always be performed during *SW–SP* experiments, whereas extensive particle layer deposition limited the frame-by-frame analysis to the first 30 s after spray injection during *NSW–NSP* experiments.

The actual status of the dispersed wax and of the wall layer of deposited wax could be controlled by adjusting the values of three temperatures:

- atomization temperature (T_a), i.e. the temperature at the atomization nozzle. This temperature must be set at values large enough to ensure good flowability and effective atomization of the wax. T_a was 110 °C and 100 °C for testing in *SW–SP* and *NSW–NSP* regimes, respectively;
- mainstream temperature (T_{ms}). This temperature determines the status of the wax immediately after atomization. Adjusting T_{ms} with respect to the wax temperature at which the liquid–solid transition occurs (around 85 °C for the wax used in the present study) enables accurate control of the physical status (liquid vs. solid) of the wax, as well as its viscosity. In this work, T_{ms} was fixed at 160 °C and 30 °C to simulate *SW–SP* and *NSW–NSP* regimes, respectively;
- wall temperature (T_w). This temperature can be varied to control the physical status and the viscosity of the wax accumulated on the wall. In this work, T_w was fixed at 140 °C and 30 °C to simulate *SW–SP* and *NSW–NSP* regimes, respectively.

In the present study, operating conditions were selected so as to reproduce the sticky wall–sticky particle (*SW–SP*) regime and the nonsticky wall–nonsticky particle (*NSW–NSP*) regime. The wax feeding rate was $W^{lean}{}_{wax}(z = 0) = 0.2–0.6$ g s^{-1}. The flow rate of mainstream air, Q_{ms}, and the flow rate of atomization air, Q_a, were treated as parameters for the purposes of exploring, evaluating and testing their effect on the phenomenology of interaction between the lean-dispersed phase and the wall layer. In particular, for the *NSW–NSP* regime, Q_{ms} ranged between 1 m^3 h^{-1} and 20 m^3 h^{-1} at 273 K (corresponding to a velocity range of about 0.04-0.8 m s^{-1}) while Q_a ranged between 0.275 m^3 h^{-1} and 0.8 m^3 h^{-1} at 273 K (corresponding to a normal-to-wall velocity component in proximity of the nozzle of about 8.5-25 m s^{-1}), with a reference case of 1 m^3 h^{-1} and 0.5 m^3 h^{-1}, respectively. Experiments in the *SW–SP* regime aimed at confirming and extending results obtained in the same regime but in a smaller (0.04 m-ID) reactor [18]. Q_a and Q_{ms} were fixed at 0.275 m^3 h^{-1} and 5 m^3 h^{-1} (at 273 K), respectively, in this case. Values of Q_a complied with the nozzle constraints and assured good wax atomization in terms of size and dispersion of droplets for both the investigated regimes. The reactor length L was varied to study the influence of the distance from the injection nozzle on the fractional mass of wax transferred form the lean-dispersed phase to the wall layer. Reactor ducts of different lengths were used for this purpose: L was varied in the 0.1–0.6 m range for the *SW–SP* case, and in the 0.1–0.45 m range for the *NSW–NSP* case.

4. Results and discussion

Experimental results included: (*a*) the quantitative assessment of the partitioning of atomized wax between the wall layer and the lean-dispersed phase entrained in the mainstream; (*b*) the qualitative and quantitative assessments of micromechanical interaction between impinging wax particles and the wall. The first goal was pursued by selective collection of entrained wax at the exit of the Pyrex duct, and the second by careful analysis of multiple events from close-up video recordings taken at the wall during the experiments.

4.1. Partitioning of atomized wax

4.1.1. Partitioning in the SW–SP regime and assessment of the influence of the scale of the model reactor

Fig. 5 compares results obtained in the present experimental campaign in the *SW–SP* regime with those obtained in a previous study [18] in a model reactor of smaller diameter ($D = 0.04$ m). The flow rate of the mainstream air was scaled as well, to keep the gas superficial velocity in the range of 0.25–0.30 m s^{-1}, values typical of industrial gasifiers. In this and in the following figures, experimental data are reported as average values of multiple tests (symbols), together with error bars corresponding to the standard deviation. Fig. 5 reports also the theoretical limiting curve for the *SW–SP* regime:

$$y^{lean}\left(\frac{z}{z^*}\right) = \begin{cases} 1 & \text{for } \frac{z}{z^*} < 1 \\ \left(\frac{z}{z^*}\right)^{-2} & \text{for } \frac{z}{z^*} \geq 1 \end{cases} \quad (5)$$

where $z^* = \frac{D}{2}\cot\theta_{max}$ (Fig. 4) and it is the axial coordinate corresponding to the intersection of the conical jet and the cylindrical reactor: $z^* =$ 0.1275 m for the 0.10 m-ID reactor (since, for this reactor, it is actually $D = 0.103$ m and $\theta_{max} = 22°$), $z^* = 0.043$ m for the previously operated 0.04 m-ID reactor ($\theta_{max} = 25°$ in this case). Eq. (5) is based on the following assumptions:

- the jet has a conical shape of fixed aperture;
- the atomized wax is evenly distributed across the jet;

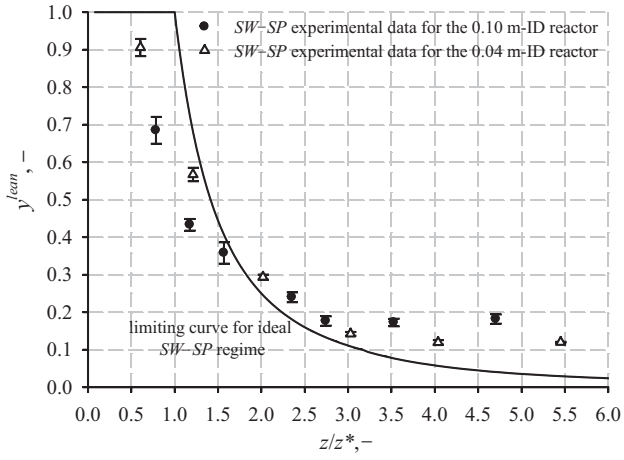

Fig. 5. *SW–SP* regime: effect of the reactor inner diameter on axial profiles of the fractional mass of wax in the dispersed phase (y^{lean}). The limiting curve represents the plot of the theoretical equation (Eq. (5)).

- the wax droplets approach the wall along radial trajectories departing from the nozzle (Fig. 4);
- the wax droplets impinge the wall under the effect of inertia and are deposited thereon without rebound.

The limiting curve shows that y^{lean} equals 1 at $z < z^*$, to decrease thereafter as a consequence of the bulk-to-wall transfer of the wax droplets.

Results obtained with the two model reactors are fairly coincident, within the experimental error, and demonstrate that no significant effect of scaling-up the reactor internal diameter is appreciated as far as the *SW–SP* regime is concerned. With reference to the 0.10 m-ID reactor, in the range of z/z^* from 0.78 ($z = 0.10$ m) to nearly 5 ($z = 0.6$ m), y^{lean} decreases from about 0.68 to asymptotically approach nearly 0.18. When the experimental data points are compared with the theoretical limiting curve it can be recognized that: (*i*) at $z/z^* > 1$, experimental data points approach the limiting curve, as the operating conditions effectively promoted the *SW–SP* regime; (*ii*) departure of experimental data at $z/z^* < 1$ is probably related to moderate backmixing of the dispersed phase associated with recirculation and entrainment in the mainstream gas establishing close to the nozzle.

4.1.2. Partitioning of wax: SW–SP versus NSW–NSP regimes

Fig. 6 shows results obtained under comparable hydrodynamic conditions ($Q_a = 0.275$ m^3 h^{-1}; $Q_{ms} = 5$ m^3 h^{-1}) when the particle–wall interaction regime is switched from *SW–SP* to *NSW–NSP*. This switch was simply accomplished by changing the mainstream temperature from 160 °C to 30 °C and the wall temperature from 140 °C to 30 °C, i.e. setting both temperatures at values well below the softening limit of the wax. It must be underlined that even at these temperatures wax particles exhibited plastic behavior upon impingement, a feature that is certainly relevant to the micromechanical interaction with the wall, as it will be discussed later.

Values of y^{lean} are plotted against the axial coordinate z of the reactor. The limiting line corresponding to the idealized *NSW–NSP* regime (the wall reflects impinging particles according to a nearly elastic interaction pattern, thus $y^{lean} = 1$ for any z) and that for the idealized *SW–SP* regime (see Eq. (5)) are reported as a reference. Switching from *SW–SP* to *NSW–NSP* regimes significantly affects wax partitioning. y^{lean} is systematically larger in the *NSW–NSP* regime along the reactor, approaching a value of nearly 0.4 for $z/z^* \gg 1$ ($z^* = 0.1275$ m), compared with 0.18 observed in the *SW–SP* regime. It is remarkable that, though larger than for the *SW–SP* regime, y^{lean} in the *NSW–NSP* regime is still substantially smaller than 1. This finding is consistent with the establishment of a near-wall segregated particle layer under the combined effect of the hydrodynamics of the confined multiphase flow, of particle adhesion/rebound and resuspension, as it will be discussed later.

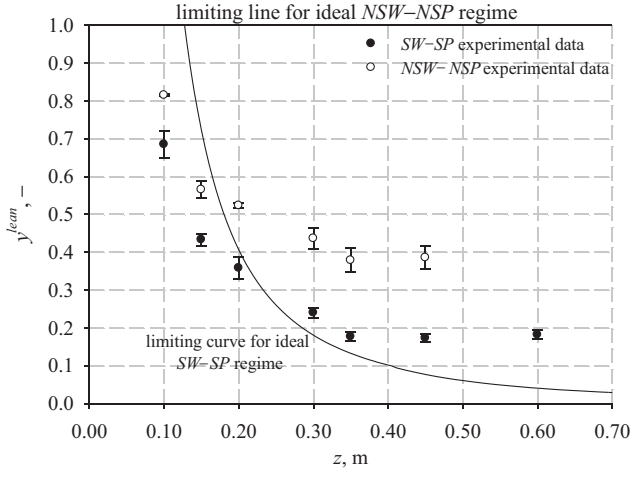

Fig. 6. Partitioning of wax: *SW–SP* versus *NSW–NSP* regime. The limiting curves representing the *NSW–NSP* and the *SW–SP* regimes are plotted as a reference.

4.1.3. Partitioning in the NSW–NSP regime: effect of operating conditions

Figs. 7–11 report the effect of the reactor operational variables on the extent and pattern of wax partitioning in the *NSW–NSP* regime.

Fig. 7 shows partitioning data at a fixed flow rate of mainstream air ($Q_{ms} = 1$ m^3 h^{-1}) while varying the flow rate of atomization air (Q_a) between 0.275 m^3 h^{-1} and 0.8 m^3 h^{-1}. Analysis of experimental data indicates that:

- increasing the atomization air flow rate shifts data points toward the *NSW–NSP* limiting line. A threshold value of Q_a is found at around 0.5–0.6 m^3 h^{-1} above which the limiting *NSW–NSP* curve is approached, under the operating conditions adopted;
- at Q_a smaller than 0.5 m^3 h^{-1}, y^{lean} decreases along with z as entrained wax is deposited on the wall. At large values of z, y^{lean} approaches 0.38 ($Q_a = 0.275$ m^3 h^{-1}), 0.53 ($Q_a = 0.4$ m^3 h^{-1}) and 0.66 ($Q_a = 0.5$ m^3 h^{-1}).

Trends of data points in Fig. 7 may be explained by considering that increasing Q_a brings about a reduction of the size of the wax particles, that can therefore more easily solidify along their trajectory to the wall. Moreover, as Q_a is increased, jet–wall interference and turbulence are promoted. Both these effects enhance particle resuspension, hence increase y^{lean}. Fig. 8 reports two SEM micrographs of the wax particles collected in the lean phase for $Q_a = 0.275$ m^3 h^{-1} (left) and $Q_a = 0.4$ m^3 h^{-1} (right). It is shown that the mean size of wax particles decreases with increasing Q_a.

Fig. 9 reports pictures of the Pyrex duct of the reactor after experimental testing in the *NSW–NSP* regime at two levels of Q_a, namely 0.5 m^3 h^{-1} and 0.8 m^3 h^{-1}. The other operational parameters, namely Q_{ms} and L, were kept at 1 m^3 h^{-1} and 0.45 m, respectively. In order to improve observation of wax deposits on the inner surface of the transparent duct, a black paper stripe was inserted into the tube to provide a dark background: accordingly, the darker the appearance of the tube, the smaller the surface coverage. During tests at $Q_a = 0.5$ m^3 h^{-1}, particles accumulate nearly uniformly along the tube, except over the last 0.1–0.15 m, consistently with the finding of a nearly constant value of y^{lean}. Increasing Q_a up to 0.8 m^3 h^{-1} results in larger jet velocities and jet-induced turbulence which contribute to prevent particle accumulation in the pre-impact zone ($z/z^* < 1$). Correspondingly the fractional mass of wax in the dispersed phase is larger, consistently with results in Fig. 7.

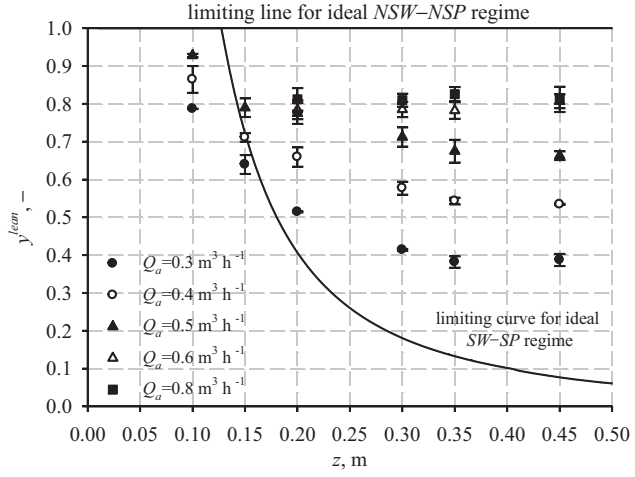

Fig. 7. *NSW–NSP* regime: effect of the atomization air flow rate (Q_a) on axial profiles of the fractional mass of wax in the dispersed phase (y^{lean}). Flow rate of mainstream air set at 1 m^3 h^{-1}. The limiting curves representing the *NSW–NSP* and the *SW–SP* regimes are plotted as a reference.

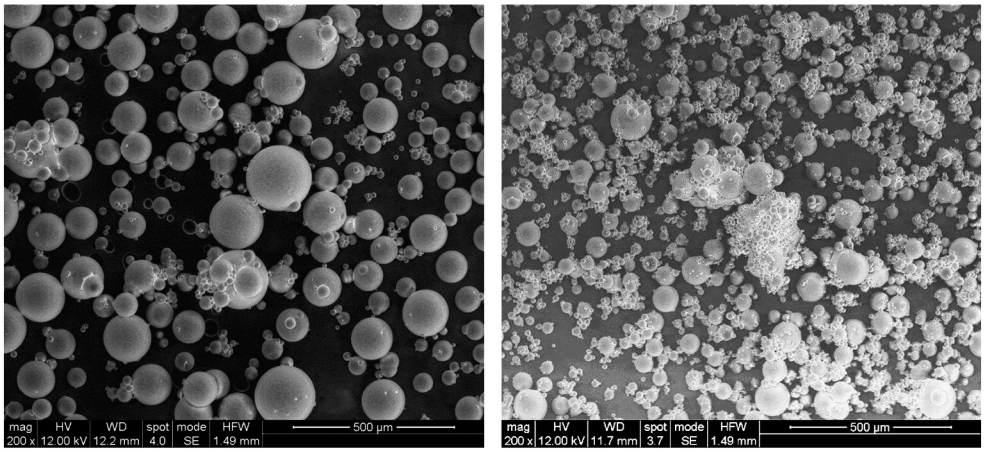

Fig. 8. SEM images of the wax particles collected in the lean phase for $Q_a = 0.275\ m^3\ h^{-1}$ (left) and $Q_a = 0.4\ m^3\ h^{-1}$ (right).

Fig. 10 reports the effect of the mainstream gas flow rate on wax deposition. Plots compare y^{lean} data for Q_{ms} ranging from 1 $m^3\ h^{-1}$ to 20 $m^3\ h^{-1}$, Q_a being fixed at 0.5 $m^3\ h^{-1}$. Profiles of y^{lean} along z are shifted toward the *SW–SP* limiting curve as the flow rate of the mainstream air increases. It is likely that the following processes concur to this somewhat unexpected trend:

- increasing the mainstream rate suppresses the vortical turbulent structure establishing at the location where the jet interferes with the wall, hence reduces resuspension of particles;
- increasing the mainstream rate may enhance near-wall particle segregation patterns of hydrodynamical nature, due to the formation of a "lean core-dense annulus" particle-laden flow, similar to the dense-dispersed phase postulated by Montagnaro and Salatino [11].

The qualitative patterns of particle deposition on the Pyrex duct in the *NSW–NSP* regime are reported in Fig. 11. Patterns corresponding to different values of Q_{ms} are compared, keeping $Q_a = 0.5\ m^3\ h^{-1}$ and $L = 0.45$ m. For $Q_{ms} = 1\ m^3\ h^{-1}$, particles accumulate nearly uniformly along the tube length, except over the lowest 0.1 m, similarly to what is reported in Fig. 9. For $Q_{ms} = 20\ m^3\ h^{-1}$ the deposition pattern is different. Particles accumulate in a relatively compact form in the upper part of the duct (i.e. the pre-impact/impact zone). Accumulation takes place in the lower duct too, but with a different morphology, as deposits have the appearance of loosely connected particle clusters, a feature that is consistent with a prevailingly hydrodynamical nature of near-wall particle segregation in this section of the duct.

4.2. Phenomenology of particle–wall micromechanical interaction

The phenomenology of droplets/liquid layer interaction in the 0.10 m-ID reactor for the *SW–SP* regime closely conforms to qualitative interaction patterns reported and discussed by Troiano et al. [18] for the same regime in a 0.04 m-ID reactor. Coalescence was by far the predominant process following the impact of sticky particles on the sticky wall, though occasional droplet resuspension into the dispersed phase was observed.

Much more complex is the phenomenology in the *NSW–NSP* regime. Video recordings were performed in this case locating the CCD camera at three different levels, namely 0.1 m, 0.15 m and 0.2 m from the nozzle (denoted as pre-impact, impact and post-impact zones, respectively). Two mainstream gas flow rates ($Q_{ms} = 1\ m^3\ h^{-1}$ and $Q_{ms} = 10\ m^3\ h^{-1}$) were investigated, while Q_a was fixed at 0.5 $m^3\ h^{-1}$. Analysis of video recordings enabled to track the fate of individual particles, to count the number of particles touching the wall, those undergoing adhesion and those being resuspended into the mainstream. Figs. 12 and 13 show a particle–wall impact/rebound event following a collision and a particle resuspension event due to entrainment in the gas flow, respectively. In particular, Fig. 12 shows the pre-impact and post-

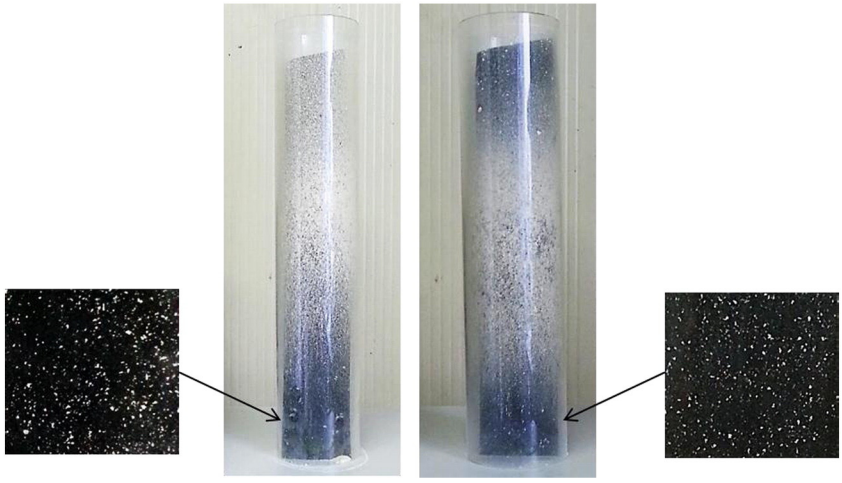

Fig. 9. Effect of the atomization air flow rate Q_a on the distribution pattern of wax particles on the walls. Left: $Q_a = 0.5\ m^3\ h^{-1}$; right: $Q_a = 0.8\ m^3\ h^{-1}$. Q_{ms} was fixed at 1 $m^3\ h^{-1}$ for both the test cases. $L = 0.45$ m. A black paper stripe, inserted in the tube, provides a dark background for improved observation of wax deposits on the inner duct.

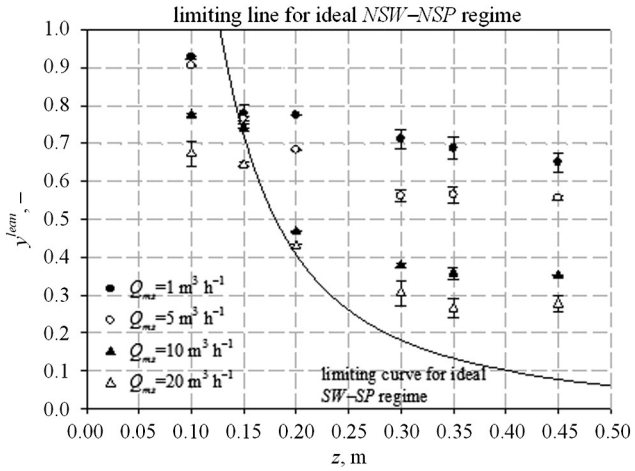

Fig. 10. *NSW–NSP* regime: effect of the flow rate of mainstream air (Q_{ms}) on axial profiles of the fractional mass of wax in the dispersed phase (y^{lean}). Flow rate of atomization air set at 0.5 m^3 h^{-1}. The limiting curves representing the *NSW–NSP* and the *SW–SP* regimes are plotted as a reference.

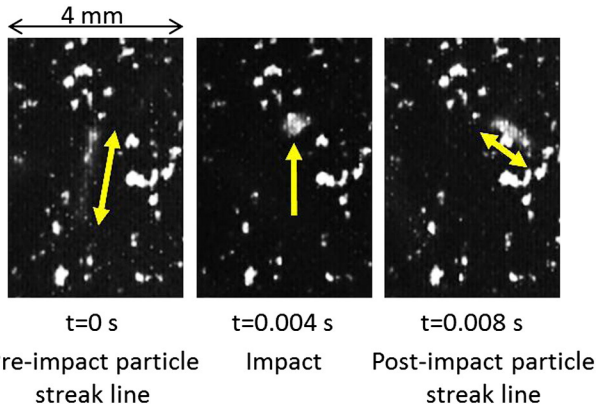

Fig. 12. Evidence of an impact/rebound event captured during video recording.

impact particle streak lines, corresponding to the rebound event. Fig. 13 shows how an adhered particle (frame a) rotates and/or rolls along the wall (frames b–e) and eventually is detached and resuspended into the mainstream, as made evident by the particle streak line (frame f). Particle resuspension due to impinging particles was never observed during the video recordings.

Analysis of frames captured at $Q_{ms} = 1$ m^3 h^{-1} and at $z = 0.1$ m from the nozzle, namely in the pre-impact zone of the duct, indicated that nearly 50% of particles hitting the wall surface adhered thereon, whereas the total fraction of particles transferred to the lean phase due to rebound and resuspension phenomena was estimated in the order of 0.5. The occurrence of rebound and resuspension phenomena was comparable. Resuspension phenomena were typically observed for larger particles and clusters of particles. Increasing z, the distance from the nozzle, namely $z = 0.15$ m (impact zone, z nearly equal to z^*) and $z = 0.2$ m (post-impact zone), the visual observations highlight that the frequency of particle–wall collisions and the occurrence of particle resuspension decrease. In particular, at $z = 0.15$ m and $z = 0.2$ m the fraction of particles transferred back into the mainstream is 0.26 and 0.13, respectively. In particular, video recordings highlighted that the occurrence of rebound events sharply decreased with the distance from the nozzle. As a consequence, particle transfer back to the mainstream flow was mostly due to resuspension.

The phenomenology of particle–wall interactions can be analyzed in the light of the hydrodynamics of gas flow and particle trajectories outlined in Fig. 14. The overall gas flow structure results from overlapping of the conical jet flow issuing from the nozzle and the mainstream flow directed along the reactor axis. The outer jet gives rise, upon interaction with the wall, to flow patterns resembling those of confined oblique stagnation flows [37], with possible establishment of recirculation patterns. As atomized particles approach the reactor wall along jet trajectories, they may either be entrained in the vortical structure establishing in the pre-impact opposed flow region (particle *A*), or be swept into the mainstream gas flow (particle *B*) in the post-impact assisted flow region. The relative importance of the mainstream flow and of the oblique stagnation flow of the outer jet is determined by the ratio between the jet and mainstream gas flow rates, which rules the level of turbulence in the pre-impact, impact and post-impact regions. The oblique stagnation flow patterns prevail at small mainstream flow rates, whereas they are suppressed at high mainstream flow rates. The vortical structure establishing close to the stagnation region ($z = z^*$) is relevant to particle resuspension, which can be assessed by calculation of the threshold gas velocity corresponding to particle detachment by lift-off, sliding or rolling, as described in Section 2. The pull-off force is a function of the particle–surface thermodynamic work of adhesion, which was estimated, for wax particles on a Pyrex surface, as 0.346 J m^{-2} [38–40]. Furthermore, the contact radius at separation is a function of the particle–surface composite Young's modulus,

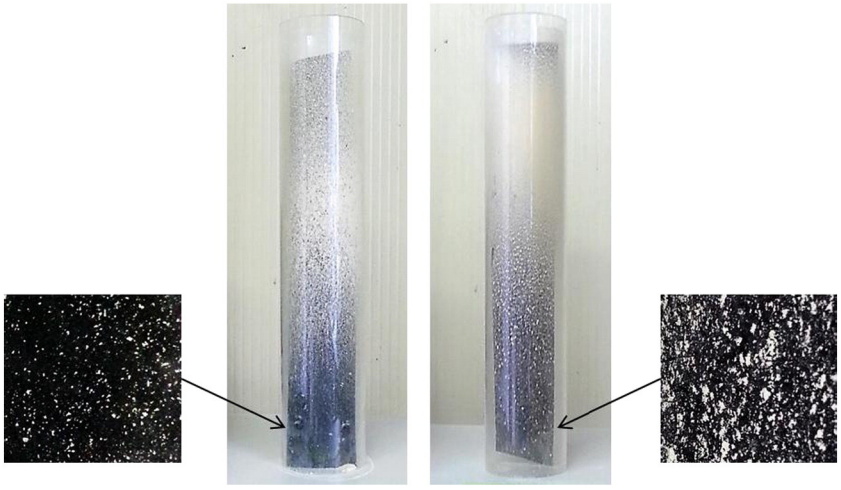

Fig. 11. Effect of the mainstream air flow rate Q_{ms} on the distribution pattern of wax particles on the walls. Left: $Q_{ms} = 1$ m^3 h^{-1}; right: $Q_{ms} = 20$ m^3 h^{-1}. Q_a was fixed at 0.5 m^3 h^{-1} for both the test cases. $L = 0.45$ m. A black paper stripe, inserted in the tube, provides a dark background for improved observation of wax deposits on the inner duct.

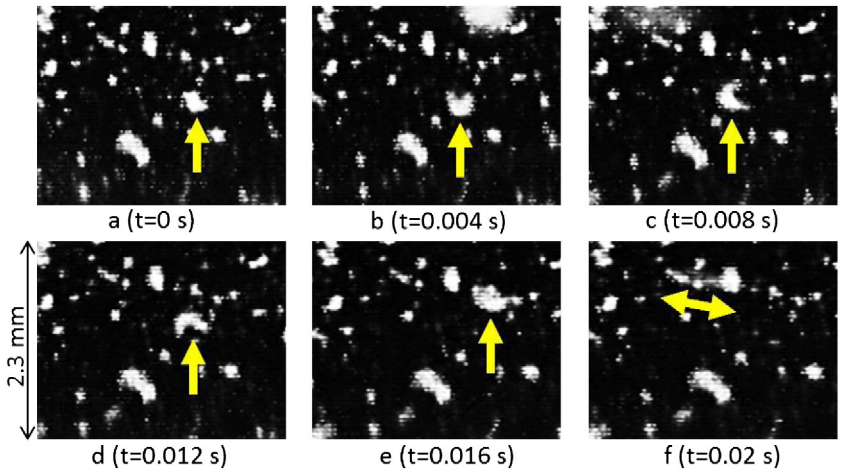

Fig. 13. Evidence of a resuspension event captured during video recording. a): particle adhered on the wall surface; b)–e): particle rotates clockwise and rolls; f) particle streak line after resuspension.

which was 4/3 GPa for wax particles on Pyrex surface [40]. Solving Eqs. (1)–(3), threshold velocities for lift-off, sliding and rolling were in the order of 56 m s^{-1}, 46 m s^{-1} and 1 m s^{-1}, respectively, for particle diameter $d_p = 100$ μm. When these velocities are compared with peak gas velocities expected in the vicinity of the wall from the combination of mainstream and jet flow (≅4 m s^{-1}), it is concluded that lift-off and sliding are not likely to occur to any appreciable extent, while rolling is the dominant mechanism for particle detachment, in agreement with results from literature [24,27]. The effect of rolling might be further emphasized if one considers that burst-sweep events may occur in the viscous sublayer, causing the occasional increase of the flow velocities [41–44]. This phenomenon can facilitate particle resuspension by lowering the detachment velocity by a factor of nearly 2.

It is noteworthy that the jet velocity (≅4 m s^{-1}) near the wall at the impact zone ($z = z^*$) is larger than the threshold gas velocity for rolling, whereas the overall mean gas velocity (0.06 m s^{-1}) is smaller. This finding confirms that resuspension is mainly related to interference of the gas jet with the wall, which dominates the hydrodynamics under these operating conditions. Rebound is relevant in the pre-impact zone, due to high normal-to-wall component of the velocity of the particles, whereas it is strongly reduced in the post-impact zone where jet streamlines are deflected by the mainstream flow.

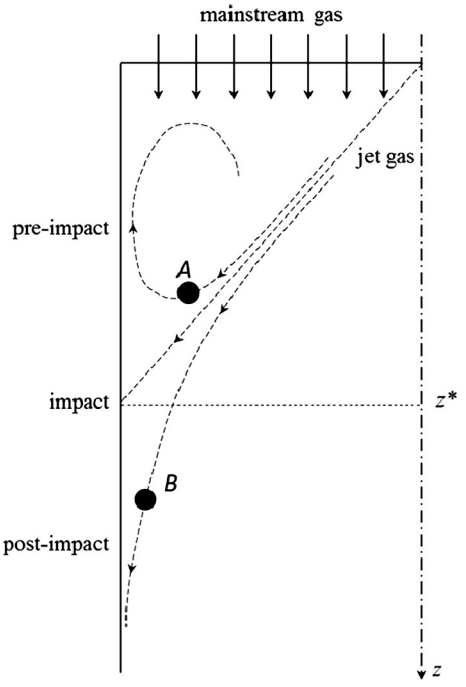

Fig. 14. Hydrodynamic patterns induced by mainstream and jet gas flows and their influence on particle trajectories.

As discussed above, increasing the mainstream flow suppresses the jet-induced turbulence and recirculation in the pre-impact and impact zones. This is confirmed by visual observation of wall interaction patterns as the mainstream air flow rate is increased up to $Q_{ms} = 10$ m^3 h^{-1}. The frequency of collisions at any z is only slightly smaller than that observed at $Q_{ms} = 1$ m^3 h^{-1}. The fraction of particles transferred to the mainstream flow is 0.20, 0.28 and 0.08, at $z = 0.1$ m, $z = 0.15$ m and $z = 0.2$ m, respectively. Under these operating conditions, particle transfer to the mainstream flow was largely due to resuspension, while only occasional rebound occurred. The comparison of these results with those observed at $Q_{ms} = 1$ m^3 h^{-1} further confirms the key role of mainstream and oblique stagnation jet flows in the balance between deposition and resuspension phenomena that ultimately leads to near-wall particle segregation in entrained flow.

5. Conclusions

The mechanics of particle–wall interactions in confined entrained flows, relevant to the fate of char and ash particles in entrained-flow slagging reactors, has been investigated by means of physical modeling. Molten wax is used as surrogate of fuel ash, and is air-atomized in an optically accessible 0.10 m-ID lab-scale cold entrained-flow reactor. Two interaction conditions were investigated, namely the "sticky wall–sticky particle" and the "nonsticky wall–nonsticky particle" regimes. Assessment of the flow and segregation patterns was based on: (*a*) quantitative assessment of the partitioning of atomized wax between the dispersed phase and the wall-deposited layer; (*b*) direct visual observation and video recording of particle–wall interaction at selected positions in the reactor. Wax loading in the lean-dispersed phase decreased with increasing distance from the atomizing nozzle, as increasingly large amounts of wax were deposited onto the wall. The fractional wax content in the lean-dispersed phase at the exhaust was minimum (≅18%) in the *SW–SP* regime, whereas it was larger in the *NSW–NSP* regime, ranging between 40% and 80% as the atomizing gas flow rate increased from 0.3 m^3 h^{-1} to 0.8 m^3 h^{-1}. The mainstream gas flow rate exerted a remarkable influence on the extent of wax deposition. The fractional wax content in the lean-dispersed phase decreased as the mainstream flow rate increased. This somewhat unexpected result was explained by considering the interaction between the mainstream flow and the oblique stagnation flow typical of the outer jet. Increasing

the mainstream rate moderates stagnation effects and suppresses local turbulence which is largely responsible for particle resuspension, thus favoring the stratification and segregation of particles in the near-wall region of the duct. This hypothesis is confirmed by close-up observation of particle–wall interaction patterns. A simple analysis of particle resuspension suggests that lift-off and sliding are not relevant to particle resuspension, whereas the rolling mechanism may be active under the experimental conditions tested even for the finer particles, and be responsible for resuspension when strong jet–wall interference takes place.

Nomenclature

a	particle–surface contact radius [m]
D	reactor internal diameter [m]
d_p	particle diameter [m]
e	coefficient of restitution [−]
F_D	drag force [N]
F_G	gravity force [N]
F_L	lift force [N]
F_{PO}	pull-off (adhesion) force [N]
k_S	static friction coefficient [−]
L	reactor length [m]
Q_a	flow rate of atomization air [$m^3\ h^{-1}$]
Q_{ms}	flow rate of mainstream air [$m^3\ h^{-1}$]
T_a	atomization temperature [°C]
T_{ms}	mainstream temperature [°C]
T_w	wall temperature [°C]
$W^{lean}{}_{wax}$	mass flow rate of wax in the dispersed phase [$g\ s^{-1}$]
X_C	carbon conversion degree [−]
X_C^{th}	threshold X_C-value [−]
y^{lean}	fractional mass of wax in the dispersed phase [−]
z	reactor axial coordinate [m]
z^*	critical axial coordinate (Fig. 4) [m]
θ_{max}	aperture angle of the conical spray [°]

Acknowledgments

The present study has been carried out in the framework of the project: “Ricerca di Sistema — Accordo MiSE-CNR Gruppo Tematico Carbone Pulito — Fondo per il Finanziamento Attività di Ricerca e Sviluppo di Interesse Generale per il Sistema Elettrico Nazionale”. The authors wish to express their gratitude to Völpker Spezialprodukte GmbH (Germany), for supplying the wax Waradur E™.

References

[1] T. Shimizu, H. Tominaga, A model of char capture by molten slag surface under high-temperature gasification conditions, Fuel 85 (2006) 170–178.
[2] T. Melchior, M. Bläsing, G. Pütz, M. Müller, Surface tension measurements of coal ash slags under reducing conditions at elevated pressures, Fuel 90 (2011) 280–287.
[3] J. Ni, G. Yu, Q. Guo, Z. Zhou, F. Wang, Submodel for predicting slag deposition formation in slagging gasification systems, Energy Fuel 25 (2011) 1004–1009.
[4] W. Song, Y. Sun, Y. Wu, Z. Zhu, S. Koyama, Measurement and simulation of flow properties of coal ash slag in coal gasification, AIChE J. 57 (2011) 801–818.
[5] C. Higman, S. Tam, Advances in coal gasification, hydrogenation, and gas treating for the production of chemicals and fuels, Chem. Rev. 114 (2013) 1673–1708.
[6] J. Wang, H. Liu, Q. Liang, J. Xu, Experimental and numerical study on slag deposition and growth at the slag tap hole region of Shell gasifier, Fuel Process. Technol. 106 (2013) 704–711.
[7] G.N. Shannon, P.L. Rozelle, S.V. Pisupati, S. Sridhar, Conditions for entrainment into a FeO_X containing slag for a carbon-containing particle in an entrained coal gasifier, Fuel Process. Technol. 89 (2008) 1379–1385.
[8] S. Li, K.J. Whitty, Physical phenomena of char–slag transition in pulverized coal gasification, Fuel Process. Technol. 95 (2012) 127–136.
[9] M. Losurdo, H. Spliethoff, J. Kiel, Ash deposition modeling using a visco-elastic approach, Fuel 102 (2012) 145–155.
[10] L. Chen, S.Z. Yong, A.F. Ghoniem, Modeling the slag behavior in three dimensional CFD simulation of a vertically-oriented oxy-coal combustor, Fuel Process. Technol. 112 (2013) 106–117.
[11] F. Montagnaro, P. Salatino, Analysis of char–slag interaction and near-wall particle segregation in entrained-flow gasification of coal, Combust. Flame 157 (2010) 874–883.
[12] F. Montagnaro, P. Brachi, P. Salatino, Char–wall interaction and properties of slag waste in entrained-flow gasification of coal, Energy Fuel 25 (2011) 3671–3677.
[13] F. Ambrosino, A. Aprovitola, P. Brachi, F.S. Marra, F. Montagnaro, P. Salatino, Investigation of char–slag interaction regimes in entrained-flow gasifiers: linking experiments with numerical simulations, Combust. Sci. Technol. 184 (2012) 871–887.
[14] F. Ambrosino, A. Aprovitola, P. Brachi, F.S. Marra, F. Montagnaro, P. Salatino, Entrained-flow gasification of coal under slagging conditions: relevance of fuel–wall interaction and char segregation to the properties of solid wastes, Fuel 114 (2013) 44–55.
[15] S.Z. Yong, M. Gazzino, A. Ghoniem, Modeling the slag layer in solid fuel gasification and combustion — formulation and sensitivity analysis, Fuel 92 (2012) 162–170.
[16] S.S. Yoon, P.E. Desjardin, C. Presser, J.C. Hewson, C.T. Avedisian, Numerical modeling and experimental measurements of water spray impact and transport over a cylinder, Int. J. Multiphase Flow 32 (2006) 132–157.
[17] K.L. Pan, C.K. Law, Dynamics of droplet–film collision, J. Fluid Mech. 587 (2007) 1–22.
[18] M. Troiano, R. Carbone, F. Montagnaro, P. Salatino, R. Solimene, A lab-scale cold flow model reactor to investigate near-wall particle segregation relevant to entrained-flow slagging coal gasifiers, Fuel 117 (2014) 1267–1273.
[19] L.N. Rogers, J. Reed, The adhesion of particles undergoing an elastic–plastic impact with a surface, J. Phys. D. Appl. Phys. 17 (1984) 677–689.
[20] C. Thornton, Z. Ning, A theoretical model for the stick/bounce behaviour of adhesive, elastic–plastic spheres, Powder Technol. 99 (1998) 154–162.
[21] S. Wall, W. John, H.C. Wang, S.L. Goren, Measurements of kinetic energy loss for particles impacting surfaces, Aerosol Sci. Technol. 12 (1990) 926–946.
[22] R.M. Brach, P.F. Dunn, Models of rebound and capture for oblique microparticle impacts, Aerosol Sci. Technol. 29 (1998) 379–388.
[23] D.A. Gorham, A.H. Kharaz, The measurement of particle rebound characteristics, Powder Technol. 112 (2000) 193–202.
[24] A.H. Ibrahim, P.F. Dunn, R.M. Brach, Microparticle detachment from surfaces exposed to turbulent air flow: controlled experiments and modeling, J. Aerosol Sci. 34 (2003) 765–782.
[25] G. Ziskind, M. Fichman, C. Gutfinger, Adhesion moment model for estimating particle detachment from a surface, J. Aerosol Sci. 28 (1997) 623–634.
[26] M. Guingo, J.P. Minier, A new model for the simulation of particle resuspension by turbulent flows based on a stochastic description of wall roughness and adhesion forces, J. Aerosol Sci. 39 (2008) 957–973.
[27] A.H. Ibrahim, P.F. Dunn, M.F. Qazi, Experiments and validation of a model for microparticle detachment from a surface by turbulent air flow, J. Aerosol Sci. 39 (2008) 645–656.
[28] I. Goldasteh, G. Ahmadi, A.R. Ferro, Monte Carlo simulation of micron size spherical particle removal and resuspension from substrate under fluid flows, J. Aerosol Sci. 66 (2013) 62–71.
[29] M.E. O'Neill, A sphere in contact with a plane wall in a slow linear shear flow, Chem. Eng. Sci. 23 (1968) 1293–1298.
[30] D. Leighton, A. Acrivos, The lift on a small sphere touching a plane in the presence of a simple shear flow, Z. Angew. Math. Phys. 36 (1985) 174–178.
[31] K.L. Johnson, K. Kendall, A.D. Roberts, Surface energy and the contact of elastic solids, Proc. R. Soc. Lond. A Math. Phys. Sci. 324 (1971) 301–313.
[32] W. Cheng, P.F. Dunn, R.M. Brach, Surface roughness effects on microparticle adhesion, J. Adhes. 78 (2002) 929–965.
[33] R. Li, N. Ashgriz, S. Chandra, J.R. Andrews, Shape and surface texture of molten droplets deposited on cold surfaces, Surf. Coat. Technol. 202 (2008) 3960–3966.
[34] M.A. Duchesne, A.Y. Ilyushechkin, R.W. Hughes, D.Y. Lu, D.J. McCalden, A. Macchi, E.J. Anthony, Flow behaviour of slags from coal and petroleum coke blends, Fuel 97 (2012) 321–328.
[35] C.T. Crowe, J.D. Schwarzkopf, M. Sommerfeld, Y. Tsuji, Multiphase Flows With Droplets and Particles, second ed. CRC Press, Boca Raton, 2012.
[36] M. Sommerfeld, N. Huber, Experimental analysis and modelling of particle–wall collisions, Int. J. Multiphase Flow 25 (1999) 1457–1489.
[37] C.Y. Wang, The unsteady oblique stagnation point flow, Phys. Fluids 28 (1985) 2046–2049.
[38] F. Restagno, J. Crassous, C. Cottin-Bizonne, E. Charlaix, Adhesion between weakly rough beads, Phys. Rev. E Stat. Nonlinear Soft Matter Phys. 65 (2002) 042301/1–042301/4.
[39] J. Drelich, G.W. Tormoen, E.R. Beach, Determination of solid surface tension from particle–substrate pull-off forces measured with the atomic force microscope, J. Colloid Interface Sci. 280 (2004) 484–497.
[40] S.R. Annapragada, D. Sun, S.V. Garimella, Prediction of effective thermo-mechanical properties of particulate composites, Comput. Mater. Sci. 40 (2007) 255–266.
[41] M. Soltani, G. Ahmadi, On particle adhesion and removal mechanisms in turbulent flows, J. Adhes. Sci. Technol. 8 (1994) 763–785.
[42] M. Soltani, G. Ahmadi, Direct numerical simulation of particle entrainment in turbulent channel flow, Phys. Fluids 7 (1995) 647–657.
[43] G. Ziskind, M. Fichman, C. Gutfinger, Resuspension of particulates from surfaces to turbulent flows — review and analysis, J. Aerosol Sci. 26 (1995) 613–644.
[44] C. Marchioli, A. Soldati, Mechanisms for particle transfer and segregation in a turbulent boundary layer, J. Fluid Mech. 468 (2002) 283–315.